KATHOLIEKE UNIVERSITEIT LEUVEN
FACULTEIT WETENSCHAPPEN
DEPARTEMENT CHEMIE
AFDELING MOLECULAIR DESIGN EN SYNTHESE
Celestijnenlaan 200F, B-3001 Leuven, België

STUDY OF ORIGIN, IMPACT AND SOLUTIONS OF PROCESSING DAMAGE IN LOW DIELECTRIC CONSTANT MATERIALS FOR ADVANCED INTERCONNECT APPLICATIONS

Examencommissie:
Prof. Dr. Stefan De Gendt (promotor)
Prof. Dr. Marc Heyns (co-promotor)
Prof. Dr. Chris Vinckier
Prof. Dr. Valeri Afanasiev
Prof. Dr. Shaun Carl
Prof. Dr. Chris Van Haesendonck
Dr. Mikhail Baklanov (IMEC)
Dr. Denis Shamiryan (IMEC)
Dr. Thierry Chevolleau (CNRS)

Proefschrift ingediend tot het behalen van de graad van Doctor in de Wetenschappen

door

Adam Urbanowicz

September 2010

In samenwerking met

imec *vzw*
International Micro-elektronica Centrum vzw
Kapeldreef 75
B-3001 Leuven, Belgium

ISBN 978-90-8649-358-6
D/2010/10.705/51

"Knowledge is recognizing what you know and what you don't."

Confucius

Preface

First I would like to acknowledge all my advisors and supervisors during my PhD. In alphabetical order they are Mikhail Baklanov, Stefan De Gendt, Marc Heyns, Ewa Rysiakiewicz-Pasek, Denis Shamiryan and Chris Vinckier. Their help was crucial to initiate, build and publish this PhD research on plasma damage of low-*k* materials. Their long experience and interest in sciences provided me with a daily example and reference to follow.

Next, I acknowledge imec, the managers involved in the interconnects and etch program, especially Werner Boullart and Gerald Beyer, and many imec employees (Annemie Kumps, Ivan Callant, Alexis Franquet, Toan Le Quoc, Herbert Struyf, Zsolt Tokei, Philippe Foubert). They made possible the execution of an important part of my research. I also thank for the financial support of imec to present all the work at many conferences all around the world (US, Sweden, Germany,...).

I would also like to thank the students that significantly contributed to my project doing their internship at imec: Alban Zaka, Bingan Chen, Maxime Cremel, Anna Miglio, Katya Ivanova. I was very lucky of working with them.

Special thanks to my officemates JF, Eddy, Craig, Alexey, Denis, Herbert, Dries, Emma, Alain, Henrik, Dirk, Ingrid, Stefan, Maxime, Eslava, Prema, Alexander, German. I really enjoyed sharing office with them. We have a lot of fun and interesting conversations apart from hard work. I learned a lot from them – and not only about science.

Last but not least, my warm thanks to my family and girlfriend for their love and support: Tato (Józef), Mama (Krystyna), and Anna.

Table of Contents

Preface ..... **i**
Table of Contents ..... **iii**
Glossary ..... **xi**
Samenvatting ..... **xvii**
List of publications ..... **xxi**
1 Introduction **1**
1.1 Integrated circuits and low dielectric constant (low-*k*) materials 1
1.2 Ways to reduce a materials' *k*-value 5
1.2.1 Porosity effect on *k*-value 6
1.2.2 Pore size distribution 7
1.3 Typical low-*k* materials 8
1.4 Properties of low-*k* materials required for their integration 10
1.5 Plasma damage of low-*k* materials 11
1.5.1 Hydrophilization 11
1.5.2 Densification 17
1.6 Plasma processing steps in Damascene technology 18
1.7 Scope of this work 21
1.8 References 23
2 Materials and methods **27**
2.1 Introduction 27
2.2 Plasma chambers 28
2.2.1 Model of operation of plasma reactors used in Damascene technology 28
2.2.2 Plasma chambers used in damascene technology 30
2.3 Characteristics of the plasma chambers used in this study 32

2.4 Basic characteristic of the low-*k* materials used in this study 32

2.5 Metrology 34

2.5.1 Ellipsometry 34

2.5.1.1 Application of ultraviolet spectroscopic ellipsometry for evaluation of amorphous carbon content in silica-based low-*k* materials ..40

2.5.2 Ellipsometric porosimetry 41

2.5.2.1 Toluene based ellipsometric porosimetery 41

2.5.2.2 Water based ellipsometric porosimetry 46

2.5.3 Secondary ion mass spectrocopy 47

2.5.4 Optical emmision spectrocopy 47

2.5.5 Fourier transform infrared spectroscopy 48

2.5.6 Near-field scanning probe microwave microscope 49

2.5.7 Nano indentation 50

2.6 References 51

3 New methods for plasma damage monitoring of low-*k* dielectrics used for microelectronic industry applications 53

3.1 Introduction 53

3.2 Oxygen Chemiluminescence in He Plasma as a Method for Plasma Damage Evaluation 54

3.2.1 Introduction 54

3.2.2 Experimental 54

3.2.3 Results and discussion 55

3.3 Evaluation of Plasma Damage in Blanket and Patterned low-*k* Structures by Near-field Scanning Probe Microwave Microscope 61

3.3.1 Introduction 62

3.3.2 Experimental 62

3.3.3 Results and discussion 64

3.3.3.1 Blanket wafers 64

3.3.3.2 Patterned wafers 67

3.4 Chapter summary 68

3.5 References 70

4 Prevention of Plasma Damage of Low-*k* Films by VUV Irradiation from He Plasma 71

4.1 Introduction 71

4.2 Experimental 72

4.2.1 Dielectric material 72

4.2.2 Plasma treatment conditions 72

4.3 Metrology 73

4.4 Results 74

4.4.1 Structural modification 74

4.4.2 Hydrophobic properties 80

4.5 Discussions 81

4.5.1 Effect of NH_3 plasma on low-*k* dielectric 81

4.5.2 Effect of He plasma on low-*k* dielectric 82

4.5.3 Mechanisms of thickness loss of low-*k* treated in NH_3, He and sequential He + NH_3 plasmas 85

4.5.4 Infrared-absorbance around 1000 cm^{-1} as a sign of active centers formation after He plasma exposure 86

4.6 Chapter summary 89

4.7 Reference 90

5 Effect of He/H_2 downstream plasmas on low-*k* dielectrics 93

5.1 Introduction 93

5.2 Experimental 95

5.3 Effect of afterglow plasma chemistry 96

5.3.1 Discussion of the obtained data in general perspective 97

5.3.2 Effect of O radicals 99

5.3.3 Effect of H radicals 100
5.3.4 Differences between H_2 and He/H_2 plasma afterglow treatments 101
5.3.5 Effect of N radicals 102
5.3.6 Combined effect of H and N radicals 103
5.3.7 Model of the film modifications 104

5.4 Temperature effect of He/H_2 afterglow 105

5.4.1 Hydrophobic properties 105
5.4.2 Structural modification 106

5.5 Time effect of He/H_2 afterglow 110

5.5.1 Change of composition 111
5.5.2 Logarithmic time dependence of porogen residue removal depth 116
5.5.3 Mechanical properties 118
5.5.4 Electrical properties 119

5.6 Chapter summary 122

5.7 References 124

6 Improving Mechanical Robustness of Ultra-low-*k* SiOCH films by Controlled Porogen Decomposition prior to UV-hardening 127

6.1 Introduction 127

6.2 Experimental procedure 128

6.3 The Effect of Porogen Residue on Film Characteristic: Comparative Study about Spin-on and PECVD films 129

6.4 Selective porogen removal from PECVD dielectric 131

6.5 Optical properties of porogen-residue-free films 132

6.6 Limited depth of porogen removal 133

6.7 Effect of porogen and porogen residues on the mechanical properties of the PECVD low-*k* films. 133

6.8 Effect of UV-wavelength used for hardening of organic-free films 136

6.8.1 Spin-on films cured by excimer UV sources: 172 nm, 222 nm, and 308 nm 137

6.8.2 PECVD films with and without porogen cured with: narrow-band 172 nm and broad band 200 nm UV sources 140

6.9 Fabrication of the porogen-free films with variable thicknesses 142

6.10 Mechanism of mechanical properties improvement 144

6.11 Chapter Summary 146

6.12 References 147

7 General conclusions and prospects 149

Glossary

Abbreviation	*Description*
AFT	After-glow treatment (also referred as downstream plasma treatment - see DSP)
BARC	Bottom anti-reflective coating
BET	Brunauer–Emmet–Teller
BEOL	Back end of line
Blanket film	Unpatterned film
CCP	Capacitively coupled plasma
CMP	Chemical Mechanical Polishing
CMOS	Complementary metal–oxide semiconductor is a technology for constructing integrated circuits.
Constitutive porosity	Porosity that depends on the original, as-deposited, arrangement of a material structure.
CVD	Chemical Vapor Deposition
Damascene	Process for Cu interconnects manufacturing, in which first the dielectric is patterned and subsequently recesses are filled by metallization
DSP	Downstream plasma (also referred as plasma afterglow treatment– see AFT).
DUV	Deep Ultra Violet
EP	Ellipsometric Porosimetry
EUV	Extreme ultra violet
FEOL	Front end of line
FTIR	Fourier Transform Infra-Red spectroscopy
FSQ	Fluorinated-silsesquioxane
Hard Mask	Capping layer
HDP	High density plasma
HSQ	Hydrogen-silsesquioxane
IC	Integrated circuit
ICP	Inductively coupled plasma
IMD	Inter-Metal Dielectric
ITRS	International Technology Roadmap for Semiconductors
IUPAC	International Union of Pure and Applied Chemistry
k- value	Relative dielectric constant/permittivity εr
k-value of SiO2	The *k*-value of native SiO_2 (thermally grown) is 3.9 at 100 kHz. However, the material used as the inter-metal dielectric is SiO_2 deposited by PECVD. Those oxides have *k*-values of 3.9~4.2. The *k*-value of 4.2 at 100 kHz is taken in this work as the worst case scenario.

Abbreviation	*Description*
Liner layer	Film onto which the low-*k* dielectric is deposited
LL	Lorentz-Lorenz equation
Mesopores	Pores with diameter between 2 nm and 50 nm (IUPAC classification)
Micropores	Pores with diameter less than 2 nm (IUPAC classification)
MIM	Metal Insulator Metal
MSQ	Methylsilsesquioxane
NCS	nano-crystaline silica
NI	Nano indentation
NSPMM	Near-field scanning probe microwave microscope
OES	Optical emission spectroscopy
Open porosity	Porosity that is interconnected and accessible for solvents
OSG	Organo-silica glass
PALS	Positron Annihilation Lifetime Spectroscopy
Pattern Density	Ratio of the metal to dielectric occupancy
PECVD	Plasma Enhanced Chemical Vapor Deposition
RI	Refractive index
RIE	Reactive ion etching
Porosity, pore fraction	The fraction p of the total volume of the film which is attributed to the pores: $p = Vp/V$, where Vp is pore volume and V is the total volume of the film.
Porogen	Organic cyclic hydrocarbons co-deposited with organo-silica matrix by PECVD or spin-on techniques. Those organic are sacrificial film phase. The removal of this phase creates film porosity.
Porogen residue (PR)	Porogen remnants after UV-curing of organo-silica based low-k film.
PSD	Pore size distribution
PSR	Parallel strip transmission line resonator
RC	Resistance-capacitance (delay)
SE	Spectroscopic Ellipsometry
SEM	Scanning Electron Microscopy
SOG	Spin-on glass
Spacing	Interline space, i.e. space between two adjacent metal lines
SSQ	Silsesquioxane
sccm	standard cubic centimeter per minute
Subtractive porosity	Porosity created by selective removal of certain parts of the original material structure.
SVP	Saturation vapor pressure

Abbreviation	*Description*
TDS	Thermal desorption spectra
TDDB	Time Dependent Dielectric Breakdown
TEOS	Tetra-Ethyl-Ortho-Silicate
TEP	Toluene-based ellipsometric porosimetry
ToF-SIMS	Time of Flight Secondary Ion Mass Spectrometry
Trenches	Recesses patterned in the dielectric, to be filled with metallization
ULSI	Ultra large scale integration
UV	Ultra-violet
VUV	Vacuum ultra-violet
WAC	wafer-less autoclean
WEP	Water-based ellipsometric porosimetry
XPS	X-ray photoemission Spectroscopy
XRR	X-ray reflection
YM	Young's modulus

Summary

Interconnects are the structures used to transmit electrical signals between active areas in semiconductor chips. Copper and low dielectric constant (low-*k*) materials are introduced into semiconductor back-end-of-line (BEOL) processing to relieve the increasing interconnect RC delay; a consequence of the critical dimension (CD) scaling down. However, the integration of low-k materials is a challenge. Processing damage can occur during different technological steps resulting in a dramatical degradation of the properties of the low-*k* materials.

Nowadays, porous low-*k* films based on silica and silsesquioxanes with 10-15% of organic (carbon containing) hydrophobic groups are the most favoured class of materials for advanced interconnect technology nodes. The exposure of these films to a (etch) plasma ambient leads to the loss of hydrophobic groups and to the densification of its silica backbone. The extent of this damage strongly depends both on the low-*k* material properties such as the porosity and on the plasma conditions such as the chemistry and the power (energy and intensity of ion bombardment and UV radiation). The main factors and mechanisms of plasma damage need to be studied to optimize process conditions. This is the main goal of this work.

The structure of this thesis is as follows: chapter 1 and 2 are an introductory part, whereas results are discussed in chapters 3-6 and summary and conclusions are presented in chapter 7. The results are divided into four parts: a first part is devoted to new metrology related to low-*k* materials (chapter 3), two other parts deal with processing damage of low-*k* dielectrics, either induced during CuOx surface passivation with NH_3 plasma (chapter 4) or during photoresist mask removal with ash plasma (chapter 5). Additionally, a fourth part deals with solutions to achieve improved PECVD low-*k* materials for further technology nodes (chapter 6). The abstract of each chapter is stated below in numerical order from chapter 1 to chapter 6.

Chapter 1 contains a general introduction to damascene processes for manufacturing of Cu/low-*k* interconnects and to the science of low-*k* materials. The plasma damage of low-*k* materials and plasma assisted processing is discussed in greater detail. Chapter 2 is dedicated to review of the plasma chambers, the materials and metrology used in this work. Both chapters 1 and 2 are necessary for introducing the main concepts and terminology recurrent in the result chapters.

Chapter 3 is devoted to new metrology for evaluation of impact of the industrial processing on low-*k* materials. We present two new methods suited for this purpose. The first method is a novel concept of evaluation of hydrophilization degree of low-*k* dielectric wafers using industrial plasma chamber coupled with optical emmission spectroscopy (OES) system. The O* (777 nm) and H* (656 nm)

intensities and are evaluated by OES when low-*k* material is exposed to an He plasma. It is proposed that He plasma causes photolysis of the H_2O in low-*k* pores. It is demonstrated that the integrated intensity of O*-related peak (product of H_2O photolysis during He exposure) gives quantitative information about the degree of hydrophilization of the studied low-*k* films. The second method can be used to evaluate *k*-value at 4 GHz and relies on microwave impedance measurements of the low-*k* materials. Conventional measurements of *k*-value of patterned low-*k* structures require their metallization (filling low-*k* trenches with Cu). The metallization however also requires low-*k* material processing that degrades the material *k*-value. We demonstrate that microwave impedance measurement allows estimation of *k*-values at 4 GHz of the dielectric directly after its patterning (etching).Therefore the impact on *k*-value of only plasma processing is evaluated (excluding metallization process impact). Furthermore an analytical model is proposed to assess the degree of sidewall damage induced by the combined effect of etch and ash plasmas.

Chapter 4 deals with plasma damage of low-*k* materials induced by NH_3 plasma. This plasma is used to reduce CuOx. It is shown that severe damage caused by NH_3 plasma can be significantly reduced by modification of the low-*k* material by preliminary He plasma treatments. The modified layer increases the recombination probability of active NH_x radicals and, therefore, decreases their concentration and depth of penetration into low-*k* materials. It is proposed that densification and activation of the top low-*k* surface is caused by high-energy EUV photons emitted by the He plasma. The thickness of the EUV-modified layer is close to 17 nm. The depth of the modification is limited because of the high absorption coefficient of silica-based low-*k* materials in the range of EUV emission of He plasma. The combined He plasma and NH_3 treatment can also cause sealing of the low-*k* film pores.

Chapter 5 is dedicated to plasma damage of low-*k* films during removal of photo resist mask from low-*k* material (plasma strip process). It is shown that this strip process cannot be performed without damage of low-*k* material since it is immersed in the strip plasma. This damage is due to an additional activation of chemical processes provided by ions or UV light from strip plasma itself as well as similar bonds structure (C-H, C-C) between photoresist mask and low-*k* film. The similar bond structure between photresist and low-*k* films causes selectivity problem. It is shown, however, that sufficient selectivity to remove photoresist without low-*k* damage can be achieved using afterglow of H_2-based plasma chemistry where effects of ions and UV light is eliminated. Moreover the latter effect cannot be achieved in other afterglow chemistries such as O_2 or N_2/H_2 due to their reactivity with Si-CH_3 bonds present in the low-*k* film skeleton. These plasma afterglow processes are investigated in great detail with focus on He/H_2 ash plasmas. We additionally found that H_2 and He/H_2 afterglows remove porogen residues (PR) from low-*k* films without scission of Si-CH_3 groups from the low-*k* skeleton. The PR is graphitized carbon-like phase present in the PECVD films introduced during their fabrication. The PR removal as result of industrial processing causes material porosity increase without its hydrophilization. Therefore, *k*-value of the low-*k* material can be even reduced during photoresist removal process (the strip process

increases the *k*-value the most). However, porosity increase results in significant mechanical properties reduction of the ultra low-*k* PECVD materials (k<2.3). This is due to higher PR content defined by their current fabrication technology. It has been stated that PR is one of the key factors limiting scalability of PECVD ultra low-*k* materials. Therefore the optimal PECVD low-k material should PR-free. The novel concept for PR-free material fabrication is the subject of chapter 6.

Chapter 6 deals with novel concept of fabrication procedure of PR-free PECVD low-*k* films. The new procedure is performed by conventional UV-curing of PECVD film skeleton when the porogen is already completely removed. The removal of the organic porogen without Si-CH_3 bonds scission is found to be possible by annealing of the low-*k* film in a H_2-based plasma afterglow (investigated in chapter 5). The proposed method allows us to obtain porogen residue-free low-*k* films with variable thicknesses. The obtained films demonstrate extraordinary high Young's modules of 5 - 9.5 GPa for open porosity in the range of 41-46 %, *k*-value of 1.8-2.6. The new PECVD films have higher YM normalized to *k*-value than other low-*k* films studied. The improved mechanical properties are explained on the basis of percolation of rigidity theory. The presented method shows the potential for fabrication of low-*k* dielectric films for future microelectronic technology nodes.

Samenvatting

Interconnecties in geintegreerde schakelingen zorgen voor de geleiding van elecktrische signalen tussen de actieve gebieden op een chip. De interconnecties worden aangebracht tijdens het 'back-end-of-line (BEOL)' gedeelte van een producktie proces. Tijdens deze stappen worden koper, als geleider, en een isolator met een lage dielectrisch constante (lage-*k* materiaal), benut voor het verminderen van de interconnectie RC vertraging, dewelke een gevolg is van de continue dimensie schaling van transistoren. Het integreren van deze lage-*k* materialen is een technologische uitdaging, aangezien er proces schade kan optreden met degradatie van de eigenschappen van de lage-*k* materialen tot gevolg.

Hedentendage worden poreuze lage-*k* materialen, gebaseerd op silica en silsesquioxanen met 10-15% organische (koolstof bevattende) hydrofobe groepen, beschouwd als de preferentiële materialen voor geavanceerde interconnectie technologieën. Blootstelling van deze lagen aan een (ets) plasma leidt tot verlies van deze hydrofobe groepen en densificatie van het silica netwerk. De draagwijdte van de schade is sterk afhankelijk van de porositeit van het lage-*k* materiaal en het vermogen van het plasma (energie en intensiteit van de ionen en de UV straling). De studie van deze bepalende factoren, het uitwerken van een mechnisme en het optimalizeren van de proces condities zijn de voornaamste doelen van dit werk.

De structuur van deze thesis is als volgt: hoofdstuk 1 en 2 geven een overzicht van inleidende begrippen en achtergrond, resultaten worden besproken in hoofdstukken 3 tot 6, samenvatting en conclusies worden in hoofdstuk 7 gepresenteerd. De resultaten kunnen opgesplitst worden in 4 delen: een eerste deel behandelt nieuwe metrologie gerelateerd aan lage-*k* materiealen (hoofdstuk 3). Hoofdstuk 4 en 5 handelen over plasma geinduceerde schade, hetzij tijdens CuOx oppervlakte passivatie in NH_3 plasma's (hoofdstuk 4), hetzij tijdens fotolak masker reiniging in een plasma (Hoofdstuk 5). In hoofdstuk 6 worden oplossingen aangereikt om sterk verbeterde PECVD lage-*k* mateiralen te deponeren voor toekomstige technologie noden. De abstract van elk hoofdstuk is hieronder opgenomen.

Hoofdstuk 1 bevat een algemene inleiding rond het damasceen proces, gebruikt voor productie van koper en lage-*k* materiaal interconnecties. Een overzicht van plasma schade en plasma geassisteerde processen van lage-*k* materialen wordt ook in detail besproken. Hoofdstuk 2 is gewijd aan een overzicht van plasma reactoren, gebruikte materialen en metrologie. Zowel hoofdstuk 1 als 2 introduceren de basis concepten en terminologie gebruikt in de daaropvolgende hoofdstukken.

Hoofdstuk 3 sptitst zich toe op nieuwe metrologie ontwikkelingen voor evaluatie van de impact van industriële processen van lage-*k* materialen. De eerste

methode is een nieuw concept, gebruikt voor evaluatie van de graad van hydrofiliciteit van lage-*k* materialen. Hiervoor wordt een industriële plasma kamer gebruikt, uitgerust met een optisch emissie spectroscopisch systeem (OES). De O* (777 nm) en H* (656 nm) intensiteiten worden met OES gemonitord tijdens blootstelling van het lage-*k* materiaal aan een He plasma. Er wordt vooropgesteld dat the He plasma fotolyse veroorzaakt van het H_2O in de poriën van het lage-*k* materiaal. Er wordt aangetoond dat de geintegreerde intensiteit van de O* gerelateerde piek (bij-produkt van de H_2O fotolyse tijdens He blootstelling) kwantitatieve informatie geeft over de graad van hydrofilisatie van de bestudeerde lage-*k* filmen.De tweede methode kan gebruikt worden voor bepaling van de *k*-waarde bij 4 GHz en maakt gebruik van microgolf impedantie metingen van het lage *k* materiaal. Traditionele metingen van lage-*k* materialen in lage-*k* patroon structuren vereist een metallizatie stap (het opvullen van de lage-*k* trench met Cu). Deze metallizatie vereist echter lage-*k* materiaal proces stappen die de dielectrische eigenschappen kunnen beinvloeden. We demonstreren dat microgolf impedantie metingen een schatting van de *k*-waarde bij 4 GHz mogelijk maken onmiddellijk na de plasma ets stap. Hierdoor is het mogelijk om enkel de impact van de plasma stap (i.e. zonder metallizatie) te meten. Daarenboven wordt ook een analytisch model uitgewerkt om de mate van zijwand schade, geinduceerd door een gecombineerd effect van plasma ets en verassing te beoordelen.

Hoofdstuk 4 behandelt plasma schade van lage-*k* materialen geinduceerd door een NH_3 plasma. Dit plasma wordt gebruikt voor de reducite van CuOx. Er wordt aangetoond dat de NH_3 plasma schade aan het lage-*k* materiaal significant verminderd kan worden door een voorafgaande He plasma behandeling. De gewijzigde film verhoogt de recombinatie waarschijnlijkheid van actieve NH_x radicalen en vermindert daardoor hun concentratie en penetratiediepte in de lage-*k* materialen. Er wordt een model voorgesteld waarbij de densificatie en activatie van de top laag van het lage-*k* materiaal veroorzaakt wordt door de hoog-energetische EUV fotonen die door het He plasma worden uitgezonden. De EUV straling modificeert de lage-*k* materialen tot een diepte van 17 nm en is voornamelijk beperkt door de hoge absortie coefficient van de silica gebaseerde lage-*k* materialen in het EUV gebied. De gecombineerde He plasma en NH_3 behandeling veroorzaakt ook ‘sealing’ van de poriën in het lage-*k* materiaal.

Hoofdstuk 5 is gewijd aan plasma schade van lage-*k* materialen tijdens het verwijderen van het fotolak masker (plasma strip proces). Er wordt aangetoond dat dergelijke strip zonder schade aan het lage-*k* materiaal onmogelijk is, omdat het materiaal zich in het plasma bevindt. De schade wordt veroorzaakt door een chemisch proces, geactiveerd door ionen of UV licht van het strip plasma. De gelijkaardigheid in binding structuur tussen fotolak en lage-*k* materialen (C-H, C-C) is mede oorzaak omdat deze selectiviteitsproblemen veroorzaakt. Er wordt aangetoond dat voldoende selectiviteit niettemin verwezenlijkt kan worden in de na gloei van H_2 gebaseerde plasama’s waar de invloed van ionen en UV licht uitgeschakeld wordt. Dit laatste effect kan niet bekomen worden in gelijkaardige O_2 of N_2/H_2 plasma’s omwille van hun reactiviteit met Si-CH_3 bindingen aanwezig in het lage-*k* materiaal skelet. Een uitgebreide studie, met nadruk op He/H_2 verassingsplasma’s wordt gerapporteerd. Bijkomend werd vastgesteld dat H_2 en

He/H_2 na gloei plasma's ook in staat zijn om porogene residues (PR) uit de lage-k materiaal porien te verwijderen zonder het breken van de $Si-CH_3$ bindingen op het lage-*k* materiaal oppervlak.

De PR is een grafietachtige fase aanwezig in PECVD filmen tijdens het productieproces. De PR verwijdering, als een gevolg van het industriële resist proces, veroorzaakt een toename in de materiaal porositeit zonder bijkomende hydrofilisatie. Hierdoor kan er zelfs een verlaging van de dielectrische constante waargenomen worden. Door de hoge PR concentratie in ultra lage-*k* materialen, resulteert de porositeitstoename in een significante reductie van de mechanische eigenschappen van ultra lage-*k* PECVD materialen (k<2.3). Hierdoor word PR beschouwd als een sletutel parameter die de schaalbaarheid van lage k materialen limiteert. Een optimaal PECVD materiaal behoort derhalve PR vrij tezijn, een concept besproken in hoofdstuk 6.

Hoofdstuk 6 behandelt een nieuw concept voor fabrikatie van PR vrije PECVD lage k materialen. De nieuwe procedure omvat een conventionele UV-cure stap van het PECVD film skelet, na volledige verwijdering van het PR. De verwijdering van het organische PR zonder $Si-CH_3$ bond breking is mogelijk door het annealen van de lage-k materiaal laag in een H_2 gebaseerd plasma nagloei proces (bestudeerd in Hoofdstuk 5). De voorgestelde methode resulteert in PR vrije lage-*k* filmen met variabele dikte. De bekomen lagen vertonen hoge Young modulus (5 – 9.5 GPa), een open porositeit van 41 tot 46% en een *k*-waarde van 1.8-2.6. De nieuwe PECVD gebaseerde lagen hebben de hoogste genormaliseerde YM (naar k-waarde). De verbeterde mechanische eigenschapen worden verklaard op basis van de percolatie van starheid theorie. De voorgestelde methode vertoont potentieel voor de fabrikatie van lage-*k* dielectrische filmen voor toekomstige micro-electronische technologie noden.

List of publications

Journal papers

(* denotes results presented in this thesis)

[1] ***A.M. Urbanowicz**, K. Vanstreels, P. Verdonck D. Shamiryan, S. De Gendt, M. R. Baklanov, "Improving Mechanical Robustness of Ultralow-*k* SiOCH Plasma Enchaced Chemical Vapor Deposition Glasses by Controlled Porogen Decomposition prior to UV-hardening" Journal of Applied Physics, 107 (10), 104122-1 (2010)

[2] E. Kunnen, G.T. Barkema, C. Maes, D. Shamiryan, **A. M. Urbanowicz**, H. Struyf, M.R. Baklanov "Integrated diffusion - recombination model for describing the logarithmic time dependence of plasma damage in porous low-*k* materials" accepted at Microelectronic Engineering

[3] E. Kunnen, M. R. Baklanov, A. Franquet, D. Shamiryan, T. V. Rakhimova, **A. M. Urbanowicz**, H. Struyf, and W. Boullart "Effect of energetic ions on plasma damage of porous SiCOH low-*k* materials", Journal of Vacuum Science and Technology B, 28 (3), 450 (2010)

[4] ***A.M. Urbanowicz**, D. Shamiryan, A. Zaka, P. Verdonck , S. De Gendt, M. R. Baklanov, " Effects of He Plasma Pretreatment on Low-*k* Damage during Cu Surface Cleaning with NH_3 Plasma", Journal of Electrochemical Society, 157, H565 (2010)

[5] K. Vanstreels and **A.M. Urbanowicz**, "Nanoindentation study of thin plasma enhanced chemical vapor deposition SiCOH low-*k* films modified in He/H_2 downstream plasma," Journal of Vacuum Science and Technology B 28 (1), 7 (2010)

[6] ***A.M. Urbanowicz**, K. Vanstreels, D. Shamiryan, S. De Gendt, M. R. Baklanov, "Effect of Porogen Residues on Optical, Chemical and Mechanical Properties of CVD Low-*k* Materials", Electrochemical and Solid-State Latters, 12, H292 (2009)

[7] ***A.M. Urbanowicz**, D. Shamiryan, M. R. Baklanov, S. De Gendt "Oxygen Chemiluminescence in a He Plasma as a Method for Plasma Damage Evaluation of Low-*k* Dielectrics", Microelectronic Engineering, 85, 2164 (2008)

[8] S. Eslava Fernandez, F. Iacopi, **A.M. Urbanowicz**, M. Baklanov, C. Kirschhock, K.Maex, and J. Martens "Ultraviolet-Assisted Curing of Organosilicate Glass Low-*k* by Excimer Lamps", Journal of Electrochemical Society ,155, G231(2008)

[9] *__A.M. Urbanowicz__, B. Meshman, D. Schneider and M.R. Baklanov, "Stiffening and hydrophilization of SOG low-*k* material studied by ellipsometric porosimetry, UV ellipsometry and Laser-induced surface acoustic waves" Physica status solidi (a), No. 4, p. 829-832 (2008)

[10] **A.M. Urbanowicz**, A. Humbert, G. Mannaert, Z. Tokei and M. R. Baklanov "Effects of bias, pressure and temperature in plasma damage of ultra low-*k* films", Solid State Phenomena Vol.134, p. 317-320 (2008)

[11] *Z. Tőkei, M. Baklanov, I. Ciofi, Y. Li and **A.Urbanowicz**, "Plasma induced low-k modification and its impact on reliability", Semiconductor Fabtech, 35-th Editon, September (2007)

[12] *__A. M. Urbanowicz__, M. R. Baklanov, J. Heijlen, Y. Travaly and A. Cockburn, "Damage Reduction and Sealing of Low-*k* Films by combined He and NH3 plasma treatment", Electrochemical and Solid-State Latters, 10 (10), p. 76-79 (2007)

Patents

[1] **A.M. Urbanowicz**, M.R. Baklanov, Denis Shamiryan, S. De Gendt " Cleaning of Plasma Chamber Walls Using Noble Gas Cleaning Step", EP 2009/2034046 A2 and US 2009/0065025 A1

[2] *__A.M. Urbanowicz__, M.R. Baklanov, "Quantification of hydrophobic and hydrophilic properties of materials" EP 2009/20342296 and US 2009/0068768 A1

[3] *__A.M. Urbanowicz__, P. Verdonck, D. Shamiryan, K. Vanstreels, M. Baklanov, S. De Gendt, "Fabrication of porogen residues free and mechanically robust low-*k* materials" US provisional application filled on 08/07/2009.

Conferences

(† denotes paper published in full in conference proceedings)

[1] *__A.M. Urbanowicz__, K. Vanstreels, P. Verdonck, E. Van Besien, C. Trompoukis, D. Shamiryan, S. De Gendt, M. Baklanov, "Effect of UV-wavelength on Hardening Process of Porogen-containing and Porogen-Free Ultra-low-*k* PECVD Glasses" submitted at 57th American Vacuum Society Conference, 17-22 October, Albuquerque, New Mexico, USA (2010)

[2] *__A.M. Urbanowicz__, K. Vanstreels, P. Verdonck, D. Shamiryan, S. De Gendt and M. Baklanov, "Improving Mechanical Robustness of Ultra-low-*k* SiOCH PECVD Materials", in 11th International Workshop on Stress-Induced Phenomena in Metallization, 12-14 April, Dresden, Germany (2010).

[3] *__A.M. Urbanowicz__, M. Cremel, K. Vanstreels, D. Shamiryan, S. De Gendt and M. R. Baklanov, "Mechanism of *k*-value Reduction of PECVD Low-*k* Films Treated with He/H2 Ash Plasma", in Plasma Etch and Strip in Microelectronic, 3-5 March, Grenoble, France (2010).

[4] J. de Marneffe, A. Jarnac, T. Conard, D. Hendrickx, C. Huffman, E. Kunnen, F. Lazzarino, A. Milenin, D. Shamiryan, H. Struyf, H.; A. Vandervorst, **A. Urbanowicz**, W. Boullart, "The small-gap technique: understanding an ion-shading method for plasma-surface interactions study", in Plasma Etch and Strip in Microelectronic, 3-5 March, Grenoble, France (2010).

[5] E. Kunnen, G.T. Barkema, C. Maes, D. Shamiryana, A. M. Urbanowicz, H. Struyfa, M.R. Baklanov "Integrated diffusion - recombination model for describing the logarithmic time dependence of plasma damage in porous

low-*k* materials" Materials for Advanced Metallization – MAM, Mechelen, Belgium , 8-10 March (2010)

[6] *,†**A.M. Urbanowicz**, K. Vanstreels, P. Verdonck, D. Shamiryan, M. Cremel, S. De Gendt and M.R. Baklanov "Porogen Residue Free Ultra Low-*k* PECVD Material: Fabrication, Optical and Mechanical Properties" XXV Advanced Metallization Conference, 13-15 October, Baltimore, USA, (2010) [proceedings in press].

[7] E. Kunnen, **A. Urbanowicz**, A. Franquet, D. Shamiryan, H. Struyf, W. Boullart, and M. Baklanov "Effect of Energetic Ions on Plasma Damage of SiCOH Low-*k* Material." American Vacuum Society Conference 8-13 November, San Jose, USA (2009)

[8] F. Clemente, M. Baklanov, **A. Urbanowicz**, T. Hantschel, "Vibrational Spectroscopy of Low-*k* Films: Exploring the Potentiality of micro-Raman Characterization", Material Research Society Spring Meeting, Symposium D, 13-17 April, San Francisco, USA (2009)

[9] †M. Gonzalez, K. Vanstreels and **A.M. Urbanowicz**, "Modeling the Substrate Effects on Nanoindentation Mechanical Property Measurement" 10th Int. Conf. Thermal, Mechanical and Multiphysics Simulation and Experiments in Micro-Electronics – EuroSimE, Delph, Nederlands p. 486-491, (2009)

[10] †H. Struyf, J. de Marneffe, D. Goossens, D. Hendrickx, C. Huffman, E. Kunnen, F. Lazzarino, A. Milenin, D. Shamiryan, **A. Urbanowicz**, A.Vandervorst, W. Boullart, "Metal hard-mask based double patterning for 22nm and beyond", Advanced Metallization Conference, 13-15 October, Baltimore, USA (2009) (invited paper) [proceedings in press]

[11] *,†**A.M. Urbanowicz**, V. Talanov, M. Pantouvaki, H.Struyf, S. De Gendt, and M. Baklanov, "Evaluation of plasma damage in patterned low-k structures by near-field scanning probe microwave microscope: effect of plasma ash chemistry" International Interconnect Technology Conference Proceedings, Hokkaido, Japan, IEEE: p. 134-136 (2009)

[12] †P.W. Mertens, T.G. Kim, M. Claes, T.Q. Le, G. Vereecke, E. Kesters, S. Suhard, A. Pacco, M. Lux., K. Kenis, **A.M. Urbanowicz**, Z. Tokei, G. Beyer "Challanges and Novel Approaches for Photo Resist Removal and Post-etch Residue Removal for 22 nm Interconnects" International Interconnect Technology Conference Proceedings, Hokkaido, Japan, IEEE: p. 237-239 (2009) (invited paper)

[13] †P. Marsik, **A. Urbanowicz**, P. Verdonck, A. Ferchichi, L. Prager , D. De Roest and M. Baklanov, "Engineering of chemical and physical properties of low-*k* materials by different wavelength of UV light" Mat. Res. Soc.:

XXIV Advanced Metallization Conference Proceedings, eds. by M. Naik, R. Shaviv, T. Yoda, K. Ueno, p. 543-549 (2009)

[14] *,†**A.M. Urbanowicz**, D. Shamiryan, P. Marsik, Y. Travaly, A. Jonas, P. Verdonck, K. Vanstreels, A. Ferchichi, D. De Roest, H. Sprey, K. Matsushita, S. Kaneko, N. Tsuji, S. Luo, O. Escorcia, I. Berry, C. Waldfried, S. De Gendt and M.R. Baklanov "Improved Low-*k* Dielectric Properties Using He/H_2 Plasma for Resist Removal" Mat. Res. Soc.: XXIV Advanced Metallization Conference Proceedings, eds. by M. Naik, R. Shaviv, T. Yoda, K. Ueno, p. 594-598 (2009)

[15] M. Baklanov, **A. Urbanowicz**, and Y. Travaly "Plasma-induced damage to low-*k* materials" MRS Spring Meeting, San Francisco CA, 24-28 March 2008 (invited paper)

[16] **A.M. Urbanowicz**, M. R. Baklanov, D. Shamiryan, F. Soberon, S. Daniels, S. De Gendt "Oxygen chemiluminescence in a He plasma as a method for plasma damage evaluation of low-*k* dielectrics" MAM 2008, Dresden, 2-5 March (2008)

[17] D. Kim, **A.M. Urbanowicz**, G. Mannaert, H. Struyf, W. Boullart, K.J. Min, C.J. Kang, J. T. Moon, and M.R. Baklanov, " Effects of Plasma Chemistry on Low-*k* Film Properties", 29th International Symposium on Dry Process, Tokyo, 13-14 November (2007)

[18] **A.M. Urbanowicz**, D. Shamiryan, D. Kim, and M. R. Baklanov, "Effect of Helium Plasma on Low-*k* damage during Dry Resist Strip", at Plasma Etch and Strip in Microelectronics 1st international workshop, Leuven, 10-11 September (2007)

[19] †P. Marsik, **A. Urbanowicz**, K. Vinokur, Y. Cohen, and M. Baklanov "Changes of UV optical properties of plasma damaged low-*k* dielectrics for sidewall damage scatterometry", accepted at Mat.Res.Soc.Symp.Proc. eds. by J. Gambino, S. Ogawa, C.L. Gan, Z. Tokei, Vol. 1079E, Warrendale, PA, paper 1079-N07-04, 2008.

[20] †F. Dultsev, **A. Urbanowicz**, and M. Baklanov "Effect of Si-O-Si bonding structure in porous carbon-doped silicon dioxide films on plasma damage" Mat.Res.Soc.Symp.Proc. , eds. by J. Gambino, S. Ogawa, C.L. Gan, Z. Tokei, Vol. 1079E, Warrendale, PA, paper 1079-N07-03 (2008)

[21] †M. Baklanov, **A. Urbanowicz**, and S. Vanhaelemeersch, "Challenges of plasma damage of low-*k* materials". In: 234th ACS Meeting. (19-23 August 2007; Boston, MA, USA.). pp.100-103 (2007) (invited paper)

[22] **A.M Urbanowicz**, B. Meshman, D. Schneider and M.R. Baklanov, "Stiffening and hydrophilization of SOG low-*k* material studied by Ellipsometric porosimetry, UV ellipsometry and Laser-induced surface

acoustic waves", accepted at 4th International Conference on Spectroscopic Ellipsometry, Stockholm, Sweden, June 11-15, (2007)

[23] M.R.Baklanov, **A.Urbanowicz**, G.Mannaert and S.Vanhaelemeersch, "Fundamentals of plasma damage in O_2 and H_2 based strip plasma" , Presented at 8th International Conference on Solid-State and Integrated-Circuit Technology, Shanghai, November (2006) (invited paper)

[24] **A.M. Urbanowicz**, A. Humbert, G. Mannaert, Z. Tokei and M. R. Baklanov "Effects of bias, pressure and temperature in plasma damage of ultra low-*k* films", Ultra Clean Processing of Semiconductor Surfaces, Antwerpen 18-20 September (2006)

[25] †M.R.Baklanov, **A.Urbanowicz**, G.Mannaert, S.Vanhaelemeersch, "Low dielectric constant materials: challenges of plasma damage" Proc. of 2006 8th International Conference on Solid-State and Integrated Circuit Technology, Part 1, page 291-294, (2006) (invited paper)

[26] †Mikhail R Baklanov, David O'Dwyer, **Adam M. Urbanowicz**, Quoc Toan Le, Steven Demuynck, Eun Kee Hong, "Moisture Induced Degradation of Porous Low-*k* Materials". Mat.Res.Soc.Symp.Proc., Vol. 914, 0914-F02-06, (2006)

1 Introduction

This chapter is devoted to the general concepts concerning the use of materials with low dielectric permittivity (low-*k* dielectrics) dielectric and Cu damascene structure for Back-end-of-line (BEOL) processing. The scope is to give the reader the necessary terminology and basic concepts to be able to fully comprehend the following chapters.

First an overview of processes for multilevel Cu metallization manufacturing is given. Subsequently, the focus is set on low-*k* materials: methods for *k*-value reduction, main material classification, and required properties for industrial application. We demonstrate that increasing material porosity is the main way of its *k*-value reduction, however it also results in weakening of mechanical properties and increased permeability of the process chemicals. Next, we show that one of the most important properties of porous low-*k* films is their hydrophobicity. The hydrophobic properties of porous low-*k* dielectrics are achieved, i.e., by introducing terminal Si-CH_3 groups. The removal and replacement of those Si-CH_3 groups with Si-OH groups caused by processing plasmas make them hydrophilic. Subsequent moisture absorption in pores significantly increases the *k*-value due to the high *k*-value of water (*k*~80 at 100 kHz). The effect of water on the *k*-value of low-*k* films is explored in more detail. Finally, plasma processing steps of low-*k* materials is explained, and related to specific goals of this thesis.

1.1 Integrated circuits and low dielectric constant (low-*k*) materials

The first integrated circuit (IC) was invented by Jack Kilby in 1958 [1]. This date is considered as a major breakthrough in the semiconductor industry. An IC allows the integration of many electronic components onto a single chip device. About 50 years later, Jack Kilby's IC containing a few transistors per cm^2 evolved into modern microprocessors containing 10^8 transistors per cm^2. Performance improvements in IC over the past few decades have been mostly achieved by increasing the transistor speed, reducing the transistor size and packing more transistors onto a single chip. In 1965 Gordon Moore formulated the transistor scaling trend known as Moore's Law, which is the empirical observation that transistor density doubles every two years [2], and later as of 1975 every 18-th months [3]. An emerging factor that may disrupt this scaling trend is the slowing speed of signal propagation within the chip's interconnect level. Signal delays

caused by interconnection wiring, increase with each generation of scaling and may soon limit overall performance of the IC.

The core of an ultra-large-scale-integrated (ULSI) microelectronic device is the semiconducting material. Mono-crystalline silicon is used as silicon wafers of 200 and 300 mm diameter (and 1-2 mm thick). Silicon forms part of the transistors and at the same time serves as substrate for the device. The IC devices are composed of many overlapping layers.

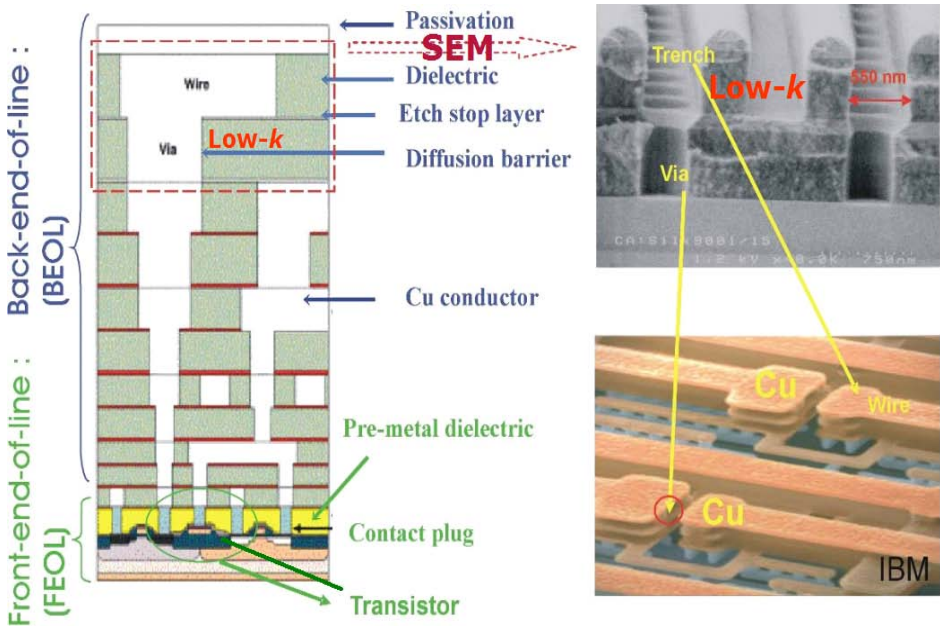

Figure 1.1 The schematic cross-section of the integrated circuit (left side). SEM images of low-*k* trenches (upper-right corner) and Cu wires (lower-right corner)

Figure 1.1 shows the schematic cross-section of the modern IC. The ICs are composed of many overlapping layers. These layers are fabricated on and within silicon wafers by sequential steps of deposition and removal of material. Structure on the required scale is achieved by photolithography. The ICs can be divided into two parts. The first part is called the Front-end-of-line (FEOL). FEOL contains electronic elements such as transistors, capacitors, resistors. The second part of the chip is Back-end-of-line (BEOL), which contains interconnect as shown in Figure 1.1 (lower-right corner). Interconnects are the structures used to transmit electrical signals between active areas of FEOL in microelectronic chips. Any interconnection can be represented as a resistor (wire) and capacitor in series (insulating dielectrics between wires) as shown in Figure 1.2.

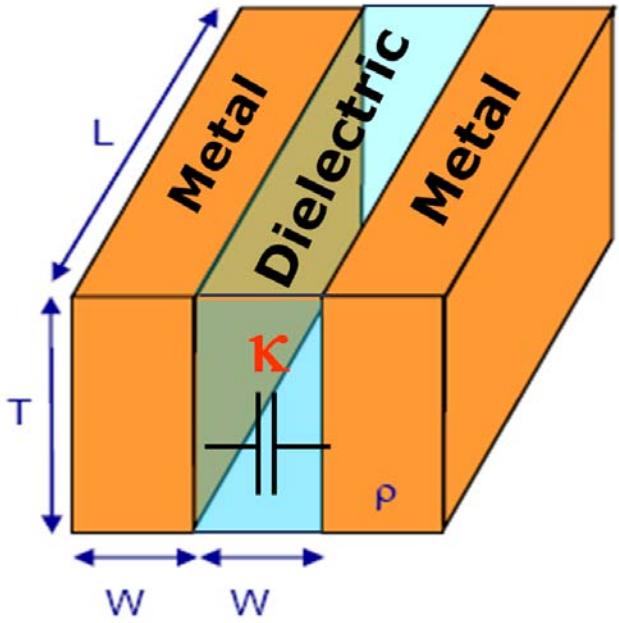

Figure 1.2. Simplified scheme of Cu/low-*k* BEOL interconnect.

A good figure of merit to characterize interconnection performance is resistance-capacitance (RC), which is a unit of time. A signal propagating through the interconnection experiences RC delay. The RC delay for the structure represented in Figure 1.2 is expressed using eq. (1-1).

$$RC \approx 2 \cdot \rho \cdot k \cdot \varepsilon_0 \cdot L^2 \cdot \left(\frac{1}{W^2} + \frac{1}{T^2} \right) \qquad (1\text{-}1)$$

where ρ is wire metal conductivity, k is dielectric constant (ε_r – relative dielectric permittivity), ε_0 dielectric permittivity in vacuum. Symbols L, W and T describe the metal wire dimensions: L – length, W – width and T – thickness. As can be seen from eq. (1-1), shrinking the wire dimensions (scaling down) increases RC delay. As a consequence, the signal propagation through the interconnection increases its contribution to the effective speed of the devices [4, 5]. The effect of interconnect was negligible at the beginning of the chip manufacturing. However, the situation has been reversed for the technology nodes with pitch smaller than 250 nm, where the signal delay at interconnection outweighs the transistor gate delays as shown in Figure 1.3.

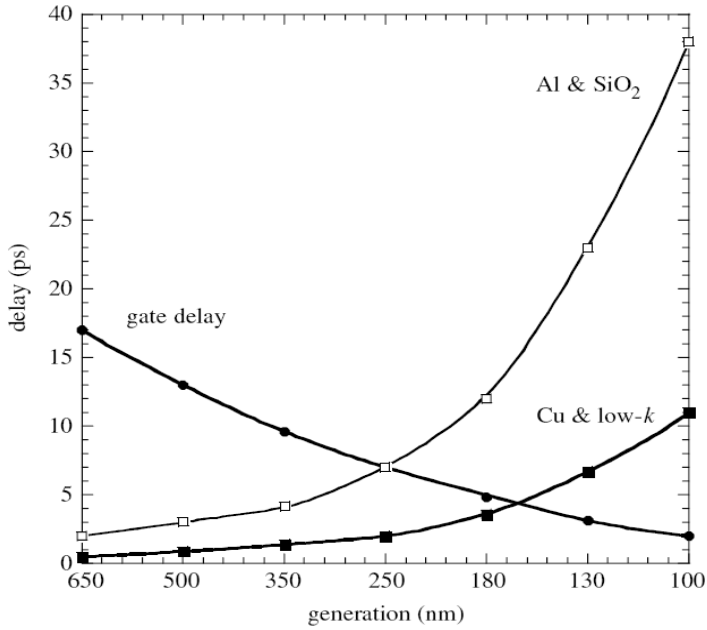

Figure 1.3 Gate and interconnection signal delays in function of the technology generation. Adapted from Baklanov et al. [6]

Additionally, the higher signal frequencies required for future generations to obtain higher carrier transit increase the dynamic power consumption [6,7]. The dynamic power P_c consumption can be described by following equations:

$$P_c = a_w \cdot C_{in} \cdot V_{av}^2 \cdot f \qquad (1\text{-}2)$$

$$C_{in} = k \cdot \varepsilon_0 \cdot G \qquad (1\text{-}3)$$

Where a_w is wire activity, C_{in} is interconnect capacitance, V_{av} is applied voltage, f is is the frequency, ε_0 is the permittivity of vacuum and G is factor describing the system architecture. Equations (1-2) and (1-3) state that a decrease in the dielectric constant, k, of insulating media leads in turn to a decrease in the dynamic power consumption P_c.

The only way to reduce RC-delay and dynamic power consumption, Pc, is to reduce the k-value of the isolator between wires and to increase the metal conductivity. The replacement of Al with Cu (with lower conductivity) was the first step taken to address RC delay issue [8]. The second step was the exchange of SiO_2 with a k-value of 4.2 of materials with lower dielectric constant, so called low-k dielectrics.

1.2 Ways to reduce a materials' *k*-value

The dielectric constant, *k*, is the ratio of the permittivity of a substance to that of free space. The quantitative relation between the dielectric constant (relative permittivity ε_r) and properties of the molecules is described by the Debye's equation:

$$\frac{\varepsilon_r - 1}{\varepsilon_r + 2} = \frac{N}{3\varepsilon_0}\left(\alpha_e + \alpha_d + \frac{\mu^2}{3k_B T}\right) \qquad (1\text{-}4)$$

with N equals the number of molecules per m^3, μ the orientation polarizability, k_B, the Boltzmann constant, and T the temperature in Kelvin degrees. The terms α_e and α_d represent the electronic and distortion polarization in the molecule, while the term $\mu^2/3k_BT$ stems from the thermal averaging of the permanent electric dipole moments in the presence of an applied field. The dipole formation is a result of electronic polarization (displacement of electrons), distortion polarization (displacement of ions) or orientation polarization (displacement of molecules) in an alternating dielectric field. These phenomena have characteristic dependencies on frequency as shown in Figure 1.4. Microelectronic devices operate at frequencies lower than 10^9 Hz. Therefore all polarization mechanisms contribute to the dielectric constant.

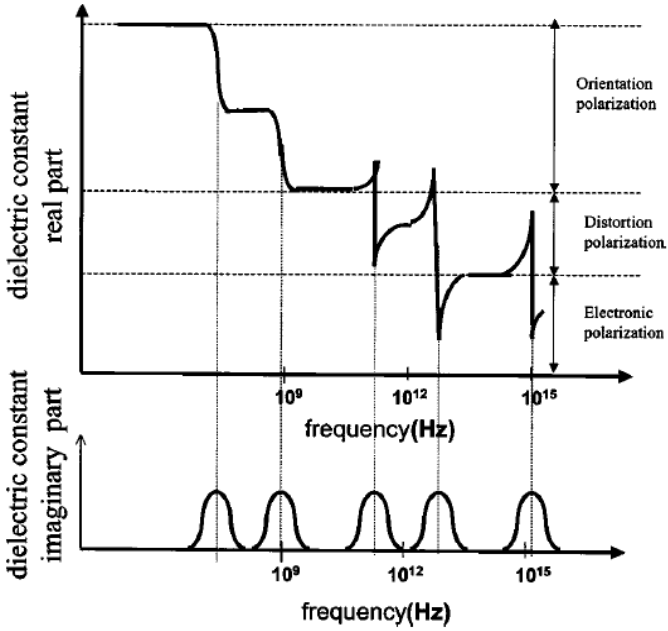

Figure 1.4 Schematic curves of the real and imaginary part of the dielectric constant of a fictive material with two orientation polarization modes and two different distorsion polarization modes. Adapted from Maex et al. [9]

Deybe's equation (1.4) shows that the permittivity (*k*-value) is smaller if materials do not contain polar molecules. Reduction of density by reducing number of molecules per m^3 *(N)* and polarizabilities α_e and α_d are also possible ways to reduce the dielectric constant. Therefore, a potential low-*k* dielectric can be made using materials with fewer polar bonds and with decreased density. The microelectronic industry has already moved to certain low-*k* materials, where some Si-O bonds have been replaced with less polar Si-F or Si-C bonds. A more fundamental reduction can be achieved by using low-polar bonds, such as C-C or C-H, for instance, in materials such as organic polymers.

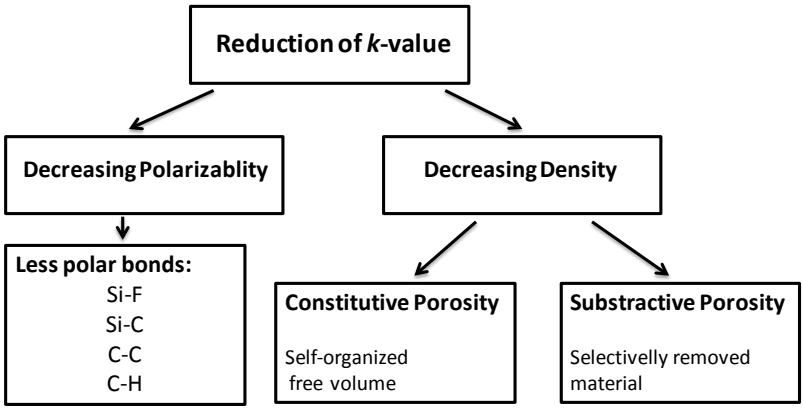

Figure 1.5 Methods to achieve lower dielectric constant. Adapted from Shamiryan et al. [10]

The density reduction can be realized by introduction of porosity to the material. A material can be made porous by either constitutive or substractive porosity [10]. Constitutive porosity refers to porosity introduced by the self-organization of a material. After manufacturing, such a material is porous without any additional treatment. Constitutive porosity is relatively low (usually less than 15 %) and the pore sizes are small, around 1 nm in diameter. Subtractive porosity involves selective removal of part of the material or incorporation of a sacrificial material. The material is removed via thermal annealing, UV-irradiation, supercritical extraction, or by selective etching. Subtractive porosity can be as high as 90% and pore sizes may vary from 2 nm to tens of nanometers. In general, the porosity in porous materials can be either open-pore or closed-pore in the structure. Closed pores are isolated from one another whereas open pores have a large degree of interconnection. Most of the subtractive porosity materials have an open pore structure.

1.2.1 Porosity effect on *k*-value

The effect of porosity incorporation on the *k*-value of a dielectric film can be estimated through the Maxwell Garnett (MG) theory (alternate formulation of Clausius-Mossotti equation) [11,12]. The average dielectric constant of the mixture

of the low-*k* matrix material with spherical intrusions (pores) is expressed by equation (1-5):

$$k_{av} = k_m \left[1 + \frac{3f(k_{por} - k_m)/(k_{por} + 2k_m)}{1 - f(k_{por} - k_m)/(k_{por} + 2k_m)} \right] \qquad (1\text{-}5)$$

where *f* is the porous fraction of the porous film, and *k*, k_{por} and k_m are the dielectric permittivities of the film, vacuum and the film matrix material, respectively. Taking the trends shown in Figure 1.6 for the *k*-value of a material versus its porous volume fraction. Those trends are strongly dependent on the permittivity of the matrix material when porous volume fraction is less than 0.5 as shown in Figure 1.6.

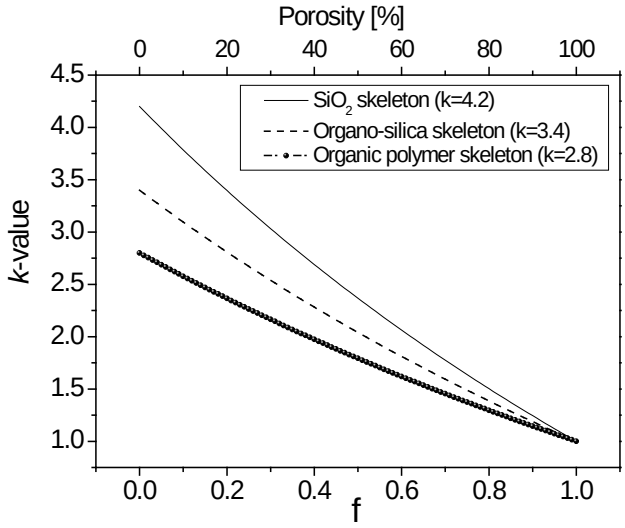

Figure 1.6 Dependence of *k*-value at 100 kHz on volume fraction filled with air as calculated using Maxwell-Garnett formula (1-5). Skeleton *k*-values of SiO_2, typical organo-silica (SiOC:H) and organic polymer.

1.2.2 Pore size distribution

The pore size distribution (PSD) of the porous materials influences their mechanical properties. Furthermore, the degree of pore interconnectivity changes diffusivity of chemicals into a porous low-*k* film structure. Figure 1.7 shows a simplified schematic of three hypothetical PSD.

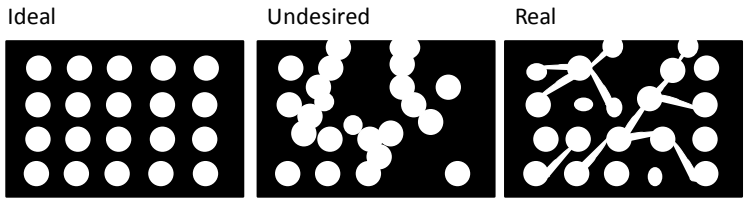

Figure 1.7 Schematics of pore structures; desired, undesired and real.

The ideal PSD (contrary to undesired) would be ordered, uniform, and containing closed pores with small pore radii. The ordered and uniform pores provide good mechanical stability, where smaller pore radii or closed porosity reduce/eliminate the diffusivity of the chemicals. However in reality the amorphous materials have interconnected and open pores with some distribution of the pore size [4]. The key factor is the degree of pore interconnectivity. The degree of pore interconnectivity increases rapidly when the porosity percolation threshold is reached [13]. The porosity percolation threshold is the threshold above which all pores in the material become interconnected. This threshold for most of the organosilica-based materials is above 25 % of material porosity [14]. This porosity level corresponds to the materials with k-values around 2.5. Materials with lower dielectric constant than 2.5 have a porosity higher than the percolation threshold that is approximately 25%. This significantly affects the characteristics of those materials: significantly reduced mechanical properties and increase diffusivity of chemicals.

1.3 Typical low-*k* materials

The main low-*k* candidates for microelectronic applications are shown in Figure 1.8. The potential low-*k* films can be divided into 3 groups.

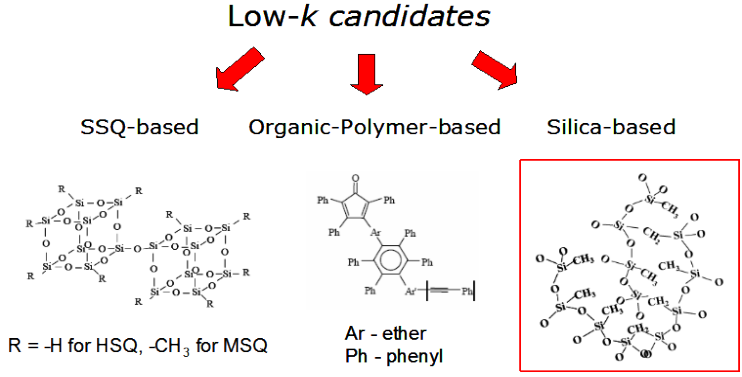

Figure 1.8 The main low-*k* candidates for microelectronics. The red frame indicate material group studied in this work. *The structure of organic-polymer-based low-*k* can be very different (SiLK from Dow Chemicals is shown as an example).

The first group contains silsesquioxane–based dielectric (SSQ). The SSQ are organic-inorganic polymers with the empirical formula $(R\text{-}SiO_{3/2})n$, where R is a functional group. The SSQ-based materials for microelectronic application are mainly hydrogen-silsesquioxane (HSQ) where functional group R is -H, and methyl-silsesquioxane (MSQ) where functional group R is $–CH_3$, or mixtures of both. MSQ have a lower dielectric constant as compared to HSQ because of the larger size of the $-CH_3$ group (2.8 and 3.0-3.2 respectively) and lower polarizability of the $Si\text{-}CH_3$ bond as compared to Si-H [9]. However, the integration of SSQ-based materials is difficult, mainly due to their poor mechanical properties and the tendency of the films to crack [15].

The second group of low-*k* materials consist of organic-polymer-based materials. The organic polymers for the low-*k* dielectric applications are mostly hydrocarbons with an aromatic structure. Saturated hydrocarbons have a lower polarizability than unsaturated, conjugated and aromatic polymers. Therefore, they may provide the lowest dielectric constants. However, the aliphatic C-C, C=C and C-N bonds generally are thermally unstable at T > 300-400 ºC. This limits compatibility with traditional technological processes developed for SiO_2-based dielectrics. Aromatic polymers contain molecules with almost purely covalent bonds such as C-C. Therefore, they are non-polar, also called low-loss (due to low dielectric losses). Non-polar polymers, by definition, have dielectric constants that are independent on frequency. The thermal stability of aromatic polymers can be improved by fluorination because the C-F bond has greater thermal stability than tbe C-H bond. Fluorine substitution also lowers the *k*-value by decreasing the polarizability and increasing the free volume. Most of the organic low-*k* films with sufficient thermal stability have a dielectric constant between 2.3-2.8 [16].

The third group of low-*k* films, silica-based materials is the most used in microelectronic technologies. The silica-based materials are based on the tetrahedral structure of SiO_2. Silica has a molecular structure in which each Si atom is bonded to four oxygen atoms, and each oxygen atom to two silicon atoms ($SiO_{4/2}$). The high frequency dispersion of the dielectric constant ($k \approx 4$ in the low frequency region and $k \approx 2.15$ in the range of visible light) is related to the high polarizability of the Si-O bonds (distortion or orientational polarization). Lowering the *k*-value can be accomplished by replacing the Si-O bond with less polarizable Si-F bond producing F-doped silica glasses (FSG). Another approach used is doping the silicate glasses with C by introducing CH_3 groups, which also lowers the *k*-value. Moreover, both F and C increase the inter-atomic distances or “free volume” of silica providing an additional decrease of dielectric constant. The elementary units of C-doped silica films form long chains with different degrees of cross-linking as shown in Figure 1.8. Apart from dielectric constant reduction, terminal groups such as $–CH_3$ provide hydrophobic properties of the silica-based low-*k* materials. For instance, porous silica cannot be used as low-*k* film because of its hydrophilic properties. The porous silica is widely used for packaging (i.e. shoes, food) to keep atmosphere dry but it is a very bad low-*k* film. Hydrophilic pores of the porous silica can be compared to large surfaces that can attract water from ambient (*k*-value of water is around 80). The *k*-value of porous silica filled with H_2O can be higher than that of bulk SiO_2 (k = 3.9 - 4.2) as demonstrated in section 1.7.1. Therefore, silica based low-*k* have

terminal C-containing groups. C-doped silica films can have dielectric constant in the range of 1.8 – 3 (dependently on the material porosity level). Nowadays, porous low-*k* films based on silica and silsesquioxanes with 10-15% of organic (carbon containing) hydrophobic groups are the most favored class of materials for advanced interconnect technology nodes [17]. Within that category these materials with *k*-values lower than 2.5 are the scope of this work.

1.4 Properties of low-*k* materials required for their integration

The implementation of the damascene technology introduces many constraints on the properties of the low-*k* materials. The properties of the low-*k* materials can be divided into four types: electrical, mechanical, chemical, and thermal. Table 1.1 lists all the requirements for the successful implementation of a low-*k* dielectric, divided into those groups. It is clear that the damascene integration of new low-*k* dielectrics brings a number of reliability concerns that include thermal or mechanical cracking or adhesion loss, poor mechanical strength, moisture absorption, lower dielectric breakdown voltage/time dependent dielectric breakdown (TDDB), texture effects and poor thermal conductivity.

Table 1.1 Properties of low-*k* materials required for their integration in Damascene technology. The exact values of the properties depent on the generation of technology.

Electrical	Mechanical	Chemical	Thermal
Low *k*-value Low leakage Low charge trapping High dielectric breakdown voltage High reliability	High elastic modulus (>5 GPa) High hardness Film thickness/ uniformity Adhesion Low shrinkage Low weight loss High crack resistance Reduced pore size (<5 nm)	High chemical resistance Low gas permeability High etch selectivity Low moisture absorption Low solubility in water High purity High storage life Environment Safety and Health compatible	High thermal stability Low thermal expansion Low thermal shrinkage High thermal conductivity

The reduced mechanical strength of porous low-*k* dielectrics is of particular concern in both processing (especially during chemical-mechanical polishing (CMP)) and packaging. Thus, mechanical properties, such as hardness, modulus, cohesive strength cracking limit, and crack propagation velocity have been key metrics for ongoing development. PECVD organo-silica low-*k* materials with *k*-

values of 2.5-2.8 have been successfully integrated for 45 nm and 60 nm technology nodes [18,19,20]. However the integration of materials with lower *k*-value than 2.5 is challenging. The challenge is mainly due to higher porosity and hydrophobic properties required to further reduce *k*-value as is discussed in sections 1.2 and 1.5. Two major drawbacks, out of many others, are related to higher porosity:

- Lower mechanical strength that results in:
  - Material degradation during chemical-mechanical polishing
  - Packaging
- Increased permeability of low-*k* films that results in:
  - Increased penetration and trapping of wet chemicals
  - Increased diffusion of reactive species from plasmas
  - Metal diffusion into the pores (i.e., TaN or TiN used for Cu barriers)

1.5 Plasma damage of low-k materials

During device fabrication, the low-*k* films are exposed to various plasmas. All of these plasmas have different properties and generate different types of wanted modifications of the low-*k* film structure. Unfortunately, also the unwanted modifications of low-*k* materials caused by plasma occurs simultaneusly and those are referred to in the literature as plasma damage of low-*k* materials [9,21]. This plasma damage is caused by physical, chemical or physicochemical plasma interactions with low-*k* materials. The physical interactions are due to UV-light, metastable atoms, ion bombardment, or hot electrons from processing plasmas. The chemical interactions are due to reactive plasma chemistry. And finally, the physicochemical plasma interactions combine both the physical and the chemical plasma effects. The typical effects of plasma interaction with low-*k* dielectric are its hydrophilization and/or densification. Both densification and hydrophilization of the low-*k* film increase its *k*-value as described by Debye's equation (1.4).

1.5.1 Hydrophilization

Interaction of the plasma with low-*k* dielectric results in damage due to hydrophilization of the low-*k* material. As such, the material will be more prone to wetting of the pores with ambient humidity. The most straightforward hydrophilization mechanism is removal of Si-CH_3 groups by O radicals generated in O_2-based plasmas. As proposed by Chang et al. [22], modification of the organo-silica glass (OSG) in O_2 plasma occurs via the overall reaction (1-6) where ≡Si designates Si bonded to three lattice O's.

$$\equiv Si\text{-}CH_3 + 4O \rightarrow \equiv Si\text{-}OH + CO_2 + H_2O \qquad (1\text{-}6)$$

Reaction (1-6) is thermodynamically favorable and the degree (carbon removal and depth) of damage in an oxygen plasma is always expected to be high.

The enthalpy for this reaction (ΔHr) is −994 kJ/mol calculated at 298 *K* [23]. The O_2-plasma damage mechanism can be represented as shown in Figure 1.9. Modification of OSG by oxygen radicals (1-6) results in formation of Si-OH groups. Moreover, the Si-OH groups are exchanged with Si-CH_3 groups with certain depth as shown in Figure 1.9. This depth is called depth of plasma damage [9].

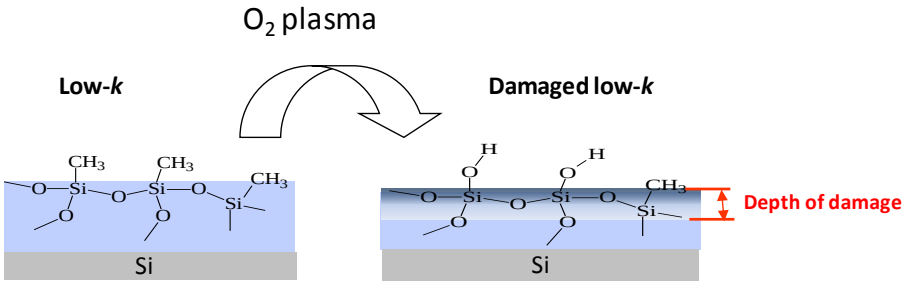

Figure 1.9 Simplified sketch of mechanism of plasma damage in O_2 plasma.

The Si-OH groups created in the OSG pores are potential centers for further moisture absorption. The Si-OH groups created in reaction (1-6) trap water that is a by-product of this reaction. Therefore partial filling of hydrophilic pores of low-*k* film with H_2O might occur during the O_2-plasma processing (*in situ* hydrophilization). However, most of water is absorbed when wafers are exposed to ambient, i.e., the humidity level is 40 % in microelectronic cleanrooms (*ex situ* hydrophilization). Figure 1.10 reflects *ex situ* and *in situ* hydrophilization mechanisms, (A) and possible initiation of stress-corrosion by the presence of the closely distributed –OH groups (B).

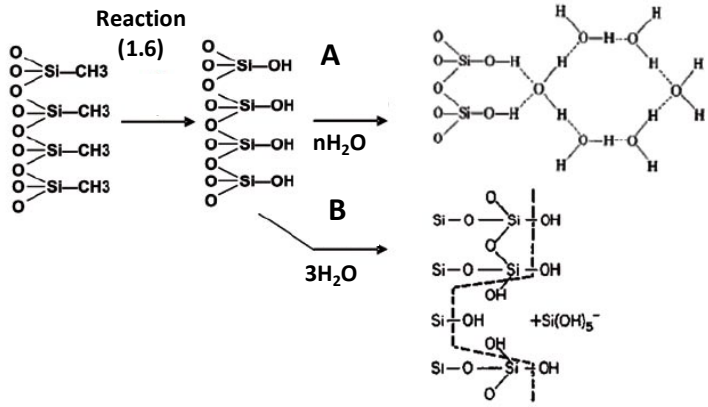

Figure 1.10 Removal of hydrophobic groups in reaction (1) leads to the formation of silanol SiOH groups. The subsequent exposure to air leads to multimolecular adsorption of water molecules that are bonded by hydrogen bonds (A) and/or irreversible degradatation (B), which is an initial stage of stress corrosion cracking (silica is soluble in water in basic solutions) [24,25].

It is also important to mention that water in hydrophilized pores can be bonded differently. There can be α, β and γ bonded water as shown in Figure 1.11.

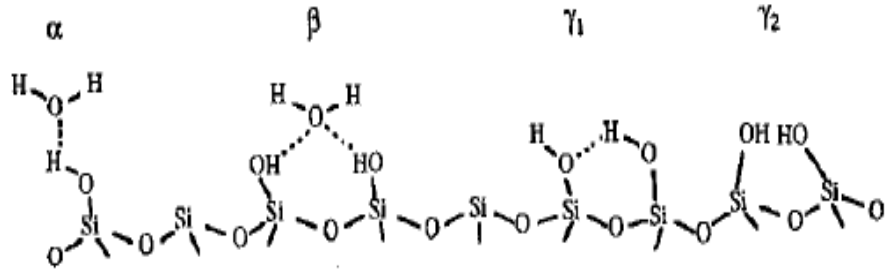

Figure 1.11 Schematic drawing of the various OH species and their relation to water bonding in siloxane-based OSG. Adopted from Proost et al. [26]

Depending on the bonding of the water molecules to the material pores, different annealing temperatures have to be used to remove the adsorbed water as shown in Table 1.2.

Table 1.2 Different formations of water into siloxane-based OSG and their removal temperatures, infrared absorbance values and activation energies.

Water	**Assigment**	**Removal temperature [°C]**	**Infrared Absorbance [cm^{-1}]**	**Ea [kJ/mol]**
α	Physisorbed water	192	3200-3700	23±2
β	Tightly hydrogen-bonded water	355	3600	55±17
γ1	Hydrogen-bonded water	631	3200-3700	89±1
γ2	Isolated silanols	730	3745	202±1

Temperatures higher than 700 °C are required to remove all water from the hydrophilic pore volume [26]. Damascene process temperatures, however typically do not exceed 450 °C to control stress and avoid thermo-degradation of the low-*k* films [27]. Therefore, annealing cannot be used to completely remove silanols from hydrophilized part of low-*k* film [25].

In summary hydrophilization of low-*k* material results in irreversible changes of its properties:

- Increase of leakage current and *k*-value [28]
- Reduced resistance to stress-corrosion cracking [25,29]

The increase of *k*-value due to plasma induced hydrophilization of low-*k* material is discussed in greater details. The hydrophilization of low-*k* dielectric lead to a substantial increase of the film permittivity due to an important contribution

from orientational polarizability in eq.(1.4). The effect of moisture incorporation on the dielectric constant of plasma damaged low-*k* films can be directly calculated using effective media approximations. Assuming, the plasma treatment increases the *k*-value because of the following. First, the dielectric constant of low-*k* matrix (k_m) increases up to about 4.2 (i.e., that of SiO_2) due to the carbon depletion i.e. by reaction (1-6) (all low polar bonds are removed). Second, removal of the hydrophobic groups Si-CH_3 from low-*k* leads to formation of hydrophilic silanol group. The silanol groups promote the moisture adsorption in the porous low-k material exposed to air (see Figure 1.10). Normally hydrophilized pore volume is not fully filled by H_2O at 40 % humidity that is present in cleanroom environment [30,31]. However, we assume that in first approximation all hydrophilized film is completely filled with H_2O when exposed to cleanroom environment. This is reasonable approximation for water confirmed in nano-pores [32]. Absorbed moisture drastically increases the total material dielectric constant because H_2O has a very large dielectric constant of around 80 [8]. Two media approximations are used to calculate the impact of H_2O (*k*~80) adsorbed in porous SiO_2 (*k*~4.2). The first approximation is Maxwell-Garnett equation (1-5) that assumes that water intrusions into SiO_2 skeleton are spherical. The second the simplest approximation is logarithmic mixture rule (1-7) that considers layer materials (i.e. H_2O and SiO_2 skeleton) with the layers either parallel or normal to the applied field [33]. The effect of incorporated water depends on pore shape because pore shape defines orientation of absorbed water dipoles towards electric field. This is main reason of differences in total *k*-value for used approximations.

$$ln\, k = f \cdot ln\, k_1 - (1 - f) \cdot ln\, k_2 \qquad (1\text{-}7)$$

$$k = exp\,[f \cdot ln\, k_1 - (1 - f) \cdot ln\, k_2] \qquad (1\text{-}8)$$

The formula derived from logarithmic mixture rule on total dielectric constant is represented by equation (1-8), where *f* is total volume filled with H_2O. The *k*, $k_1 = 4.2$ and $k_2 = 80$ are respectively dielectric permittivity of film, SiO_2 as material matrix and water at 100 kHz. The dielectric permittivity of SiO_2 film filled with different fractions of water calculated using Maxwell-Garnett (1-5) and logarithmic mixture formula is shown in Figure 1.12.

The absorbed moisture in the damaged part of the film has detrimental effect on its dielectric properties as shown in Figure 1.12. For instance, 25 % of a porous SiO_2 film fully filled with H_2O has a *k*-value in the range of 7.63 to 8.77 dependently on the formula used for approximation. Therefore, the *k*-value of the damaged low-*k* film can be higher than that of SiO_2 used as dielectric in the older Al/SiO_2 technology (see section 1.1). Assuming the analysis stated above, the porous low-*k* dielectrics might lose advantage over bulk SiO_2 when plasma processing is not optimized and the plasma damage is too large. This is especially true for smaller dimensions where the thickness of the dielectric layer between two Cu lines becomes extremely small. In order to demonstrate this, we calculated the influence of the *k*-value of the damaged part of low-*k* film on total *k*-value of

dielectric between two Cu wires. This can be done using the equivalent electrical scheme as shown in Figure 1.13.

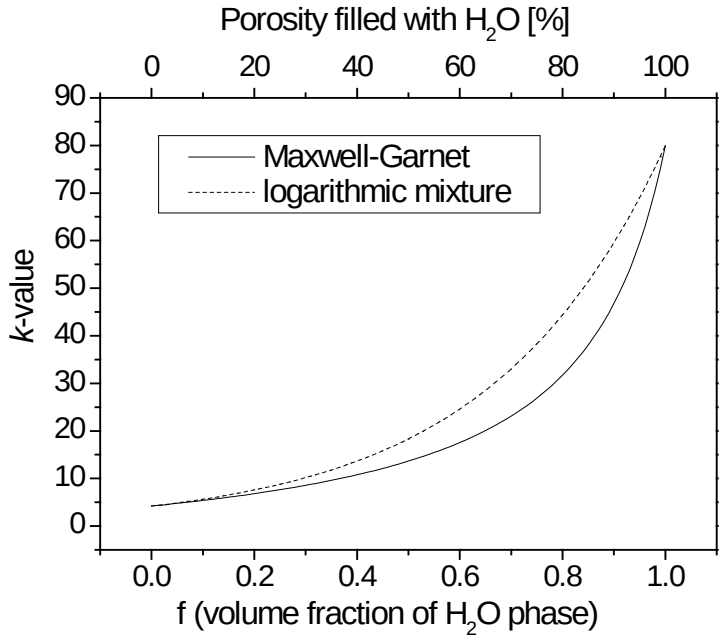

Figure 1.12 The *k*-value at 100 *k*Hz of SiO_2 filled with different amount of H_2O calculated using Maxwell-Garnet and logarithmic mixture formulas.

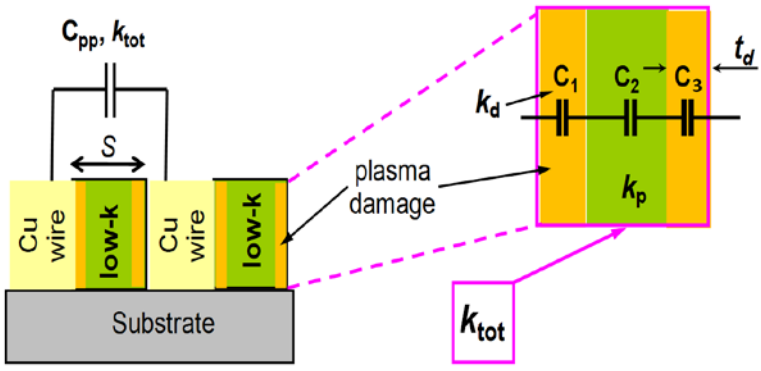

Figure 1.13 Schematic of sidewall damage induced to the dielectric by patterning plasmas. The parallel plate contribution to interline capacitance can be approximated by 3 capacitors in series: C_2, having the pristine *k*-value of the dielectric (k_p), and C_1 and C_3, both characterized by a thickness and a relative permittivity k_d, with $k_d > k_p$.

The total interline capacitance can be separated into a parallel plate and a fringing contribution, where impact of the fringing capacitance is less than 5% for *k*-values of dielectric in the range of 2 to 10 [34]. Therefore, a damage/modification of the dielectric between the interconnect lines would influence primary the parallel plate capacitance. The parallel plate capacitance (C_{pp}) can be calculated by considering a series of three capacitors as Figure 1.13 [34]. C_1 and C_3 are equal and related to the portions of damaged dielectric along the sidewalls, characterized by the parameters t and k_d. C_2 is related to the remaining part of the undamaged dielectric, with thicknesses equal to the difference between the interline spacing (S) and the damaged portions ($2t$), and with *k*-value k_p.

$$C_{pp} = \varepsilon_0 k_{tot} \frac{A}{S}; C_1 = C_3 = \varepsilon_0 k_d \frac{A}{t}; C_2 = \varepsilon_0 k_p \frac{A}{S-2t} \qquad (1\text{-}9)$$

According to the scheme in Figure 1.13 the parallel capacitance (C_{pp}) of the series of capacitors (1-9) can be expressed in equation (1-10). This equation can be re-written using definitions of capacitors from (1-9) as equation (1-11). And finally, equation (1-11) can be transformed to achieve the final equation (1-12) that expresses the total *k*-value of the damaged dielectric (k_{tot}).

$$\frac{1}{Cpp} = \sum_1^3 \frac{1}{C_i} = \frac{2}{C_1} + \frac{1}{C_2} = \frac{1}{\varepsilon_0 A}\left(\frac{2t}{k_d} + \frac{S-2t}{k_p}\right) \qquad (1\text{-}10)$$

$$\frac{S}{k_{tot}} = \frac{2t}{k_d} + \frac{S-2t}{k_p} \qquad (1\text{-}11)$$

$$k_{tot} = \frac{S}{\frac{2t}{k_d} + \frac{S-2t}{k_p}} \qquad (1\text{-}12)$$

The total *k*-value of the film versus spacing is plotted in Figure 1.14 using equation (1-12). Besides the *k*-values of the pristine and damaged layer of the dielectric, the most important parameters are depth of damage (*td*) and spacing (S) between wires. The depth of damage depends on dielectric and plasma process characteristics, while spacing between wires is defined by microelectronic technology node.

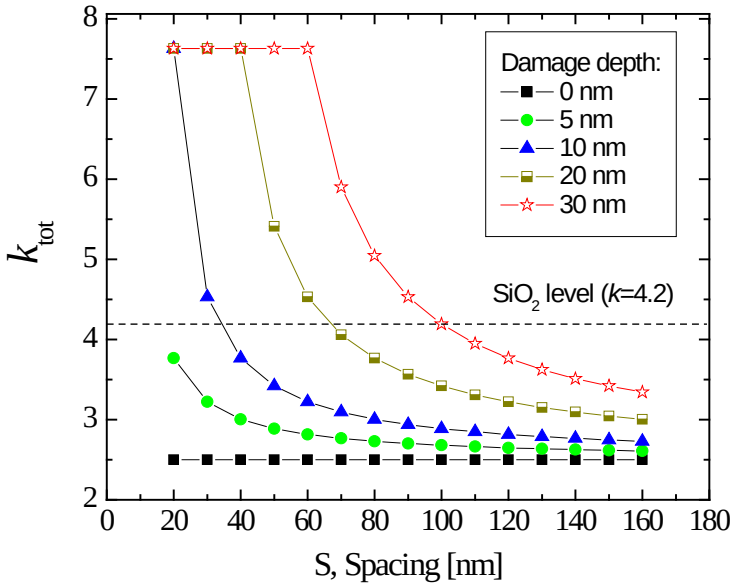

Figure 1.14 Total *k*-value at 100 kHz of the damaged film versus spacing (20 nm – 160 nm) for the various depths of damage. The *k*-value of the damaged layer is assumed to be of 7.63 as for 25% porous silica-like film with spherical intrusions fully filled with H_2O.

It is clear that to have advantage of using low-*k* dielectric in Damascene technology over SiO_2 for 32 nm node the depth of damage has to be limited to about 5-10 nm. However with grater spacing (older technology node i.e. > 32 nm spacing), the influence of damaged layer is smaller. For instance, for damage depth of 10 nm (calculated for 25% porous dielectric fully filled with H_2O) the technology nodes with spacing bigger than 40 nm still have advantage over SiO_2, etc. The model presented above shows the worst-case scenario. In reality, *k*-value 25% porous and hydrophilized low-*k* film is lower than 7.63 due to moisture level in the cleanroom (40 % humidity) and processes involving thermo-desorption of H_2O as was also discussed above. Moreover, it is important to mention that plasma damage also degrades other low-*k* material characteristics such as breakdown voltage, leakage current or mechanical robustness. However, the above model clearly shows the main idea of this work that plasma damage of low-*k* materials must be minimized by avoiding/reducing film hydrohilization and/or by minimizing of the depth of plasma damage.

1.5.2 Densification

Another plasma damage effect of low-*k* dielectric is its densification. The effect on *k*-value is usually lower than the effect of hydrophilization. This is due to

the fact that the densified layer cannot exceed the *k*-value of SiO_2 (4.2) unless it is also hydrophilized or other elements than H, Si, O, C are incorporated. In reality, the densification and hydrophilization of the low-*k* film occurs at the same time. This is due to the mechanism of this phenomenon that involves extensive bond breakage (silicon dangling bond generation) to achieve film cross-linking. The densification is mainly caused by ion-assisted, UV-light assisted or chemical assisted cross-linking. For instance, in the case of O_2-plasma damage, the bond breakage caused by O radicals from the O_2-plasma occurs within the SiCOH matrix and that results in the formation of activated silyl sites. The activated silyl sites are then available to react with other activated silyl species to form Si–Si crosslinks or possibly with Si-OH to generate a Si-O-Si crosslink. [35,36] The Si-OH groups are generated in O-plasma as described by reaction (1-6). The literature indicates possibility of cross-linkage by the following reaction:

$$\equiv Si\text{-}OH + OH\text{-}Si\equiv \rightarrow \equiv Si\text{-}O\text{-}Si + H_2O \qquad (1\text{-}13)$$

$$(\Delta Hr = 0\ kJ/mol\ at\ 293\ K)$$

The enthalpy value (ΔHr) in equation (1-13) is based on gas phase interations. And therefore this value is only indication of the thermodynamic stability of Si-OH groups.

1.6 Plasma processing steps in Damascene technology

The wiring in modern ULSI chips is realized using damascene technology [37]. The damascene technology involves etching trenches of vias in an insulating layer which is then filled with metal. The current technological approach use a dual-damascene approach that involves metal hard-masks [38]. However, for simplicity, the single damascene approach (without metal hardmask) is given as an example. The simplified single Cu/low-*k* damascene processing scheme is shown in Figure 1.15. The Cu/low-*k* damascene approach includes the following steps:

- Dielectric deposition
- Trench formation in the dielectric using dry (plasma) etch (a)
- Depositions of the diffusion barrier (TiN or TaN) (b)
- Deposition of copper (c)
- Chemical mechanical polishing (CMP) of copper such that the excess is removed from the top surface (d)

The combination of a porous low-*k* material with copper provides significant technological challenges [9,39]. The challenges arise from a number of drawbacks of copper and the vulnerability of low-*k* materials when they are exposed to plasmas and chemicals. Copper, which is known for its high diffusivity, can easily diffuse into a porous dielectric destroying its insulating properties (creating leakage paths, decreasing breakdown voltage etc.) [40,41]. A diffusion barrier such as TiN (or TaN) (as shown in Figure 1.15b) is needed between the dielectric and the copper

to prevent this copper diffusion. A far less complicated solution would be to first pattern the Cu and then fill the spaces with dielectric material as it was done in older technology nodes that were aluminium-based. Unfortunately, contrary to aluminium, copper cannot be patterned by dry etch as it readily forms precipitates with typical metal etch gases (e.g., Cl_2). [42] Therefore, a damascene patterning scheme must be adopted. This requires many subsequent process steps as shown in Figure 1.16. Especially process steps where the low-*k* dielectric is exposed to a plasma holds potential risk for damage of the low-*k* properties (as discussed in the previous section).

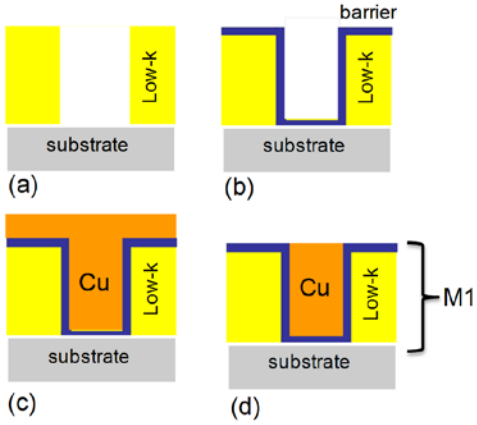

Figure 1.15 A simplified scheme of the damascene technological process steps required to create a M1 structure. A cross-section of a metallization line after (a) trench patterning, (b) diffusion barrier deposition, (c) copper deposition, (d) copper CMP.

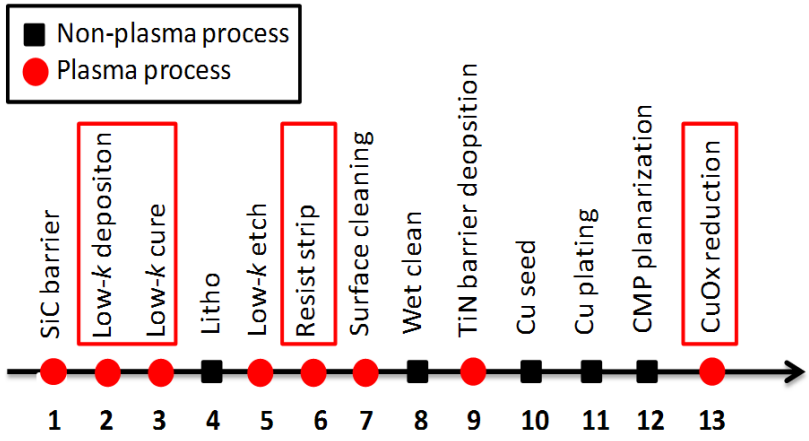

Figure 1.16 Chronological sequence (numbers on X axis) of the technological process in photoresist-based patterning scheme required to create M1 structure. The frames denote the processes that are the scope of this work.

The graph in Figure 1.16 presents the chronological sequence of the technological steps required to create first metallization level (M1) shown in Figure 1.15. The processes in Figure 1.16 are divided into two categories. Squares on the time axis denote process steps that do not involve plasma and circles correspond to a single process step that involves a plasma step. It is clear that advanced patterning in damascene technology strongly relies on the use of plasma-based processes. More than 50 % processes require direct or indirect plasma usage. The plasma is used mainly for (the numbers in the brackets denote process step sequence in X-axis in Figure 1.16):

- plasma enhanced chemical vapor deposition: low-k(2) and SiC (1) and TiN/TaN barriers (9)
- patterning: dielectric etch (5)
- polymer removal: photoresist strip (6) and surface cleaning (7)
- surface treatment: CuOx reduction (12)
- indirect plasma effect: generation of radicals during UV-irradiation (3)

This is because plasmas allow both chemical and physical etch interactions. The patterning and polymer removal rely on the ability of forming volatile compounds out of the materials to be removed; this means that a plasma of a gas mixture with highly reactive molecules is usually needed. Typically, fluorine or chlorine compounds are used for etching films with an inorganic backbone, while highly oxidizing or reducing chemistries are often used for the removal of organics or for surface passivation [43]. Usually those processes are performed using an 'ion-assisted' etching regime, where ion bombardment helps to remove etch products from the surface. Ion-assisted etching is especially important where the directionality (anisotropy) of the process is needed; i.e. in the patterning process. The purely chemical plasma processing (where only plasma radicals are used) is efficient and selective, but lacks directionality, which is a fundamental requirement for deep submicron feature patterning. However, pure chemical plasma processing still can be used in some cases for surface passivation or polymer removal processes.

Apart from low-k material processing, a plasma is used for the fabrication of low-k materials. Plasma usage can be direct, such as during the material deposition, or indirect, such as radical generation during UV-irradiation (curing) of the low-k material. The direct plasma usage occurs during plasma enhanced process deposition (PECVD) method. In contrast to conventional CVD, the PECVD method is a non-equilibrium technique, where the process is controlled mainly by the energy of the electrons in the plasma. [4] The energy of the electrons in a plasma is defined by an average energy but it has a Druyvesteyn-type distribution with a tail extending to energies much larger than the average one. [44] As a result, the plasma dissociates the molecules in the gas phase into a variety of radicals, which recombine on the substrate to form a variety of different bonds. The films deposited by PECVD are usually amorphous materials such as low-k dielectrics. The plasma generation can be indirect as well, i.e., during UV-irradiation of low-k films. This

indirect usage of the plasma is related to the excitation of gaseous reaction products by the UV itself.

This work focuses on the plasma modifications of the low-*k* materials that occur in the processes marked by the red frames in Figure 1.16. The scope of this work is explained in general picture in the next section.

1.7 Scope of this work

The damascene processing involves many process steps (as discussed in previous section). The successful implementation of the damascene technology requires understanding of all of the process steps and their impact on each other. This is a very complex task that requires involvement of many research and development teams. Obviously this problem cannot be resolved or even precisely specified in a single doctoral thesis. However, the author's attempt is to show how the contribution of this doctoral thesis can be related to some of the challenges of the damascene processing. The illustration of the key parameters in damascene processing of low-*k* dielectrics and their relation to this thesis is shown in Figure 1.17.

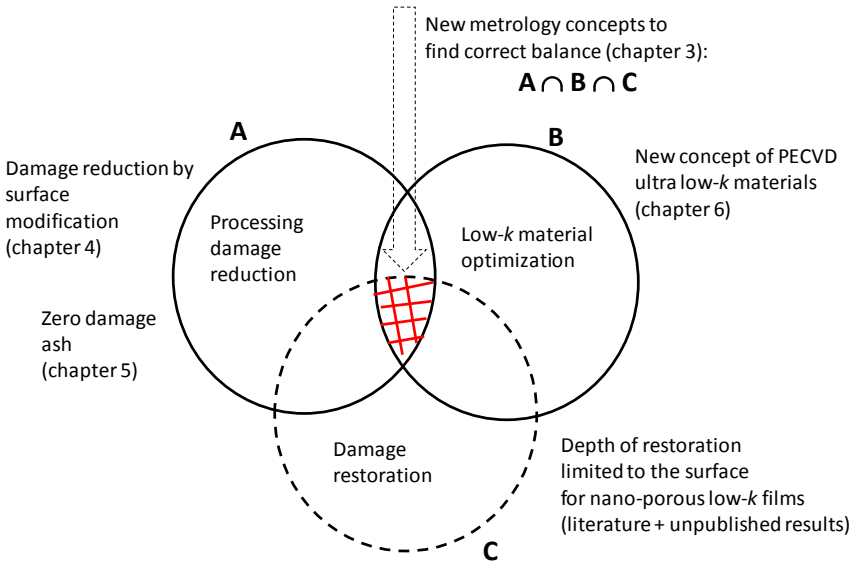

Figure 1.17 The schematic illustration of the key parameters in the damascene processing of the low-*k* materials versus contribution of this work. The dotted circle denotes processes out of the scope of this work, however important for a general picture. The finding about damage restoration is partly based on the following papers [45,46,47].

The optimal damascene processing can be represented in its three contributing variables (A,B,C). The set A represents all ways of optimization of the

processing of low-*k* (i.e., plasma damage reduction), B represents the ways of optimization of the low-*k* films (i.e., increasing their plasma damage resistance), C represents the ways of the processing damage restoration (i.e. restoration of hydrophobic properties of the low-*k* material surface. The optimal process, can be mathematically described as the intersection (denoted as $\cap$) of three efforts A and B and C. The intersection means that all efforts (A,B,C) should be also optimized in respect to each other to give the optimal result for the whole process sequence. In other words only some solutions out of many others in the set A are compatible with B and C and *vice versa*. For instance, optimization of the low-*k* materials to achieve the highest mechanical properties per achieved *k*-value requires avoiding porogen residue phase in the material (mechanically weak phase) (chapter 6). However, the presence of porogen residue in the films makes them more resistant to plasma damage in the most of the processes. In this case the best compromise would be introduction Si-C-H-Si links [48] and avoiding the porogen residues that should results in mechanically robust and plasma damage film. Another example is usage of the idea of densification of the top layer to reduce plasma damage [chapter 4 (set A)] in combination with chemical restoration of the low-*k* film (set C). This obviously is also an inappropriate combination because identified surface completely limits the depth of penetration of the restoration chemicals (therefore A and C are disjoint in this case $A \cap B = \emptyset$).

As mentioned earlier, the goal of this doctoral thesis is the investigation of the process induced damage of low-*k* dielectrics, methods of damage prevention and evaluation. This thesis can be divided into four parts: the first part deals with new metrology related to low-*k* materials (chapter 3), two other parts deal with damage induced through plasmas used for Cu surface cleaning (chapter 4) and by plasmas for photeresist mask removal (chapter 5). The fourth part is devoted to novel approach of PECVD low-*k* materials (chapter 6). The contribution of each chapter the challenges of the damascene processing is indicated in Figure 1.17.

1.8 References

[1] J. S. Kilby, United States Patent 3,138,745 (1959).
[2] G. E. Moore, Electronics 38, 114 (1965).
[3] G.E. Moore, IEDM Technical Digest, 21, 11 (1975).
[4] G. Dubois, R. D. Miller, W. Volksen, in Dielectric Films for Advanced Microelectronics, M.R. Baklanov, M. Green, K. Maex, Editors, Chapter 2, Elsevier Inc.: John Wiley & Sons: England (2007).
[5] S.P. Murarka, in Interlayer Dielectrics for Semiconductor Technologies, S.P. Murarka, M. Eizenberg, A.K. Sinha, Editors, Chapter 2, Editors, Chapter 2, Elsevier Inc.: London, England (2003).
[6] M. R. Baklanov and K. Maex, Philosophical Transactions of the Royal Society a-Mathematical Physical and Engineering Sciences, 364, 201 (2006).
[7] R. H. Havemann and J. A. Hutchby, in High-Performance Interconnects: An Integration Overview, p. 586, IEEE (2001).
[8] D. Shamiryan, T. Abell, F. Iacopi and K. Maex, Materials Today, 34 (2004).
[9] K. Maex, M. R. Baklanov, D. Shamiryan, F. Iacopi, S. H. Brongersma and Z. S. Yanovitskaya, J. Appl. Phys., 93, 8793 (2003).
[10] D. Shamiryan, T. Abell, F. Iacopi and K. Maex, Mater. Today, January 34 (2004).
[11] O. Levy and D. J. Bergman, Physical Review B 46 (11), 7189-7192 (1992).
[12] J.C.M. Garnett, Philos. Trans. R. Soc. London Ser. A, vol. 203, pp. 385-420, (1904).
[13] Y. Li, P. Weng, in Dielectric Films for Advanced Microelectronics, M.R. Baklanov, M. Green, K. Maex, Editors, Chapter 11, p. 456 , Elsevier Inc.: John Wiley & Sons: England (2007).
[14] A. Zenasni, F. Ciaramella, V. Jousseaume, C. Le Cornec and G. Passemard, J.Electrochem. Soc., 154, G6 (2007).
[15] G.Dubois, R. D. Miller, W. Volksen, in Dielectric Films for Advanced Microelectronics, M.R. Baklanov, M. Green, K. Maex, Editors, Chapter 1, Elsevier Inc.: John Wiley & Sons: England (2007)
[16] S.J. Martin, J.P. Godschalx, M.E. Mills, E. O Shaffer, and P.H. Townsend, Adv. Mater., 12 (23), 1769-1778 (2000).
[17] Z. Tokei, M. Baklanov, I. Ciofi, L. Younglong and A. Urbanowicz, Semiconductor Fabtech, 110 (2007).
[18] C. H. Jan, N. Anand, C. Allen, J. Bielfield, M. Buehler, V. Chikamane and K. Fisher, A 90 nm High Volume Manufacturing Logic Technology Featureing Cu Metalization and CDO Low-k ILD Interconnects on 300 mm Wafers, in, p. 205, Tech. Dig. IEEE Int. Interconnect Tech. Conf. (2004).
[19] C. Jeng, W. K. Wan, H. H. Li, M. S. Liang, K. H. Tang, I. C. Kao, K. S. Lo, T. C. Huang, C. H. Yao, C. C. Lin, M. D. Lei, C. C. Hsia and M. S. Liang, BEOL process integration of 65nm Cu/low k interconnects, in, Tech. Dig. IEEE Int. Interconne Tech. Conf. (2004).
[20] R. Fox, O. Hinsinger, E. Richard, E. Sabouret, T. Berger, C. Goldberg and A. Humbert, High performance k=2.5 ULK backend solution using an improved

TFHM architecture, extendible to the 45nm technology node, in, Tech. Dig. IEEE Int. Electron Devices Meeting (2005).
[21] W. Volksen, D. M. Miller and G. Dubois, Chem. Rev., 110, 56 (2010).
[22] T. C. Chang, P. T. Liu, Y. S. Mor, T. M. Tsai, C. W. Chen, Y. J. Mei, F. M. Pan, W. F. Wu and S. M. Sze, J. Vac. Sci. Technol. B, 20, 1561 (2002).
[23] M. A. Worsley, S. F. Bent, S. M. Gates, N. C. M. Fuller, W. Volksen, M. Steen and T. Dalton, J. Vac. Sci. Technol. B, 23, 395 (2005).
[24] R.K. Iler, The Chemistry of Silica, John Willey & Sons, Inc., New York p.62-63 (1979).
[25] Z. Tokei, M. Baklanov, I. Ciofi, L. Younglong, A. Urbanowicz, Semiconductor Fabtech 2007, 110
[26] J. Proost, M. Baklanov, K. Maex, L. Delaey, J. Vac. Sci. Technol. B, 18, 303, (2000).
[27] A. L. Loke, Process Integration Issues of Low-permittivity Dielectrics with Copper for High-Performance Interconnects, in Electrical Engineering, Stanford University, Stanford, p.17 (1999).
[28] Y. Li, I. Ciofi, L. Carbonell, N. Heylen, J. Van Aelst, M. Baklanov, G. Groeseneken, K. Maex, Z. Tokei, J. Appl. Phys., 104, (2008).
[29] H. Li, T. Y. Tsui, J. Vlassak, J. Appl. Phys., 106, (2009).
[30] M. R. Baklanov, D. O'Dwyer, A. M. Urbanowicz, Q. T. Le, S. Demuynck and E. Hong, Moisture Induced Degradation of Low-k Dielectrics, in Mat. Res. Soc. (2006).
[31] F. S. Baker and K. S. W. Sing, Journal of Colloid and Interface Science, 55, 605 (1976).
[32] T. Ohba, H. Kanoh and K. Kaneko, Nano Latters, 5, 227 (2004).
[33] W. D. Kingery, H. K. Bowen and D. R. Uhlmann, Introduction to Ceramics, p.947-948 John Wiley & Sons, New York (1976).
[34] F. Iacopi, M. Stucchi, O. Richard and K. Maex, Electrochem. Solid-State Lett., 7, G79 (2004).
[35] M. A. Worsley, S. F. Bent, S. M. Gates, N. C. M. Fuller, W. Volksen, M. Steen and T. Dalton, J. Vac. Sci. Technol. B, 23, 395 (2005).
[36] N. Posseme, T. Chevolleau, T. David, M. Darnon, O. Louveau and O. Joubert, J. Vac. Sci. Technol. B, 25, 1928 (2007).
[37] J. Davis and J. D. Meindl, Interconnect technology and design for gigascale integration, p. 37, Kluwer Academic Publishers, Boston (2003).
[38] R. Doering and Y. Nishi, Handbook of semiconductor manufacturing technology, Ch.2 p. 6 v,CRC Press, Boca Raton (2008).
[39] T. A. Spooner, J. C. Arnold, D. Canaperi, H.-C. Chen, S.-T. Chen, S. M. Gates, A. Isobayashi, P. Leung, S. S. Papa Rao, M. Sankarapandian, H. Shobha and O. van der Straten, ECS Trans., 25 (2009).
[40] O. R. Rodriguez, W. N. Gill, J. L. Plawsky, T. Y. Tsui and S. Grunow, J. Appl. Phys., 98 (12), (2005).
[41] O. R. Rodriguez, W. Cho, R. Saxena, J. L. Plawsky and W. N. Gill, J. Appl. Phys., 98 (2) (2005).
[42] R. Doering and Y. Nishi, Handbook of semiconductor manufacturing technology, p. 40 Ch.21 CRC Press, Boca Raton (2008).

[43] R. Doering and Y. Nishi, Handbook of semiconductor manufacturing technology, p. 43 v. Ch.21 , CRC Press, Boca Raton (2008).
[44] A. Grill, Cold Plasma in Materials Fabrication: From Fundamentals to Applications, Wiley-IEEE Press, Hoboken, NJ, (2001).
[45] J. Bao, H. Shi, J. Liu, H. Huang, P. S. Ho, M. D. Goodner, M. Moinpour and G. M. Kloster, J. Vac. Sci. Technol. B, 26, 219 (2008).
[46] A. P. Singh, D. D. Gandhi, E. Lipp, M. Eizenberg and G. Ramanath, Journal of Applied Physics, 100 (2006).
[47] M. S. Nadiye-Tabbiruka and J. M. Hayenes, Colloid & Polymer Science, 272, 1602 (1994).
[48] S. M. Gates, A. Grill, D. M. Miller, D. A. Neumayer and S. Nguyen, SiCOH Film Preparation Using Precursors with Built-in Porogen Functionality, in IBM patent US2007/0161256 A1 (2007).

2 Materials and methods

2.1 Introduction

The knowledge about plasma chambers, material properties and characterization methods is of key importance for the fundamental understanding of the plasma damage phenomenon of low-*k* materials. This chapter is devoted to the plasma chambers, the dielectric materials and the metrology techniques used in this work. Those items are dealt within three subsections. Firstly, we focus on the plasma chambers used for damascene processing of the low-*k* materials. Secondly, we discuss basic characteristics of the low-*k* dielectric. Finally, we present the measurements techniques suitable for the characterization of the low-*k* dielectric modified by the plasma or UV.

The design of the plasma chamber determines the basic plasma characteristics. The plasmas that can be achieved are dependent on the specific plasma chamber designs and results in different densities or/and ion energies. Therefore, an output of the different experiments can be partly predicted by knowing the plasma chamber design. Analogically, the basic properties of the porous low-*k* materials such as pore size and porosity define the depth of penetration of the chemically-active plasma radicals. The depth of the plasma radical penetration in the low-*k* pores determines an extent of the plasma damage. For example, the extent of plasma damage can be a few times higher for mesoporous dielectrics with high porosity levels in comparison with nanoporous dielectric with low porosity levels [1,2]. Furthermore, plasma damage of low-*k* materials is a complex phenomenon that results in change of their bonding structure, pore morphology and carbon concentration [3]. The complexity also increases due to fact that porous low-*k* dielectrics are usually amorphous materials with a random pore structure [4]. Therefore, an adequate study of the plasma induced modifications of low-*k* dielectrics requires variety of analytical techniques. For instance, techniques such as ellipsometry for thickness measurements, ellipsometric porosimetry for pore size evaluation, over Fourier transform infrared spectroscopy (FTIR) for changes in the bonding structure, and secondary ion mass spectrometry for bulk concentration profiles of the basic components are typically used for low-*k* characterization.

2.2 Plasma chambers

One of the major aims of this work is an investigation of the plasma interaction mechanisms during damascene processing of low-*k* dielectrics. The basics of damascene processing steps were discussed in section 1.8. In general, the plasma processing can be physical, i.e. ion sputtering; chemical when only the plasma radicals are in contact with the wafer (low-*k*); or physicochemical when ions, UV light, and plasma radicals interact with the material. This section deals with three specific designs of plasma chambers that are typically used for the damascene processing of low-*k* materials. Those three designs can have significant impact on the processing, i.e., ion-assisted plasma etching or purely chemical cleaning can be achieved (see chapter 1). The various designs of the plasma chambers used by researchers result in contradictory conclusions about the same plasma chemistry effects on the same low-*k* materials, as discussed in chapter 5. Therefore this background is necessary for further discussion of the subsequent chapters.

2.2.1 Model of operation of plasma reactors used in Damascene technology

Typically three plasma reactors designs are used in Damascene processing: the inductively-coupled plasma (ICP), coactively-coupled plasma (CCP) and downstream plasma chambers. Those specific designs make them suitable for the different damascene processing steps. The ICP, CCP and downstream-plasma chamber designs are illustrated in Figure 2.1. The downstream chamber significantly differs from the CCP and ICP systems. In the downstream chamber, the plasma area is separated from the wafer area by a special grids that neutralize the effect of ions or UV-light from the plasma.

In all these chambers, the plasma is ignited by an amplitude modulated (AC) current. However, the downstream plasma chamber typically uses a microwave-frequency current for the plasma generation while ICP and CCP chambers use a radio-frequency (rf) current (Figure 2.1). The use of microwave plasma in downstream plasma chambers is due to the requirement for a high concentration of the reactive species that can be provided by the microwave discharge. The fraction of ionized gas and, therefore, reactive species concentration in microwave-discharge is higher in comparison with other discharges [5] (i.e. rf-discharge). In contrast, ICP and CCP chambers use rf-discharge which has a higher etch uniformity as compared to microwave-discharge [6].

In the ICP and CCP chambers the rf-power creates displacement currents inside the plasma. The rf power can interact with plasma either inductively for ICP chambers (Figure 2.1a) or capacitively for CCP chambers (Figure 2.1b). The inductive case transfers the power to the plasma in the same way as a transformer transfers the power from one line to another. Schematically, a coil connected to the rf power supply is wrapped around a plasma quartz tube causing the energy to be transferred

in an inductive way. A rf current flowing through the coils generates an electromagnetic wave that penetrates in the plasma chamber, and azimuthically accelerates electrons and sustains the plasma. The rf used varies between frequencies of 10 kHz and 30 MHz, typically 13.56 MHz (wavelength 22 m) to avoid interference with radio-communication [5]. In the case of the capacitively coupled rf plasmas, two electrodes connected to the rf power source are used instead of coils. This method is operated with frequencies between 1 and 100 MHz, typically 2 and 27 MHz. In this case the plasma is heated directly by the rf electric field between the electrodes.

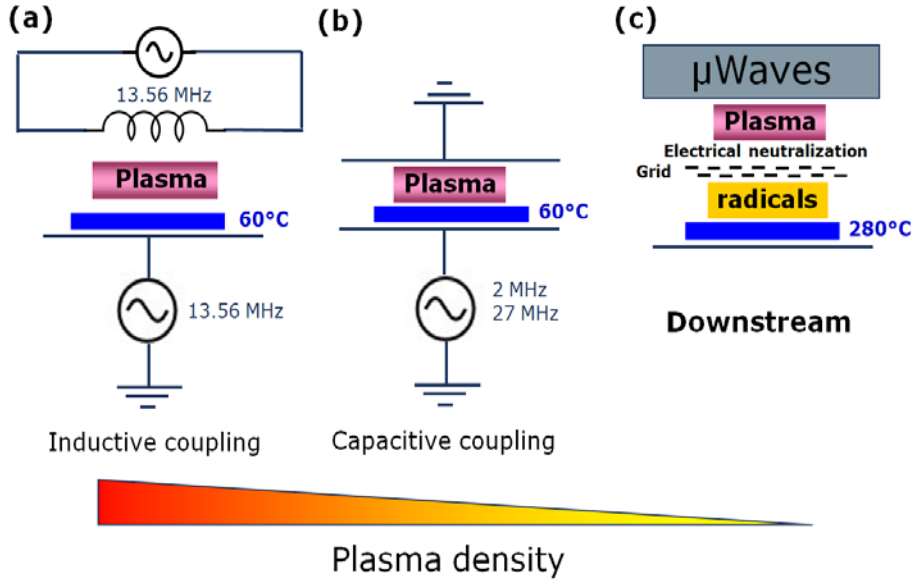

Figure 2.1 Schematic representation of plasma chambers in damascene processing. The letters (a), (b) and (c) denote ICP, CCP and downstream plasma chambers respectively. The red-yellow bar indicates qualitatively the difference in plasma density interacting with the wafer in these 3 system designs.

The fundamental difference between CCP and ICP designs is the way the plasma discharge is inducted as well as plasma density. The low-pressure ICP discharges (>100 mTorr) operate at electron densities of 10^{11}-10^{12} cm^{-3}, exceeding those in CCP more than 10-fold; therefore, ICP discharges are also referred to as the high density plasma (HDP) [7]. This difference in plasma density leads to a different relative species concentration in ICP and CCP plasmas.

Furthermore, an important advantage of ICP chambers over CCP chambers is an independent control of the ion kinetic energy because of an additional capacitively coupled rf source called the rf bias. This rf bias drives the electrode on which the substrate for material treatment is placed, as shown in Figure 2.1a. Thus, ICP chambers are able to provide independent control of the ion and radical fluxes

by means of the main ICP source power and the ion-bombarding energies by means of the power of the bias electrode [7].

In summary, the key differences between three chambers' designs described above can be represented in Figure 2.1. The plasma chambers used in damascene processing can be divided into three categories considering electrical design:

- Inductively coupled plasma reactors (ICP)
  - high plasma density
  - independent control of ion energy and plasma density
  - typical wafer temperature range 20 – 80 ºC
- Capacitively coupled plasma reactors (CCP)
  - medium plasma density
  - ion kinetic energy cannot be fully controlled
  - typical wafer temperature range 20 – 80 ºC (200 – 300 ºC for PECVD systems)
- Downstream plasma systems
  - Plasma area is separated from the wafer – "zero plasma density"
  - Pure chemical process controlled by substrate temperature
  - typical wafer temperature range 200 – 300 ºC

2.2.2 Plasma chambers used in damascene technology

In order to explain functions and basics parameters of typical plasma chambers used in the damascene technology we discuss plasma etching in general (Figure 2.2). The main aim of introduction of plasma etching instead of wet chemical etching in the microelectronics was the required high etching anisotropy (directionality of etch) that can be provided by the presence of ions in the etch plasmas [8]. However, to achieve a desired profile of the nanostructures the proper balance between the etch process anisotropy and the selectivity must be established as shown in Figure 2.2. The selectivity can be defined as the ratio of the etch rates between two etched materials. One example to define the selectivity in etching is the photoresist-based etching of the low-*k* dielectric. The photoresist mask is deposited on top of the low-*k* material and therefore etching occurs only in places defined by photoresist pattern (see also chapter 1). However, the plasma chemistry should be selected as such to etch only the dielectric material without etching of the photoresist mask; otherwise the mask would be removed during low-*k* etching. Therefore the etching selectivity of the low-*k* dielectric towards photoresist should be high. This means that the etch rate of low-*k* material has to be significantly greater than the etch rate of photoresist mask.

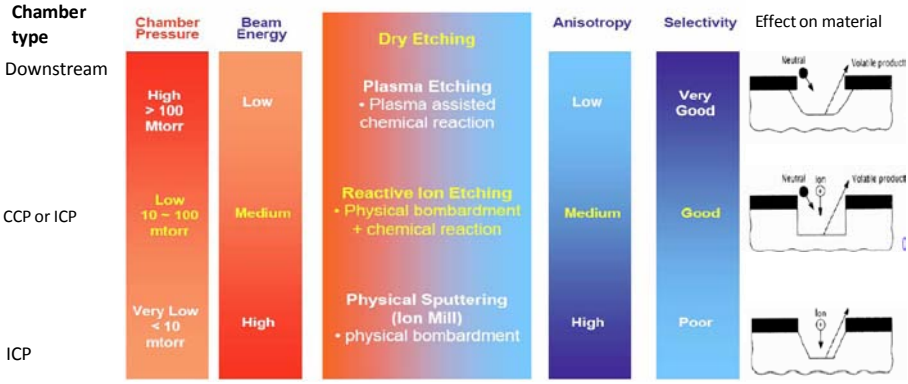

Figure 2.2 The schematic representation of plasma conditions such as pressure and beam energy and their effect on anisotropy and the selectivity of the process. Adopted from Heyns et al. [8].

Figure 2.2 represents the correlation between typical pressures and beam energies (~plasma densities, ion kinetic energies) and their effects on anisotropy and selectivity of the etch process. Starting from the top the scheme (Figure 2.2) the downstream plasma chambers can be used to achieve etching driven only by the gas chemistry. In downstream configuration the plasma area is separated from the wafer area by a special grid system that cuts of UV-light and ions. Therefore pure chemical etching can be achieved. The downstream plasma chambers require gas pressures higher than 100 mTorr, typically from 0.7 up to 4 Torrs to achieve sufficient concentrations of the active plasma radicals. A key advantage of downstream systems is a very high selectivity due to lack of ions or UV-light that might enhance etching. However, the lack of ions make it impossible to achieve the anisotropic etch in the downstream chamber. The downstream plasma chamber designs are typically used for processes that do not require anisotropy such as photoresist removal or surface cleaning (see also chapter 1). The middle of the scheme as shown in Figure 2.2 indicates the optimal conditions for etching. The typical pressures are higher than 10 mTorr up to 300 mTorr. Both ICP and CCP designs can be used. The major differences between ICP/CCP and downstream systems design is that in the former there is no separation (i.e. grid) between wafer area and plasma area. Therefore the effects of ions, electrons and UV or metastable atoms always have an impact on the processing. This results in reduction of the selectivity because of reactions enhancement by ions or UV light (i.e. ion-assisted chemical sputtering). On the other hand, the presence of ions and the possibility of their directional acceleration perpendicular to the wafer allows to achieve good etch anisotropy at a reasonably low loss of selectivity. Finally very high anisotropy can be achieved in ICP chambers at pressures lower than 10 mTorr. The very high anisotropy is achieved at the expanse of poor selectivity. The poor selectivity is due to the fact that ions sputter all materials independent of their chemical structure. It is important to note that photoresist removal or surface cleaning processes can be realized in all of the discussed conditions, while the patterning of materials that requires ion-based processes in the last two only (CCP and ICP chambers). However, it is demonstrated

in chapter 5 that the photoresist removal process without low-*k* dielectric damage requires extremely high selectivity which can only be provided in the downstream plasma reactors.

2.3 Characteristics of the plasma chambers used in this study

In this work 4 plasma chambers were used. The basic characteristics of the systems are specified in Table 2.1.

Table 2.1 Basic characteristics of the plasma chambers used in this work. All chambers were used for processing of 300 mm wafers.

Chamber type	Equipment name	Discharge type	Operation Pressure [mTorr]	Wafer Temperature [ºC]
ICP	LAM 2300® Verys®	rf (13.56 MHz)	5-80	20-80
CCP	LAM 2300® Exelan®	rf (2 MHz and 27 MHz)	5-300	20-80
	ASM Eagle 12	rf (13.56 MHz) (sample grounded)	1000-5000	20-350
Downstream	LAM 2300® Asher	microwave (2.4 GHz)	100-5000	20-350
	Radiant Strip320LK	microwave (2.4 GHz)	100-10000	20-350

2.4 Basic characteristic of the low-k materials used in this study

The low-*k* dielectrics used in this work can be divided into two groups. The first group consists of the low-*k* films deposited by a PECVD method using a porogen-based approach to create porosity. The second group consists of the films

deposited by spin-on method using a templating of silica-nanoparticles (self-assembly approach) to create porosity. It is important to mention that spin-on technique can also use porogen-approach (as in PECVD) as well as many other approaches to introduce porosity (see section 6.1). However, this work focuses on spin-on films mentioned above.

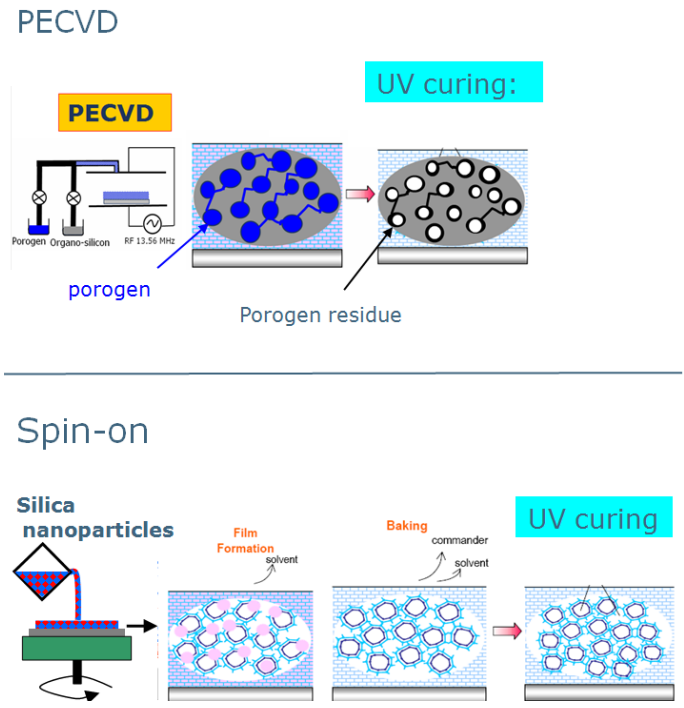

Figure 2.3 The schematic representation of differences in fabrication procedure between spin-on (nano-templating of Si nano-particles) and PECVD films (porogen based approach).

The basics differences between PECVD and spin-on (nano-templating of silica-nanoparticles) deposition methods of low-*k* materials are reflected in Figure 2.3. In the PECVD deposition approach the organo-silica matrix was deposited simultaneously with organic porogen (typically cyclic aromatic hydrocarbons). The PECVD SiOCH low-k films were deposited on 300 mm Si wafers. After the deposition, the films were UV cured in nitrogen ambient at temperatures close to 430 °C using broadband and narrowband UV-sources [9]. After UV-curing some part of the porogen is removed and some of it still remains in film pores. This remaining porogen parts is referred as porogen residue (PR) as shown in Figure 2.3. The effect of PR on film properties and processing compatibility is discussed in chapters 5 and 6. Furthermore, application of UV-SE for PR and porogen detection is discussed in section 2.5.1.1.

The *k*-values were targeted in the range of 2.3 – 2.5 as shown in Table 2.2. Additionally, the nano-clustered silica film of 140 nm with $k \sim 2.3$ was deposited by

a spin-on method [10]. The spin-on deposition was done at room temperature and ambient pressure, by dispensing an amount of liquid precursor on the substrate, placed on a spinner (Figure 2.3 bottom graph). The rotation of the substrate creates centrifugal forces that ensure the uniform distribution of material on the surface. The spinning step is followed by a thermal step (baking) at temperatures of 250°C, aimed at a complete removal of the solvents. This step usually also initiates cross-linking of the film. Finally, a UV-curing at temperature of 300°C was performed to obtain a stable film. This step promotes the full cross-linking of the polymer chains, till the achievement of a mechanically stable film structure. The basic characteristics of all low-*k* dielectric films used in this work are shown in Table 2.2.

Table 2.2.Basics characteristic of the low-*k* films used in this work. The letters marking film type are used in the next chapters. UV curing denotes UV wavelength used for film curing (see Figure 2.4). CVD is used for films fabricated by PECVD with *k*-values around 2.5 (CVD 2.5) and 2.3 (CVD 2.3). SOG is used for film deposited by spin on method the film has *k*-value 2.3. RI_{632nm} and YM denote film refractive index at 632 nm and Young's modules, respectively. The mean pore radii and open porosity were determined by TEP.

Film	UV-curing	Open porosity	k at 100 kHz	Mean pore radii [nm]	RI632nm	YM [GPa]
CVD 2.5						
B2	>200 nm	23 %	2.5	0.7	1.343	7.43
E2	~172 nm	24 %	2.5	0.7	1.363	7.47
CVD 2.3						
Ea	~172 nm	32 %	2.3	0.9	1.378	4.48
Eb	>200 nm	34 %	2.3	1.0	1.339	3.8
B3	>200 nm	36 %	2.2-2.3	1.1	1.341	5.54
SOG 2.3						
N	>200 nm	32%	2.3	1.0	1.277	6.54

2.5 Metrology

2.5.1 Ellipsometry

Spectroscopic ellipsometry is a well established technique for studying thin films [11,12,13]. The fundamental principles of elliposometry are well known [11] and therefore are only briefly discussed. Some optical properties and thickness of thin films can be determined by analysing the change of polarization of light. The fundamental idea of ellipsometry is shown in Figure 2.4. Ellipsometry measures a

change of polarization of light after its reflection from the studied material. This change of polarization can be fitted using ellipsometric models to find optical properties and thickness of the material in question.

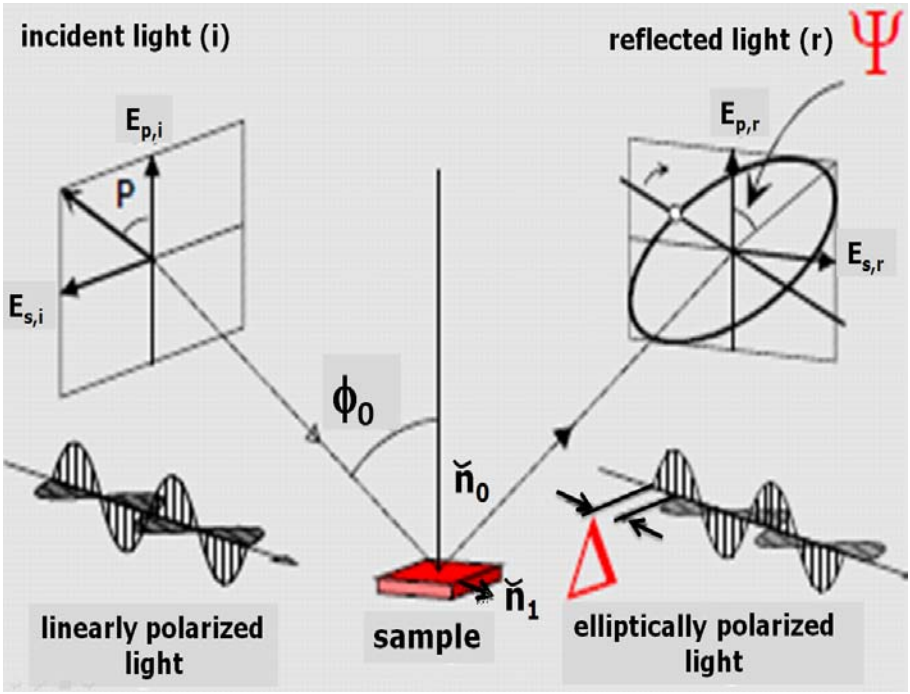

Figure 2.4 The schematic representation of fundamental idea of ellipsometry.

The incident electric field vector E_i (incident light) can be decomposed as a sum of two vectors; $E_{p,i}$ vector describing the electric field parallel with the incidence plane and $E_{s,i}$ vector perpendicular to the incidence plane (see Figure 2.4). The indexes p and s ("sankrecht" from German) denote parallel and perpendicular components of the electric field vector. Furthermore, the indexes i and r denotes incoming and reflected light (electric field). The amplitude ratios for p and s polarization for reflection can be described by complex Fresnel amplitude reflectance coefficients as described by equations (2-1) and (2-2):

$$r_p = \frac{E_{p,r}}{E_{p,i}} = \frac{\breve{n}_1 cos\phi_0 - \breve{n}_0 cos\phi_1}{\breve{n}_1 cos\phi_0 + \breve{n}_0 cos\phi_1} = |r_p| e^{i\delta_p} \qquad (2\text{-}1)$$

$$r_s = \frac{E_{s,r}}{E_{s,i}} = \frac{\breve{n}_0 cos\phi_0 - \breve{n}_1 cos\phi_1}{\breve{n}_0 cos\phi_0 + \breve{n}_1 cos\phi_1} = |r_s| e^{i\delta_s} \qquad (2\text{-}2)$$

where $\breve{n}_0 \; and \; \breve{n}_1$ denote complex refractive indexes of ambient and material, respectively (see Figure 2.4 and Figure 2.5a). The complex refractive index is defined by equation (2-3):

$$\check{n} = n - ik \qquad (2\text{-}3)$$

where n is refractive index and k is the extinction coefficient. The multiplication of the equations (2-1) and (2-2) leads to formula (2-4) describing the complex reflection ratio ρ. The ρ expressed by ellipometric angles Ψ (amplitude ratio upon reflection) and Δ (phase shift) is called the fundamental ellipsometry equation [11].

$$\rho = \frac{r_p}{r_s} = |r_p|/|r_s| e^{i(\delta_p - \delta_s)} = tan(\Psi)\, e^{i\Delta} \qquad (2\text{-}4)$$

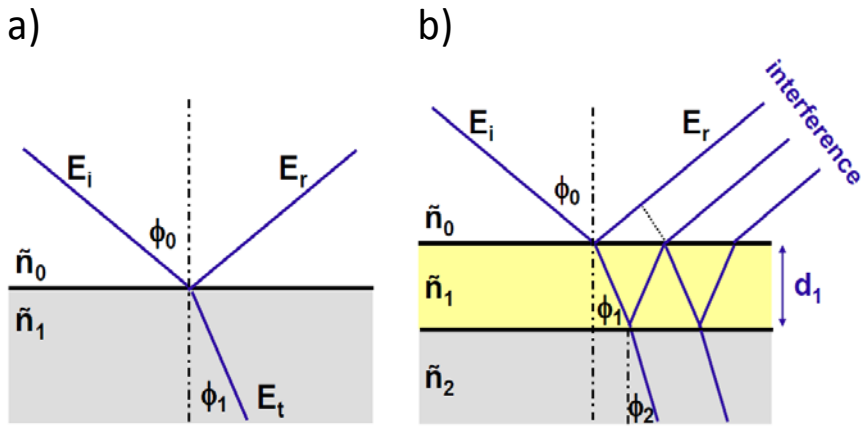

Figure 2.5 The electromagnetic field reflected (Ei) and transmitted (Er) from (a) substrate without native oxide and surface roughness (b) ambient/film/substrate interface. Adapted from Bender et al. [14]

Only optical properties of a substrate without a film on top (Figure 2.5a) can be directly calculated from measured elliposometric angles Ψ and Δ. The complex refractive index of the substrate can then be expressed by equation (2-5) [14]. In this equation ρ is the complex reflection ratio expressed by fundamental ellipsometric equation (2-4). For the measurement performed in the air $\check{n}_0 \cong 1$.

In all other cases a fitting procedure must be used i.e. for single or double

$$\check{n}_1 = \check{n}_0 sin \sqrt{1 + \left(\frac{1-\rho}{1+\rho}\right)^2 tan^2 \phi_0} \qquad (2\text{-}5)$$

layer films deposited on a substrate. The complex reflection ratio ρ for multilayered film stacks is a mathematical function of many more parameters such as refractive indices and thicknesses of the layers in the stack. For instance, considering one layer of the material deposited on substrate ρ can be derived taking into account reflection

on all interfaces and multiple internal reflections (Figure 2.5b). The phase shift β due to one internal reflection is defined by equation:

$$\beta = 2\pi\left(\frac{d_1}{\lambda}\right)\check{n}_1 cos\phi_1 \qquad (2\text{-}6)$$

The amplitude ratios for *p* and *s* polarization for reflection for ambient/film/substrate stack marked by indexes 0,1,2 can be described by equations (2-7) and (2-8):

$$r_p = \frac{r_{01p} + r_{12p}\, e^{-2i\beta}}{1 + r_{01p} r_{12p}\, e^{-2i\beta}} \qquad (2\text{-}7)$$

$$r_s = \frac{r_{01s} + r_{12s}\, e^{-2i\beta}}{1 + r_{01s} r_{12s}\, e^{-2i\beta}} \qquad (2\text{-}8)$$

Considering discussion above the complex reflection ratio ρ for ambient/film/substrate stack is function of: optical properties of the layers ($\check{n}_0, \check{n}_1, \check{n}_2$), thickness of the film (d_1), angle of incidence (ϕ_0) and wavelength λ of the incident light. This is reflected in equation (2-9):

$$\rho = \frac{r_p}{r_s} = f(\check{n}_0, \check{n}_1, \check{n}_2, d_1, \phi_0, \lambda) \qquad (2\text{-}9)$$

Two out of six above mentioned parameters are determined by the ellipsometric fitting (the rest are defined): film thickness and complex refractive index. Furthermore, the complex refractive index (equation (2-3)) can be considered as two independent variables; real refractive index (n_1) and extinction coefficient (k_1). Therefore for films with non-zero value of k1 (i.e. polymers in UV range) three parameters need to be fitted: n_1, k_1, and d_1. In order to find optical properties and the film thickness the measured ellipsometric angles Ψ and Δ are compared with those derived from a layer model representing the system by applying the Fresnel equations as shown in Figure 2.6. The initial values of theoretical ellipsometric angles Ψ and Δ are based on the assumed initial thickness and optical properties of the film stack in question. The calculated ellipsometric angles are compared to the measured ones, and the model parameters are successively adjusted by regression using a nonlinear minimization procedure typically based on Marquardt–Levenberg algorithm [15]. The regression is satisfactory when the average square deviations between calculated and measured ellipsometric angles divided by the experimental errors reach a minimum.

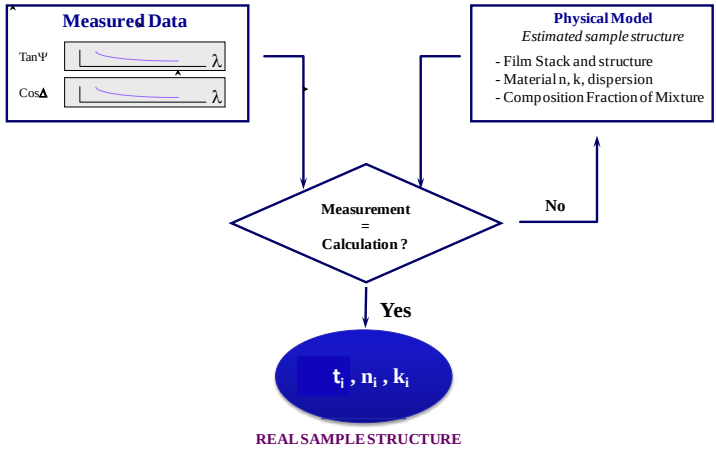

Figure 2.6 The scheme of the fitting procedure of film properties as measured by spectrocopic ellipsometry.

As was discussed above, the ellipsometry strongly relies on the modelling. Therefore, selection of the appriopriate ellipsometric model and a good definition of the initial film parameters are crucial for the accurate analysis. In this work two ellipsometric models were used: Cauchy and harmonic oscillator models. Their basic characteristics are summarized in Table 2.3. The Cauchy model is used for all measurements in the visible light range (EP) while harmonic oscillator model is used for advanced ellipsometric measurements in visible and ultra-violet range [13]. The Cauchy model is only valid for regions of normal dispersion (refractive index decreases monotonically with increasing wavelength) in the visible wavelength region from 350 nm to 800 nm. In the infrared, and UV the equation becomes inaccurate. Despite this, its mathematical simplicity makes it useful in some applications such as evaluation of dielectric films in the visible light range. The harmonic oscillator model (based on Lorentz oscillator [16]) has a physical meaning and can be used for any material. The harmonic oscillator model is derived from equations describing movement of an electron in a damping medium subject to an electric field. The dispersion of the dielectric function ε and therefore the complex refractive index can be expressed as a sum of oscillators H_j (2-10):

$$\varepsilon = (\check{n}_1)^2 = (n_1 - ik_1)^2 = f\left(\sum_j \nu_j H_j\right) \qquad (2\text{-}10)$$

where H_j can be expressed as (2-11) where visualisation and definition of parameters is show in Figure 2.7:

$$H_j(E) = A\frac{N_{osc\_j}}{E_{nj}^2 - E^2 + iE_{gj}E}e^{-i\phi_k} \qquad (2\text{-}11)$$

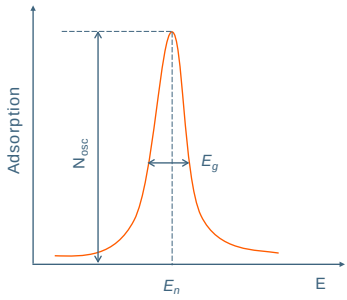

Parameter	Definition
H_j	Contribution of oscillator j
E_n	Resonant energy
N_{osc}	Density of oscillators
E_g	Damping energy
$\boldsymbol{\nu_j}$	Local field correction factor
$\boldsymbol{\phi}$	Phase shift

Figure 2.7 The parameters of harmonic oscillator model (a) graphical illustration (b) definitions of parameters

The optical properties of the low-*k* dielectric in the UV-range are modelled using the harmonic oscillator model. One particular example of application of harmonic oscillator model is measuring the amount of graphitized carbon present in low-*k* dielectric films. The graphitized carbon contains sp2 bond hybridization that absorbs the light around 4.5 eV. This corresponds to En_1 of 4.5 eV for one of the oscillators defined in the model. Another oscillator with En_2 can correspond to the band gap or the material in question. This specific application of UV-SE is relatively new and discussed in next section. We use UV-SE for graphitized carbon detection (in porogen/porogen residues) in chapters 5 and 6.

Table 2.3 The basic characteristic of Cauchy and harmonic oscillator models.

Material model type	Model dispersion type	Typical application	Advantages	Disadvantages
Cauchy	$n = n_1 + \frac{n_2}{\lambda^2} + \frac{n_3}{\lambda^4}$ $k = k_1 + \frac{k_2}{\lambda^2} + \frac{k_3}{\lambda^4}$	Dielectric films in visible light	Simple	Works only in visible light range for normal dispersion
Harmonic oscillator	Host material containing damped oscillators (electrons) driven by an electric field (incident light).	All films	Works for all films in whole spectral range	Complex model definition

2.5.1.1 Application of ultraviolet spectroscopic ellipsometry for evaluation of amorphous carbon content in silica-based low-*k* materials

The application of UV-SE for the analysis of different types of amorphous carbons containing sp^2 hybridized chemical bonds have been reported in literature [17,18,19]. FTIR spectroscopy traditionally used for chemical analysis has limited sensitivity to *trans symmetrical* C=C vibration mode [18] and therefore application of UV-SE is extremely important when the detection of small amount of sp^2 carbon is needed.

The amorphous (sp^2) carbon in low-*k* films mainly originates from PR generated during PECVD fabrication (see PECVD fabrication scheme in Figure 2.3). It has already been proven that PR embedded in PECVD low-*k* films contains sp^2 carbon as was shown by Raman spectroscopy [20]. The electronic transition in graphite $\pi \rightarrow \pi^*$ (C=C sp^2) occurs at 4.24 eV (292 nm), and therefore light with similar energy should be absorbed [21]. Consequently, the amount of C=C bonds in PR should correlate with its absorption coefficient (which is proportional to extinction coefficient). Figure 2.8 shows such correlation for PR (UV-cured porogen) [19]. The amount of C=C bonds in PR is reflected in absorbance around 1600 cm^{-1} as measured by FTIR (Figure 2.8). It is clear that film absorption (extinction coefficient) increases with the porogen UV-curing time and therefore with amount of PR. Moreover extinction of PR film shows maximum around 4.5 eV.

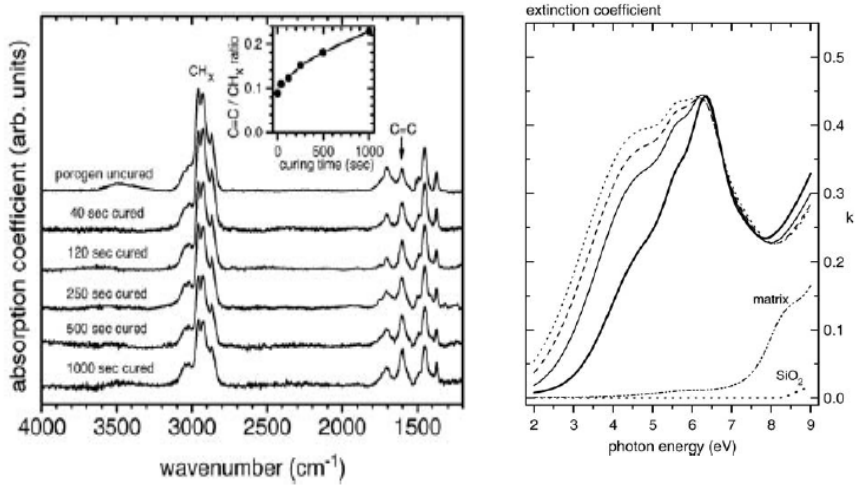

Figure 2.8 Infrared absorption (FTIR) and extinction coefficient (UV-SE) of porogen films UV-cured for various curing times from 0 s (solid thick black line) to 1000 s (dotted line). The extynction coefficient of SiO_2 and as deposited the matrix material are plotted for comparison. Adopted from Marsik et al. [19]

Second important observation is that the optical contrast (difference between extinction coefficients) between organo-silica matrix and PR is significant (Figure 2.8). This allow quantitative evaluation of PR using effective media approximations (PR/matrix/air) in order to evaluate percentage content of PR in low-k matrix as was presented by Marsik et al. [19]. Analogically this is also true for porogen.

Quantitative detection of PR is also possible by Raman spectroscopy, as mentioned above, but this metrology sometimes is challenging because of overlap of PR related absorption and photoinduced luminescence. Therefore, the faster and more reliable metrology has to be developed for industrial applications such as presented UV-SE.

2.5.2 Ellipsometric porosimetry

Ellipsometric porosimetry (EP) is a relatively new method for characterization of the porous films [22,23,24,25]. The EP is a new version of the adsorption-based porosimetry method. The EP can be used for the characterization of the open porosity, average pore size, and pore size distribution (PSD) in thin porous films deposited on top of any smooth solid substrate. *In situ* ellipsometry is used to determine the amount of adsorptive which adsorbed/condensed in the film. The change in the refractive index is used to calculate the quantity of adsorptive present in the film. In this work EP is used for characterization of the open porosity, PSD, and bulk hydrophobic properties of the porous low-*k* dielectric films. The open porosity and PSD are determined using toluene as the absorbent and bulk hydrophobic properties are determined using water as the absorbent. The two combinations of EP with toluene and water are denoted in the next chapters as the toluene-based EP (TEP) and the water-based EP (WEP).

The ellipsometer is mounted on a vacuum chamber that can be filled with a solvent vapor (such as toluene or water) in a controllable way as shown in literature [3, 4]. The ellipsometric porosimeter EP-10 is equipped with a SENTECH 801 spectroscopic ellipsometer (λ = 350–850 nm).

2.5.2.1 Toluene based ellipsometric porosimetery

Toluene-bassed ellipsomertic porosimetry (TEP) measures a change of refractive index of the porous film due to adsorption of toluene. The open porosity of the film can be calculated from the Lorentz-Lorenz equation using refractive index of material before and after fully filling with toluene. The study of the toluene absorbtion/desorption isotherms achieved by measuring toluene content in the film at different vapor pressures allows to determine pore size distribution. The pore size distribution is calculated on the basis of Kelvin and Dubinin-Radushkevich equations. The Kelvin equation taking into account Brunauer–Emmet–Teller (BET) correction is used to evaluate mesopore size (2-50 nm). Dubinin-Radushkevich (DR) equations are used to determine micropore size (<2nm). The DR equations are used due to the fact that sizes comparable with size of the adsorptive molecule (0.6 nm

for toluene) the concept of a meniscus become meaningless and therefore Kelvin equation is no longer valid.

Open porosity measurements. The open porosity can be extracted from the film refractive indices measured in vacuum and after the full adsorption of toluene (the film is completely filled with toluene at saturated pressure). The relation between the optical constants and properties of a multi-component system is described by the Lorentz-Lorenz equation:

where B_{eff} is the effective polarizability of a unit of volume, n_{eff} is the

$$B_{eff} = \frac{3}{4\pi} \cdot \frac{(n_{eff}^2 - 1)}{(n_{eff}^2 + 2)} = \sum N_i \alpha_i \qquad (2\text{-}12)$$

effective refractive index of the multi component film, N_i and α_i are the number of molecules and molecular polarizability of each component, respectively. If a film consists of two components: matrix and pores and the relative amount of pores (porosity, in other words) is P, then the equation (2-12) can be rewritten as follows:

$$B_{eff} = B_p \cdot P + B_m \cdot (1 - P) \qquad (2\text{-}13)$$

or, taking into account the relation between polarizability and refractive index, as

$$\frac{(n_{eff}^2 - 1)}{(n_{eff}^2 + 2)} = \frac{(n_p^2 - 1)}{(n_p^2 + 2)} \cdot P + \frac{(n_m^2 - 1)}{(n_m^2 + 2)} \cdot (1 - P) \qquad (2\text{-}14)$$

where subscripts p and m denote refractive indices of pores and matrix, respectively. The equations (2-13) and (2-14) are valid regardless of presence or absence of any substance in pores. When at zero toluene pressure all pores are empty, n_p=1 and, therefore, B_p=0. In this case, the first term of equation (2-13) turns to 0 and the equation can be written as:

$$B_0 = B_m \cdot (1 - P) \qquad (2\text{-}15)$$

where B_0 denotes polarizability of the film at 0 toluene pressure. At the saturated pressure, when all the pores are filled with toluene equation (2-13) becomes

$$B_{sat} = B_{tol} \cdot P + B_m \cdot (1 - P) \qquad (2\text{-}16)$$

where B_{sat} is the polarizability of the film at saturated toluene pressure and B_{tol} is the polarizability of toluene.

Combining equations (2-15) and (2-16) the porosity can be expressed through polarizabilities:

$$P = \frac{B_{sat} - B_0}{B_{tol}} \qquad (2\text{-}17)$$

or, taking into account the relation between polarizability and refractive index:

$$P = \frac{\frac{n_{sat}^2 - 1}{n_{sat}^2 + 2} - \frac{n_0^2 - 1}{n_0^2 + 2}}{\frac{n_{tol}^2 - 1}{n_{tol}^2 + 2}} \qquad (2\text{-}18)$$

The last equation is used to calculate open porosity. One can see that this equation does not contain the unknown refractive index of the film matrix. Effective refractive indices of the empty film (n_0) and the film filled with toluene (n_{sat}) are measured while the refractive index of toluene is well known (n_{tol}=1.496 at 632.8 nm at room temperature).

The total porosity can be calculated if the refractive index of the matrix is known. When pores are empty one can see from equation (2-18) that

$$P = 1 - \left(\frac{n_{eff}^2 - 1}{n_{eff}^2 + 2}\right) \Big/ \left(\frac{n_m^2 - 1}{n_m^2 + 2}\right) \qquad (2\text{-}19)$$

where n_{eff} is n_0 – the refractive index of the film at zero toluene pressure. Equation (2-19) is also known in ellipsometry as the Bruggeman model of an effective medium.

Pore size distribution of mesopores. The pore size distribution is calculated from isotherms that describe the amount of toluene adsorbed in a porous film as a function of relative pressure. Toluene is condensed in the pores at pressures below saturation (P_0) because the pressure in a liquid below a concave meniscus (which is formed in a pore) is lower than that below a flat surface. The meniscus curvature radius r_m and the relative pressure P/P_0 are related by the Kelvin equation:

$$\frac{1}{r_m} = \frac{RT}{\gamma V_L \cos\theta} \ln\left(\frac{P}{P_0}\right) \qquad (2\text{-}20)$$

where R is the universal gas constant, T is temperature (in K), γ and V_L are the surface tension and the molar volume of the liquid, respectively, and θ is the contact angle. By selecting a solvent with a small contact angle such as toluene $\cos\theta$ is turned to 1. The mean radius of curvature of the meniscus is defined as [26]:

$$\frac{2}{r_m} = \frac{1}{r_1} + \frac{1}{r_2} \qquad (2\text{-}21)$$

Here, r_1 and r_2 are two principal radii of the meniscus. These radii of curvature are defined by taking two planes at right angles to each other, and each of them passes through a normal vector from a point on the meniscus. Let us consider how the mean meniscus radius r_m and pore radius r are related to each other when capillary condensation occurs in pores.

During desorption, when all pores are filled with liquid, the meniscus has a hemispherical shape as depicted in Figure 2.9(a). In that case two perpendicular planes containing the normal vector cross-sect a pore along its axis and r_1 and r_2 are the pore radii in two perpendicular directions. If the pore has a cylindrical shape, then $r_1 = r_2 = r$ and from equation (2-21) it is obvious that $r_m = r$

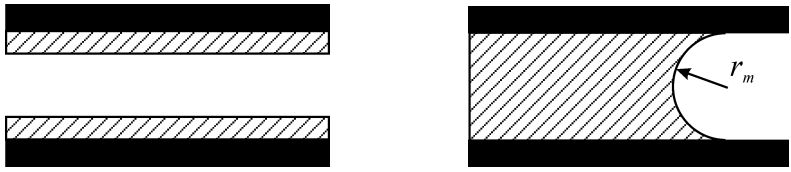

(a) (b)

Figure 2.9 The schematic diagram of the meniscus during (a) desorption and (b) adsorption.

During adsorption, when pores are initially empty, the meniscus takes the cylindrical shape as shown in Figure 2.9 (b). One plane containing the normal vector cuts the pore and, therefore, $r_1 = r$. Another plane perpendicular to the first one and containing the normal vector cuts the pore along its axis and hence its principal radius $r_2 = \infty$. Using equation (2-21), we obtain:

$$r_m = 2r \qquad (2\text{-}22)$$

From this consideration we see that during adsorption a higher pressure is needed for condensation to occur as compared to desorption. As a result of this difference, a typical adsorption-desorption isotherm usually exhibits a hysteresis loop (see Figure 2.10). In EP, the relative adsorbate volume in pores is calculated from the effective refractive index of a film partially filled with solvent. Substituting refractive index at the saturated pressure n_{sat} by the refractive index at given pressure n_{pres} in equation (2-18), it is possible to calculate the relative volume of adsorbate at the given pressure.

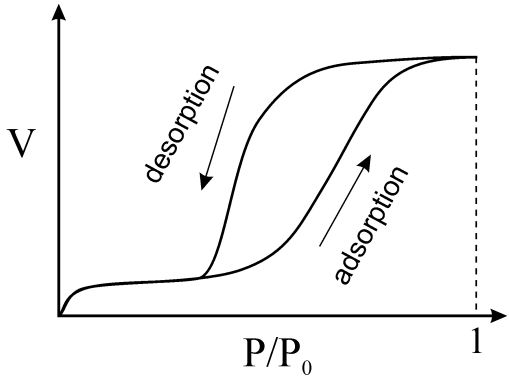

Figure 2.10 Adsorption/desorption isotherm in mesoporous solids.

It should be noted that the meniscus radius is not exactly equal to the pore radius as some molecules could be adsorbed at pore walls prior to capillary condensation (the branch at low P/P_0 in Figure 2.10). In this case, the meniscus radius will be smaller than the pore radius by the thickness t of the layer already adsorbed on pore walls:

$$r_m = r - t \qquad (2\text{-}23)$$

The thickness t can be obtained from measurements of adsorption on non-porous flat surfaces having the same chemical composition as the porous material in question. The BET equation (named after developers of the adsorption theory Brunauer, Emmett and Teller [27]) is used to estimate the t value:

$$t = \frac{t_0 \cdot C \cdot K \frac{P}{P_0}}{\left(1 - K\frac{P}{P_0}\right) \cdot \left(1 + K \cdot (C-1)\frac{P}{P_0}\right)} \qquad (2\text{-}24)$$

where t_0 is the thickness of one monolayer of adsorbate, C is the BET constant, K is a coefficient satisfying the requirements that at $P=P_0$ $t \leq$5-6 monolayers [28]. Equations (2-23) and (2-24) are used for correction of the pore radii calculated using the Kelvin equation (2-20). The correction becomes significant when pore radii are smaller than 5 nm.

Pore size distribution of micropores. A method based on a semi-empirical theory developed by Dubinin and Radushkevich [29] (DR) is used to analyse films containing micropores. The DR method uses change in adsorption potential when the pore diameter is comparable with the size of the adsorptive molecules. The process involved is the micropore volume filling rather then layer-by-layer adsorption on the pore walls. The dependence of the adsorbate volume V on adsorption potential A is expressed by the following equation (known as the Dubinin-Radushkevich equation):

$$A = RT \ln\left(\frac{P_0}{P}\right) \qquad (2\text{-}25)$$

where the logarithm of the amount adsorbed is linearly proportional to the square of the adsorption potential (B is a constant).

$$lnV = lnV_0 - BA^2 \qquad (2\text{-}26)$$

Writing this equation explicitly in terms of pressure, we have:

$$V = V_0 \exp\left[-\frac{1}{(\beta E_0)^2}\left(RT \ln\frac{P}{P_0}\right)^2\right] \qquad (2\text{-}27)$$

where E_0 is called the solid characteristic energy towards a reference adsorbate, the parameter β is a function of the adsorptive only. The linear plot of ln$V$ versus A^2 leads to determination of V_0, which has the meaning of the total micropore volume, and βE_0, which is the isosteric heat of adsorption. It was shown that micropore radius and the energy E_0 related to each other as

$$r = \frac{K}{2E_0} \qquad (2\text{-}28)$$

where $K \approx 12$ is an empirical constant slightly changing with E_0. [28,29] Therefore, it is possible to extract the pore radius from the aforementioned linear plot. It should be noted, though, that the constant β is unknown and measurement of the absolute pore size could be ambiguous. As β, however, depends only on adsorptive, the comparison between porous materials is possible if the same adsorptive is used. The absolute pore size determination requires calibration with other methods.

2.5.2.2 Water based ellipsometric porosimetry

Water-based ellipsometric porosimetry (WEP) measures change of refractive index of the porous film due to adsorption of water. The WEP can be used for quantitative evaluation of the degree of bulk hydrophilization of plasma damaged low-*k* dielectric [30]. Comparative evaluation showed that the degree of hydrophilization and the depth of plasma damage has qualitative agreement with the carbon depletion determined by WEP, HF dip test and TOF SIMS. The basic idea of WEP is similar to TEP [22,24]. WEP allows changing of water vapor pressure from 10^{-3} torr to saturated ones of approximately 20 Torr at room temperature. Amount of the adsorbed water (C_{wat}) is calculated from change of refractive indices happening during the water adsorption by using Lorenz-Lorentz equation (2-19). The amount of the adsorbed water in pristine low-*k* films reflects concentration of active centers

like isolated hydroxyl groups. Technological damage increases number of the active centers and starting from a certain concentration, the adsorbed water forms continuous layer. As soon as it happens, the bulk condensation of water occurs [31]. Adsorption isotherms measured in the wide range of water vapor pressure allow characterization of hydrophilic properties that normally are quantified through the contact angle.

2.5.3 Secondary ion mass spectrocopy

Secondary ion mass spectrocopy (SIMS) is widely used for depth profiling and analysis of trace elements in solid materials, especially semiconductors and thin films [35]. SIMS is based on the emission of atomic and molecular particles (secondary ions) from the surface of a solid under bombardment with primary particles (ions) [32]. Continuous analysis while sputtering a solid by primary ions produces information as a function of depth, called a depth profile. There are two types of SIMS analysis: static and dynamic.

The slow sputtering mode is called static SIMS and is more sensitive to surface composition in contrast to dynamic SIMS which is used for depth profiles. In this work we use only dynamic SIMS with time of flight (TOF) mass spectrometry to detect secondary ions. This combination is called dynamic TOF-SIMS. In dynamic TOF-SIMS analysis, the sample is placed in an ultrahigh vacuum environment (10^{-9} Torr) and primary ions bombard and sputter atoms, molecules, and molecular fragments from the sample surface [32]. The mass of the ejected particles (i.e., secondary ions) is analyzed via time-of-flight mass spectrometry. In the TOF analyzer, ejected ions are accelerated into the analyzer with a common energy (but result in different velocities depending on the particle mass). Due to the differences in velocities, smaller ions move through the analyzer more rapidly than the larger ions. The mass of the secondary ions is determined by their travel time through the analyzer.

The dynamic TOF-SIMS is used to evaluate carbon depth profiles in plasma damaged low-*k* materials. It was shown that carbon depletion is related to the removal of Si-CH_3 bonds from low-*k* dielectric [33,34]. We demonstrate, in addition to the literature data, that some part of depleted carbon is related to amorphous carbon (porogen residues) present in PECVD low-*k* films. We demonstrate in chapter 5 that this amorphous carbon can be removed by annealing of the low-*k* material in hydrogen atmosphere without Si-CH_3 bonds destruction. The further dynamic TOF-SIMS analysis reveals porogen residue depth profile in the film. Such a way of sample preparation, in combination with dynamic TOF-SIMS analysis, can be considered as a new analytical method of evaluation bi-phase low-*k* PECVD films.

2.5.4 Optical emmision spectrocopy

Optical emission spectroscopy (OES) is widely used in microelectronic industry to monitor plasma processing [35]. OES measures the radiation emitted by

excited atoms, excited molecules and monoatomic ions [36]. Excited species relax to ground state as show in Figure 2.11. Their relaxation results in the emission of the light, producing line spectra in the visible and UV regions of the spectrum. These emitted atom and ion lines can be used for semi-qualitative identification of the reaction products present in processing plasma and for the quantitative analysis of such elements at concentrations ranging from ppb (parts per bilion) to percent.

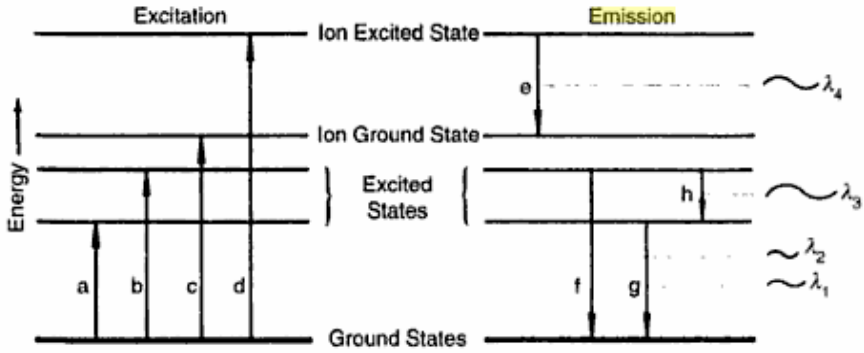

Figure 2.11 Schematic diagram of the excitation and emission process. The energies a and b represent atomic excitation, c represents ionization and d represents ionization and excitation. Four possible emission energies and their respective wavelength are shown; e is ionic emission and f, g, and h are atomic emission. Adopted from Robinson et al. [36]

Industrial plasma sources such as ICP or CCP (see section 2.2.1) are high-energy sources that permit the excitation of most of the elements, both metals and non-metals, and results in very line-rich spectra. This is one of the advantages of OES combined with ICP/CCP plasma chamber; many elements, as atoms and ions, emit multiple wavelengths simultaneously. This allows selection of several wavelengths for each element (or molecule) and the ability to measure multiple elements concurrently. However disadvantage is that as the number of emission wavelengths increases, so does the spectral interference from overlapping lines. This mandates the use of high-resolution spectrometers.

The industrial OES system mounted on ICP plasma chamber was used in chapter 3 to monitor the degree of hydrophilization of low-*k* materials. This novel application of OES is discussed in detail in chapter 3.

2.5.5 Fourier transform infrared spectroscopy

Fourier transform infrared spectroscopy (FTIR) is well established method to study bonding structure of the materials [37, 38]. The FTIR is one of the variants of infrared spectroscopy. The FTIR is based on the idea the interference of radiation between two beams to yield an interferogram. The latter is a signal produced as a function of change of pathlength between two beams. The two domains distance and

frequency are interconvertible by the mathematical method of Fourier-transformation [37].

FTIR is the measurement of the wavelength and intensity of the absorption of mid-infrared light by a sample in question. The mid-infrared radiation is sufficiently energetic to excite molecular vibrations to higher energy levels. The wavelengths of the infrared absorption bands are characteristic for specific types of chemical bonds, and infrared spectroscopy finds its greatest utility for identification of organic and organometallic molecules. FTIR involves examination of the twisting, bending, rotating and vibrational motions of atoms in a molecule. Simple diatomic molecules have only one bond and only one vibrational band. If the molecule is symmetrical, e.g. N_2, the band is not observed in the IR spectrum, but only in the Raman spectrum [37]. Unsymmetrical diatomic molecules, e.g. CO, absorb in the IR spectrum. More complex molecules have many bonds, and their vibrational spectra are correspondingly more complex, i.e., big molecules have many peaks in their IR spectra.

2.5.6 Near-field scanning probe microwave microscope

Near-field scanning probe microwave microscope (NSPMM) is non-contact capacitance measurement at microwave frequency [39,40]. The NSPMM uses micro-wave radiation transmitted through the material to evaluate its capacitance at 4 GHz. The capacitance of the film with known thickness can be recalculated into *k*-value at 4 GHz. The NSPMM is promising metrology for investigation of the *k*-values of the patterned low-*k* dielectrics. All NSPMM measurements were performed at Solid State Measurements, Inc., Pittsburgh, PA, USA Company. We study industrial applicability of NSPMM in chapter 3.

The schematic of this technique is shown in Figure 2.12. The near-field probe is a half-lambda parallel strip transmission line resonator (PSR). PSR is microfabricated from a quartz bar tapered down to a few micron tip size and sandwiched between two aluminium strips (frame in Figure 2.12). The PSR is mounted inside a metallic sheath with the tip protruding out via an opening in the sheath wall and operates in a 4 GHz balanced odd mode. The near-zone field is mostly confined in between the Al strips. The tip sampling E field (similar to the fringe field of a parallel plate capacitor) forms a well-confined “cloud” with a characteristic dimension on the order of the tip size D 5–10 μm. When a dielectric sample is brought in close proximity to the tip, the reactive energy stored in this field is reduced, and consequently the probe resonant frequency F decreases. Since the tip is much smaller than the radiation wavelength, a lumped element network can be used to describe the tip-sample interaction.

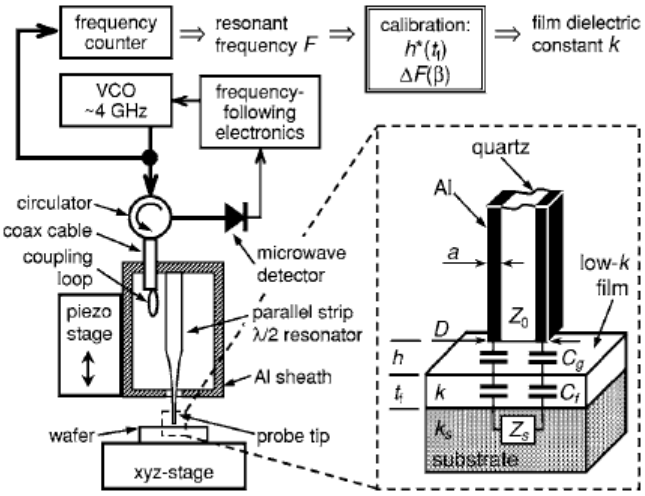

Figure 2.12 NSMNP schematic and the lumped element scheme for the tip impedance in the case of a thin dielectric film on arbitrary substrate. Tip-sample distance h~50-100 nm; tip size D~5-10 μm. Adapted from Talanov et al. [39]

2.5.7 Nano indentation

The mechanical properties of the low-*k* dielectrics were evaluated by nano-indentation (NI). This technique utilises a diamond tip that is pressed into the films, and subsequently retracted, while monitoring the required force *P* and the indent depth *h*. The hardness and elastic modulus were the variables of interest. They were calculated in continuous stiffness measurements (CSM) with a Berkovich tip to yield continuous elastic modulus and hardness data as a function of indent depth. Elastic modulus and hardness were extracted at a 10% of indentation depth to dismiss surface and substrate effects. Poisson's ratio used was usually approximated to that of fused silica (0.18). The tool was a MTS Nanoindenter XP with a differential confocal microscopy head (DC). The detialed discussion about NI measurements in this study and related errors was published in literature [41].

2.6 References

[1] D. Shamiryan, M. R. Baklanov, S. Vanhaelemeersch and K. Maex, J. Vac. Sci. Technol. B, 20, 1923 (2002).

[2] D. Moore, R. Carter, H. Cui, P. Burke, P. McGrath, S. Q. Gu, D. Gidley and H. Peng, J. Vac. Sci. Technol. B, 23, 332 (2005).

[3] K. Maex, M. R. Baklanov, D. Shamiryan, F. Iacopi, S. H. Brongersma and Z. S. Yanovitskaya, J. Appl. Phys., 93, 8793 (2003).

[4] W. Volksen, D. M. Miller and G. Dubois, Chem. Rev., 110, 56 (2010).

[5] S. Eliezer and Y. Eliezer, The Forth State of Matter, IOP Publishing, Ltd, Bristol, p.83 (2001).

[6] R. Doering and Y. Nishi, Handbook of semiconductor manufacturing technology, Ch. 21, p. 12, CRC Press, Boca Raton (2008).

[7] A. Friedman, Plasma Chemistry, p.224 Cambridge University Press, Cambridge (2008).

[8] M. Heyns, R. De Keersmaecker, "Basics of VLSI Processing: Dry Wet Etching" (2009).

[9] N. Kemeling, K. Matsushita, N. Tsuji, K.-i. Kagami, M. Kato, S. Kaneko, H. Sprey, D. de Roest and N. Kobayashi, Microelectron. Eng., 84, 2575 (2007).

[10] M. Ikeda, S. Nakahira, Y. Iba, H. Kitada, N. Nishikawa, M. Miyajima, S. Fukuyama, N. Shimizu, K. Ikeda, T. Ohba, I. Sagiura, K. Suzuki, Y. Nakata, S. Doi, N. Awaji and E. Yano, in IEEE International Interconnect Technology Conference, p. 71 (2003).

[11] R. M. A. Azzam and N. M. Bashara, Ellipsometry and polarized light, North-Holland Publishing Co., Amsterdam (1977)

[12] H.G. Tompkins, in "An user's guide to ellipsometry", Academic Press, Inc., San Diego (1993).

[13] G. T. Harland and A. I. Eugene, Hanbook of Ellipsometry, William Andred Publishing and Springer-Verlag GmbH & Co. KG, NY and Heidelberg (2005).

[14] H. Bender, Spectroscopic Ellipsometry, in Material Characterization Techniques, IMEC, Leuven (2009).

[15] D. W. Marquardt, J. Soc. Ind. Appl. Math., 11, 431 (1963).

[16] G. T. Harland and A. I. Eugene, Hanbook of Ellipsometry, William Andred Publishing and Springer-Verlag GmbH & Co. KG, NY and Heidelberg, p.128 (2005).

[17] S. Eslava, G. Eymery, P. Marsik, F. Iacopi, C. E. A. Kirschhock, K. Maex, J. A. Martens and M. R. Baklanov, J. Electrochem. Soc., 155, G115 (2008).

[18] E. Pargon, K. Menguelti, M. Martin, A. Bazin, O. Chaix-Pluchery, C. Sourd, S. Derrough, T. Lill and O. Joubert, J. Appl. Phys., 105 (2009).

[19] P. Marsik, P. Verdonck, D. De Roest and M. R. Baklanov, Thin Solid Films, 518, 4266 (2010).

[20] M. Matsuura, K. Goto, N. Miura, J. M. Haag, S. Hashii and K. Asai, Film Characterization of Ultra Low-k Dielectrics Modified by UV Curing with Different Wavelength Bands, in Mat. Res. Soc. Symp., T. T. Tsui, Y.-C. Joo, L. Michaelson, M. Lane and A. A. Volinsky Editors, p. F01, Mater. Res. Soc. Symp. Proc., San Francisco, CA (2006).

[21] A. R. Forouhi and I. Bloomer, Physical Review B, 34, 7018 (1986).
[22] M. R. Baklanov, K. P. Mogilnikov, V. G. Polovinkin and F. N. Dultsev, J. Vac. Sci. Technol. B, 18, 1385 (2000).
[23] K. P. Mogilinikov, M. R. Baklanov, D. Shamiryan and M. P. Petkov, Jpn. J. Appl. Phys. Part 1 - Regul. Pap. Brief Commun. Rev. Pap., 43, 247 (2004).
[24] M. R. Baklanov and K. P. Mogilnikov, Microelectronic Eng., 64 (1/4), 335, (2002).
[25] D. Shamiryan, Novel Applications of Ellipsometry And Solvent Probes For Characterising Cu/Low-k Dielectrics Materials for Advanced Semiconductors Interconnects, in Faculteit Toegepaste Wetenschappen: Departement Elektrotechniek, p. 113, Katholieke Universiteit Leuven, Leuven (2004).
[26] Defay and Prigogine, Surface tension and adsorption, Longman, London (1966).
[27] S. Brunauer, P. H. Emmet, and E. Teller, J. Am. Chem. Soc., 60, 309 (1938).
[28] S. J. Gregg and S. W. Sing. Adsorption, surface area and porosity, 2nd ed., (Academic press, NY, 1982).
[29] M. M. Dubinin, Chem. Rev., 60, 235 (1960).
[30] M. R. Baklanov, K. P. Mogilnikov and Q. T. Le, Microelectron. Eng., 83, 2287 (2006).
[31] T. Ohba, H. Kanoh, and K. Kaneko. Nanolatters, 5(2), 227 (2005).
[32] J. C. Riviere and S. Myhra, Handbook of Surface and Interface Analysis: Methods for Problem Solving, Marcel Dekker, Inc., New York (1998).
[33] K. Maex, M. R. Baklanov, D. Shamiryan, F. Iacopi, S. H. Brongersma and Z. S. Yanovitskaya, J. Appl. Phys., 93, 8793 (2003).
[34] W. Volksen, D. M. Miller and G. Dubois, Chem. Rev., 110, 56 (2010).
[35] R. Doering and Y. Nishi, Handbook of semiconductor manufacturing technology, CRC Press, Boca Raton (2008).
[36] J. W. Robinson, E. M. Frame and G. M. Frame II, Undergraduate Instrumental Analysis, p. 449-450, Marcel Dekker, New York (2005).
[37] B. Stuart, Infrared Spectroscopy: Fundamentals and Applications, John Wiley & Sons Ltd., Chichester (2004).
[38] W. S. Lau, Infrared Characterization for Microelectronics, World Scientyfic Publishing Co. Pte. LtD, Danvers, MA (1999).
[39] V. V. Talanov, A. Scherz and A. R. Schwartz, Appl. Phys. Lett., 88 (2006).
[40] V. V. Talanov, A. Scherz, R. L. Moreland and A. R. Schwartz, Appl. Phys. Lett., 88 (2006).
[41] K. Vanstreels and A. M. Urbanowicz, J. Vac. Sci. Technol. B, 28, 7 (2010).

3 New methods for plasma damage monitoring of low-*k* dielectrics used for microelectronic industry applications

The results that are presented in this chapter have been partly published in:

A. M. Urbanowicz, V. V. Talanov, M. Pantouvaki, H. Struyf, S. De Gendt and M. R. Baklanov, in International Interconnect Technology Conference, p. 237, Hokkaido, Japan (2009).
A. M. Urbanowicz, M.R. Baklanov, "Quantification of hydrophobic and hydrophilic properties of materials" EP 2009/20342296 and US 2009/0068768 A1 (2009)
A. M. Urbanowicz, D. Shamiryan, M. R. Baklanov and S. De Gendt, Microelectronic Engineering, 85, 2164 (2008).

3.1 Introduction

In order to avoid degradation of the *k*-value of the low-*k* materials when integrated, both process optimization and development are needed (as discussed in chapter 1) [1]. However, process optimization and development are very time consuming since currently only *ex situ* plasma damage metrology is available. The plasma damage, which occurs during etch and strip processing, is evaluated using complex analytical methods such as Fourier Transform Infra Red Spectroscopy (FTIR), Water Vapor Ellipsometric Porosimetry (WEP) and Thermo Desorption Spectroscopy (TDS), etc. [1,2]. Moreover, most of those techniques are not suitable for patterned wafers comprising dense structures (i.e., to analyse damage on sidewalls of dense structures). Ultimately, electrical characterisation is used for final examination of the integrated low-*k* dielectric quality [2]. However, this measures the sum of all low-*k* damage occurred during all integration steps. Furthermore it is expensive and time consuming. Therefore, it is important to develop simple and non-destructive methods, which allow the evaluation of the plasma damage immediately after investigated process step. In this chapter we present two new methods suited for plasma damage evaluation of low-*k* materials. The first method is based on optical emission spectroscopy (OES) measurements of O* and H* intensities. It is applied when the low-*k* dielectrics deposited on 300 mm wafer are exposed to He plasma. The O* and H* intensities indicate the degree of the low-*k* dielectric hydrophilization that occurs during plasma processing. The second method relies on microwave impedance measurements of the patterned low-*k* structures. Those measurements allow us to extract *k*-value of the low-*k* dielectrics in

microwave frequency of 4 GHz. The advantage of this method over conventional *k*-value extraction is that the measurement can be performed without Cu metallization of low-*k* trenches (damaging and time consuming). Therefore damage impact of the etch processes only can be extracted. The new fast methods of plasma damage evaluation are of key importance for the optimization of the plasma-based processes of the low-*k* materials in respect to plasma damage of low-*k* materials.

3.2 Oxygen Chemiluminescence in He Plasma as a Method for Plasma Damage Evaluation

We propose a method for evaluating the hydrophilization degree of low-*k* films upon plasma damage. The evaluation is based on OES analysis of O* emission during He plasma exposure of sample in question. The O* is desorbed from damaged low-*k* film by vacuum-ultraviolet radiation from He plasma. The new method correlates well with other methods for plasma damage characterization such as FTIR (section 2.5.5) and WEP (section 2.5.2.2). The presented method gives a unique opportunity to assess the degree of hydrophilization of low-*k* films immediately after processing.

3.2.1 Introduction

One of the fundamental plasma damage mechanisms of low-*k* dielectrics is replacement of hydrophobic Si-CH_3 groups into hydrophilic Si-OH groups as discussed in section 1.7.3. Further moisture absorption into the porous structure increases the dielectric constant of the material. Therefore, the degree of damage is proportional to the degree of hydrophilization. In this section we propose a new method of plasma-damage evaluation based on Optical Emission Spectroscopy (OES) analysis during He plasma exposure of a low-*k* sample [3]. We argue that He plasma exposure causes photolysis of water incorporated into the pores of the low-*k* material. Products of this reaction can be detected by OES. The analysis of 777 nm peak intensity related to O* (5P->5S transition) radicals gives quantitative information about the degree of damage induced by a plasma process such as strip and etch. To verify the new method we compared it with already established method for plasma-damage evaluation (WEP and FTIR).

3.2.2 Experimental

All experiments are carried out in an industrial ICP plasma source (LAM Versys2300 STAR in Table 2.1) on 300 mm silicon wafers. The wafer temperature is kept at 30°C by He backside cooling (electrostatic chuck), while the anodized

aluminum (Al_2O_3) walls of the chamber are kept at 50° C. The plasma is excited by feeding an antenna (lying on a quartz window) with 13.56 MHz rf power, while the energy of the ions bombarding the wafer is independently controlled by a second 13.56 MHz rf power supply. During all experiments a second power supply is switched off. Therefore ion bombardment has negligible effect on the experiments. To obtain a high reproducibility of the results, the plasma chamber walls are cleaned before every experiment with a standard WAC (wafer-less autoclean) recipe, consisting of O_2/SF_6 plasma [4] and subsequent He plasma. The additional He plasma cleaning is introduced to remove oxygen from the chamber walls [3]. The plasma chamber is equipped with an industrial OES-based endpoint detection system with the sensor located on the side of the reaction chamber. The light emitted by the plasma is directed on a dispersive element followed by a CCD array of 2048 pixels. The OES spectra are recorded in the range of 250 nm – 850 nm (with spectral resolution 2.5 nm).

The following samples are used (all wafers are 300 mm in diameter): bare silicon wafers, wafers with 1.8 μm of photoresist and wafers with porous low-*k* dielectrics. The low-*k* materials used for the damage tests are porous carbon-doped silica films (SiOC:H) with thickness of 180 nm deposited by Plasma Enhanced Chemical Vapor Deposition (PECVD) on silicon substrates. The low-*k* films have open porosity close to 22% and pore radius 0.8-0.9 nm, as measured by TEP (section 2.5.2.1), dielectric constant in the range of 2.4-2.5 and refractive index of 1.35 at 633 nm. In order to introduce damage, the low-*k* films are treated with a 19:1 O_2/Cl_2 photoresist strip plasma. The coil power is 1000 W and pressure 20 mTorr. We used exposure times of 5 s, 10 s, 20 s, and 30 s. The varied time of treatment is used to induce different level of hydrophilization of the low-*k* films. For the evaluation of hydrophobic properties of the studied materials we use 777 nm line amplitude (O*) measured by OES recorded during 20 s. Each wafer was treated with 30 mTorr 400 W (coil power) He plasma.

The bonding structure of the low-*k* films before and after plasma treatments was analyzed using a Biorad QS2200 ME FTIR system. The bulk hydrophilicity (amount of adsorbed water) was measured by using WEP equipped with SENTECH 801 spectroscopic ellipsometer (λ=350-850 nm) as described in section 2.5.2.2 [5].

3.2.3 Results and discussion

First we recorded OES spectra during He plasma exposure of an empty plasma chamber. All peaks except those at 656 nm and 777 nm are related to He (Figure 3.1). The peak of 656 nm is related to H radicals with optical transitions: 2P→2D, 2P→2S and 2S→2P (7 lines). The second corresponds to 5P→5S (3 lines) transition of electronically excited oxygen radicals [6]. It is not obvious why a constant level of 656 nm and 777 nm intensities is observed during He plasma exposure of an empty chamber. The constant level of 656 or 777 nm lines might be due to residual moisture in the chamber (i.e., introduced during the wafer loading procedure). Another possiblity might be due to resputtering of O from SiO_2 (kwartz)

window. On the other hand O* and H* impurites in He gas are exculded due to high purity of He gas used, that is 5 N (99,999%).

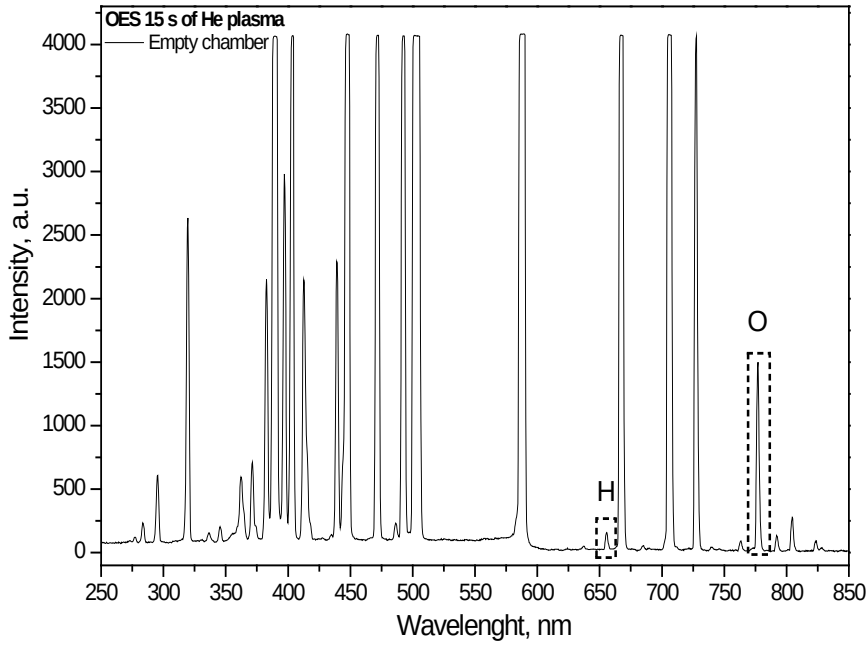

Figure 3.1 OES of He plasma recorded in empty chamber. The frames indicate intensities related to O* (777 nm) and H* (656 nm) lines.

The O* and H* are products of photodissociation of water molecules adsorbed on chamber walls by vacuum-ultraviolet (VUV) radiation from the He plasma. To verify this we studied the OES emission during He plasma exposure of hydrophilic and hydrophobic substrates. We chose the 777 nm peak as it is more intense and it is not overlapped with other He lines. If the presence of O* in He plasma reflects desorption of O* from a substrate, then we should see a more intense O* release from the hydrophilic substrate compared to the hydrophobic one. As a hydrophilic substrate we chose bare Si which is hydrophilic due to native oxide presence on the surface. The hydrophobic substrate is represented by photoresist deposited on blanket Si which is hydrophobic due to the presence of carbon containing-polymers. We exposed those samples to He plasma for 20 s. The time traces of the 777 nm peaks are shown in Figure 3.2.

We can see that O intensity in the case of Si (hydrophilic substrate) is higher than the level of the empty chamber. This might be related to photo-dissociation of OH groups from top surface of Si. The intensity of O* for the photoresist mask (hydrophobic substrate) is below the empty chamber level. This can be explained by recombination/reaction of O* with the carbon-rich photresist mask. In summary, the results presented in Figure 3.2a indicate that we are able to distinguish hydrophobic and hydrophilic substrates by analysis of 777 nm peak intensity during He plasma exposure.

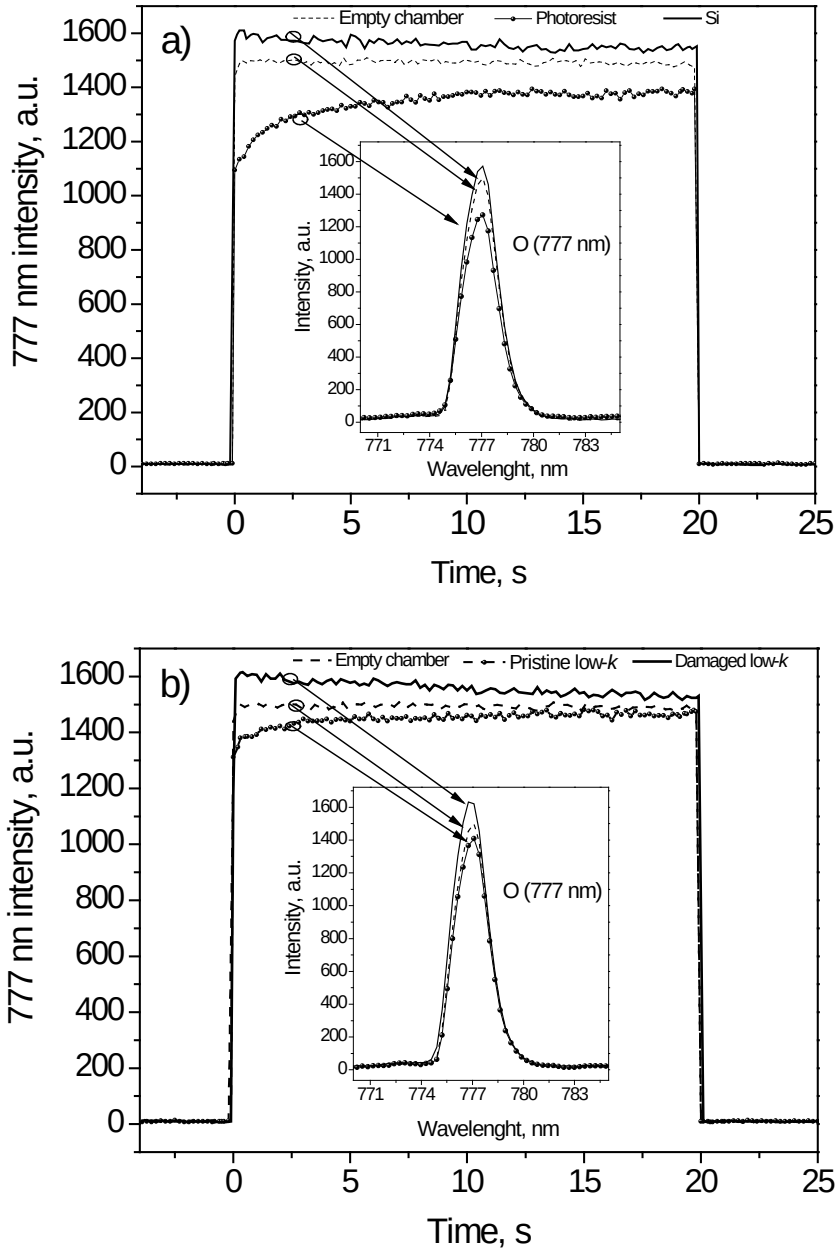

Figure 3.2 Time traces and OES after 2 s of plasma process (zoomed area): (a) empty chamber, photoresist polymer on the top of Si wafer and bare Si, and (b) empty chamber, pristine low-*k*, and damaged low-*k*.

Then we extended our study to low-*k* materials. The damaged low-*k* samples contain H_2O in the pores [1] so we should observe higher O* intensity from the damaged sample. We performed the tests on as deposited (pristine) and damaged low-k dielectrics as shown in Figure 3.2b indicate that we are able to distinguish between pristine and damaged low-*k* samples.

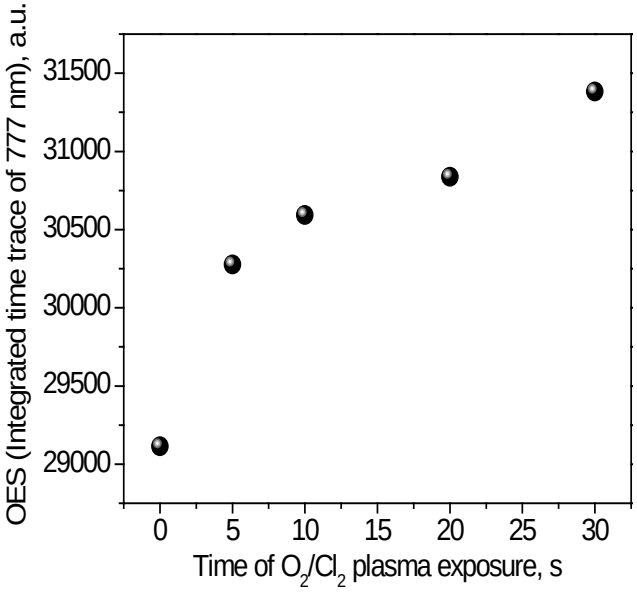

Figure 3.3 Time of O_2/Cl_2 plasma treatment of low-*k* dielectric versus integrated 777 nm intensity.

If the intensity of the O* peak is proportional to the amount of adsorbed OH groups and water molecules (bonded by hydrogen bridges) then the damaged low-*k* film should release more O*. The appearance of O* radicals is related to photolysis of adsorbed water by EUV and VUV photons from He plasma [7] from the bulk of the porous low-*k* film. The moderately low processing temperature (20 - 60 ^{0}C) and low pressure (20 - 200 mTorr) during processing is insufficient to desorb the hydrogen bonded water. Part of the water molecules remains adsorbed inside the pores of the low-*k* film as discussed in section 1.7.1. However the adsorbed moisture and OH groups can be photo-desorbed by UV radiation from He plasma. The water shows an intense UV absorption between 140 nm and 190 nm due to X^1A_1-A^1B_1 transition [8]. As the extinction coefficient of SiOC:H low-*k* film rises sharply at the wavelength below 160 nm [9,10] (see also Figure 6.1), the film is quite transparent to longer wavelength where water shows high adsorption.

Consequently, the amount of O* is proportional to the damage degree (bulk hydrophilization degree). To evaluate the damage degree of the low-*k* dielectrics, we decided to measure the amount of desorbing O* as a function of damage introduced by O_2/Cl_2 plasma (varied time). The amount of released O* was estimated using the integrated 777 nm intensity using equation (3-1):

$$I_i = \int_{t=0s}^{t=20s} I(t)dt \qquad (3\text{-}1)$$

where I_i is the integrated 777 nm peak intensity, t is time of the He plasma exposure. The time traces were recorded as shown in Figure 3.3 (integral is an area under 777 nm curve). One can see that the amount of desorbed O* increases with increase of the O_2/Cl_2 treatment time. We can conclude that by monitoring the O* peak during He plasma treatment we are able to distinguish the different degree of damage on the low-*k* film.

In order to compare the OES technique to more conventional technique for estimation of plasma damage, we studied the plasma damaged low-*k* by FTIR and WEP. The FTIR is used to study changes in the bonding structure. The WEP measures the amount of water adsorbed in the internal pore network of the low-*k* film.

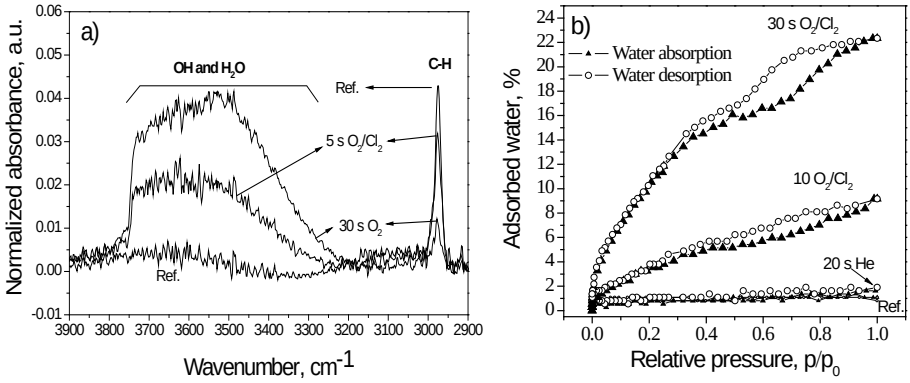

Figure 3.4 Absorbance of 3900-2900 cm^{-1} as measured by FTIR (a) Percentage amount of water absorbed in low-*k* volume as measured by WEP (b).

The hydrophilization is proportional to the amplitude of the Si-OH absorbance band as shown in Figure 3.4. The amplitude of the Si-OH (3900-3100 cm^{-1}) absorbance increases due to hydrophilic OH group incorporation [11] while the absorbance for C-H (2970 cm^{-1}) decreases as a result of carbon depletion (Si-CH3 to Si-OH conversion) as shown in Figure 3.4a. The degree of hydrophilization can be estimated by integrating the OH absorbance band area represented in Figure 3.4a using equation (3-2):

$$A_i = \int_{k=3100cm^{-1}}^{k=3900cm^{-1}} A(k)dk \qquad (3\text{-}2)$$

where A_i is the integrated absorbance and k is the wavenumber. For a reference sample (as deposited low-k dielectric) the amplitude of OH groups is close to zero and the intensity of C-H peak is maximal. The next curve shows the reference sample exposed to 20 s He plasma which we use for the damage evaluation test. This spectrum reflects the damage introduced by the method itself. The absorbance of OH groups is slightly increased. The intensity of the C-H absorbance band is reduced indicating some carbon depletion. The damage in the pure He plasma is very small in comparison with damage induced by O_2-based plasma. Therefore, the damaging effect of the method itself is minimal. The next sample is the low-k exposed to 5 s of O_2/Cl_2 plasma. In this case, we observe a much higher degree of damage compared to the case of the sample treated with He plasma only. The highest degree of damage is found in the film which was exposed to 30 s of O_2/Cl_2 plasma.

Another method to estimate the degree of hydrophilization is WEP. It was found that the amount of water absorbed into the dielectric pores at saturated vapor pressure increases with O_2/Cl_2 exposure time as shown in Figure 3.4b. In the case of the pristine sample the amount of absorbed water was around 1. 6 %. The sample treated for 30 s in O_2/Cl_2 plasma absorbs of 22 % vol. water at saturated vaporpressure. The amount of adsorbed water for the sample treated for 30 s is equal to the total porosity due to total hydrophilization of pore sidewalls. As we can see, both FTIR and WEP techniques are sensitive to hydrophobic properties and therefore, to the damage degree of the low-k film. They give similar results as shown in Figure 3.5 where both integrated absorbance measured by FTIR and amount of adsorbed water measured by WEP are plotted versus O_2/Cl_2 exposure time.

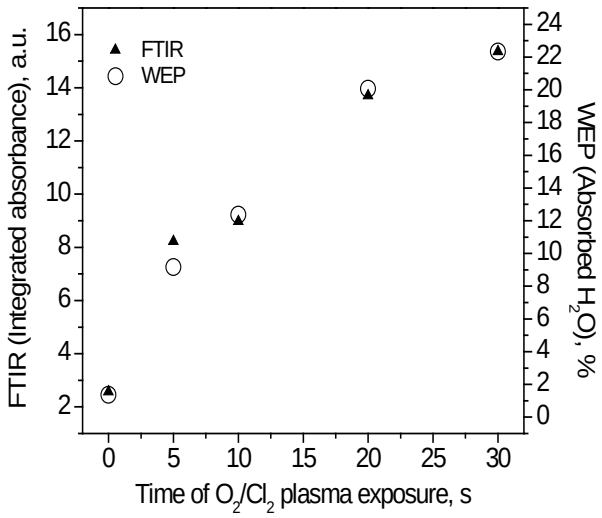

Figure 3.5 Time of O_2/Cl_2 plasma exposure of low-k dielectrics versus integrated absorbance (as measured by FTIR) and absorbed water in saturation pressure (as measured by WEP).

In order to compare the new method (OES) with the established ones (FTIR and WEP) we plotted FTIR and WEP data versus OES data as shown in Figure 3.6. One can see a linear correlation between OES on the one hand and FTIR and WEP on the other hand. We can conclude that our method is suitable for the quantitative evaluation of the hydrophilization degree of the plasma damaged dielectric.

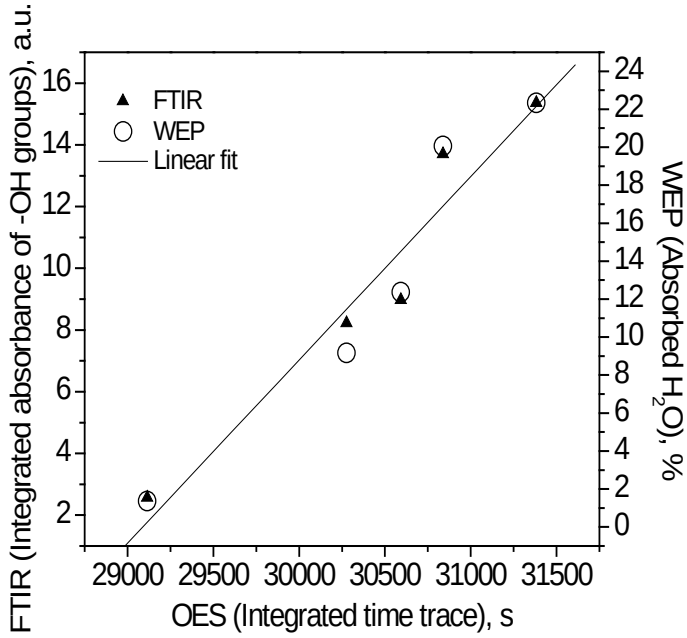

Figure 3.6 Integrated time traces (as measured by OES) versus integrated absorbance in range 3900-3100 cm^{-1} (as measured by FTIR) and absorbed water in saturation pressure (as measured by WEP).

3.3 Evaluation of Plasma Damage in Blanket and Patterned low-*k* Structures by Near-field Scanning Probe Microwave Microscope

The effect of the ash chemistry on the dielectric constant of blanket and patterned low-*k* was studied using near-field scanning probe microwave microscope, known commercially as NeoMetriK™ technology. Two common photoresist ash approaches with the same etch sequence were studied: plasma assisted sublimation of photoresist at elevated temperature and ion-assisted ash at room temperature. The results for blanket low-*k* agree well with the FTIR and WEP. The amount of sidewall damage measured in patterned structures before metallization confirms the expected trends.

3.3.1 Introduction

In this section we present the results obtained using a non-contact dielectric constant metrology based on a near-field scanning probe microwave microscope (NSPMM) as described in section 2.5.6. This method allows extracting the effective dielectric constant of low-*k* material after every processing step on patterned structures without metallization. In order to investigate a feasibility of the microscope for in-line monitoring of pattered low-*k* stacks we study the effect of ash processes known to result in low and high degree of the dielectric damage. Two common approaches have been used: (i) a low temperature, low pressure, anisotropic plasma, where the photoresist is removed by an ion-assisted physical process [4], using oxidizing or reducing plasma chemistries at low temperatures and (ii) an isotropic downstream plasma using a He/H_2 gas mixture where the resist is removed at high temperatures by a thermally activated chemical process [5, 6] as also discussed in Chapter 5. We additionally evaluated the NSPMM capabilities on blanket wafers with various degrees of ash-induced plasma damage. It is shown that the microwave microscope is a good non-destructive tool for the real-time electrical evaluation of blanket and patterned low-*k* stacks at every processing step.

3.3.2 Experimental

Sample preparation. Both blanket (100-nm-thick low-*k*) and patterned low-k stacks were deposited on low resistivity 300 mm Si wafers. Single damascene structures were fabricated by patterning the porogen-based SiOC:H materials with 25% porosity and pristine k_p=2.5 as shown in Figure 3.7. The low-*k* plus BARC and low-*k* etch was performed using an industrial capacitively coupled plasma (CCP) reactor for dielectric etch applications. For the etch 3:16 CHF_3/CF_4 plasma was applied. The photoresist was stripped using two plasma ash chambers. The first chamber was a high temperature downstream plasma (DSP) reactor for 20:1 He/H_2 anisotropic ash at elevated temperatures. The second one was a CCP reactor with two N_2/H_2 and O_2 chemistries. We additionally induced different degrees of ash damage to blanket low-k stacks using inductively coupled plasma reactor (ICP) where the plasma of higher density than in CCP reactor produces severe low-*k* damage [4].

Table 3.1 Characteristics of used etch and ash processes. The chambers were described in section 2.2.

Wafer type	Treatment	Chamber	Chemistry	Time [s]
patterned	Etch	CCP	CHF_3/CF_4 3:16	n/a
	Ash	CCP	O_2	10, 20
		CCP	N_2/H_2 2:1	30
		DSP	He/H_2 20:1	11
blanket	Ash	ICP	O_2	10, 20, 30

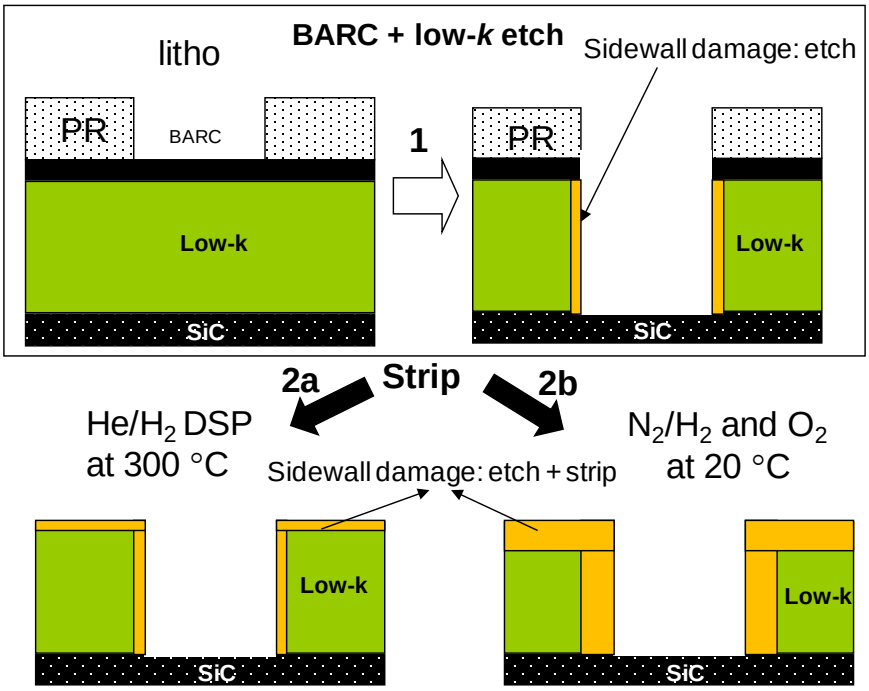

Figure 3.7 Photoresist-based etch scheme. Step 1: BARC and low-k etch. Step 2a: plasmas assisted sublimation based strip at elevated temperature. Step 2b: ion-assisted strip at room temperature.

Measurement techniques. Dielectric constant measurements at 4 GHz and ambient conditions were performed by NSPMM on conventional meander-fork structures without metallization. All structures had 50% pattern density with the width (spacing) ranging from 90 nm to 150 nm. The schematic for the microwave measurement is shown in Figure 3.8a, where the probe is a parallel strip transmission line made of quartz sandwiched between two Al strips. The probe sampling area was about 10×10 μm^2 to address multiple trenches. Because both the "signal" and "ground" probe electrodes are located above the sample and capacitively coupled to it, there is no need to make a contact to or ground the wafer. Figure 3.8**b** shows a lumped element scheme of capacitance measured by the probe, where C_{ag} describes the probe-sample air gap ~100nm. The chemical bonding structure of blanket low-k films before and after plasma treatments was analyzed using a Biorad QS2200 ME FTIR system. The bulk hydrophilicity (amount of adsorbed water) was measured by using WEP (ellipsometric porosimetry with water source) equipped with SENTECH 801 spectroscopic ellipsometer (350-850 nm) [7].

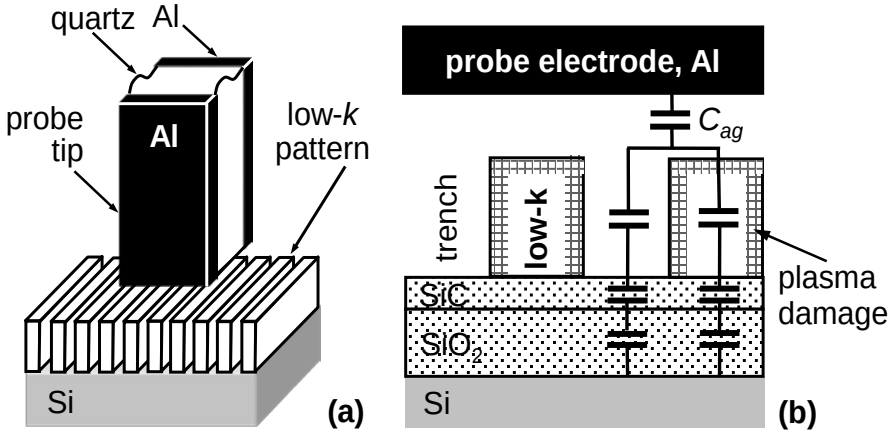

Figure 3.8 The probe tip of a near-field scanning probe microwave microscope located above patterned structure (a). Equivalent electrical scheme of the capacitance measured by the probe (b).

3.3.3 Results and discussion

3.3.3.1 Blanket wafers

Several blanket low-*k* wafers were exposed to O_2-based ash plasma in order to induce various degrees of field plasma damage. We used the exposure times of 10, 20, and 30 seconds to induce different amounts of low-*k* film hydrophilization evaluated by WEP as shown in Figure 3.9. In the case of pristine sample the amount of absorbed water is around 1.6 % by volume (at saturated vapor pressure), while the sample treated for 30 s in O_2 plasma absorbs 22 % due to the hydrophilization of pore sidewalls, which nearly equals the total material porosity. Those trends have also been confirmed by FTIR measurement (see Figure 3.9).

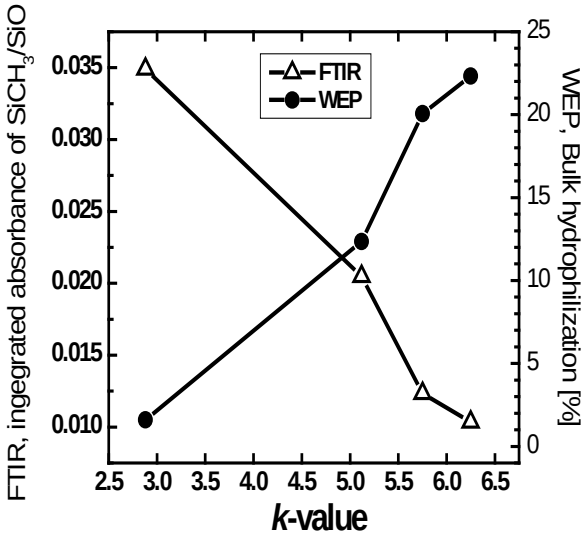

Figure 3.9 The dependence of the *k*-values at 4 GHz (as measured by NSPMM) on $SiCH_3/SiO_2$ absorbance bands ratio (as measured by FTIR) and bulk hydrophilization (as measured by WEP) of the as deposited and plasma damaged low-*k* films.

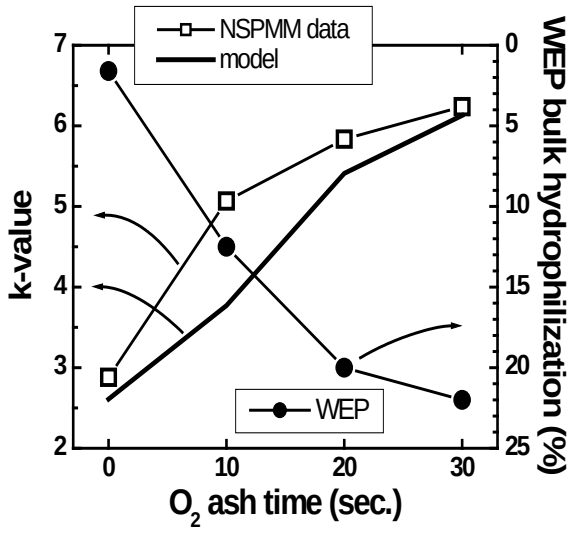

Figure 3.10 Time of exposure to O_2 plasma in ICP reactor versus the *k*-value at 4 GHz (as measured by NSPMM and calculated from simple model based on Maxwell-Garnett theory) and absorbed water at saturation pressure (as measured by WEP) of blanket low-*k* films.

The plasma treatment increases the *k*-value, as measured by the NSPMM (see Figure 3.10), because of the following. First, the dielectric constant of low-*k* matrix increases up to about 4.2 (i.e., that of SiO_2) due to the carbon depletion. Second, removal of the hydrophobic groups Si-CH_3 from low-*k* leads to formation of hydrophilic silanol groups, which promotes the moisture adsorption into low-*k* exposed to air as described in section 1.7.1 (see Figure 3.9). This drastically increases the material average dielectric constant since water has a very large dielectric constant of k_{H20}=75+i14.5 at 4 GHz at 25° C [8]. Therefore, considering polarizabilities of all possible bonds formed in low-k after O_2 plasma modification, the physisorbed water molecules are mostly responsible for the dipolar contribution to the dielectric loss [9]. For spherically shaped pores the Maxwell-Garnett theory [10] yields for the average dielectric constant of porous low-*k* material as also discussed in Chapter 1:

$$k_{av} = k_m \left[1 + \frac{3f(k_{por}-k_m)/(k_{por}+2k_m)}{1-f(k_{por}-k_m)/(k_{por}+2k_m)}\right] \qquad (3\text{-}3)$$

where k_m is the matrix dielectric constant, k_{por} is the dielectric constant of the material filling up the pores, and f is the pore fraction. From the WEP data we can estimate the damaged layer thickness as $t_d = t_{film} 100\ WEP/f$, where t_{film} is the total film thickness, and WEP is the percentage of water by volume (see Figure 3.9). Assuming a two layer model for the blanket low-k with a field damage, the dielectric constant of the entire film is:

$$k_{meas} = \frac{k_{av} k_p t_{film}}{k_p t_d + k_{av}(t_{film} - t_d)} \qquad (3\text{-}4)$$

where k_{av} is given by equation The real part of (3-3) is shown in Figure 3.9 by the solid line for k_m=4.2, k_{por}= k_{H20}, k_p=2.5, f=0.25, and t_d determined from the WEP measurements (assuming uniform film modification). One can see that there is a agreement in trend between the NSPMM measurements and the model for fully hydrophilized film (30 s of O_2/Cl_2 plasma). However, model/measurement data deviate for medium degree of hydrophilization (10 and 20 s of O_2/Cl_2 plasma). The deviation of measurement data from the model is due to gradient character of plasma damage (i.e., gradient of bulk-C conentration shown in Chapter 4/Figure 4.1). The model assumes that the damaged surface is uniformly hydrophilized. However, in reality the bulk hydrophilization have a gradient character for the shorter times of exposure. In contrast, long exposure time is sufficient to damage whole bulk of low-*k* film and therofere gradient effect can be neglected. This explains the agreement between model and data for fully damaged film (30 s O_2/Cl_2 plasma exposure). Furthermore, increase of bulk hydrophilization is followed by increase of *k*-value for both model and measurements. This shows that NSPMM is gives physical relative trends in *k*-vale for films with different degree of plasma damage (hydrophilization).

3.3.3.2 Patterned wafers

The effective *k*-value of patterned structures (see Figure 3.11) as measured by the NSPMM is shown in Figure 3.12. The upturn observed at smaller pitches is due to the sidewall damage. Solid lines are the fits to the parallel plate capacitor model of Figure 3.7b using the damaged layer thickness td as the only free parameter [11]. Nominal *k*-values and geometry were assumed for all layers. The dielectric constant of damaged sidewalls was assumed to be 7.6 according to (1) with k_m=4.2, k_{por}= k_{H2O}, and f=0.25.

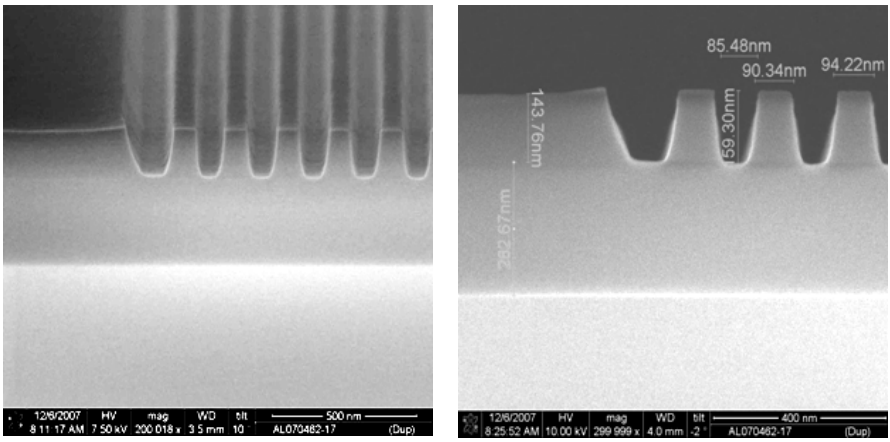

Figure 3.11 SEM cross-section of 90/90 nm L/S structures after low-*k* etch and O_2 strip: a) tilted view b) no tilt

The results agree well with the expected trends. The O_2 ash-induced damage increases with the time of the O_2 plasma treatment. In the case of He/H_2 DSP strip the sidewall damage is much less as compared to O_2 and N_2/H_2 CCP. It is well known that He/H_2 DSP strip does not damage low-*k* [12] while ion assisted strip chemistries result in substantial low-*k* damage as also discussed in Chapter 1. The observed upturn in *k*-value in the case of He/H_2 DSP strip may be explained by two reasons. The first is the uncertainty of the geometry estimation of the stack, which may also explain a poor agreement between the model and experiment for the 20 s O_2 strip. The second reason may be the damage induced by the trench etch chemistry or interaction of the post trench etch modified layer with He/H_2 DSP ash chemistry.

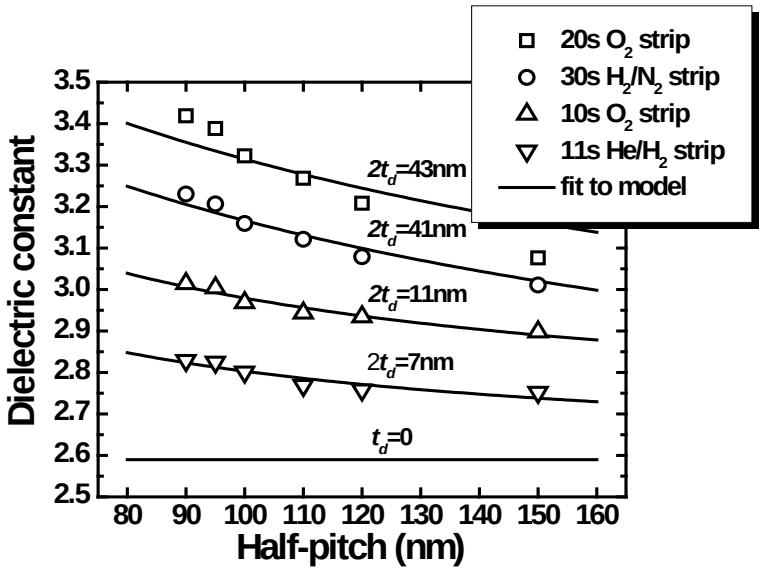

Figure 3.12 Effective dielectric constant of patterned structures with 50 pattern density as measured by NSPMM versus half-pith size for different ash processes. Solid lines are the fits to the parallel plate capacitor model shown in Figure 3.8b using t_d as the free parameter.

3.4 Chapter summary

Two new methods suitable for the plasma damage evaluation of low-*k* materials were presented. The first method is based on OES measurements of O* and H* intensities when the low-*k* dielectric is exposed to He plasma. We show that the time dependence of 777 nm peak intensity related to O* that is released during He exposure of the wafer can be used to evaluate the plasma damage of porous low-*k* materials. It is found that the integrated intensity of O*-related peak gives qualitative information about the degree of hydrophilization of the studied low-*k* films. The obtained results correlate well with FTIR and WEP data. The second method relies the microwave impedance measurements of the blanket and the patterned low-*k* dielectric structures. The microwave impedances of the dielectric structures were measured by near-field scanning probe microwave microscope. Results showed that this technique is a good method for non-invasive real time in-line monitoring of the blanket and the patterned low-*k* structures at plasma-based steps during interconnect integration. Those measurements allowed us to extract *k*-value at 4 GHz of patterned structures. We demonstrated that while the pristine low-*k* exposed to ambient air retains its as-deposited properties, the plasma damaged low-*k* may absorb water into the hydrophilized pores which substantially increases its dielectric constant.Such *k*-values reflected damage induced by processing plasma only in contrast to standard capacitance evaluation. The standard capacitance measurements require metallization of low-*k* trenches that also relies on many

damaging processes such as chemical-mechanical polishing or metallic barrier deposition. The comparison of the relative trends in *k*-values between empty (etched) and Cu-filled (metalized) trenches might allow extraction of the contributions of metallization and plasma etching and cleaning steps. This evaluation is a key importance for fundamental understanding of processing damage that occurs on patterned damascene structures.

3.5 References

[1] K. Maex, M. R. Baklanov, D. Shamiryan, F. Iacopi, S. Brongersma and Z. Sh. Yanovitskaya. J.Appl.Phys. 93(11) 8793- 8841(2003).

[2] Z. Tőkei, M. Baklanov, I. Ciofi, Y. Li and A.Urbanowicz, Semiconductor Fabtech, August (35), p.110-115(2007)

[3] A. M. Urbanowicz, D. Shamiryan, D. Kim, and M. R. Baklanov, 1st international workshop on Plasma Etch in Microelectronic, Leuven, 10-11 September (2007).

[4] G. Cunge, B. Pelissier, O. Joubert, R. Ramos and C. Maurice, Plasma Sources Sci. Technol., 14, 599 (2005).

[5] M.R.Baklanov, K.P.Mogilnikov, and Q.T.Le. , Microelectron. Eng., 83, p. 2287-2291 (2006).

[6] A. R. Striganov and N. S. Sventitskii, "Tables of Spectral Lines of Neutral and Ionized Atoms", IFI/Plentun, New York-Washington 1968, p. 77-79 and 141-145.

[7] T. Tatsumi, S. Fakuda and Shingo Kadomura, Jpn. J. App. Phys. Vol. 33 (1994)

[8] H. Okabe, Photochemistry of Small Molecules,Willey, New York, (1978)

[9] S. Eslava, G. Eymery, P. Marsik, F. Iacopi, Ch. E. A. Kirschock, K. Maex, J. A. Martens and M. Baklanov, J. Electrochem. Soc., 155 (5) (2008)

[10] A.M. Urbanowicz, B. Meshman, D. Schneider, and M.R. Baklanov, phys. stat. sol. (a), 1-4 (2008)

[11] A. M. Urbanowicz, A. Humbert, G. Mannaert, Z. Tokei and M. R. Baklanov, Solid State Phenomena, Vol.134, p. 317-320, (2008).

4 Prevention of Plasma Damage of Low-*k* Films by VUV Irradiation from He Plasma

The results that are presented in this chapter have been partly published in:

A.M. Urbanowicz, M.R. Baklanov, J. Heijlen, Y. Travaly and A. Cockburn, Electrochem. Solid-State Lett., 10, G76 (2007).
A.M. Urbanowicz, D. Shamiryan, A. Zaka, P. Verdonck, S. De Gendt and M. Baklanov, J. Electrochem. Soc., 157, H565 (2010).

4.1 Introduction

This chapter deals with plasma damage that occurs during the cleaning of the Cu/low-*k* stack after planarization by CMP (see also section 1.8). The purpose of the post CMP cleaning is the reduction of Cu oxide on the Cu surface. Therefore, only reducing plasmas can be used for this purpose. NH_3 plasma treatment is a popular approach because this plasma enables both the reduction of Cu oxides without deterioration of the adhesion with the subsequent dielectric liner and the removal of residual particles [1.2]. However, NH_3 plasma treatment leads to a significant modification of the chemical composition and degradation of low-*k* films (carbon depletion and subsequent hydrophilization). This degradation is related to the penetration of active radicals from NH_3 plasma into porous low-*k* materials. Therefore, low-*k* materials with porosity larger than 20 % require process optimization with respect to plasma damage.

One of the effective strategies to reduce bulk low-*k* damage is surface activation in order to trap the radicals at the surface. The reduction of O and NO_2 plasma damage by using He plasma pre-treatment were reported by Wang et. al. [3] and Yanaiet al. [4], respectively. However, the mechanism of plasma damage reduction was not discussed. We demonstrate that the preliminary exposure of the low-*k* surface to He plasma makes it more resistant to NH_3 plasma and proposed the mechanism of plasma damage reduction. The extreme ultra-violet (EUV) emission from He plasma creates chemically active sites and decreases pore radii on the low-*k* surface, which leads to the recombination of active radicals on the surface. In certain cases, the activated surface could stimulate and localize chemical reactions, providing sealing of low-*k* materials. The layered structure of the modified surface is evaluated by X-ray reflectivity (XRR) and spectroscopic ellipsometry (see section 2.5.1). The sealing properties of the cap layer were evaluated by toluene-based

ellipsometric porosimetry TEP (see section 2.5.2.1). We discuss the effect of the NH_3 plasma on the low-*k* dielectric and the effect of He plasma pre-treatments at different radio-frequency (rf) powers and exposure times on the NH_3 plasma damage resistance of the low-*k* dielectric. Furthermore, we show that differential FTIR spectroscopy (see section 2.5.5) can be used to monitor the pore sealing efficiency in the sequential He + NH_3 plasma treatment.

4.2 Experimental

4.2.1 Dielectric material

Porogen-based low-*k* films (E2 in table Table 2.2) with a *k* value of 2.5 were used for the experiments [5]. Approximately 180 nm thick films were deposited by plasma-enhanced chemical vapor deposition (PECVD) on 300 mm Si wafers The porosity of the deposited low-*k* films was typically close to 25% with a mean pore radius of 0.7 nm, measured by TEP (see section 2.5.2.1).

4.2.2 Plasma treatment conditions

All experiments were carried out in the Eagle 12 plasma chamber from ASM (see table Table 2.1). This reactor is a capacitive-coupled plasma (CCP) system, using a radio frequency (rf) of 13.56 MHz, the rf power was varied from 400 W to 1400 W. The effect of ion bombardment was minimized because the wafer was placed on a grounded electrode. The wafer temperature was approximately 350 ºC. For the damage evaluation, blanket low-*k* films were exposed to NH_3, He and successive He and NH_3 plasma treatments. The experimental conditions are summarized in Table 4.1. The effect of the NH_3 plasma was evaluated after the exposure of low-*k* samples to 900 W NH_3 plasma for 15 s at a gas pressure of 530 Pa and a gas flow of 400 sccm.

Successive He + NH_3 plasma treatments. The He plasma exposure was followed by the NH_3 plasma exposure. The NH_3 plasma treatment was the same for all experiments (as described above). All the He pretreatments were performed using the same gas pressure of 630 Pa and gas flow of 1000 sccm. Two parameters of He plasma were varied for successive He + NH_3 plasma treatments: rf power (400 W, 600 W, 800 W, 1400 W) using the constant time of 20 s, and time (20 s, 40 s, 60 s) with a constant rf power of 1400 W. Furthermore, we used 600 W of rf power for 60 s. This additional experiment was done to evaluate the influence of rf power on surface sealing of the low-*k* material.

He plasma treatments. To study the effect of He plasmas, we first used 400 W and 800 W of rf power and a constant time of 20 s. Furthermore, 1400 W He plasma with times of 40 s and 60 s and additionally 60 s of 600 W plasma treatments were used.

Table 4.1. Summary of experimental conditions for differently treated E2 films (see also Table 2.2). Table shows main parameters during film processing such as time, pressure and rf powers. Those parameters for NH_3 plasma were always the same, while for He plasma times and rf powers were varied.

Parameter	He plasma pretreatment	NH_3 plasma treatment
Time [s]	0-60	0 and 15
Pressure [Pa]	630	530
RF power [W]	400 - 1400	900
He flow [sccm]	1000	0
NH_3 flow [sccm]	0	400

4.3 Metrology

Thickness and refractive index of reference and plasma treated films were measured by a SENTECH 801 spectroscopic ellipsometer (SE) mounted on to a vacuum chamber. The measurements under vacuum allow us to eliminate the effect of adsorbed moisture on the optical properties of the hydrophilic films. The spectra were recorded in the wavelength range of 350-850 nm. Optical properties and thickness were determined by fitting models to the measured spectra of the ellipsometric polarization angles at 70º by single and double layer optical models using the Marquardt-Levenberg algorithm. The film thickness was estimated using a double layer SE model based on the Cauchy approximation (see section 2.5.1). The bottom layer was assumed to have optical properties of the as deposited film, while the optical characteristics of the top modified layer were determined by fitting. The open porosity, pore size distributions and surface sealing effects (i.e. top surface densification by plasma treatment) of the low-*k* films were evaluated by TEP (see section 2.5.2.1). TEP was also used to evaluate surface sealing effects caused by plasma modifications of the porous low-*k* film [6,7,8]. The surface sealing effect appeared when the pore necks size at top surface decreases. This results in a decrease of the toluene diffusion rate through the densified surface layer as reflected in the delay between toluene adsorption and desorption isotherms (Figure 4.5). The full surface sealing effect appeared when the toluene absorption is not observed (Figure 4.5b). In this case the pore neck size is comparable with the toluene molecule size (6 Å).

The hydrophilization of low-*k* materials was characterized by three methods. The first one was water-based ellipsometric porosimetry WEP (see section 2.5.2.2). This method was sensitive to the bulk hydrophilicity of low-*k* films. The volume fraction of the porous low-*k* film filled with water at SVP reflected the degree of the hydrophilization of the porous bulk film. The second method was water-based goniometry that measures the water contact angle (WCA) with the film surface. The WCA reflects hydrophobic properties of the film surface. The third method was FTIR spectroscopy to study the integrated absorbance of –OH and H_2O groups.

The molecular bands of low-*k* films before and after plasma treatments were analyzed using FTIR spectroscopy (Biorad QS2200 ME). The spectra were recorded in the range of 4400-400 cm^{-1} in nitrogen ambient. The nitrogen ambient was applied to reduce absorbance from ambient such as moisture and CO_2. In certain cases, the spectrum before the plasma treatment was subtracted from the spectrum after the treatment. The obtained differential spectra reflect the difference in absorbance between the as deposited and the plasma-damaged film and allowed us to analyze the small modifications that were not pronounced in normal spectra.

Time of flight secondary-ion mass spectroscopy (TOF-SIMS) was used to obtain the concentration profile of the film components (see section 2.5.3). The data were obtained using an IONTOF IV instrument in a non-interlaced dual beam mode with a Xe sputtering beam and a bunched 15 keV Ga analysis beam to detect negative secondary ions. The Ga analysis beam was rastered over a 100x100 μm^2 area. The Xe sputtering beam was used with 1 keV of impact energy and 80 nA of current using a raster size of 500x500 μm^2.

4.4 Results

4.4.1 Structural modification

The reduction in the concentration of organic hydrophobic agents (carbon depletion) is one of the consequences of plasma damage. The depth of carbon depletion as measured by TOFSIMS is shown in Figure 4.1.One can see that the pure He plasma (20 s He 800 W) causes minimal C-depletion while the NH_3 plasma (15 s NH_3 900 W) produces the highest C-depletion. The degree of C-depletion is strongly reduced by a He plasma treatment preceding the exposure to the NH_3 plasma (i.e 20 s He 1400 W + NH_3). This effect becomes more pronounced at higher rf power levels of the He plasma pretreatment. The depth of the C-depletion is improved by the factor of two after the combined 1400 W He + NH_3 plasma, when compared with the pure NH_3 plasma treatment.

The bonding structure of the low-*k* material was studied by FTIR. FTIR spectra of reference and 15 s NH_3 plasma treated low-*k* films are shown in Figure 4.2. The investigated low-*k* is characterized by the Si-O-Si backbone (1000-1200 cm^{-1}), Si-CH_3 (1274 cm^{-1}) and Si-H (2250 and 890 cm^{-1}) bonds. The appearance of the absorbance of the Si-OH and H_2O group (3900-3100 cm^{-1}) depends on hydrophobic properties of the film. The intensities of the Si-CH_3 and Si-H absorbance values are decreased after NH_3 plasma treatment while the absorbance values of the Si-OH groups are increased. The absorbance of the Si-OH groups significantly increases after NH_3 plasma due to the film hydrophilization and subsequent ambient moisture absorption to film pores.

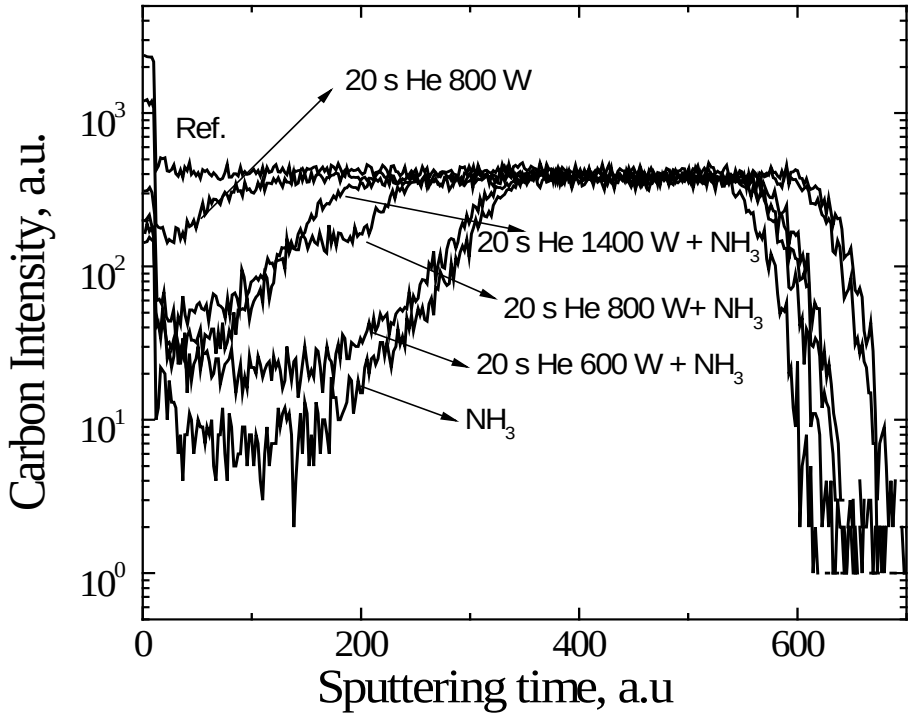

Figure 4.1 Carbon depth profile of the as deposited and plasma treated films as measured by TOFSIMS. The as deposited film (ref.) thickness was around 180 nm. Therefore sputtering time of around 650 corresponds to 180 nm of sputtered film. However, density gradient in plasma modified films makes complex the precise film thickness comparison by using sputtering time.

To compare all low-*k* films, the amount of Si–CH_3 groups is expressed as a ratio of integrated absorbance of Si-O (970-1260 cm^{-1}) and Si-CH_3 (1260 -1290 cm^{-1}) groups as shown in Figure 4.3. The reduction of Si-CH_3/Si-O ratio indicates the removal of Si-CH_3 groups. The dotted line represents the Si-CH_3/Si-O ratio of the as deposited film (reference level). One can see that the removal of the Si-CH_3 groups is observed after each plasma treatment, but the biggest C-depletion occurs after NH_3 only and 400 W He + NH_3 plasma treatments. FTIR data (Figure 4.3) support these conclusions based on TOF-SIMS results that the minimal C-depletion occurs in He plasma and the degree of depletion is reduced by the combination of He and NH_3 plasma treatments starting from a He rf power of 600 W.

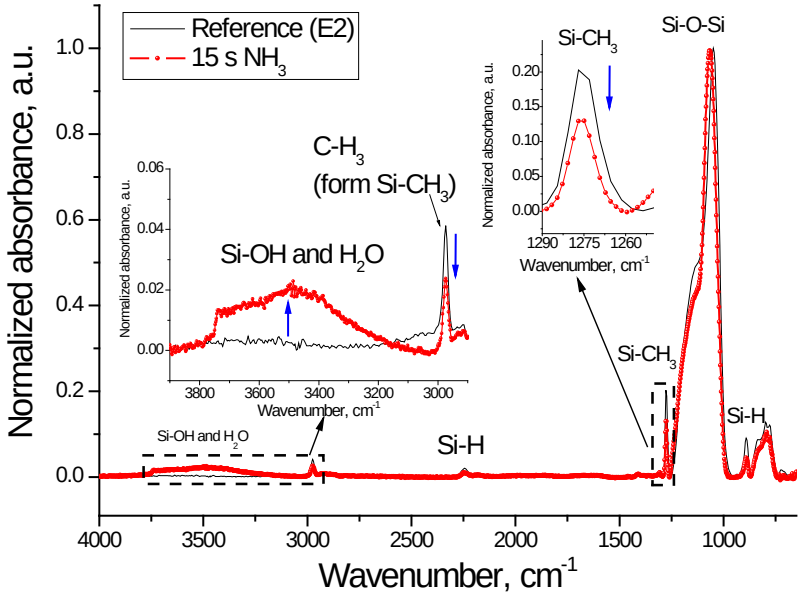

Figure 4.2 FTIR spectra of as deposited low-k film (E2) and E2 film treated with 15 s of NH_3 plasma. The enlarged spectral areas shows absorbance values related to Si-OH, H_2O, and Si-CH_3 groups that are the most important for our analysis. The blue arrows in enlarged spectral areas indicate major changes in bonding structure due to NH_3 plasma damage: Si-CH_3 group depletion and H2O, Si-OH bonds incorporation. The H_2O and Si-OH absorbance values are shown in Table 1.2.

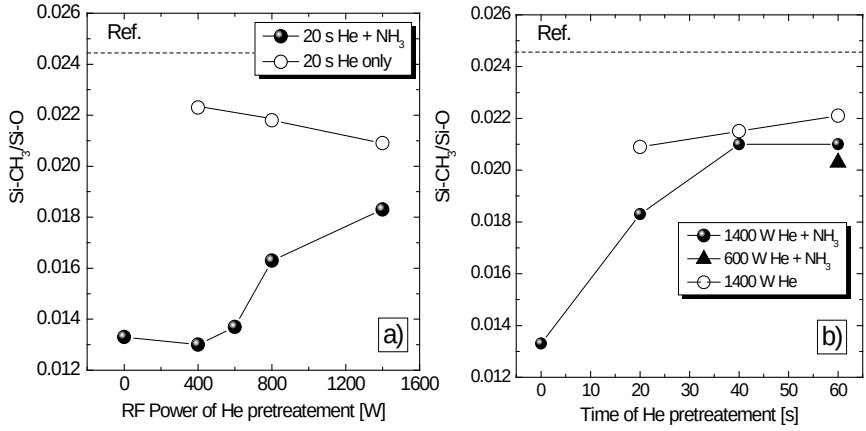

Figure 4.3 The ratio of integrated absorbance of Si-CH_3 and Si-O (as measured by FTIR) versus: (a) RF power of He pretreatment, (b) time of He pretreatment. The ration was obtained by integrating spectra in the wavenumber range that correspond to Si-CH_3 and Si-O bond vibrations. That is from 1265 cm^{-1} to 1280 cm^{-1} for Si-CH_3 and 950 cm^{-1} to 1250 cm^{-1} for Si-O.

Figure 4.3b represents the Si-CH_3/Si-O ratio versus time of the He plasma treatment. The Si-CH_3 bond depletion is limited for combined He + NH_3 plasma treatments and decreases with time of He pretreatment. For a constant time of 60 s, the higher power of He pretreatment (1400 W) results in a more effective reduction of the Si-CH_3 bond depletion. Figure 4.4 shows open porosity as measured by the toluene-based EP. The pristine low-*k* film has 25% of open porosity. The open porosity increases slightly by 1-2 % after the NH_3 plasma treatment. On the contrary, the pure He plasma treatment reduces the open porosity by 3-4 %.

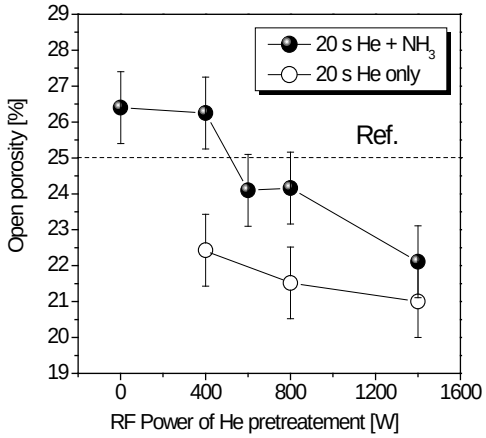

Figure 4.4. Open porosity versus RF Power of He pretreatment as measured by TEP. The dotted line represents porosity level for as deposited low-*k* film.

We found that increasing rf power (starting from 600 W) of 20 s He pretreatment inhibits the effect of porosity increase imposed by the NH3 plasma. However, we did not find any evidence of surface sealing effect. The adsorption and desorption isotherms followed the same trend as in the pristine material as shown in Figure 4.4a. In contrast, longer exposure times (40s and 60 s) of He plasma with a maximal power of 1400 W in the combined He + NH_3 treatments caused the surface sealing effect as shown in Figure 4.5b and Figure 4.6.

The hysteresis loop between adsorption and desorption branches of the isotherms is related to a delay in the pore filling and emptying during the adsorption and desorption cycles (Figure 4.5b). The integral refractive index measured in vacuum increases slightly from 1.367 for a reference sample to 1.382 after the 60 s He + 15 s NH_3 plasma treatment. This suggests that the total porosity changes insignificantly and, therefore, the bulk of the film is still porous. Therefore, the diffusion limitation of the toluene penetration is only related to densification of the top part of the film. Such “partial sealing” indicates a decrease in size of the pore necks at the surface. In this case, it is not possible to calculate the pore size distribution. We can only conclude that the effective pore size in the top part of the film becomes comparable with the size of toluene molecules, approximately 6 Å.

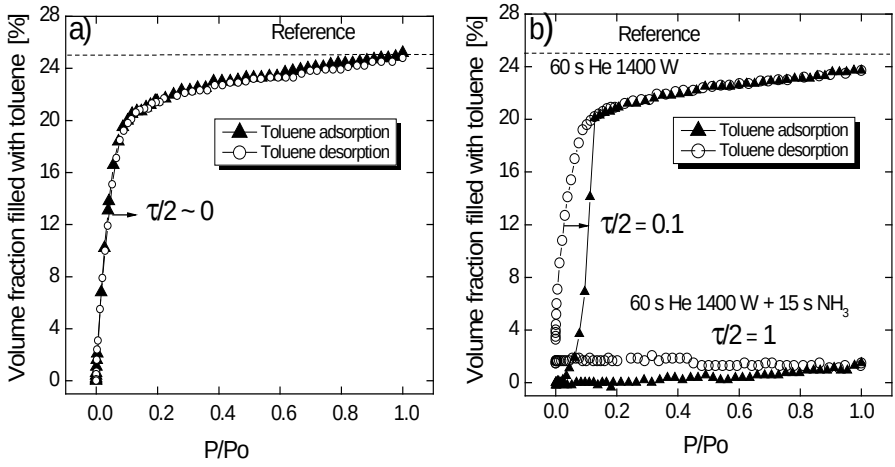

Figure 4.5 Adsorption/desorption isotherms (as measured by toluene EP): pristine sample (a), after He and He + NH_3 plasma (b). The pictures reflect 3 values of *τ/2*; *τ/2 ~ 0* for uniform porosity (a – reference film), *τ/2 = 0.1* for top layer porosity smaller than bottom (b - partly sealed film after He + NH_3 treatment), and *τ/2 = 1* for non-porous top surface or pore size comparable with toluene particle size (b - film is not permeable by toluene after He + NH_3 treatment).

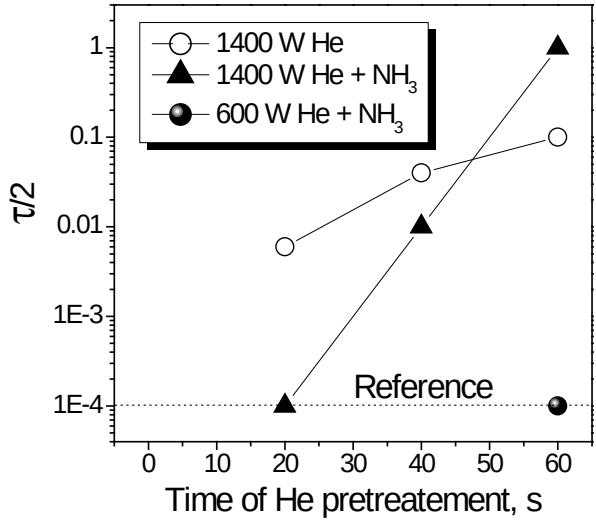

Figure 4.6. The delay between adsorption and desorption isotherms (τ/2) in logarithmic scale versus time of He pre-treatment. The meaning τ/2 were explained in Figure 5.4. However, for τ/2 ~ 0 value of 0.0001 is taken as reference (marked by dotted line) since logarithm 0 does not exist.

Quantification of the sealing efficiency can be based on the "delay" between the toluene adsorption and desorption branches $\tau/2$ versus time of the plasma treatment. The $\tau/2$ is the difference between the values of P/Po on the adsorption and desorption curves that correspond to the pores' filling of 50% as indicated by an arrow in Figure 4.5b. In all these experiments, the rate of the pressure change was the same. Therefore, this delay reflects the change in the toluene diffusion rate through the top densified layer. A longer delay corresponds to a smaller size of the remaining pores. The $\tau/2$ increases with the time of the He plasma treatment as shown in Figure 4.6. Therefore, the degree of densification of the top densified layer depends on the time of the He plasma treatment. Porous low-*k* film after subsequent 60 s He and NH_3 plasma treatment does not show any toluene adsorption (Figure 4.5b). This proves that the pore size approaches the toluene molecule size of 6 Å (surface sealing effect). The surface sealing effects can also be studied using the EP-system and analyzing a solvent filling time at the solvent saturated vapor pressure (SVP) [7]. The solvent penetration increases with the filling time dependent on the barrier integrity (surface sealing efficiency) [7,8]. To study this, the fully sealed sample treated with 60 s He + 15 NH_3 plasma kept in EP absorption chamber for approximately 3000 s. The toluene vapor pressure was increased from 0 to 24 Torr (toluene SVP) in 2000 s. Next, a 1000 s sample was kept in a vacuum chamber at a toluene pressure of 24 Torr. After 1000 s, the change in refractive index was less than 0.003. This shows that after this time the diffusivity of toluene through the densified layer was close to 0.

The thickness loss after all plasma treatments was measured by SE (Figure 4.7). The thickness was extracted from the best fits of a Cauchy model (see section 2.5.1). It was found that the NH_3 plasma reduces the thickness of the low-*k* film by about 20 nm. On the contrary, the thickness loss for the pure He plasma treatment is smaller than 8 nm. The thickness loss after NH_3 plasma is reduced in the He pretreatment with rf power higher than 600 W.

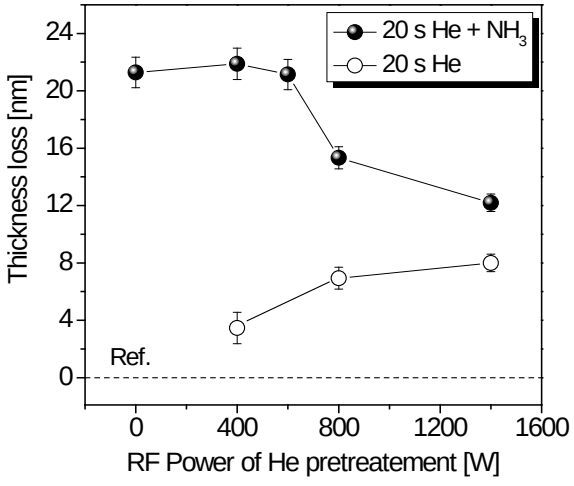

Figure 4.7. The thickness loss as measured by VIS SE. The thickness loss is expressed as a difference between as deposited and plasma modified film.

4.4.2 Hydrophobic properties

Figure 4.8 shows the amount of adsorbed water measured by water EP for different (a) rf powers and (b) times of He plasma pretreatments. The dotted line represents the water adsorption in a pristine film (1.6 %). After 15 s of NH_3 plasma treatment, the amount of adsorbed water increased up to 16%. Comparing this value with the total open porosity (24%), one can conclude that more than 50% of the film becomes hydrophilic. The pure He plasmas of 400 W and 800 W almost do not change the hydrophilicity of the film bulk. Pre-treatments in He plasmas reduce the degree of bulk hydrophilization imposed by the NH_3 plasma. This reduction increases with rf power of (a) the He plasma and (b) the time of the plasma treatment. The treatment of the 1400 W He + NH_3 plasma results in 5.5 % of adsorbed water. The combined treatment of the 60 s He 1400 W + 15 s NH_3 plasma results in hydrophilization of 1.6 %. which is equal to the as deposited sample (Figure 4.8b). The water contact angle (WCA) of the as deposited film is 95º. The reduction in the WCA is observed after all treatments. However, it was possible to distinguish two groups: only He plasma and all treatments containing NH_3. For pure He, the WCA was higher than 20°. For all NH_3 containing treatments, the WCA was lower than that after He plasma only. Therefore, contrary to the bulk properties, the low-*k* surface becomes hydrophilic after all the plasma treatments.

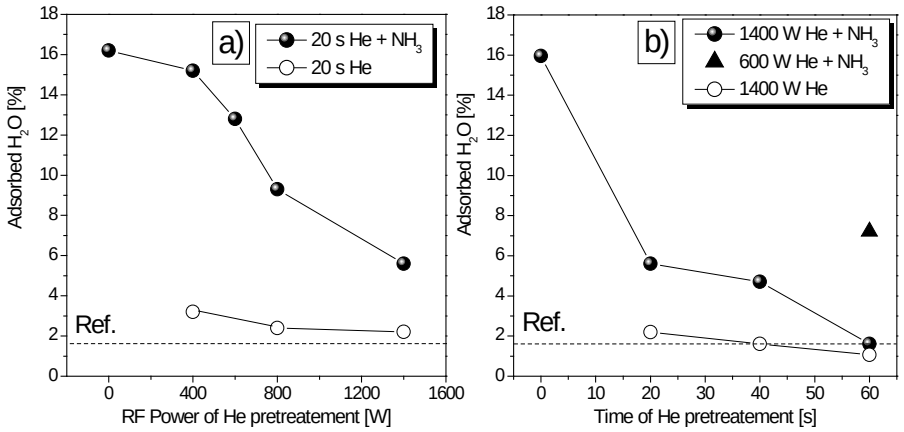

Figure 4.8. The amount of adsorbed water of as deposited, He plasma treated and He + NH_3 plasma treated low-*k* films versus RF power (a) and time (b). The ration was obtained by integrating spectra in the wavenumber range that correspond to H_2O and -OH bond vibrations. That is from 3200 cm^{-1} to 3900 cm^{-1} for Si-CH_3 and 3100 cm^{-1} to 3900 cm^{-1} for Si-O.

Figure 4.9a shows the integrated absorbance of –OH groups (3100-3800 cm^{-1}) obtained by FTIR. The hydrophilization is proportional to the amplitude of the Si-OH absorbance band. The dotted line represents the reference data for the as deposited film. The reference films reveal the –OH absorbance close to 0. The He plasma increases the –OH amount. This increase, however, is smaller than that for all NH_3 containing treatments. The pure NH_3 plasma treatment resulted in the

highest –OH incorporation. The He pretreatment reduced –OH group incorporation imposed by the pure NH_3 plasma. This reduction was proportional to the rf power of the He plasma.

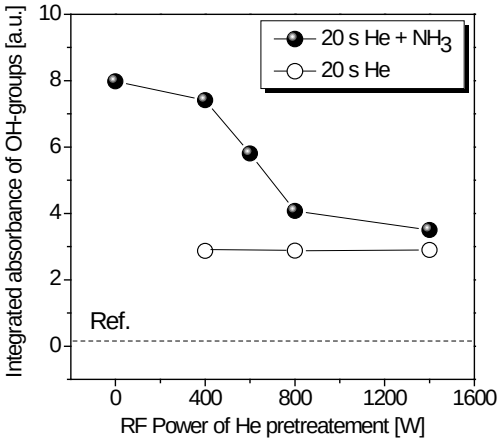

Figure 4.9. Integrated absorbance of OH groups as measured by FTIR versus RF power of He plasma pretreatment. The dotted line indicates OH-group level for as deposited sample E2.

4.5 Discussions

The presented experimental data demonstrated that pure NH_3 plasma produces significant damage to the low-*k* material. On the other hand, structural and chemical modification of the bulk of the exposed low-*k* material is minimal in pure He plasmas. Additionally, the He plasma pretreatment before exposure to NH_3 plasma has beneficial effects, such as possibility of sealing of the low-*k* surface, and therefore reduction of plasma damage. The sealing efficiency depends on the time and power of He plasma pretreatment. In the following section, we analyze the nature of the observed phenomena.

4.5.1 Effect of NH_3 plasma on low-*k* dielectric

The most important active components formed in NH_3 plasma are NH_2, N_2H_4 and H radicals. Hydrogen radicals play a key role in the Cu oxide reduction required after the post CMP cleaning step. However, most of these radicals are chemically active with respect to SiOC:H based low-*k* materials and result in their damage (see section 1.7). The different effects of the NH_3 plasma have already been discussed in the literature in addition to the papers reporting damage of low-*k* materials [9,10]. Peng *et al*. [10] reported that NH_3 plasma in certain conditions is able to seal the surface of the MSQ-based low-*k* film.

The chemical effect of H, N and mixture of H and N radicals is discussed in details in chapter 5. It will be shown that H radicals do not remove Si-CH_3 groups from low-*k* film. Also N radicals cause moderate film modification but a mixture of N and H radicals results in Si-CH_3 group depletion, thickness reduction and subsequent hydrophilization of low-*k* films. However, in the PECVD chamber the films are additionally exposed to the UV-radiation and metastable atoms from plasma besides the reactive radical environment. The additional physical activation results in a very complex mechanism of low-*k* dielectric modification in this NH_3 plasma. The exposure of the films in NH_3 plasma results in their thickness loss, increase of porosity and removal of Si-CH_3 groups.

We focus on then chemical reactivity of highly strained silica rings that might react with NH_3. Those strained rights can be generated in low-*k* film by its exposure to He plasma (Figure 4.12). The Si-NH_2 groups on the silica surface might be formed by the reaction of NH_3 molecules with "highly strained" or ionic siloxane bridges [11,12]. The reaction is represented by the following equation:

$$Si\text{-}O\text{-}Si_{\alpha<144^\circ} + NH_3 \rightarrow Si - NH_2 + SiOH \qquad (4\text{-}1)$$

It is also important to analyze the role of NH_x radicals in structural changes occurring in low-*k* dielectrics. We simulated IR Si-O-Si absorbance after NH_3 plasma exposure [13]. The band related to CH_3 groups shifts to the lower frequencies, which is also evidence of a strong increase in the π-bonding contribution in the Si-O-Si system. Because an increase in the π-bonding causes an increase in the Si-O-Si angle, a pore of 1 nm in radius can increase by 0.4-0.5 Å (that is, by about 2 %). This calculation supports the experimental data. We observed an increase in the porosity after the NH_3 plasma treatment of about 1-2% and also a small increase in the pore size. The increased pore size might be also due to the removal of porogen residues by NH_3 plasma (amorphous carbon and cyclic hydrocarbons) embedded in the low-*k* matrix as discussed in chapter 5. The porogen residues (PR) are generated during the UV curing step of PECVD low-*k* material. The PR might actively react with NH_3 plasma radicals and be removed from low-*k* matrix, that results in the increased pore size (see section 5.5).

4.5.2 Effect of He plasma on low-*k* dielectric

The effect of the ion bombardment in a He plasma is not significant because the wafer is placed on the grounded electrode (only self-bias is applied to He ions), and moreover, the mass of He atoms is relatively small. We argue that the major modifications caused by He plasma are due to the energy transfer from extreme ultra-violet (EUV) photons and 2^1S He metastable atoms [14] to the low-*k* structure. He has intense spectral lines below 60 nm as shown in Figure 4.10.

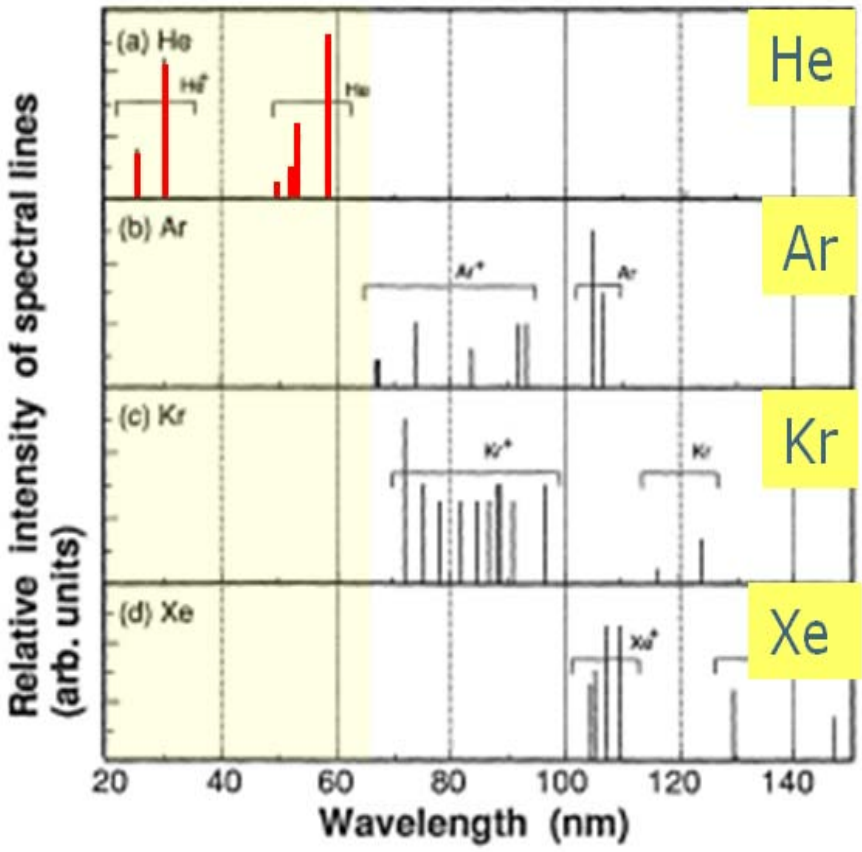

Figure 4.10 The relative intensity of spectral lines for the chosen noble gasses. Adapted from Vandyck et al. [14]. It is clear that He has the most intense spectral lines in the range of 20 to 60 nm.

The modification of SiO_2 layers caused by EUV radiation from He plasma has been reported [15,16]. The EUV light is able to break Si-O bonds on the SiO_2 surface and form so called "E' defects" (oxygen vacancies). Using the absorption coefficients reported by Philipp *et al.*[17] one can calculate the penetration depth of EUV photons from the He plasma into the silica. These calculations show that the intensity of EUV light with wavelengths of 60-100 nm decreases to 1/*e* within the first 10 nm of silica. Therefore, most photochemical modifications of a silica-based low-*k* film should be restricted to 10-20 nm of the top layer. One can see that this thickness is in reasonably good agreement with XRR data, which showed densification of the top 17 nm (Figure 4.11).

We also consider the effect of He metastable atoms on the low-*k* surface. They were reported in literature to cause damage to the porous silica [18]. The typical energies of metastable He atoms are 19.82 eV (2^3S state) and 20.62 eV ($2\ ^1S$ state) [19], which are close to the energies of EUV photons. The high-energy

metastable atoms could create electron-hole pairs in the film [19]. The effect of metastable atoms is reported to be localized in the top 1-2 nm of the film [18].

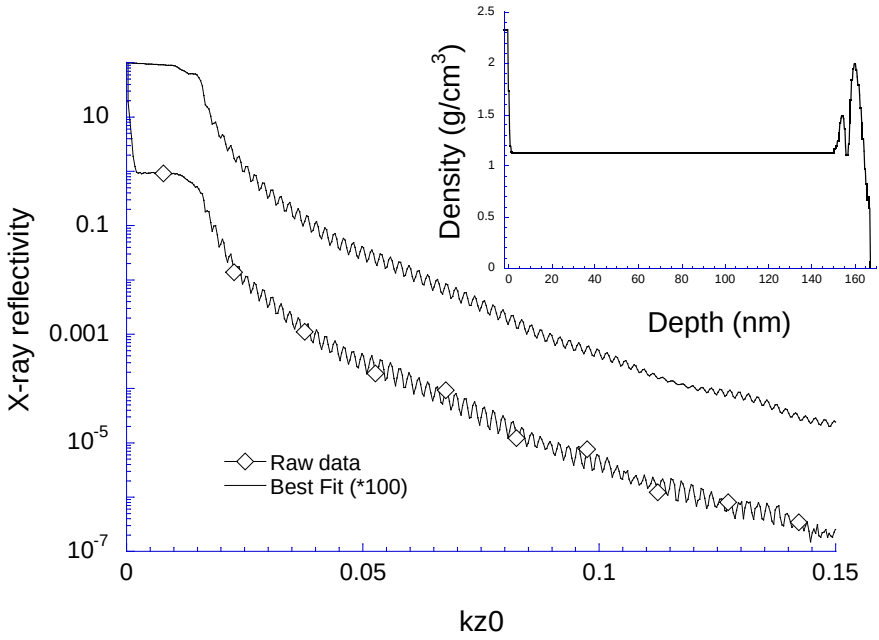

Figure 4.11 Results of XRR analysis of a 40 s He plasma-treated 160 nm thick low-*k* film. The big graph represents raw data (*kz0* is proportional to X-ray reflection angle) and fitted curve. The embedded graph represents the modelled sample density profile. Top layer of the (~17 nm) of the sample shows higher density.

The defects formed by EUV light and metastable atoms are chemically active and could result in the formation of surface active centers localizing the chemical reactions to the surface. The oxygen vacancies are centers for the chemisorption of active radicals. Another important factor of He plasma pre-treatment is a decrease of the size of pore necks.

It is less clear how the He + NH_3 plasma treatment reduces the pore neck size. It was speculated [13] that a rupture of a proton from a CH_3 group also occurs when exposed to the He plasma, resulting in a shift of the Si-O-Si bond angles distribution toward larger angles. Subsequent treatment of the film in NH_3 plasma, after He, promotes cross-linking over these -CH_x groups, as well as Si atoms; -NH_x may serve as a bridge. As a result, the pore size decreases, or the pores get sealed, because the reaction proceeds at the very pore entrance. Because of this, if porosity is measured on the basis of the refractive index, one would not see any essential changes. The number of built-in NH_2 groups may be small because building-in occurs only at the surface; this may be the reason why these groups do not manifest themselves in the IR spectra.

Another factor that might influence the plasma damage reduction is the surface roughening induced by the He plasma. The effect of the different He rf power levels on the low-*k* surface roughness was studied by Yanai et. al. [4] Using atomic force microscopy they found that the mean surface roughness (MSR) was in the range of 0.18 nm - 0.39 nm. The as deposited film showed an MSR of 0.39 nm. With irradiation with He plasma at 100 W, the surface became smoother (MSR=0.18 nm); when plasma power was increased to 500 W (MSR=0.31 nm), the surface became rougher. Yanai et al, [4] presumed that the rougher surface is due to surface carbon depletion at the first monolayer. No correlation between the surface roughness and the damage reduction effect of the He plasma was found. The main effect on damage reduction was related to the densified surface by EUV radiation from He plasma. This corresponds to our conclusion that the reduced mean pore size in 10-20 nm of the modified film layer is the most important factor that reduces depth of radical penetration, and therefore, the depth of the plasma damage. The mean travel distance of the chemically active radical is significantly reduced due to multiple collisions in narrow pore necks. The multiple collisions significantly increase the probability of recombination or chemisorption of active radicals.

4.5.3 Mechanisms of thickness loss of low-*k* treated in NH_3, He and sequential He + NH_3 plasmas

The mechanism of thickness loss in processing plasmas at elevated wafer temperatures (350 °C) can be caused by chemical (reactive plasma radicals) and physical plasma effects (UV radiation and hot electrons) [20]. Higher thickness loss in the pure NH_3 plasma than in the He plasma (Figure 4.7) suggests that the chemical effect is dominating. The bond breakage caused by NH_x radicals from the NH_3 plasma occurs within the SiCOH matrix that results in the formation of activated silyl sites. The activated silyl sites are then available to react with other activated silyl species to form Si-Si cross-links or possibly with SiOH to generate a SiOSi cross-link (see section 1.7.3). The chemical-assisted cross-linkage results in the film thickness loss. The thickness loss in the pure He plasma is much smaller because only the UV, and electron-beam and He meatastable atoms are interacting with the film. The effect of UV and metastable atoms is limited to the surface. In the combined He + NH_3 treatment the thickness loss is prevented due to the reduced penetration depth of NH_3 plasma radicals, which reduces the effect of the chemical-assisted cross-linking as shown in Figure 4.7.

The thickness loss can also be due to the etching of the dielectric in the studied plasmas. It was proposed by Worsley et al. [29] that the total depth of ash plasma damage is the sum of etch depth and the modification depth. They studied the reducing Ar/H_2 ash-plasma in the CCP-type plasma chamber at room temperature, where samples were placed on a biased electrode. Worsley et. al [29] showed that the etch depth increases with the porosity of low-*k* film and the physical sputtering element of etching (ion bombardment). In our case, however, the ion bombardment effect is minimal because films were placed on the grounded electrode. The only possibility to induce film etching would be volatilization of the

Si-containing reaction products due to increased temperature of the substrate (350 ˚C). However, only a small fraction of the thickness loss might be due to etching, because the reactivity of the NH_3 plasma chemistry with Si-O bonds is very low. Therefore, the most of the thickness loss is due to the effect of chemical assisted cross-linking as described in the chapter 1.

4.5.4 Infrared-absorbance around 1000 cm^{-1} as a sign of active centers formation after He plasma exposure

The absorbance band around 1000 cm^{-1} as shown in Figure 4.12 indicates suboxide or strained ring formation in SiO_2-based materials [21,22]. In this section we discuss the IR absorbance at1000 cm^{-1} after studying plasma treatments using the differential FTIR spectroscopy. We presume that the evolution of the 1000 cm^{-1} peak might explain the damage reduction mechanism in the combined He + NH_3 treatment. We propose two possible explanations based on the differential FTIR spectroscopy measurements. The first is that the suboxide appearance after He plasma treatment might indicate an oxygen deficiency development. The oxygen deficiency might serve as a recombination center for NH_3 plasma radicals. The second possibility is that the NH_3 plasma radicals might react with strained rings, which are mainly formed on the top surface of the low-*k* film after He plasma treatment as described by equation (4-1). Therefore, fewer radicals penetrate the bulk of the low-*k* material. The strained rings play a major role in chemical reactivity and defect formation in porous SiO_2 based materials [22,23].

Figure 4.12 shows FTIR spectra of low-*k* film before and after exposure to the various plasmas. The top graph of the figure shows FTIR spectra of the as-deposited and the NH_3 plasma treated sample in the range of 800 - 1300 cm^{-1}. The FTIR spectra typical of SiOC:H-type materials contain an absorption band related to the Si-O-Si network (1040-1070 cm^{-1}), a shoulder of a cage-like structure (1100-1150 cm^{-1}), a suboxide absorption band (1000-1030 cm^{-1}) and an absorption band related to Si-CH_3 bonds (1250-1300 cm^{-1}). The SiOC:H film also contains bonds localized at 1200–1000 cm^{-1} from C–O–C, or Si–O–C asymmetric stretching vibrations[24]. However, the identification is difficult because they overlap with the Si–O–Si asymmetric stretching band. After the NH_3 plasma treatment, a clear shift to higher wavenumbers of the Si-O-Si absorption band is observed. This shift is also reflected in the differential spectrum (bottom graph). However, the characteristic changes are much smaller after He plasmas due to the small thickness of the modified layer of 10-20 nm (around 10% of the film thickness). Therefore, we used the differential FTIR to study the changes after successive exposure in He and NH_3 plasmas as shown in Figure 4.12 (bottom graph). The change in absorbance at 1275 cm^{-1} arises from Si-CH_3 groups [25], and decreases the most after the NH_3 plasma treatment.

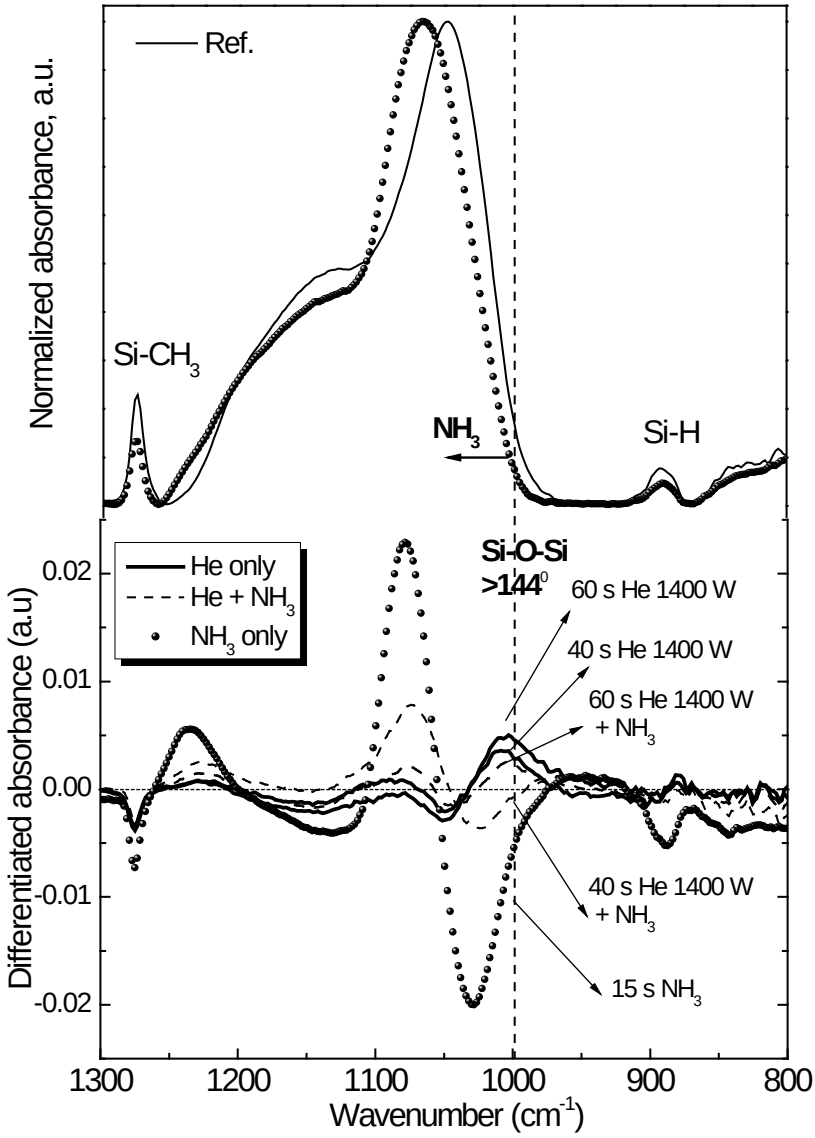

Figure 4.12 Absorbance and differentiated absorbance for He and/or NH_3 plasma treatments as measured by FTIR and differential FTIR, respectively.

The peaks of the differential spectra related to Si-O-Si have been reported elsewhere [22]. The negative peak located close to 1150 cm^{-1} is related to the Si-O-Si (angle ~ 150º) cage-like structure. The positive peak around 1070 cm^{-1} (angle ~144º) is related to the Si-O-Si network. The highest positive maximum of the network peak appears after pure NH_3 plasma. The peak around 1000 cm^{-1} arises from the Si-O-Si suboxide or/and strained silica rings (angle < 144 º). This peak appears after He plasma treatment. The amplitude of this peak increases with the

time of plasma treatment. The smallest amplitude appears after the successive exposure to He (60 s) and NH_3 (15 s) plasmas. To evaluate the effect of the plasma treatment, the amplitude change of 1000 cm^{-1} peak was estimated by the integration of differentiated absorbance using equation (4-2):

$$A_i = \int_{k=1030\ cm^{-1}}^{k=970\ cm^{-1}} A(k)dk \qquad (4\text{-}2)$$

where Ai is the integer of differentiated absorbance and k is wavenumber. The obtained results are shown in Figure 4.13.

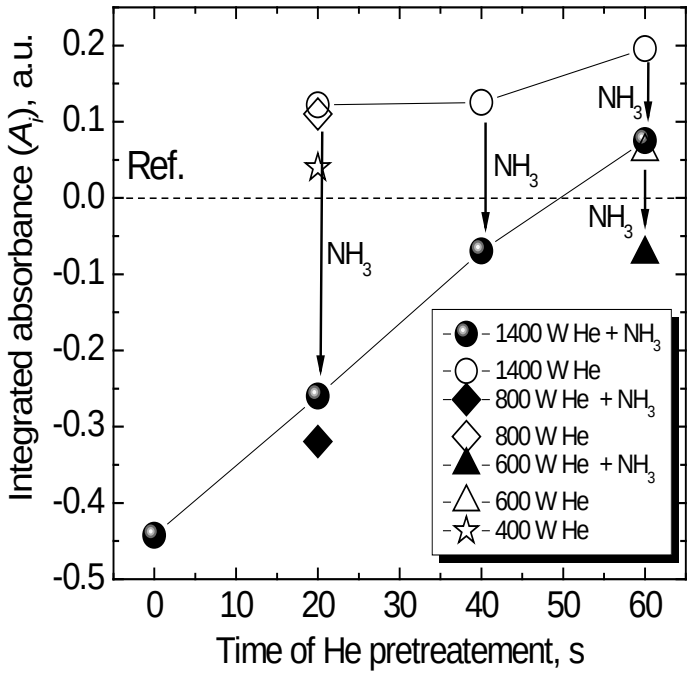

Figure 4.13. Integrated absorbance (*Ai*) versus plasma conditions. Arrows indicate the difference after subsequent NH_3 plasma treatment (after He plasma).

One can see that the A_i is always formed when the pure He plasma is applied (empty symbols). Moreover, the *Ai* grows with time and power of He plasma treatment. The absorbance peak around 1000 cm^{-1} disappears when the NH_3 plasma treatment is applied (as indicated by the arrows). The only exception is the 60 s He + 15 s NH_3 plasma treatment when the integrated absorbance (A_i) is still positive, and the film is fully sealed.

4.6 Chapter summary

The effect of the combined He and NH_3 plasma treatments on a CVD SiOC:H low-*k* dielectric is evaluated. The pure NH_3 plasma has a detrimental effect on the low-*k* material. The NH_3 plasma treatment leads to bulk hydrophilization of the low-*k* material.

The He plasma causes surface modification without damaging the bulk of the low-*k*. The major modifications caused by He plasma might be due to energy transfer from EUV photons and 2^1S He metastable atoms to the low-*k* structure.

The defects in low-*k* structure generated during the He plasma treatment trap chemically active radicals on the pore walls. Moreover the He plasma pre-treatment decreases the size of pore necks on the surface, which increases the collision frequency of chemically active radicals with the pore walls. The increased collision frequency increases the chance of radical recombination or chemisorption at the first surface monolayers. As a result, the He plasma pretreatment makes the low-*k* material more resistant to the subsequent treatment in the NH_3 plasma. The plasma damage reduction is proportional to the He plasma density which is proportional to rf power during the He plasma exposure. Furthermore, the low-*k* surface is sealed if the He pretreatment exceeds a critical level. The analysis of available literature data suggests that the threshold for plasma sealing in NH_3 and combined He + NH_3 plasmas depends on the type of low-*k* material and chamber used for the plasma treatment. A possible nature of the sealing capability of NH_3 plasmas might be related to the promoted cross-linking over the $-CH_x$ groups formed in He plasma where $-NH_x$ may serve as a bridge.

Differential FTIR spectroscopy might be used to monitor the pore sealing efficiency in the combined He + NH_3 plasma treatment. The amplitude of absorbance around 1000 cm^{-1} grows with time and power of the He plasma treatment. Subsequent NH_3 plasma treatment reduces the 1000 cm^{-1} absorbance. The only exception when the differential 1000 cm^{-1} peak is still positive is when the porous low-*k* film is fully sealed after the combined He + NH_3 plasma treatment.

4.7 References

[1] Y. Travaly, J. Van Aelst, V. Truffert, P. Verdonck, T. Dupont, E. Camerotto, O. Richard, H. Bender, C. Kroes, D. De Roest, G. Vereecke, M. Claes, Q. T. Le, E. Kesters, M. Van Cauwenberghe, J. Baynet, S. Kaneko, H. Struff, M. Baklanov, K. Matsushita, N. Kobayashi, H. Sprey and G. Beyer, in International Interconnect Technology Conference, IEEE Electron Devices Society, p. 52 (2008).

[2] A. Humbert, L. Mage, C. Goldberg, K. Junker, L. Proenca and J. B. Lhuillier, Mictroelectr., Eng., 82, 399 (2005).

[3] Y. H. Wang, D. Gui, R. Kumar and P. D. Foo, Electrochem. Solid-State Lett., 6, F1 (2003).

[4] K. Yanai, T. Hasebe, K. Sumiya, S. Oguni and k. Koga, Mat. Res. Soc. Bull., 863, B2.3 (2005).

[5] P. Verdonck, D. De Roest, S. Kaneko, R. Caluwaerts, N. Tsuji, K. Matsushita, N. Kemeling, Y. Travaly, H. Sprey, M. Schaekers and G. Beyer, Surface & Coatings Technology, 201, 9264 (2007).

[6] D. Shamiryan, M.R. Baklanov, and K. Maex, J. Vac. Sci. Technol. B 21 (1), (2003).

[7] W. Puyrenier, V. Rouessac, L. Broussous, D. Rebiscoul, and A. Ayral, Microporous and Mesoporous Materials 106, 40 (2007).

[8] D. Rebiscoul, L. Broussous, W. Puyrenier, V. Rouessac, and A. Ayral, J. Phys.: Conf. Series 152, (2009).

[9] N. Posseme, T. Chevolleau, T. David, M. Darnon, O. Louveau and O. Joubert, J. of Vacuum Science & Technology B, 25, 1928 (2007).

[10] H. G. Peng, D. Z. Chi, W. D. Wang, J. H. Li, K. Y. Zeng, R. S. Vallery, W. E. Frieze, M. A. Skalsey, D. W. Gidley and A. F. Yee, J. Electrochem. Soc., 154, G85 (2007).

[11] J. B. Peri, Journal of Physical Chemistry A, 70, 2937 (1966).

[12] G. A. Blomfiel and L. H. Little, Canadian Journal of Chemistry-Revue Canadienne De Chimie, 51, 1771 (1973).

[13] F. N. Dultsev, A. M. Urbanowicz and M. R. Baklanov, Plasma Modifications of Si-O-Si Bond Structure in Porous SiCOH Films, in Mat. Res. Soc., Mat. Res. Soc. Proc. (2008).

[14] R. S. Van Dyck, H. A. Shugart and C. E. Johnson, Phys. Rev. A, 5, 991 (1972).

[15] K. Yokogawa, Y. Yajima, T. Mizutani, S. Nishimatsu and K. Suzuki, Jap. J. Appl. Phys. Part 1-Regular Papers Short Notes & Review Papers, 29, 2265 (1990).

[16] T. Tatsumi, S. Fukuda and S. Kadomura, Jap. J. Appl. Phys. Part 1-Regular Papers Short Notes & Review Papers, 33, 2175 (1994).

[17] H. R. Philipp, in Handbook of Optical Constants of Solids, E. D. Palik Editor, p. 749, Academis Press, Orlando (1985).

[18] K. Kurihara, T. Ono, K. Kohmura, H. Tanaka, N. Fujii, N. Hata and T. Kikkawa, J. Appl. Phys., 101 (2007).

[19] T. Ono, N. Itabashi, I. Ochiai, S. Yamamoto and K. Mochiji, Jap. J. Appl. Phys. Part 1-Regular Papers Short Notes & Review Papers, 36, 6718 (1997).

[20] V. Jousseaume, A. Zenasni, L. Favennec, G. Gerbaud, M. Bardet, J. P. Simon and A. Humbert, J. Electrochem. Soc., 154, G103 (2007).
[21] A. Grill and D. A. Neumayer, J. Appl. Phys., 94, 6697 (2003).
[22] D. R. Hamann, Physical Review B, 55, 14784 (1997).
[23] H. Hosono, Y. Ikuta, T. Kinoshita, K. Kajihara and M. Hirano, Physical Review Latters, 8717, 4 (2001).
[24] A. Grill, V. Sternhagen, D. Neumayer, and V. Patel, J. Appl. Phys., 98, 074502 (2005).
[25] T. R. Crompton, The Chemistry of Organic Silicon Compound, p. 416, Willey, New York (1989).

5 Effect of He/H_2 downstream plasmas on low-*k* dielectrics

The results that are presented in this chapter have been partly published in:

A.M. Urbanowicz, K. Vanstreels, D. Shamiryan, S. De Gendt and M. Baklanov, Electrochem. Solid State Lett., 12, H292 (2009).
A.M. Urbanowicz, D. Shamiryan, P. Marsik, Y. Travaly, A. Jonas, P. Verdonck, K. Vanstreels, A. Ferchichi, D. De Roest, H. Sprey, K. Matshushita, S. Kaneko, N. Tsuji, S. Luo, O. Escorcia, I. L. Berry, C. Waldfried, S. De Gendt and M. R. Baklanov, in Mat. Res. Soc. Proc. of Adv.Met. Conf., p. 594 (2009).
A.M. Urbanowicz, D. Shamiryan, A. Zaka, P. Verdonck, S. De Gendt and M. Baklanov, J. Electrochem. Soc., 157, H565 (2010).
A. M. Urbanowicz, M. Cremel, K. Vanstreels, D. Shamiryan, S. De Gendt and M. R. Baklanov, "Mechanism of k-value Reduction of PECVD Low-*k* Films Treated with He/H_2 Ash Plasma", in PESM, 5-6 March, Grenoble, France (2010).
K. Vanstreels and A. M. Urbanowicz, J. Vac. Sci. Technol. B, 28, 7 (2010).

5.1 Introduction

One of the most critical challenges during the integration of porous low-*k* dielectrics in ULSI devices is their degradation during ash plasma treatments as discussed in chapter 1. The removal of a carbon-based photo-mask on the top of carbon containing low-*k* materials brings selectivity problem. Both low-*k* dielectric and photo mask contain C-H bonds. Therefore chemistries used to remove photo mask also removes the carbon containing hydrophobic groups from low-*k* material. Further moisture adsorption leads to the film degradation as discussed in section 1.7.1. In addition, the damage caused by ion or UV radiation during plasma processing can also be problematic. Although these effects are discussed in many papers, the dominant factors of plasma damage are still a subject of intensive discussions as shown in Table 5.1. The table contains the topical literature search about the effect of oxidizing or reducing plasma chemistries on low-*k* structure. It has been shown that O_2-based plasmas cause damage, manifested as undesirable chemical modification (Si-CH_3 group removal), while H_2-based plasmas show a variety of different effects on low-*k* films. Some authors report no effect in low-k films, which others report, that plasma processes enhances the film properties, and yet others indicate severe damage.

Table 5.1 Summary of the topical literature search about oxidizing and reducing ash plasmas effect on blanket low-*k* films. 25 papers were selected using key words: ash, plasma damage, low-*k*.

Plasma chemistry	Extent of damage	Amount of papers	Reference number
Oxidizing	Severe damage	16	1,2,3,4,5,6,7,8,9,10,11,12,13,14,15,16
Reducing	Severe damage	11	1, 5 ,7, 8,11,17,18,19,20,21
	No damage	5	16,22 ,23,24
	Improvement	1	25

The results of this literature study can be reflected on a bar graph as shown in Figure 2.1. The different reported results are due to a wide range of plasma chambers used by the authors. Three main types of the chambers are used for photoresist ash; ICP, CCP and downstream plasma systems (see section 2.2.1). In the first two systems the low-*k* wafer interacts directly with the rf-plasma, therefore physical or physicochemical interactions always play a role. In contrary, downstream plasma (DSP) systems involve only pure chemical interactions. The plasma source (usually microwave) is separated from the wafer area by a special grid. This grid neutralizes electrically charged species (electrons and ions) and also UV-light. Therefore only the afterglow of the plasma interacts with the wafer. Authors who report no damage or even improvement of low-*k* film used DSP systems. Those effects are reported for afterglows of the following plasmas: H_2 or mixture of H_2 with noble gases such He and Ar.

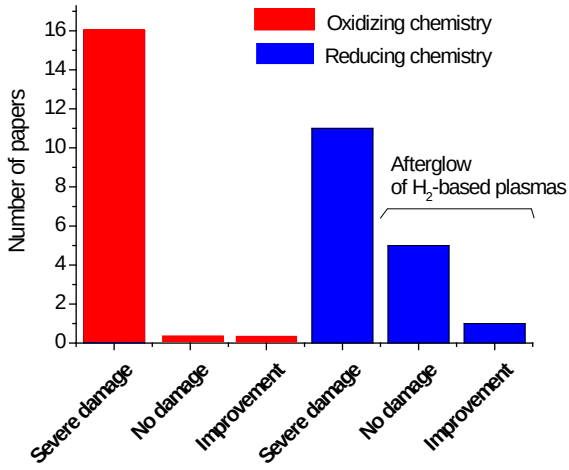

Figure 5.1 Summary of ash plasma chemistry effect on low-k films on the basis of literature search in Table 5.1.

Taking into account the type of plasma system used for the resist removal in the Cu/low-*k* integration process can be divided into two approaches:

- a low temperature, low pressure, anisotropic plasma process, where the photoresist is removed by an ion-assisted physical process, using oxidizing or reducing plasma chemistries at low temperatures (CCP and ICP chambers)
- an isotropic DSP using a He/H_2 gas mixture where the resist is removed at high temperatures by a thermally activated chemical process [26,27] (downstream chambers).

Normally, the usage of CCP or ICP chambers for ash (ion-assisted processing) is a more cost effective solution, because those chambers are also used for dielectric etch and other processes that requires ion-assisted interactions. Contrary to CCP and ICP chambers, the downstream systems cannot be used for etching as this requires directionality that can be only provided by an ion-assisted process (ref. Section 2). However, the main advantage of the ion-free chemical processing is selectivity that is the major requirement for a low-*k* damage-free ash process.

In this chapter the effect of DSP photo resist strip approach is discussed in details with focus on He/H_2 ash plasmas. The effect of DSP chemistry, process temperature, and treatment time is investigated. The following matters are dealt with:

- Effect of DSP chemistry including O_2, H_2, N_2/H_2, N_2, He/H_2 plasma afterglows at constant time and temperature
- Substrate temperature effect during He/H_2 plasma afterglow treatments
- Time effect of He/H_2 plasma afterglow at constant temperature

5.2 Experimental

The films used in this chapter were described in Table 2.2. The films were treated in two microwave DSP chambers (Table 2.1). The first chamber was Lam 2300 Asher used in sections 5.3 and 5.5. The second chamber was Radiant Strip320LK used in section 5.4. The experimental parameters for Lam microwave stripper are summarized in Table 5.2. Six different DSP strip conditions (He, H_2, O_2, N_2, He/H_2, H_2/N_2) were studied in section 5.3. Additionally, control wafer was annealed for the same time as DSP treated samples (heat up) to check the temperature effect. Furthermore, varied He/H_2 DSP exposure times (20 s -700 s) of low-*k* films were studied in section 5.5.

The temperature effect of He/H_2 20:1 DSP treatment reported in section 5.4 were performed using Radiant Strip320LK. The time of 35 s was used for all treatments of Ea films. The four treatment temperatures were studied: 20 ºC, 200 ºC, 300 ºC, 350 ºC.

Table 5.2 Summary of experimental conditions for differently treated low-*k* films (Table 2.2) in Lam microwave stripper (Table 2.1). Table shows the main parameters during processing of the low-*k* films. The wafer temperature of 280 ºC, microwave power of 2000 W, and pressure of 133 Pa were constant for all experiments in sections 5.3 and 5.5 . The constant time of 35 s of He/H_2 DSP was used all treatments in section 5.3, while varied times (20 s -700 s) were used in section 5.5.

Treatment	Gas ratio	Gas flows [sccm]	Temp. [ºC]	Pressure [Pa]	Time [s]
Heat Up	-	-	280	-	35
He	-	4200	280	133	35
H_2	-	950	280	133	35
He/H_2	20:1	4000/200	280	133	20-700 s
N_2/H_2	24:1	1900 (mixture H_2/N_2)	280	133	35
N_2	-	1900	280	133	35
O_2	-	950	280	133	35

5.3 Effect of afterglow plasma chemistry

We studied the effect of plasma chemistry on low-*k* materials using afterglow of microwave plasma at elevated temperatures. The time of afterglow plasma treatments and wafer temperature were kept the same for all experiments. The thermal annealing and afterglow of He, H_2, He/H_2, N_2, N_2/H_2, O_2 plasmas effects at 280 ºC were investigated. Results show that modifications are minimal for treatments using thermal annealing and annealing in pure He plasma afterglow. Furthermore, the hydrogen radicals from He/H_2 and H_2 DSPs induce no damage on the low-*k* films, showing no $Si\text{-}CH_3$ group depletion and no hydrophilization. However, the increased porosity and mass loss were observed. The depth of modification measured on the basis of optical properties of modified film by spectroscopic ellipsometry was 50 % larger for He/H_2 plasma afterglow than for H_2 treatment. By contrast, the mixtures of H and N radicals and O radicals have detrimental effect on the low-*k* dielectrics, showing carbon depletion ($Si\text{-}CH_3$ group loss) and subsequent hydrophilization. We found that the best known strip chemistry is He/H_2 plasma while the worst ones are the afterglows of N_2/H_2 and O_2 plasmas. The findings confirm the literature study that after-glow of H_2-plasmas do not degrade film's *k*-value and shows that H_2 and He/H_2 cause unexpected mass loss of the film without their thickness reduction.

The results of all experiments are summarized in Table 5.3. First, those data are discussed in more general perspective. Next, the effects of O_2, H_2, He/H_2, N_2, N_2/H_2 plasma chemistries are discussed in greater details and compared with literature. Finally the model of plasma modifications is proposed on the basis of analysis of the obtained data.

5.3.1 Discussion of the obtained data in general perspective

The plasma damage of the low-*k* dielectrics results in their hydrophilization and densification after plasma exposure as discussed in chapter 1. The hydrophilization of the films is reflected in reduced WCA measured by water-based goniometry and increased water absorption measured by water-based EP. The densification of the films is reflected in decrease of porosity measured by EP and the increase of the Young's modulus of the film measured by nano-indentation. The mass change before and after treatment is measured by mass balance metrology on 300 mm wafers. The mass gain (denoted by "+") of the films is due to its hydrophilization, while mass loss (denoted by "-") might be due to film etching or removal of its organic part. The thickness loss of the films measured by UV-SE might be related to both: etching or shrinkage/densification of the films by studied treatments.

Table 5.3 The properties of dielectric material Ea before and after 35 s of after-glow plasmas and heat treatments. The abbreviations WCA and YM denote water contact angle and Young's modulus, respectively. Furthermore, AW is amount of absorbed water as measured by WEP at SVP and MD is film modification depth as measured by SE. MAS denotes mass difference before and after treatment.

Chemistry	**WCA**	**AW H_2O**	**MAS**	**Thick. Loss**	**Open Porosit**	**YM**	**MD depth**
	deg	[%]	[mg]	[%]	[%]	GPa	[nm]
Reference	95	3.0	-	0	32	4.48	0
Heat only	103	3.0	- 0.20	0	31	4.42	0
O_2	0	25.0	+ 1.06	23	25	10.65	140
N2	59	13.5	+ 0.52	2	30	5.00	2
H_2/N_2 24:1	27	20.0	+ 0.12	14	29	7.09	65
He	87	3.0	+ 0.04	0	31	4.47	0
H_2	102	2.7	- 0.40	1	41	3.75	30
He/H_2 20:1	90	2.6	- 0.51	1	46	3.49	45

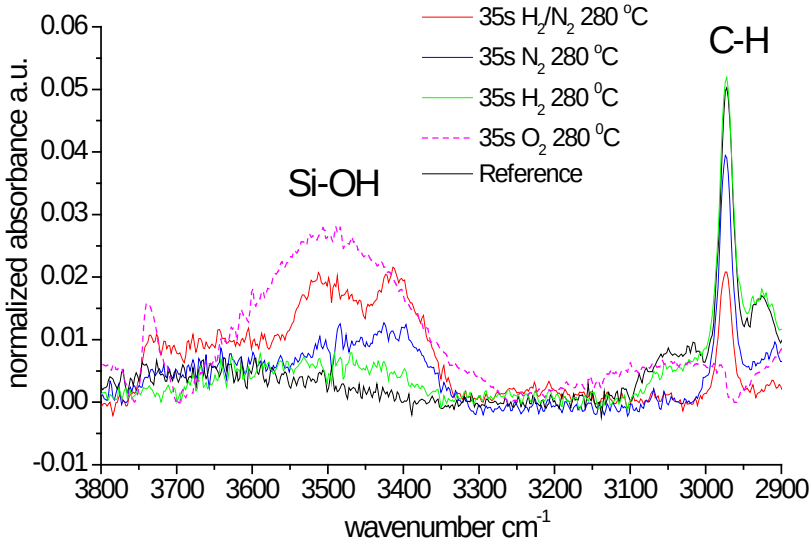

Figure 5.2 FTIR spectra in the range of 3800 cm^{-1} to 2900 cm^{-1} of as deposited Ea films and films treated with afterglows of N_2, O_2, H_2 and H_2/N_2 plasmas.

Furthermore, the damage depth can be evaluated by UV-SE when the optical contrast (difference in refractive index and extinction coefficient) between the damaged and the non-damaged layer is sufficiently high. The damage depth reflects how much of the bulk of the film is modified. Analysis of all characteristic shown in Table 5.3 allows us to depict real effect of plasma on low-*k* films. Considering hydrophobic properties, the studied films can be divided in the two groups. The first group contains the films that remained hydrophobic after thermal annealing and He, H_2, He/H_2 plasma AFTs. Those films show WCA higher than 87 degree and less than 3.0 % of water absorption at 100 % humidity. The second group contains the films hydrophilized after O_2, N_2/H_2, N_2 plasma AFTs. The films have WCA less than 59 degree.

The bulk of those films is hydrophilized as measured by water-based EP. The degree of bulk hydrophlization is varied from O_2 where 100 % film bulk is hydrophilized (film volume filled with H_2O is equal to open porosity) to N_2 where degree of hydrophilization is around 50 %. The hydrophilization degree starting from maximal is the following: O_2> N_2/H_2> N_2. The hydrophilization degree also correlates with OH group amplitude as shown in Figure 5.2. Moreover, degree of the film hydrophilization and OH group amplitudes correlate with reduction of absorption bands related to Si-CH_3 groups as shown in Figure 5.3.

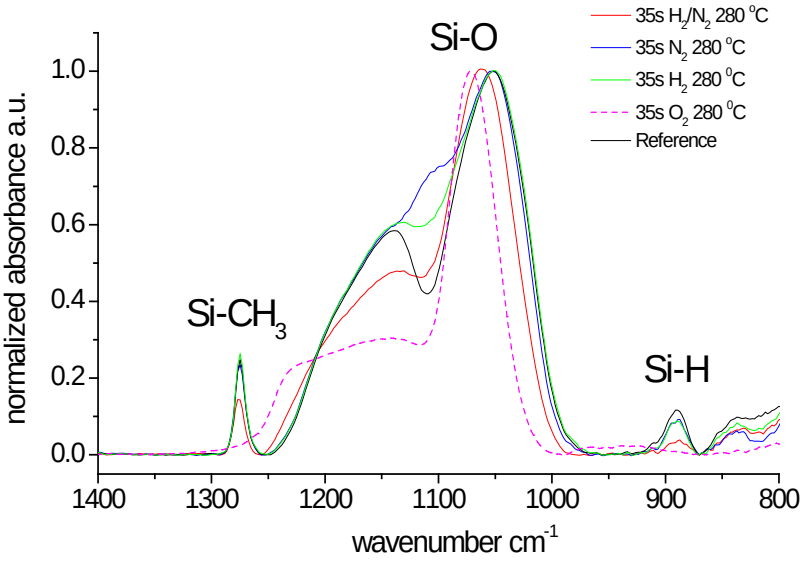

Figure 5.3. FTIR spectra in the range of 1400 cm^{-1} to 800 cm^{-1} of as deposited and films treated with afterglows of N_2, O_2, H_2 and H_2/N_2 plasmas.

If we further analyse hydrophobic films we can clearly see that the films treated with H_2 and He/H_2 plasma afterglows show different behaviour than the annealed and He afterglow treated ones. The films treated with H_2-based plasma afterglows show mass loss with minimal thickness loss accompanied with porosity increase and YM reduction. This indicates that some material is removed from the films without film etching or hydrophilization. The latter phenomenon is due to porogen residue removal by H radicals that is investigated in the next chapter. In the next paragraphs the detailed mechanism of radical's interaction with low-k films is discussed.

5.3.2 Effect of O radicals

As proposed by Chang et al. [28], modification of the OSG in O_2 plasma occurs via the overall reaction (3-1) where ≡Si designates Si bonded to three lattice O's.

$$\equiv Si\text{-}CH_3 + 4O \rightarrow \equiv Si\text{-}OH + CO_2\uparrow + H_2O \qquad (5\text{-}1)$$

$$\equiv Si\text{-}OH + OH\text{-}Si\equiv \rightarrow \equiv Si\text{-}O\text{-}Si + H_2O \qquad (5\text{-}2)$$

Reaction (5-1) is thermodynamically favorable and the degree of damage in an oxygen plasma is always expected to be high. The enthalpy for this reaction (ΔHr) is−994 kJ/mol calculated at 298 K as reported by Worsley et al. [29]. Modification of OSG by oxygen radicals results in the formation of Si-OH groups

(Figure 5.2) with removal of Si-CH_3 groups (Figure 5.3). Hydrophilic SiOH groups can either induce moisture absorption or react between each other to form SiOSi absorption band as described by reaction (5-2). The cross-linking of the film as result of reaction (5-2) leads to film shrinkage and is reflected in thickness loss and porosity decrease as shown in Table 5.3. Moreover, other possibilities can be considered that lead to film shrinkage. For instance, the bond breakage caused by O radicals that occur within the SiCOH matrix results in the formation of activated silyl sites. The activated silyl sites are then available to react with other activated silyl species to form Si–Si crosslinks or possibly with Si-OH to generate a Si-O-Si crosslink as described in section 1.7.3.

5.3.3 Effect of H radicals

The effect of H radicals on low-*k* films has been extensively studied and is well documented (see Table 5.1) because of the wide applications of the hydrogen-based plasmas for the resist strip and post-dry-etch cleaning (see chapter 1). However, the H_2-based plasmas are reported in literature to cause many different effects as discussed in section 5.1. Some groups report H_2-plasmas have no effect on the SiOC:H film [22,23] others report that it enhances the dielectric properties [25] and yet others indicate that H_2 plasmas cause significant damage [5,30]. Thus, a detailed analysis of the mechanisms involved in H_2-plasma modifications in necessary to understand the different findings reported in the literature. The reaction describing interactions of H radicals with Si-CH_3 groups from low-*k* material were proposed in literature [5, 31]. The replacement of -CH_3 groups by H atoms with a formation of more polar Si–H groups (5-3) and the breakage of Si–O–Si groups with a formation of hydrophilic silanol groups (5-4) were proposed. The enthalpies at 298 K (ΔHr) of exothermic reaction (5-3) were reported ΔHr = -411 kJ/mol by Worsley et al. [5] and ΔHr = -418 kJ/mol by Posseme et al.[31], respectively. Furthermore, enthalpies at 298 K of reaction (5-4) ΔHr = -325 kJ/mol by Worsley et al. [5].

$$\equiv Si\text{-}CH_3 + 2H \rightarrow \equiv Si\text{-}H + CH_4\uparrow \qquad (5\text{-}3)$$

$$\equiv Si\text{-}O\text{-}Si\equiv + 2H \rightarrow \equiv Si\text{-}H + Si\text{-}OH \qquad (5\text{-}4)$$

The negative enthalpy at 298 K of the reaction (5-3) proposed in the literature indicates that reaction is exothermic and presumably possible at room temperature. However, the thermodynamics do not dictate reaction kinetics. Indeed, detailed analysis of the available data (FTIR) shows that the ability of the H_2-based plasma to break Si–CH_3 bonds strongly depends on experimental conditions. According to our study, H radicals formed in afterglows of H_2 and He/H_2 plasmas do not reduce the concentration of Si–CH_3 groups at the temperature of 280 ºC as shown in Figure 5.3. Moreover, this observation agrees well with the literature data, demonstrating no low-*k* damage in afterglow of H_2, He/H_2, and He/Ar plasmas [22,25,31]. However, if certain additional activation is provided, for instance, by ion radiation and UV light, this makes these reactions possible, causing the difficulty to realize damage-free processes in the reactive ion etching (RIE) condition [25,32]. For instance, Matshushita et al. [25] showed that the damage during the H_2 plasma treatment depends on the type of chamber used. The processes were damage-free in

the ion-free discharge. The effect of charged species from H-plasmas for cleaning in the pressure range of 200–400 mTorr was also discussed by Fu et al.[33]. The authors compared the H_2 plasma effect on low-*k* with and without plasma leakage reduction (PLR) hardware to reduce the plasma density. They found no Si–CH_3 depletion only when the PLR hardware was used. Similar work and conclusions have also been presented by Lazzeri et al. [30]. In order to prove the arguments below we also exposed film Ea (see Table 2.2) at 200 mTorr H_2 plasma in RIE conditions using Lam Excelan CCP reactor (see Table 2.1). It is evident from FTIR spectra shown in Figure 5.5 that Si-CH_3 bonds are removed when the wafer is immersed in the plasma in CCP reactor. In this case UV light, H+ ions, electrons also play role in low-*k* dielectric modification.

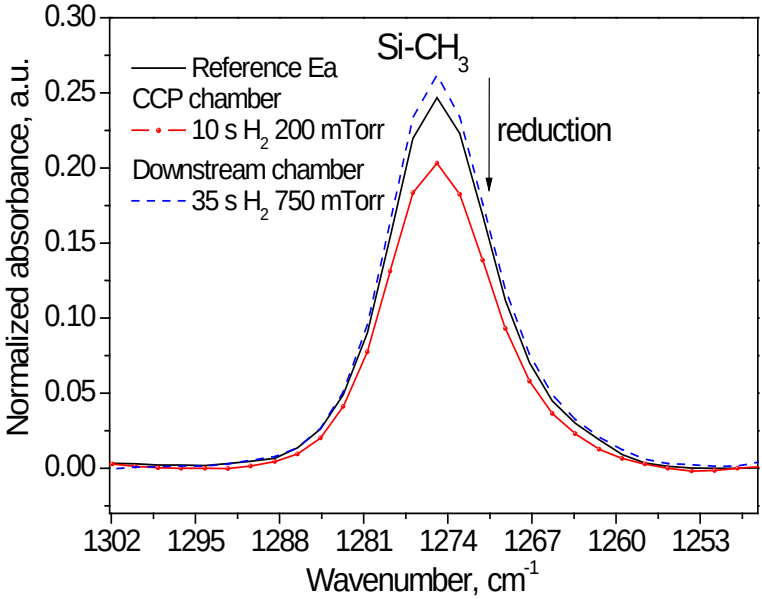

Figure 5.4. FTIR spectra in the range of 1400 cm^{-1} to 800 cm^{-1} of as deposited and films treated Ea film exposed in H_2-plasma in CCP reactor (Lam Exelan 2300 in Table 2.1).

5.3.4 Differences between H_2 and He/H_2 plasma afterglow treatments

We have found that H_2 and He/H_2 mixtures have similar effect on the Ea film structure except that the latter treatment results in higher depth of the film modification. After both treatments neither Si-CH_3 group depletion (Figure 5.3) nor hydrophilization is observed (Table 5.3). The major difference is the depth of modification because of porogen residue removal. (see section 5.4). The depth of modification was measured by Spectroscopic Ellipsometry. The double layered structures were observed after the H_2-based afterglow plasma treatment. The

thicknesses of the modified layers were 45 nm and 30 nm for He/H_2 and H_2-plasma afterglow treatments, respectively. Moreover, we performed removal rate test of bulk material for both treatments: aliphatic-C based photo resist mask. We found that a photo resist removal rate of 24 nm/s for H_2 and 30 nm/s for He/H_2 mixture. We argue that the higher removal depth of porogen residue and higher photoresist removal rate are due to higher concentration of H radicals achieved from He/H_2 20:1 microwave discharge.

In order to prove our above statement, we postulate that only H radicals interact with the film at 280 ºC and any effects related to UV-light or metastable atoms (i.e. He) from plasma area are excluded. The UV-light and metastable atoms (i.e. from He) effect is cancelled by the design of the plasma chamber (special grid and distance of plasma area from the wafer area). In order to demonstrate this experimentally we exposed Ea films to He based AFT at 280 ºC and compared this with film annealed at 280 ºC (see Table 5.3). No significant changes were observed. The film surface remains hydrophobic. Moreover UV-SE measurements do not reveal any densification of the top layer. In summary, the experiments show that physical plasma effects are negligible in our plasma system. Therefore, the kinetics of the reaction of porogen residues or C-based photo resist mask with H radicals is dictated by Arrhenius law. This inclines that two key process parameters should determine the reaction kinetic: wafer temperature and concentration of H radicals. The wafer temperature was the same for both He/H_2 and H_2 plasma afterglow treatments. Therefore radical concentration should play a key role. Higher concentration of H radicals in He (95%)/(5%) H_2 mixture might be explained by increase of average He* concentration using the dilution of reactive gas (H_2) with noble gas and thereby diminishing the electron energy losses on rotational-vibrational excitation of H_2 molecules [34]. Similar findings about microwave discharges based on He or Ar mixtures with H_2 were reported elsewhere [35,36,37,38]. In the next chapters the He/H_2 20: 1 mixture is used.

5.3.5 Effect of N radicals

The effect of *N* radicals has been studied in the literature [31, 39]. It was shown that N_2-plasma damages only the top surface of low-*k* materials and makes it hydrophilic. This is also demonstrated by our results as shown in Table 5.3. The WCA is reduced from 95 deg to 59 degree which reflects surface hydrophilization. Moreover some part of the film bulk is also hydrophilized as measured by WEP (see section 2.5.2.2). The amount of absorbed water increased from 3 % to 14.5 %. This shows that for film of 30 % open porosity almost 50 % of open pore volume is hydrophilized. The bulk hydrophlization is also evident in mass gain (Table 5.3) and increased absorbance of –OH groups (Figure 5.2). Moreover, in contrast to O_2-based and H_2-based plasma afterglows some nitrogen incorporation in the surface area has also been observed for N_2-based treatments. The appearance of C-N and N-H_2 bonds can be demonstrated in the FTIR absorption bands in the range of 1500 to 1700cm^{-1} as shown in Figure 5.5.

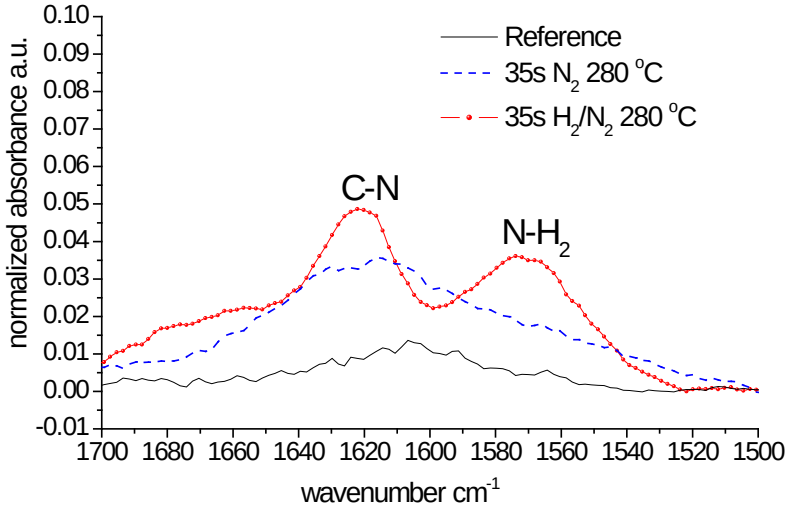

Figure 5.5. FTIR spectra in the range of 1700 cm^{-1} to 1500 cm^{-1} of as deposited and films treated with afterglows of N_2 and H_2/N_2 plasmas.

5.3.6 Combined effect of H and N radicals

The H radicals are shown to have negligible effect on Si-CH_3 bonds, furthermore the film hydrophilization is not observed. The N radicals have much lower effect on low-*k* materials showing small degree of the Si-CH_3 group removal and hydrophilization. However, a mixture of N_2 and H_2 radicals has detrimental effect on the low-*k* films. This is presumably due to increased amount of possible reaction pathways that leads to the film hydrophilization. One of the possible hydrophilization mechanisms is the replacement of Si–CH_3 bonds by Si–NH_2 bonds, which are in turn replaced by Si–OH bonds (the latter as result of hydrolysis with ambient moisture). The reactions that results in the Si-NH_2 bond creation are described by equations (5-5) and (5-6). The existence of NH_2 bond is proven by FTIR as shown in Figure 5.5. The next step in the hydrophilization mechanism is hydrolysis of the Si–NH_2 groups described by the reaction (5-7) that was proposed by Posseme et al.[31]. The hydrolysis of Si-NH_2 bonds can be proven by measurement (ie. FTIR or XPS) under vacuum conditions directly after film treatment and comparison with measurement of the film that was exposed to air. This test was demonstrated in literature by Posseme et al. [31] using in situ and *ex situ* X-ray photoemission spectroscopy analyses. The nitrogen content in low-*k* films treated in NH_3-RIE plasma has been strongly reduced after air exposure, and the surface became hydrophilic.

$$\equiv Si\text{-}CH_3 + NH_2 + H \rightarrow \equiv Si\text{-}NH_2 + CH_4\uparrow \quad (5\text{-}5)$$

$$\equiv Si\text{-}CH_3 + N + 3H \rightarrow \equiv Si\text{-}NH_2 + CH_4\uparrow \quad (5\text{-}6)$$

$$\equiv Si\text{-}NH_2 + H_2O \rightarrow \equiv Si\text{-}OH + NH_3\uparrow \quad (5\text{-}7)$$

$$\equiv Si\text{-}O\text{-}Si\equiv + NH_2 + H \rightarrow \equiv Si\text{-}NH_2 + \equiv Si\text{-}OH \quad (5\text{-}8)$$

$$\equiv Si\text{-}O\text{-}Si\equiv + N + 3H \rightarrow \equiv Si\text{-}NH_2 + \equiv Si\text{-}OH \quad (5\text{-}9)$$

An additional supportive argument of Si-NH_2 bond hydrolysis is the value of the enthalpy of reaction (5-7), $\Delta Hr = -258$ kJ mol^{-1} at 298 K [31]. This explains the Si-CH_3 group removal (Figure 5.3) and the film hydrophilization (Figure 5.2 and Table 5.3). The other possible hydrophilization mechanism of low-*k* films is NH_x, H and N radicals' interaction with Si-O bonds that are described by reactions (5-8) and (5-9).

5.3.7 Model of the film modifications

As a summary we propose a simplified scheme of our experimental results as shown in Figure 5.6. We divided the effects of the studied treatments on low-*k* structure into four groups. The first group consist of the treatments which have negligible effect on the low-*k*: annealing in N_2 gas and He plasma afterglow treatment. In the second group are He/H_2 and H_2 plasma treatments. Results showed no thickness and hydrophobicity loss, no Si-CH_3 scission and PR removal which results in higher porosity. By comparing the optical properties, the modified layer by H_2-based plasma has lower refractive index due to increased porosity and lower extinction coefficient due to porogen residues removal. For the He/H_2 mixture, He addition in H_2 chemistry increase depth of modification of the low-*k* material. The third group is the H_2/N_2 treatment. The film treated with N_2/H_2 plasma shows thickness loss with hydrophilization, carbon depletion and porosity reduction in 65 nm of damaged layer. It demonstrates that the H_2/N_2 mixture treatment has enhanced damaging effect compared to N_2 only, which may be caused by formation of NH_x radials. The NH_x radicals can increase the amount of possible chemical reactions which lead to damage of the low-*k* structure as discussed above. And finally the forth group is damage related to O radicals. The whole bulk of the film is hydrophilized and all Si-CH_3 bonds are removed from the material. The reduced porosity and increased YM and 24% of thickness loss indicate severe film shrinkage.

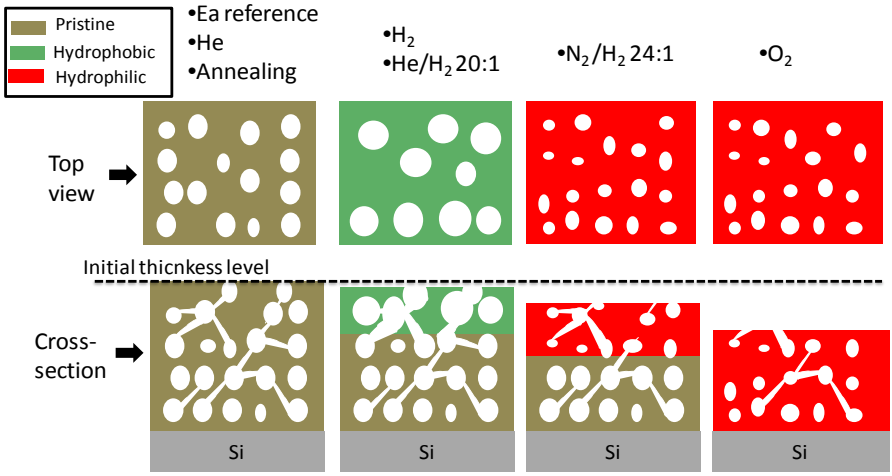

Figure 5.6. Simplified scheme of structural changes induced to Ea film by the following treatments: annealing at 280 ºC and afterglows of He, H_2, He/H_2 20:1, N_2/H_2 24:1, O_2 microwave plasmas. The model shows total thickness of modified layer, the possible gradient of density is not included. The N_2 DSP modifications are similar to N_2/H_2 DSP however the modification extent is lower.

5.4 Temperature effect of He/H_2 afterglow

Different substrate temperatures have been investigated for the He/H_2 process on advanced porous low-*k* materials. The results show that extended He/H_2 DSP (downstream-plasma) exposure may lead to *k*-value reduction due to porosity increase without hydrophilization of the modified layer. The porosity increase is explained by porogen residue removal from low-k films during ash processes. Four temperatures were used for the study: 25 ºC, 200 ºC, 300 ºC and 350 ºC. It is shown that He/H_2 DSP induced modifications depends strongly on temperature. This strip is compared with the conventional low-temperature-anisotropic strip using 10 s of O_2 plasma exposure.

5.4.1 Hydrophobic properties

Hydrophobic properties were evaluated using three metrology techniques (see section 2.5) : (1) Water contact angle (WCA) to determine surface hydrophobic properties, (2) Water-based Ellipsometric Porosimetry (WEP) [40], to determine hydrophobic properties of the pore network, and (3) Fourier Transform Infrared

Spectroscopy (FTIR), to determine the absorbance of H_2O and –OH groups and to possibly detect carbon depletion.

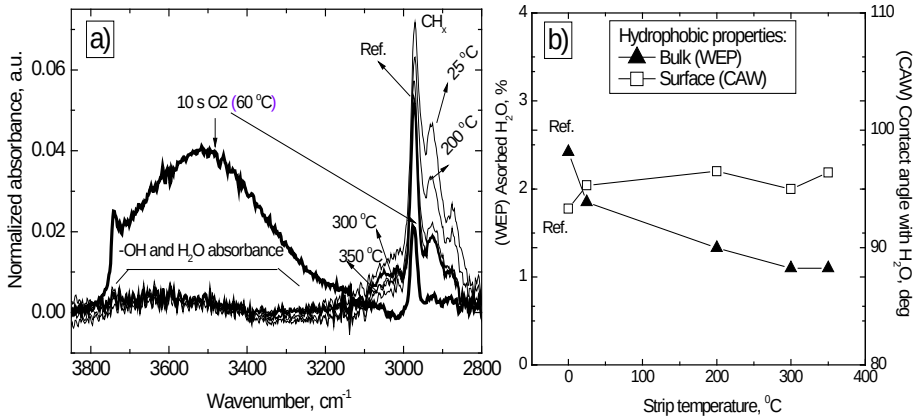

Figure 5.7. The -OH and CH_x groups absorbance as measured by FTIR (a) bulk and surface hydrophobic properties as measured by WEP and WCA, respectively (b) of as deposited and plasma treated films.

All three methods confirm that the He/H_2 DSP exposure results in no hydrophilization of the porous low-*k* films. The water contact angle for He/H_2 DSP treated films was determined to be around 90° (equivalent to the pristine films) and the amount of absorbed water is less than 2%, which is even smaller than that of the pristine film, as measured by WEP (Figure 5.7b). The absorbance of H_2O and –OH groups as well as Si-CH_3 (C-H originated from Si-CH_3) groups are the same or higher as for the pristine film (Figure 5.7a). The higher CH_x groups absorbance at 25 ºC and 200 ºC might be related to residual photoresist deposition from processing chamber walls (the low-k is the coolest surface in the chamber for temperatures below <200 ºC). An FTIR spectrum of the same film treated with the low pressure anisotropic O_2 plasma is added for comparison and shows significant increase in H_2O and –OH groups.

5.4.2 Structural modification

Time of Flight Secondary Mass Spectroscopy (TOF-SIMS) (Figure 5.8a) and SEM analysis (Figure 5.8b) shows that the Ea films treated at higher temperatures exhibit a double-layer structure. Moreover TOFSIMS reveal a lower C-content in the top layer. However, the C-depletion is one order of magnitude less than in the case of the anisotropic O_2 plasma exposure. It is presumed that this depletion is due to residual porogen removal. This postulate is supported by FTIR results that show no Si-CH_3 group loss (Figure 5.8c), and by Spectroscopic Ellipsometry (SE) measurements showing the disappearance of absorption peaks that are attributed to porogen signatures [41] upon the H_2/He DSP treatment. TOF-SIMS also indicates that the time required to sputter the film after the He/H_2 DSP treatments at 300 ºC and 350 ºC is reduced. This could, in principle, be due to a decrease in thickness or the result of reduced film density.

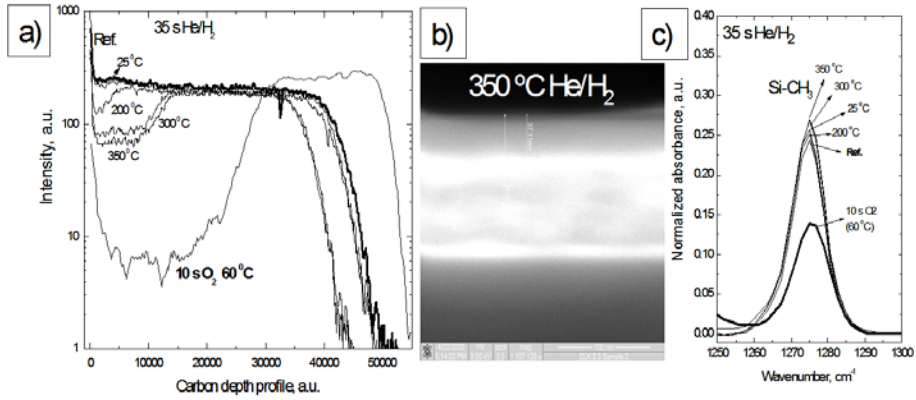

Figure 5.8. TOFSIMS depth profile for as deposited Ea (see Table 2.2) and treated Ea films (a) SEM of 35 s He/H_2 DSP at 300 ºC treated film Ea. No treated film Ea does not have double-layer structure (b) The $Si-CH_3$ groups absorbance as measured by FTIR for the same films as for TOFSIMS (c).

Three metrology methods, X-Ray Reflectometry (XRR), Ellipsometric Porosimetry (EP) and SE, were applied to probe if the top layer is thinner or less dense, and all three methods indicate a lower density of the top layer. XRR determined a lower critical angle (θ_c) for the He/H_2 DSP treated films at 300 ºC and 350 ºC, signifying lower density of the top layer (Figure 5.9b). A lower density of the top layer should translate into a higher total open porosity of the film. This was indeed confirmed by EP, which concluded higher porosity (Figure 5.9a) and bigger mean pore radius of 1.3 nm of the films treated at 300 ºC and 350 ºC. Increased porosity and pore size translate into higher toluene diffusion rates inside the low-*k* films (Figure 5.9c). The toluene diffusion was measured as described in literature [42]. The sharp increase in toluene diffusivity is related to higher porosity and pore interconnectivity of the top modified layer.

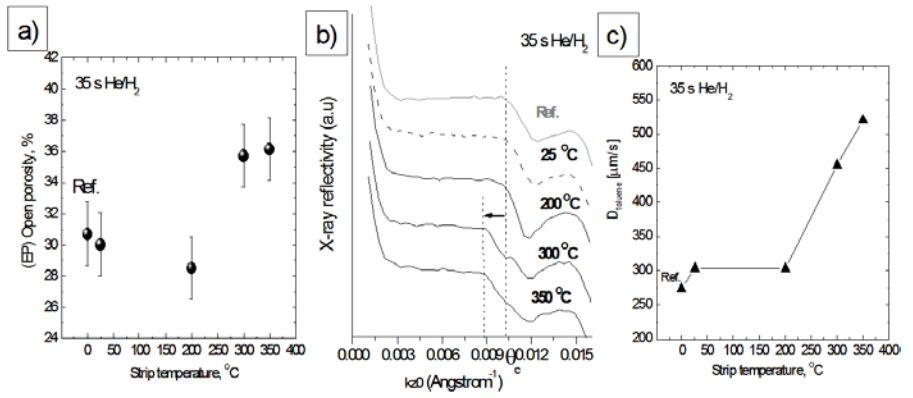

Figure 5.9 The open porosity as measured by EP (a), the X-ray reflectivity as measured by XRR(b), toluene diffusion coefficient (c)

The structural modifications and density changes are also reflected in optical properties of the film. The modifications can be divided into two groups (Figure 5.10a). The first group consisted of temperatures up to 200 ºC when PR removal is very limited and changes might be due to organics deposition and/or diffusion from the reactor chamber walls. The second group is for the temperatures of 300 ºC and 350 ºC when the depth of modification is higher. Both the refractive index and the extinction coefficient of the top layer are lower than those of the bottom layer (which was presumed to be unchanged in the as deposited film) indicating PR removal (Figure 5.10b).

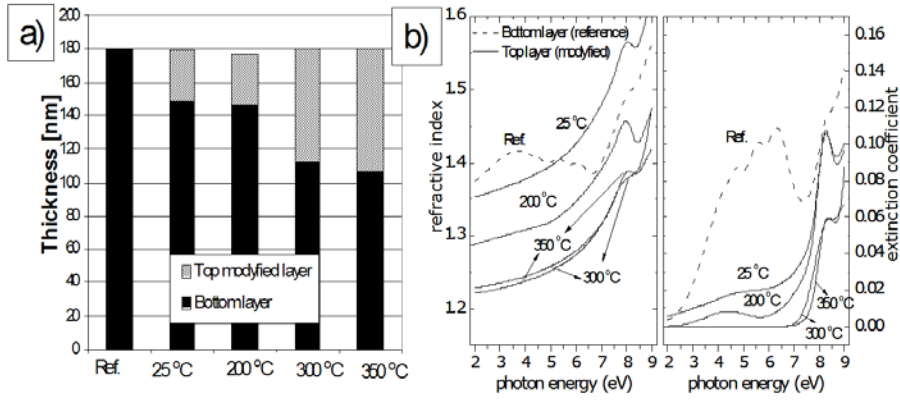

Figure 5.10. The thickness (a) and optical properties (b) of the top and bottom layer of Ea (see Table 2.2) and Ea He/H_2 treated films at different temperatures as measured by SE.

It is important to understand the mechanism of removal of the porogens in H_2-AFT. We propose that the porogen removal mechanism at high temperatures (around 300 °C) is similar to the photo mask removal mechanism in H_2-AFT plasma [21] as shown in Figure 5.11. Heating the low-*k* in H_2-based plasma atmosphere supports the evaporation of porogen residue. The H radicals promote dissociation of the high mass porogen chains render generation of volatile short chain alkyl molecules. Additionally, depth of penetration of H radicals into low-*k* pores should also be considered due to H radical loss as a result of recombination on low-*k* pore walls. In summary, the porogen residue removal process is a complex phenomenon. The clear temperature dependence versus depth and degree of porogen removal is observed. However, activation energy for this process in not trivial to calculate. In first approximation the total activation energy is superposition of three phenomena: activation energy for porogen residues reaction with H radicals, activation energy of diffusion of H radicals into pores and activation energy for recombination of H radical on pore walls. Moreover the activation energy for recombination of H radicals on pore walls of material depends on specific recombination mechanisms such as Langmuir-Hinshelwood and Eley-Rideal [43].

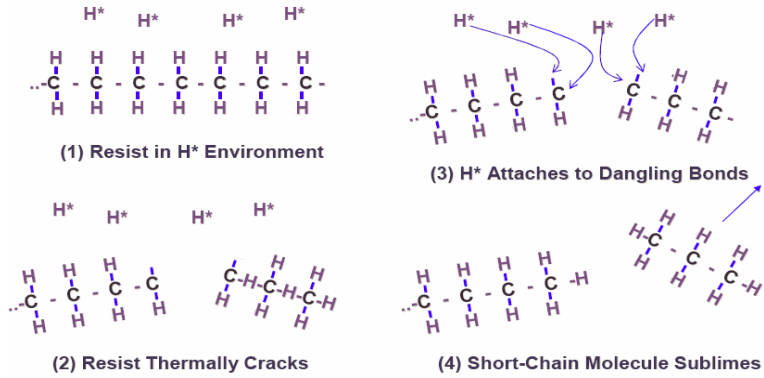

Figure 5.11 Schematic sketch of possible organic polymer removal mechanism by annealing in hydrogen plasma after-glow atmosphere [21]. (Note: Originally porogen is cyclic hydrocarbon, however after deposition in PECVD process, its structure is difficult to define. Even more complex transformation occurs for UV cured porogen – PR. Therefore the above sketch is rough approximation of the real effect).

Mechanical properties were examined using Nano Indentation (NI). Since the film thicknesses were relatively low, only a relative study was possible. NI showed a small reduction of the Young's modulus for the films treated at higher temperatures (Figure 5.12a), which can be attributed to the reduced density of the top layer. The electrical measurements using Hg-probe indicate a small reduction of the effective *k*-value as a result of the lower dielectric constant of the top modified layer (Figure 5.12b). The results, however, have measurement uncertainty due to the potential error in determining the thickness of the top modified layer. Similar electrical results were observed by Matshushita et al. [25]. The *k*-value of the low-*k* film was reduced after He/H_2 DSP plasma exposure. However, the mechanism of such low-k modification was not discussed.

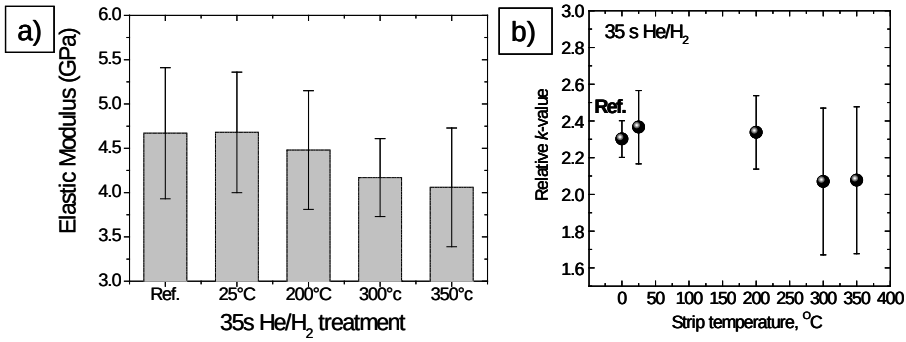

Figure 5.12. The mechanical properties of Ea (see Table 2.2) and Ea He/H_2 treated films at different temperatures as measured by NI (a) k-value as measured by Hg-probe (b)

He/H_2 ash DSP treatments impose no damage to the subjected porous low-*k* films as they remain hydrophobic, in contrast to the conventional low temperature anisotropic O_2 ash plasma. He/H_2 DSP exposure at temperatures higher than 300 ºC result in a modified top layer, with reduced density and increased porosity. These modifications are believed to be a result of residual porogen removal and therefore not detrimental, but rather beneficial. The decrease in material density leads to an improvement in dielectric constant with relatively small reduction of the mechanical strength. Therefore the next section considers time dependence of He/H_2 DSP treatment on depth of low-*k* modification. This allows us to estimate the time dependence on penetration depth of H radicals into low-*k* pores. Moreover, the study of the time dependence of He/H_2 DSP treatment will provide more insight in change of material characteristic of different dielectric materials.

5.5 Time effect of He/H_2 afterglow

We have shown in the previous chapters that afterglow of He/H_2 plasma do not remove $Si\text{-}CH_3$ groups from low-*k* materials. Therefore, degradation of the dielectric constant is minimal and these processes are considered as the most attractive options for the microelectronic industry. However, the modifications of top film surfaces were observed such as density loss as result of porogen removal. In order to get insight into those processes we study time effect of He/H_2 DSP on PECVD low-*k* films with different porosity.

The porosity in advanced PECVD low-*k* films is created after deposition by removal of a sacrificial phase (porogen) by ultra-violet (UV) assisted thermal curing. UV curing also results in formation of Si-O-Si network with improved mechanical properties [44,45]. The porogen molecules are normally cyclic hydrocarbons [46] that are photo-dissociated by UV light with formation of volatile hydrocarbons and non-volatile carbon rich residues [47,48]. The effect of the porogen residues on the low-*k* properties and the plasma processing compatibility are largely unknown. FTIR spectrometry has limited sensitivity to amorphous carbon (C=C and C-C bonds) and this is the reason why it is difficult to monitor porogen residues with this technique. Recent studies using Raman spectroscopy and UV spectroscopic ellipsometry (UV-SE) allowed quantitative evaluation of PR (see section 2.5.1.1).

In this section (5.5), using FTIR spectroscopy, TOFSIMS, and UV-SE and mass measurements we demonstrate that the PR actively react with hydrogen radicals and are removed during the processing in He/H_2 DSP. It is demonstrated that the PR removal has a significant impact on the mechanical properties of low-*k* films. The main purpose is the evaluation of the amount and properties of PR formed in low-*k* films with different pore size and porosity and also effects of UV curing conditions. For this reason we evaluated 4 different low-*k* materials in great detail.

Table 5.4 The summary of basic characteristic of the studied PECVD low-*k* films important for the next paragraph (see also Table 2.2).

Film	Open Porosity [%]	Targeted *k*-value	Thickness [nm]	Young's Modulus [GPa]	Curing UV source wavelength [nm]
B2	23	2.5	180	7.43	>200 (broad band)
B3	36	2.2	500	5.54	>200 (broad band)
Ea	32	2.3	180	4.48	~172 (narrow band)
Eb	34	2.3	180	3.8	>200 (broad band)

5.5.1 Change of composition

The changes in IR absorbance of low-k materials before and after exposure in He/H_2 DSP are close to the measurement errors. Therefore, only magnifications of the selected absorbance bands are shown. One can see that there is neither reduction of $Si\text{-}CH_3$ concentration (Figure 5.13) and nor -OH group incorporation (Figure 5.14).

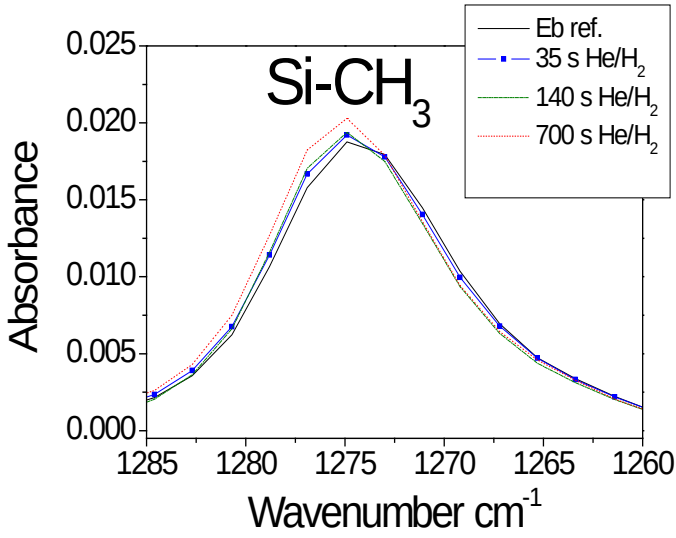

Figure 5.13 The chosen magnification of FTIR spectra reflecting the absorbance band of $Si\text{-}CH_3$ groups (1285 cm^{-1} -1260 cm^{-1}) of as deposited and He/H_2 DSP treated Eb film.

Only discrete changes are observed: the redshift of the $Si\text{-}CH_3$ absorbance and a minimal H_2O amplitude increase (around 3200 cm^{-1}) presumably due to an increase of the low-*k* pore radii after the He/H_2 DSP plasma exposure. The observations are typical for all studied films. The FTIR results are supported by H_2O-goniometery measurements showing that surface contact angles with H_2O remain higher than 80° for all the studied low-*k* films. Therefore, both surface and

bulk of the low-*k* films remained hydrophobic and one can conclude that no plasma damage of the low-*k* matrix has occurred.

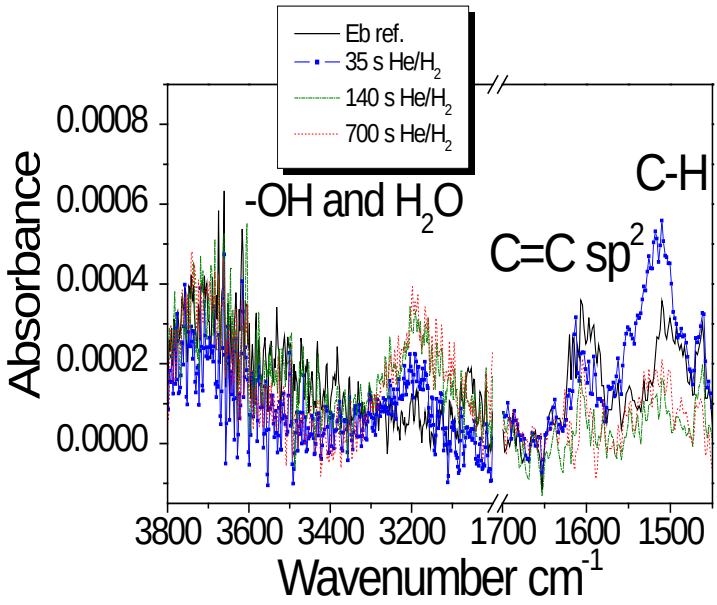

Figure 5.14 The chosen magnification of FTIR spectra showing absorbance bands related to Si-OH, H_2O groups (3800 – 3000 cm^{-1}) and C-H and C=C sp^2 groups (1700 – 1450 cm^{-1}).

Figure 5.14 shows a magnification of the FTIR spectra in the 1450-1700 cm^{-1} range that indicates reduction of 1600 cm^{-1} absorbance band related to C=C sp^2 bond with time of He/H_2 DSP treatment and some changes in C-H groups (1475-1550 cm^{-1}) [47]. The presence of C=C and C-H groups is described in literature as the signature of porogen residues [47,49]. A reduction of absorbance bands of C=C and C-H groups might indicate a removal of the porogen residues after the He/H2 DSP exposure (Figure 5.14). Although, the C=C and C-H group amplitudes were found to be very small, and it is in agreement with literature [47,49].

ToF-SIMS analysis (Figure 5.15) shows reduction of carbon concentration as a result of DSP exposure. The depth of carbon depletion depends on the exposure time (zoomed area in Figure 5.15). The sputtering time in ToF-SIMS in first approximation is proportional to the film thickness. Therefore, one can see that the depth of carbon depletion has a tendency to saturate with time, which allows us to assume that this process is limited by diffusion of H radicals from He/H_2 DSP plasma. This tendency is logarithmic (and will be elaborated further in the section 5.5.2). The penetration depth of the H radicals must be determined by properties of low-*k* film such as pore size, open porosity, porogen content and the recombination coefficient of H radicals on the pore walls.

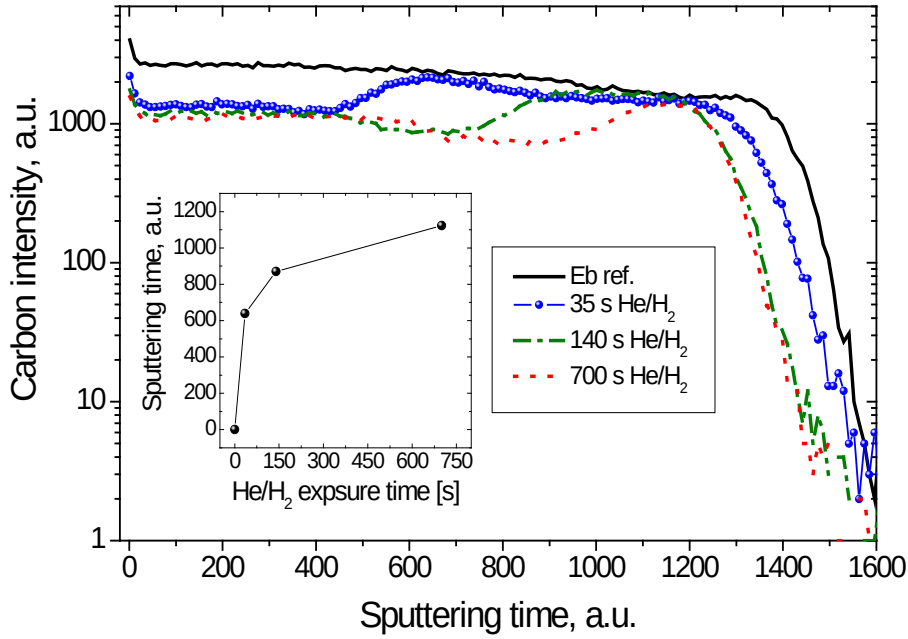

Figure 5.15 C-depth profile for as deposited and He/H_2 DSP treated E_b film as measured by ToF-SIMS. The embedded graph presents the sputtering time proportional to depth of modification (C-depletion) versus He/H_2 DSP exposure time. The time of around 1400 a.u. corresponds to 180 nm of sputtered Ea film [the thickness of as deposited film (Eb ref.) was around 180 nm]. Differences in sputtering time are mainly due to differences in density between samples.

It is important to note that the reduction of carbon concentration is limited: the carbon concentration in the top part of the films stays the same after 35 s, 140 s and 700 s (Figure 5.15). Therefore, this carbon depletion process is limited by porogen residue content in the film matrix (it is not related to carbon removal from covalent $Si\text{-}CH_3$ groups). The change of carbon concentration is in qualitative agreement with the mass measurements (Figure 5.16). The mass of low-*k* films is reduced as a result of exposure to the plasma and also has a tendency to saturate at sufficiently long exposure time. This agrees with TOF-SIMS result and suggests that the depletion of carbon concentration in TOF-SIMS and mass loss has the same nature.

The phenomena observed in TOF-SIMS and mass balance measurements have a seeming contradiction with the FTIR results (no $Si\text{-}CH_3$ group depletion). Therefore, TOF-SIMS and mass balance reflect the concentration change of the carbon compounds, which bonding structure is almost invisible in FTIR spectra. We showed above that FTIR has limited sensitivity to amorphous carbon-like porogen residue (Figure 5.14). Therefore, the most reasonable assumption is that the carbon depletion and mass loss are related to removal of the porogen residue.

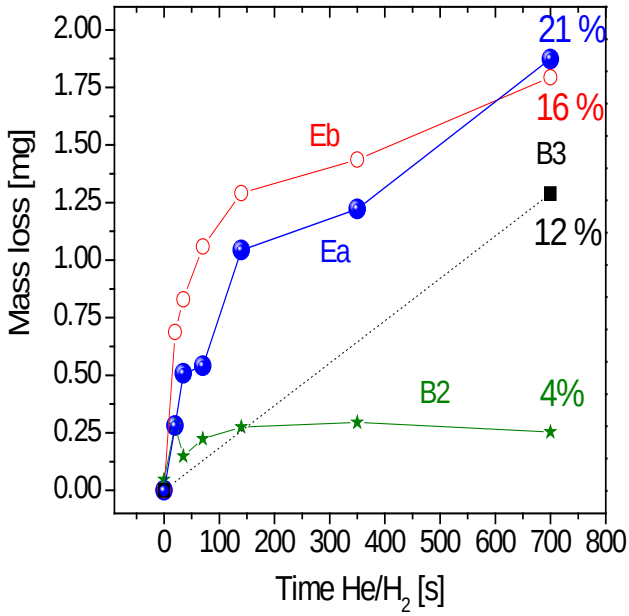

Figure 5.16 Mass loss after He/H_2 DSP modification as measured by mass balance on 300 mm wafers. The numbers show percentage mass loss in modified layers (700 s) assuming modification depths as measured by UV-SE (Table 5.5).

To prove this assumption we studied the plasma exposed samples by UV-SE. The spectra of as deposited (solid lines) and 700 s He/H_2 DSP modified (dashed lines) films are shown in Figure 5.17. One clearly can see that the refractive indices and extinction coefficients are different from the film to the film. According to recent results reported by Marsik et al. (see section 2.5.1.1) absorption bands located between 4.13 eV (200 nm) – 6.2 eV (300 nm) are related to presence of amorphous carbon like PR. Therefore, the difference in absorption spectra of these films is mainly related to different amount of porogen residues.

The films Ea and Eb were deposited in exactly the same conditions but they were cured by light with different wavelengths. It is clear from Figure 5.17 that the curing by light with λ > 200 nm (6.2 eV) (Eb) leaves less PR. Plasma exposure completely removed the PR from both Ea and Eb films and the final absorption spectra are becoming similar to the UV spectra of the low-*k* matrix material. Refractive indices of these two films after the PR removal are the same. This is additional proof that all PRs were removed independently on the wavelength of UV light used for curing.

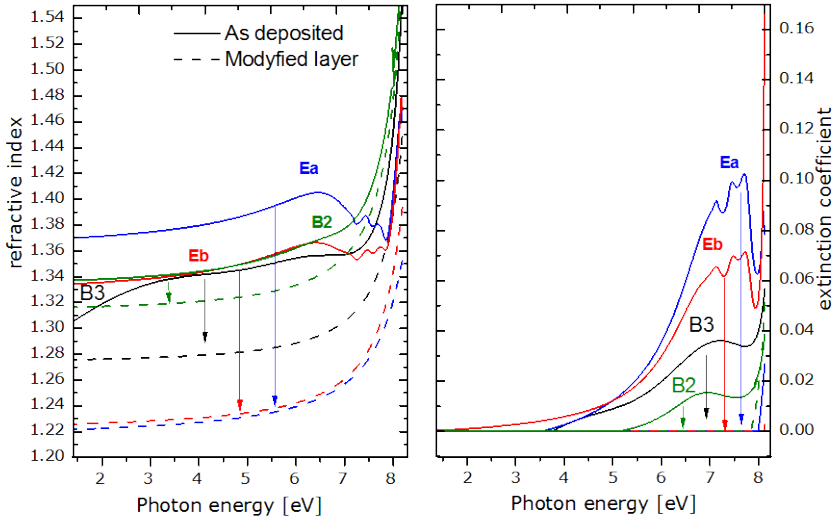

Figure 5.17 Optical properties in the range of 8.27 eV (150 nm) – 1.38 eV (900 nm) of as deposited and 700 s He/H_2 DSP modified films as measured by UV-SE. The letters in the graph correspond to Table 2.2.

The low-*k* films B2 and B3 were deposited in the same PECVD chamber and cured by the same broadband lamp with $\lambda > 200$ nm (Table 5.4). However, they have different porosity that was provided by different ratio of matrix and porogen precursors. Both these films contain less PR in comparison with the films Ea and Eb. The film B3 has higher porosity (Table 5.4) and contains more PRs in comparison with B2. The disappearance of absorption bands between 4.13 eV (200 nm) – 6.2 eV (300 nm) for He/H_2 treated films B2 and B3 indicates complete removal of the PR. However, the complete PRs removal for B2 and B3 films result in smaller changes of refractive indices than for Ea and Eb films. This fact suggests that the relatively low porosity and pore size of the films Ea and Eb (see Table 2) were defined by large amount of PR deposited on pore wall.

Reduction of the refractive index suggests increase of porosity [50]. Therefore, the damage-free strip based on He/H_2 DSP, can significantly change the films properties if the deposition and curing conditions were not sufficiently optimized (i.e. leaves too much PR). One of the most expected problems, related to PR removal can be a change of the mechanical properties that directly depends on porosity.

5.5.2 Logarithmic time dependence of porogen residue removal depth

In the previous section we discussed the structural changes related to PR removal from the low-*k* films. The carbon depth profiles of Eb films with 3 different He/H_2 DSP treatment times were studied (Figure 5.8). It is shown that the depth of carbon depletion due to the PR removal saturates with time. We presumed that the depth of the PR removal increases logarithmically with time. In this section we validate this logarithmic time dependence using the UV-SE and the mass measurements. We already demonstrated that the PR free surface has significantly different optical properties than non-modified one (Figure 5.17). This allows us to build reasonable ellipsometric models in order to evaluate the depth of modification of the varied low-*k* dielectrics. The UV-SE measurements of the modification depth are shown in Figure 5.18.

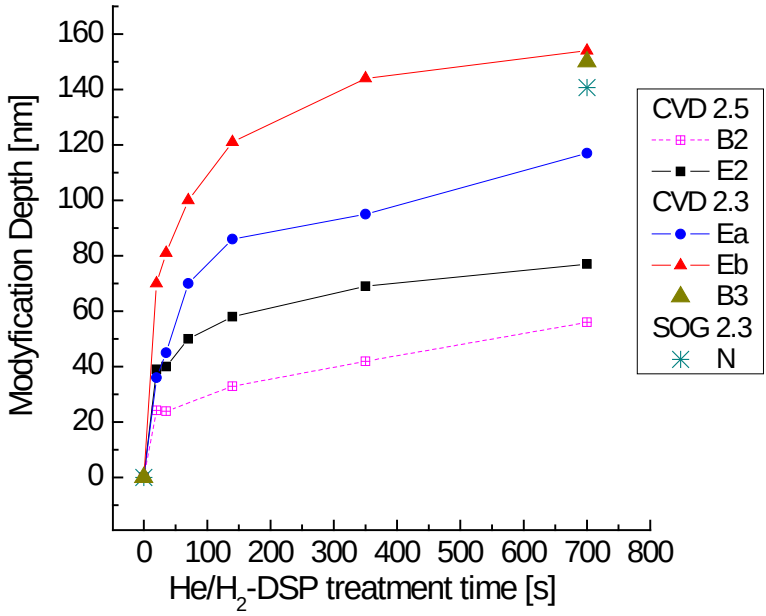

Figure 5.18 Modification depth versus time of He/H_2 DSP treatment as measured by UV-SE. The legend in the graph corresponds with Table 2.2.

In order to demonstrate the logarithmic time dependence is valid, the data in Figure 5.18 are re-plotted in logarithmic time scale and fitted with linear regression as shown in Figure 5.19a. Furthermore, in order to validate SE data we additionally re-plotted mass balance data from Figure 5.16 in the logarithmic time scale as shown in Figure 5.19b (adding more measurement points for other low-*k* materials in Table 2.2). Those data are represented in Figure 5.20a. It is clear that both SE and mass balance measurements shows logarithmic time dependence. The

variation of mass for Ea film might be due to minor OH group incorporation as discussed in section 5.5.4 that might cause variation in the film mass.

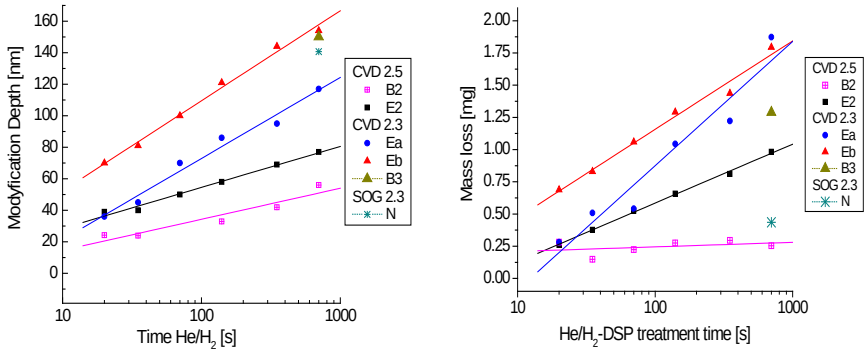

Figure 5.19 Time of He/H_2 DSP treatment presented in logarithmic scale versus (a) modification depth as measured by SE (b) mass loss as measured by mass balance on 300 mm wafers. The legend in the graph corresponds with Table 2.2.

Above study of the depth of modification as a function of time could reveal more insight in the PR removal mechanism. It is clear that modification depth is larger for CVD 2.3 and SOG 2.3 (with *k*-value $\leq$ 2.3) films with higher porosity and pore size than for CVD 2.5 films (with *k*-value ~ 2.5) with lower porosity and pore size. Films with higher porosity and pore size should be more permeable for He/H_2-DSP radicals that actively react with PR. Furthermore, all films show the logarithmic time dependence of modification depth, which is more difficult to explain.

The radical modification mechanisms of nano-porous materials were studied in literature [51,52,53,54]. For instance, Goldman et al.[52] studied time dependent depth of modification of low-*k* materials exposed in O_2-plasma. Authors proposed that a damaging front (modification depth with O_2-plasma) that penetrates the low-*k* can be described by a Deal-Grove model (originally used to describe mechanism of thermal oxidation of Si) [55]. Damaging front moves fast for relatively short times (diffusion limited regime) and slows down for larger times (1^{st} order reaction limited regime). Our experiments show a similar initial steep increase in modification depth with time and a levelling for longer times (Figure 5.18). However, in the presented case, the behaviour is more accurately described by a logarithmic law over the whole range while Deal-Grove model assumes parabolic time dependence for longer times and linear dependence for shorter times.

The PR removal mechanism from nano-porous low-*k* films is a complex phenomenon. The combined diffusion and atom recombination processes and their reaction with PR in porous materials have to be modelled considering adsorption, desorption and recombination at active sites on the pore walls. One of the

approaches to simulated PR process is the Monte-Carlo simulation [53]. The reaction, recombination can be translated into probabilities of the events in MC algorithm. And this should be as subject of the future work in order to understand radical transport and their reaction mechanism with PR in nano-porous low-*k* dielectrics.

5.5.3 Mechanical properties

The amount of the removed PR and corresponding change of the films properties after 700 s of He/H_2 DSP plasma exposure are summarized in Table 5.5. Change of the mass related to PR removal (Figure 5.16) was normalized to the thickness of the top modified layer (MD in Table 2). The degree of porogen removal (DPR) was the highest for Ea film (0.0137 mg/nm) and approximately 3.7 times lower for B2 film with the lowest porogen content (0.0037 mg/nm). The porosity was calculated using Lorentz-Lorenz (LL) equation [50], assuming that removed porogen has RI value close to the film skeleton (the first approximation). It was also found that porosity is increased in all cases (for all films).

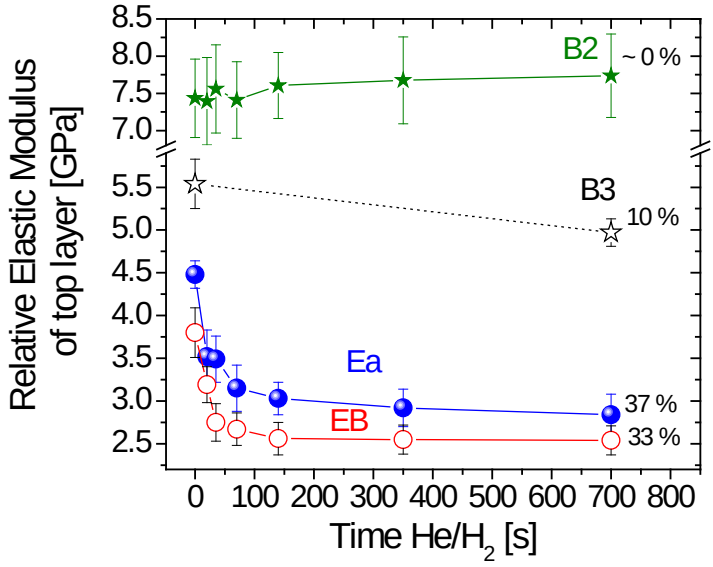

Figure 5.20 Relative EM of the He/H_2 DSP modified layer for different low-k films as measured by NI. The legend in the graph corresponds with Table 2.2

The mechanical properties of low-*k* films were evaluated using NI (see section 2.5.7). NI showed a reduction of the elastic modulus (EM) for all films except B2 (Figure 5.20). The film B2 which has the lowest PR content as indicated by both, UV-SE and mass balance measurements (Figure 5.17 and Figure 5.16). The reason of lower level of PR content is a lower porosity (less porogen was used during deposition) and optimized deposition and curing conditions in comparison with the films Ea and Eb. The film Ea with the highest PR content shows the highest relative reduction of EM. We clearly see that reduction of mechanical

properties during the exposure to He/H_2 DSP plasma is proportional to the initial porogen content in the low-*k* material. Furthermore, it is clear that initial mechanical properties of films Ea and Eb are very much determined by PRs. PR provides relatively high EM, although the skeleton of these films are much softer that in the films B2 and B3.

Table 5.5 Summary of as deposited and 700 s He/H_2 DSP treated film properties. The porosity change was calculated using L-L equation and mean pore size was measured by EP.

S	MD (UV SE)	DPR	EM [GPa] (mean value)		RI_{632nm} (top layer)		LL porosity, % (top layer)		Mean Pore Radii [nm] (top layer)	
	[nm]	[mg/ nm]	Before	After	Before	After	Before	After	Before	After
B2	69	0.0037	7.43	7.74	1.343	1.320	23	28	0.7	0.7-0.8
B3	150	0.0084	5.54	4.97	1.341	1.279	36	47	1.1	n.a.
Ea	117	0.0137	4.48	2.84	1.378	1.226	32	58	0.9	1.6
Eb	154	0.0120	3.8	2.54	1.339	1.230	34	56	1.0	1.6

The mechanical strengthening of silica-based porous materials by C-based polymer additions was already discussed by Laventis et al. [56]. Furthermore, Maidenberg at al. [57] found that controlled porogen decomposition during UV-curing process improves the fracture energy of MSQ low-*k* materials.

5.5.4 Electrical properties

In this paragraph we describe a mechanism of the *k*-value reduction of PECVD films in He/H_2 DSP ash. Additionally, we compare over-ash effect on PECVD and porogen-residue-free spin-on glass (SOG) films. And, finally, we show that optimal over-ash time in combination with PECVD film with *k*-value of 2.5 results in *k*-value reduction without degradation of mechanical properties of the film.

The short He/H_2-DSP treatment (<100 s) results in *k*-value reduction of PECVD films (Figure 5.21). This *k*-value reduction is proportional to the mass loss due to PRs removal from PECVD materials by He/H_2-DSP (Figure 5.16 and Figure 5.19b). The porogen/matrix ratio and the UV-source used for the curing defined the final PRs content in the PECVD films. The PECVD films with the higher initial porogen load “CVD 2.3” shows more mass loss as compared with the films with the lower initial porogen load “CVD 2.5”. Furthermore, the E2 and B2 films with the lower porogen load show a rise in *k*-value when He/H_2-DSP treatment time exceeds 100 s. This rise in *k*-value could be explained by the minor silanol group incorporation. The Figure 5.22 shows increase of absorbance related to polar OH groups after 700 s of He/H_2 DSP treatment. This increase, however, is small and comparable with the measurement noise level. In order to show the increase for all the studied films we integrated OH groups absorbance in the range of 3100-3900

cm^{-1}. Such integrated absorbance versus time of He/H_2 DSP exposure was plotted in Figure 5.23.

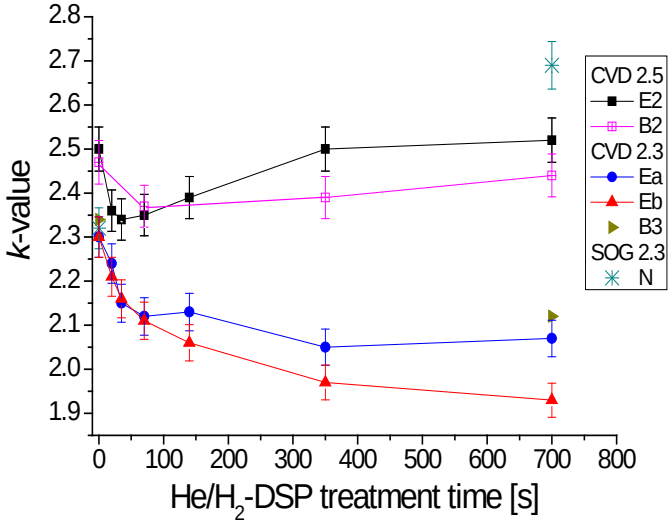

Figure 5.21 The *k*-values of blanket low-*k* films as measured by Hg-probe system at 100 kHz versus He/H_2-DSP treatment time. The legend in the graph corresponds with Table 2.2

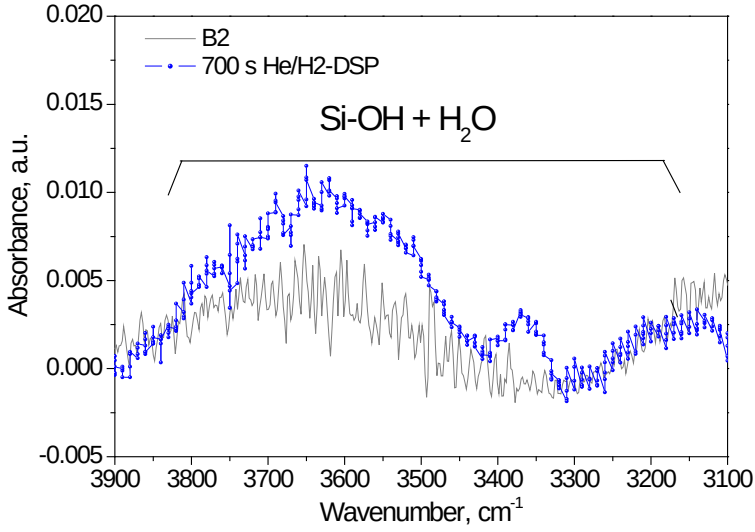

Figure 5.22 The silanol group absorbance as measured by FTIR of as deposited film and treated with 700 s He/H_2-DSP.

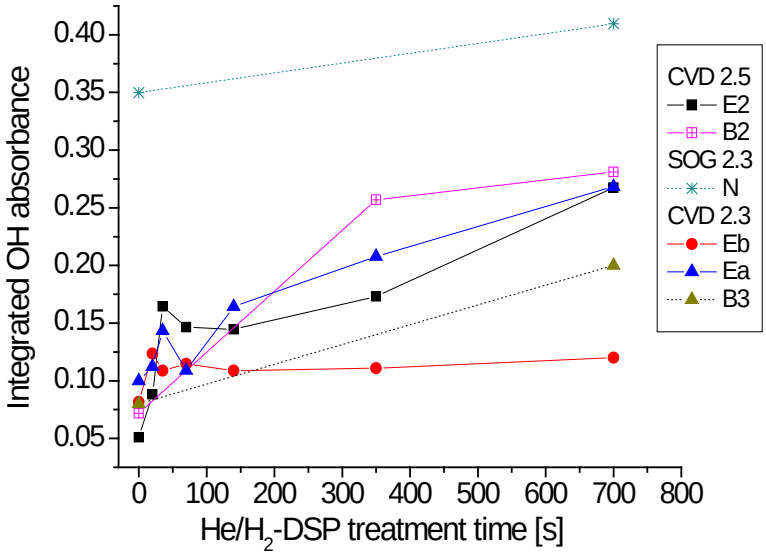

Figure 5.23 The integrated absorbance of silanol groups (3900 cm^{-1}-3100 cm^{-1}) as measured by FTIR versus He/H_2-DSP treatment time of blanket low-k films. The legend in the graph corresponds with Table 2.2

The minimal silanol content present in the PECVD materials treated in He/H_2-DSP also explains why the rise in k-value is not observed for the "CVD 2.3" films (Figure 5.23). The "CVD 2.3" films show more mass loss (porosity increase) in comparison with the "CVD 2.5", but similar level of silanol group incorporation (Figure 5.23). Therefore, *k*-value of the PECVD materials treated with the He/H_2-DPS is defined by two competing phenomena: (i) porosity increase due to PR removal that results in *k*-value reduction and (ii) minor silanol group incorporation that results in *k*-value increase. In order to confirm our hypothesis we treated PR-free SOG material with 700 s of the He/H_2-DSP. The treated SOG film shows some organic removal much smaller than any 2.3 PECVD films. Indeed, the *k*-value was increased due to the minor silanol group incorporation as shown in Figure 5.21.

In summary we demonstrated that He/H_2 DSP can reduce dielectric properties of PECVD films due to progen residues removal. This reduction in certain cases results in degradation of the mechanical properties (section 5.5.3). In order to depict this trend we represented YM of all investigated films versus their mechanical properties as shown in Figure 5.24. We found that the effect of He/H_2 DSP treatment can be divided into 3 groups. The first group contains films where the effect is beneficial: *k*-value reduction is achieved without change of YM. All CVD 2.5 films treated with the times shorter than 100 s belong to the first group. The second and the third groups reflect the unwanted modifications of the low-*k* films. In the second group all CVD 2.5 films treated longer than 100 s and SOG film are classified. For all those films *k*-value is increased without change in YM. And finally the third group contains all CVD 2.3 films with the highest PR content. Those films show both YM and *k*-value reduction.

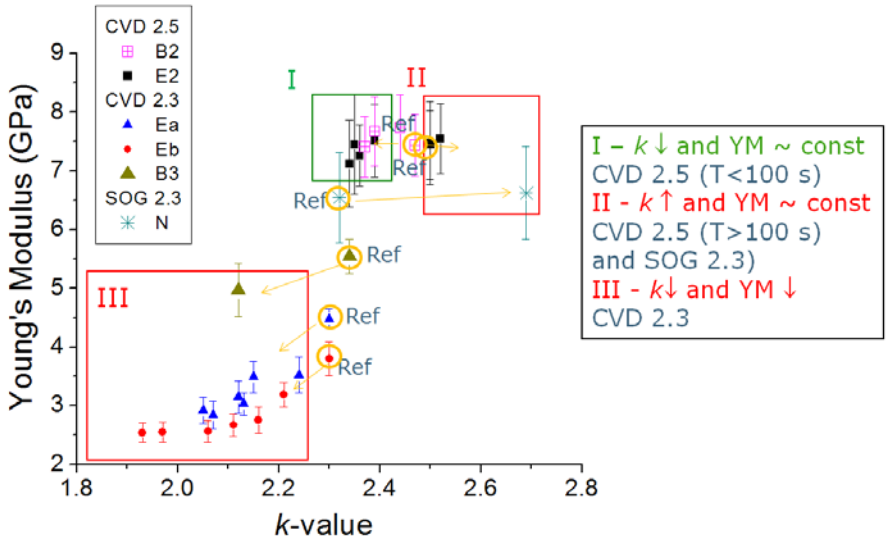

Figure 5.24 The YM as measured by Nano-Indentation versus *k*-value as measured by Hg-probe at 100 kHz of the PECVD and the spin-on film treated with varied times of He/H_2 DSP. The yellow circles represent the referential films while yellow arrows indicate the modified films. The squares I, II and III correspond with the legend and represent the classification of the following effects: *k*-value reduction and without change of YM, *k*-value increase without change of YM, and *k*-value reduction accompanied with YM reduction.

5.6 Chapter summary

The effect of different ash chemistries in downstream plasma chamber was investigated. We found that the best strip chemistry is He/H_2 DSP while the worst ones are the afterglows of N_2/H_2 and O_2 plasmas. The findings confirm the literature search results that after-glow of H_2-plasmas do not degrade film's *k*-value. Furthermore, results showed that H_2 and He/H_2 DSP cause unexpected mass loss of the film without thickness reduction. The nature of this modification was investigated further. For this purpose the temperature and time effects of He/H_2 DSP ash on PECVD and spin-on film with different porosity was studied. It was found that all PECVD films contain different amounts of PR that can be removed by He/H_2 or H_2 DSP treatments. The PR is a nonvolatile product of UV photochemical dissociation of porogen with chemical composition close to amorphous carbon and carbon rich hydrocarbons. This PR is introduced into film during its fabrication. The amount of PR depends on: deposition conditions and porosity. If more porogen is used during the deposition (to get more porous films), more PR remains after the curing. Curing process with wavelength 172 nm generates more residue than curing process with wavelength longer than 200 nm. The PR can be removed by He/H_2 or H_2 plasma afterglows at elevated temperatures (higher than 200 ºC). The depth and degree of porogen removal is controlled by process temperature. Moreover, the

depth of removal is determined by penetration depth of the H radicals into low-*k* material and decreases logarithmically with time. The porogen depleted layer becomes more porous, which is reflected in the mass loss, *k*-value reduction and the optical properties change after the plasma treatment. It is shown that the good mechanical properties of the blanket films can be provided by presence of dense PRs. Removal of this residue by He/H_2 DSP significantly reduces the Young's Modulus suggesting that the films matrix would not remain sufficiently stiff after a regular UV curing. The controlled degradation of the mechanical properties and change of pore size after He/H_2 DSP presents for additional challenges during the integration for PECVD films with k-value lower than 2.3. Therefore, the problem of damage-free strip must be solved in combination with improvement of deposition precursors, conditions and curing of low-*k* film's. And this is the subject of the next chapter.

5.7 References

[1] W. Chen, Q. Y. Han, R. Most, C. Waldfried, O. Escorcia and I. Berry, J. Electrochem. Soc., 151, F182 (2004).

[2] Y. Furukawa, R. Wolters, H. Roosen, J. H. M. Snijders and R. Hoofman, Microelectron. Eng., 76, 25 (2004).

[3] P. T. Liu, C. W. Chen, T. C. Chang and T. Y. Tseng, Electrochem. Solid-State Lett., 7, F5 (2004).

[4] H. Y. Song, C. W. Kim, S. G. Park, J. K. Yang and C. W. Lee, Journal of Vacuum Science & Technology A, 23, 886 (2005).

[5] M. A. Worsley, S. F. Bent, S. M. Gates, N. C. M. Fuller, W. Volksen, M. Steen and T. Dalton, J. Vac. Sci. Technol. B, 23, 395 (2005).

[6] K. Yonekura, K. Goto, M. Matsuura, N. Fujiwara and K. Tsujimoto, Jpn. J. Appl. Phys. Part 1 - Regul. Pap. Brief Commun. Rev. Pap., 44, 2976 (2005).

[7] X. F. Hua, M. S. Kuo, G. S. Oehrlein, P. Lazzeri, E. Iacob, M. Anderle, C. K. Inoki, T. S. Kuan, P. Jiang and W. L. Wu, J. Vac. Sci. Technol. B, 24, 1238 (2006).

[8] F. Iacopi, Y. Travaly, M. Van Hove, A. M. Jonas, J. M. Molina-Aldareguia, M. R. Elizalde and I. Ocana, Journal of Materials Research, 21, 3161 (2006)

[9] H. W. Kim, J. H. Myung, N. H. Kim, H. S. Lee, S. G. Park, J. G. Lee, C. W. Chung, W. J. Park, C. J. Kang, C. G. Yoo, K. H. Ko, J. H. Woo, S. D. Choi and D. K. Choi, Thin Solid Films, 506, 222 (2006).

[10] M. A. Worsley, S. F. Bent, N. C. M. Fuller, T. L. Tai, J. Doyle, M. Rothwell and T. Dalton, J. Appl. Phys., 101, 11 (2007).

[11] M. Darnon, T. Chevolleau, T. David, N. Posseme, J. Ducote, C. Licitra, L. Vallier, O. Joubert and J. Torres, J. Vac. Sci. Technol. B, 26, 1964 (2008).

[12] H. Shi, J. Bao, R. S. Smith, H. Huang, J. Liu, P. S. Ho, M. L. McSwiney, M. Moinpour and G. M. Kloster, Appl. Phys. Lett., 93 (2008).

[13] E. Vinogradova, C. E. Smith, D. W. Mueller and R. F. Reidy, Electrochem. Solid-State Lett., 11, H255 (2008).

[14] T. V. Rakhimova, O. V. Braginsky, A. S. Kovalev, D. V. Lopaev, Y. A. Mankelevich, E. M. Malykhin, A. T. Rakhimov, A. N. Vasilieva, S. M. Zyryanov and M. R. Baklanov, IEEE Trans. Plasma Sci., 37, 1697 (2009).

[15] D. L. Moore, R. J. Carter, H. Cui, P. Burke, P. McGrath, S. Q. Gu, D. Gidley and H. Peng, J. Vac. Sci. Technol. B, 23, 332 (2005).

[16] D. L. Moore, R. J. Carter, H. Cui, P. Burke, S. Q. Gu, H. G. Peng, R. S. Valley, D. W. Gidley, C. Waldfried and O. Escorcia, J. Electrochem. Soc., 152, G528 (2005).

[17] H. Cui, R. J. Carter, D. L. Moore, H. G. Peng, D. W. Gidley and P. A. Burke, J. Appl. Phys., 97, 8 (2005).

[18] A. Grill, V. Sternhagen, D. Neumayer and V. Patel, J. Appl. Phys., 98, 7 (2005).

[19] A. Grill and V. Patel, J. Electrochem. Soc., 153, F169 (2006).

[20] S. L. Xu, C. Qin, L. Diao, D. Gilbert, L. Hou, A. Wiesnoski, E. Busch, R. McGowan, B. White and F. Weber, J. Vac. Sci. Technol. B, 25, 156 (2007).

[21] G. J. Stueber, G. S. Oehrlein, P. Lazzeri, M. Bersani, M. Anderle, E. Busch and R. McGowan, J. Vac. Sci. Technol. B, 25, 1593 (2007).

[22] I. L. Berry, Q. Han, C. Waldfried, O. Escorcia and A. Becknell, in SEMI® Technical Symposium: Innovations in Semiconductor Manufacturing (2004).

[23] F. Blaschta, S. E. Schulz and T. Gessner, Microelectron. Eng., 82, 427 (2005).
[24] Q. Han, B. White, I. L. Berry, C. Waldfried and O. Escorcia, Sol. State Phen., 103-104, 341 (2005).
[25] Matshushita, A., N. Ohashi, et al. Low Damage Ashing using H_2/He Plasma for Porous Ultra Low-k. International Interconnect Technology Conference, Burlingame, CA. (2003).
[26] I.L. Berry, Q. Han, C. Waldfried, O. Escoria, A. Becknell, SEMICON, (2004)
[27] Q. Han, B. White, I. L. Berry, C. Waldfried, and O. Escorcia, Solid State Phenomena, Vols 103-104 (2005), p. 341-344, (2005)
[28] T. C. Chang, P. T. Liu, Y. S. Mor, T. M. Tsai, C. W. Chen, Y. J. Mei, F. M. Pan, W. F. Wu and S. M. Sze, J. Vac. Sci. Technol. B, 20, 1561 (2002).
[29] M. A. Worsley, S. F. Bent, S. M. Gates, N. C. M. Fuller, W. Volksen, M. Steen and T. Dalton, J. Vac. Sci. Technol. B, 23, 395 (2005).
[30] P. Lazzeri, G. J. Stueber, G. S. Oehrlein, R. McGowan and E. Busch, J. Vac. Sci. Technol. B, 24, 2695 (2006).
[31] N. Posseme, T. Chevolleau, T. David, M. Darnon, O. Louveau and O. Joubert, J. Vac. Sci. Technol. B, 25, 1928 (2007).
[32] Q. Han, I. L. Berry, P. Sakthivel and C. Waldfried, Plasma ashing process, in, H01J 37/32 (20060101); H01L 21/02 (20060101); H01L 21/311 (20060101); G03F 7/42 (20060101); ed., I. Axcelis Technologies Editor, USA (2003).
[33] X. Fu, J. Forester, J. Yu, P. Gopalraja, S. Ahn, A. Demos and P. Ho, in IEEE, sponsored by Electron Devices Society, p. 51 (2006).
[34] Y. A. Mankelevich, A. T. Rakhimov, N. V. Suetin and S. V. Kostyuk, Diamond and Related Materials, 5, 964 (1996).
[35] J. Griffin and P. C. Ray, Nanotechnology, 17, 1225 (2006).
[36] J. Ma, M. N. R. Ashfold and Y. A. Mankelevich, J. Appl. Phys., 105 (2009).
[37] Y. A. Mankelevich, M. N. R. Ashfold and J. Ma, J. Appl. Phys., 104 (2008).
[38] O. J. L. Fox, J. Ma, P. W. May, M. N. R. Ashfold and Y. A. Mankelevich, Diamond and Related Materials, 18, 750 (2009).
[39] S. L. Xu, C. Qin, L. Diao, D. Gilbert, L. Hou, A. Wiesnoski, E. Busch, R. McGowan, B. White and F. Weber, J. Vac. Sci. Technol. B, 25, 156 (2007).
[40] M.R.Baklanov, K.P.Mogilnikov, and Q.T.Le. , Microelectron. Eng., 83, 2287 (2006).
[41] P, Marsik, P. Verdonck, D. Schneider, D. De Roest, K. Kaneko, and M. Baklanov, Phys. Stat. Sol. c, Vol5(5), p. 1253-1256, (2008).
[42] P. Mogilnikov, M.R. Baklanov, D. Shamiryan and M. Petkov, Jap. J. of Appl. Phys, Vol. 43, No.1, p. 247, (2004).
[43] R. I. Masel, Principles of Adsorption and Reaction on Solid Surfaces, p. 445, John Wiley & Sons, Inc., New York (1996).
[44] F. Iacopi, Y. Travaly, B. Eyckens, C. Waldfried, T. Abell, E. P. Guyer, D. M. Gage, R. H. Dauskardt, T. Sajavaara, K. Houthoofd, P. Grobet, P. Jacobs and K. Maex, J. Appl. Phys., 99, 053511 (2006).
[45] A. Zenasni, F. Ciaramella, V. Jousseaume, C. Le Cornec and G. Passemard, J. Electrochem. Soc., 154, G6 (2007).
[46] A. Grill and V. Patel, J. App. Phys., 104, 024113 (2008).
[47] M. Matsuura, K. Goto, N. Miura, J. M. Haag, S. Hashii and K. Asai, Mat. Res. Soc. Proc., 914, F01-06 (2006).

[48] P. Marsik and M. Baklanov, in 9th International Conference on Solid-State and Integrated-Circuit Technology, p. 765, Beijing, China (2008).
[49] A. Zenasni, V. Jousseaume, P. Holliger, L. Favennec, O. Gourhant, P. Maury, and G. Gerbaud, J. App. Phys., 102, 094107 (2007).
[50] M. R. Baklanov, K. P. Mogilnikov, V. G. Polovinkin and F. N. Dultsev, J. Vac. Sci. Technol. B, 18, 1385 (2000).
[51] J. Marschall and J. E. Boulter, J. Phys. D-Appl. Phys., 39, 3849 (2006).
[52] M. A. Goldman, D. B. Graves, G. A. Antonelli, S. P. Behera and J. A. Kelber, J. Appl. Phys., 106 (2009).
[53] Y. A. Mankelevich, O. V. Braginsky, A. S. Kovalev, D. V. Lopaev, E. M. Malykhin, T. V. Rakhimova, A. T. Rakhimov, A. N. Vasilieva, S. M. Zyryanov and M. R. Baklanov, Spatially resolved dynamics of methyl groups removal from SiOCH films by oxygen atoms: Monte Carlo model of O atoms behaviour in nanoporous material, in Materials for Advanced Metallization Conf., 7-10 March, Mechelen, Belgium (2010).
[54] V. E. Arkhincheev, E. Kunnen and M. R. Baklanov, Active species in porous media: random walk and capture in traps, in Materials for Advanced Metallization Conf., 7-10 March, Mechelen, Belgium (2010).
[55] B. E. Deal and A. S. Grove, J. Appl. Phys., 36, 3770 (1965).
[56] G. Zhang, A. M. M. Rawashdeh, C. Sotiriou-Leventis and N. Leventis, Polymer Preprints, 44, 35 (2003).
[57] D. A. Maidenberg, W. Volksen, R. D. Miller and R. H. Dauskardt, Nat Mater, 3, 464 (2004).

6 Improving Mechanical Robustness of Ultra-low-*k* SiOCH films by Controlled Porogen Decomposition prior to UV-hardening

The results that are presented in this chapter have been partly published in:

A.M. Urbanowicz, K. Vanstreels, P. Verdonck, E. Van Besien, C. Trompoukis, D. Shamiryan, S. De Gendt, M. Baklanov, "Effect of UV-wavelength on Hardening Process of Porogen-containing and Porogen-Free Ultra-low-k PECVD Glasses" submitted at 57th American Vacuum Society Conference, 17-22 October, Albuquerque, New Mexico, USA (2010)
A.M. Urbanowicz, K. Vanstreels, P. Verdonck, D. Shamiryan, S. De Gendt and M. R. Baklanov, J. Appl. Phys.107 (1), 104122 (2010)
A.M. Urbanowicz, K. Vanstreels, P. Verdonck, D. Shamiryan, M. Cremel, S. De Gendt and M. R. Baklanov, in AMC, Baltimore, MA (2009) [proceedings in press].
A.M. Urbanowicz, P. Verdonck, D. Shamiryan, K. Vanstreels, M. Baklanov, S. De Gendt, "Fabrication of porogen residues free and mechanically robust low-k materials" US provisional application filled on 08/07/2009.
A.M. Urbanowicz, B. Meshman, D. Schneider and M. R. Baklanov, Physica Status Solidi a-Applications and Materials Science, 205, 829 (2008).

6.1 Introduction

In the previous chapter we demonstrated that porogen residue removal from ultralow-*k* dielectrics during processing degrades their mechanical properties. This chapter is devoted to a novel solution for porogen-based ultralow-*k* materials. We demonstrate that we can obtain porogen residue-free ultra low-*k* films. This modification results in significant improvement in films mechanical properties normalized to film *k*-value.

The nanometer-scale porosity is deliberately introduced to reduce the dielectric constant (*k*), making organo-silica glass (OSG) suitable for use as insulating layers around thin metal lines that carry electrical signals in microelectronic devices (see section 1.2). However, incorporating the porosity also degrades the mechanical properties of OSG, presenting a challenge for their integration into ultra large-scale microelectronic devices [1,2,3,4]. Microelectronic industry uses two different deposition approaches of the porous OSG: spin-on (from liquid solutions/gels) and plasma enhanced chemical vapor deposition (PECVD). The spin-on approach is well explored [5], the OSG with wide range of porosity up to 99 % has been achieved using various ways to introduce porosity, e.g. silica-particles nano-templating[13], sacrificial-porogen method, or templated sol-gel

polymerization of bridged silsesquioxane precursors [6]. In contrast, PECVD glasses are less explored but presently they are more popular in microelectronic due to the better compatibility with technology requirements [7,8,9,10]. The introduction of porosity into PECVD ultra low-*k* SOG is mainly realized by using sacrificial porogens [11] (see also section 2.4). The matrix material is co-deposited with porogen molecules. Precursors of the matrix materials are alkylsilanes, the porogen molecules are usually cyclic hydrocarbons [9]. To create porosity, the porogen is removed by UV-assisted-thermal curing process (hardening step) in which a formation of the reinforced Si-O-Si network occurs simultaneously [12]. However, not all porogen is removed during the curing, it is partially converted by UV-light into non-volatile graphitized-carbon residues (porogen residue). Therefore, such prepared OSG can be considered as a dual-phase system containing a rigid organo-silica skeleton and soft porogen residues (PR). The total Young's modulus (YM) of such a dual-phase OSG is expected to be smaller than that of single-phase OSG containing mostly rigid Si-O-Si links and terminal organic groups ($Si-CH_3$). In this chapter we discuss PR detection using spectroscopic ellipsometry. We argue that the conventionally fabricated PECVD glasses with ultra-low *k*-value (highly porous) contain PR in contrast to spin-on fabricated glasses using PR-free approach that results in higher YM and better electrical characteristic of the spin-on films. We discuss effect of UV-wavelengths used for curing of the organic-free films. For this purpose we performed additional experiments with excimer-gas mixture UV sources and conventional UV curing systems. And finally we propose the new approach of fabrication PR-free PECVD films by selective porogen removal prior to UV-assisted hardening step. This approach is demonstrated to be beneficial for both low-*k* value and mechanical properties of the dielectric film.

6.2 Experimental procedure

Materials and experimental procedure. The organo-silica matrix was co-deposited with organic porogen by PECVD on 300 mm Si wafers at 300 ^oC. The OSGs with thicknesses of 65 nm, 120 nm and 190 nm were obtained as described in literature [31] and deposition conditions correspond to Ea films (Table 2.2 in section 2.4). Next the films were treated with four combinations of the H_2 after-glow plasma treatment (H_2-AFT) and UV-curing: UV, H_2-AFT, H_2-AFT + UV, UV + H_2-AFT. The H_2-AFT treatments were performed at a wafer temperature of 280 °C using 350 s of the He/H_2 20:1 downstream microwave plasma treatment in a 300 mm asher from LAM research (Table 2.1 in section 2.3). He was used to dilute H_2 and increase its dissociation efficiency. Pure H_2 has a similar effect on SOG films except that the depth of porogen removal is smaller due to lower H radical concentration. The effect of UV-radiation from plasma area was neutralized by special a design of the chamber. The UV-curing was performed in a nitrogen ambient at temperature close to 430 °C. The new curing procedure was performed using a narrow-band 172 nm UV-source [31]. In order to compare porogen removal efficiency of H_2-AFT with the different wavelengths of UV irradiation, an additional experiment with a broadband UV-source with wavelengths higher than 200 nm was performed.

Instrumentation. *The* surface hydrophobic properties before and after the plasma treatments were evaluated using water contact angle measurements (WCA). Optical properties were determined by spectroscopic ellipsometry (SE) in the spectral range of 150 nm to 895 nm at an incidence angle of 70 deg using Aleris SE from KlaTencor. The results were fitted by a single and a double layer optical model using the Marquardt-Levenberg algorithm. The optical models were constructed as described in the literature [16]. The depth of modification and the optical properties of 190 nm films were estimated using a double layer SE model. The bottom layer was assumed to have optical properties of the as deposited film, while the optical characteristics of the top modified layer were determined by fitting. The mass change related to plasma treatments was measured by mass balance metrology on 300 mm wafers (Metrix: Mentor SF3). The open porosity and pore size distributions were evaluated using toluene based ellipsometric porosimetry (TEP) as described in section 2.5.2.1) Mechanical properties, Young's modulus and hardness of the low-*k* dielectric films were measured using a nano indenter XP system (MTS Systems Corporation) with a dynamic contact module (DCM) and a continuous stiffness measurement (CSM) option under the constant strain rate condition (see section 2.5.7). A standard three-sided pyramid diamond indenter tip (Berkovich) was used for the indentation experiments. As the indenter tip is pressed into each sample, both depth of penetration (h) and the applied load (P) are monitored. The YM values of thin OSGs could be influenced by the Si substrate effect. The Si substrate effect might vary depending on film thickness. In order to exclude potential error in YM values the film with different thicknesses are investigated in this study. The more detailed discussion about nano-indentation (NI) measurement of thin porous OSGs is reported in literature [25,26].

6.3 The Effect of Porogen Residue on Film Characteristic: Comparative Study about Spin-on and PECVD films

The effect of the porogen residue (PR) on optical, chemical and mechanical properties of PECVD deposited SOG was discussed in section 5.5. It was shown that PR increases the extinction coefficient of OSG in the UV-range (see section 2.5.1.1). Figure 6.1 reflects extinction of PECVD and spin-on [13] OSG's with k=2.3 and PECVD deposited matrix material (without porogen) and SiO_2 films. One can see that the extinction coefficient of spin-on film and PECVD matrix material deposited without porogen are more close to SiO_2. The PECVD glass prepared by standard co-deposition of organo-silica matrix and porogen followed by UV-curing show significantly higher extinction than the rest of the films. In addition, the low energy shoulder with a maximum at 4.5 eV in the extinction coefficient reflects the presence of sp^2 hybridized carbon (PR) as discussed in section 2.5.1.1.

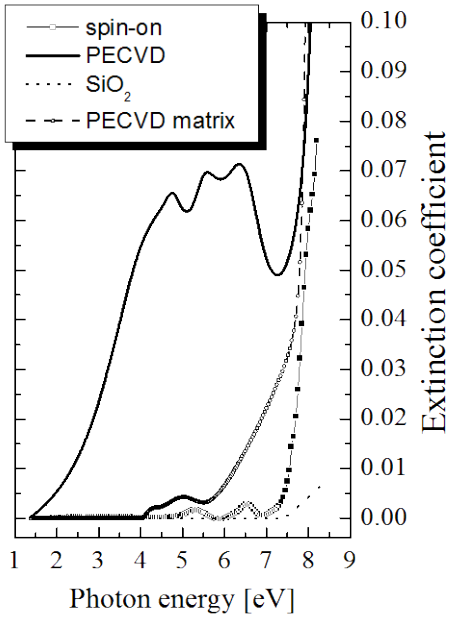

Figure 6.1 Extinction coefficient (as measured by UV spectroscopic ellipsometry) of SiO_2 deposited by PECVD using SiH_4 as a precursor, PECVD matrix material, standard spin-on nano- clustered silica (N in Table 2.2), and PECVD low-*k* (Ea in Table 2.2) films.

Although porogen is needed to introduce porosity in PECVD glasses, the PR has a negative impact on the fundamental properties of OSG's and their industrial processing compatibility. The presence of PR with conjugated C=C bonds increases the leakage current and decreases the breakdown voltage of these materials (–C=C-C=C-C=C is a classical conducting polymer) [14,15]. Moreover, organic-free nano-clustered silica OSG [13] deposited by spin-on shows higher YM of 6.54 GPa than OSG deposited by PECVD that has YM of 4.6 GPa for the same *k*-value of 2.3 as shown in Table 6.2 (similar porosity level). This indicates that PR-phase present in PECVD glass might be the reason of its lower YM than spin-on glass. Furthermore, the industrial processing, such as a photo mask removal from PECVD OSG also removes PR from the latter that results in porosity increase and subsequent degradation of mechanical properties as demonstrated in section 5.5.3.Therefore, development of a new curing approach allowing preparation of PR-free and a mechanically robust PECVD ultra low-*k* films is the main goal of this chapter.

In order to explain higher mechanical robustness of spin-on OSG in comparison with PECVD ones, we investigated their fabrication steps with emphasis on the role of organic residues. There are two differences out of many others

between spin-on organo-silica particles nanotemplating and PECVD fabrication approaches of OSG that are important for our consideration (see also section 2.4, Figure 2.3). The first difference is that the spin-on glass is normally deposited at room temperatures, while the PECVD glass at temperatures typically higher than 180°C (300 °C in our case) [16, 17]. The higher deposition temperature of PECVD glass results in partial cross-linking of organic phase with film skeleton making it more difficult to remove. The second difference is that the spin-on glasses contain low amount of organics that are easily removed during thermal annealing (aging process), where the pre-hardening of Si-O-Si matrix occurs simultaneously. Moreover, UV-curing of spin-on dielectric occurs in a (or alternatively e-beam curing or thermal curing) separate process step [18]. On the contrary, the PECVD approach realizes the final film hardening and the organic porogen removal in one UV-curing process that results in PR-creation [19]. Therefore, a possible solution to avoid PR-creation (which has negative effect on YM) is to remove the organic part (porogen) from the PECVD film matrix before the regular UV-curing, similar to the spin-on deposition approach. The PECVD deposition process occurs at sufficiently high temperature of 300 °C, so we can assume that similar phenomena occur as in aging process of spin-on films. The porogen agglomeration in the film should occur already during the film deposition. Therefore, the matrix should be sufficiently stiff (should not collapse) to allow porogen removal prior to regular UV-curing.

6.4 Selective porogen removal from PECVD dielectric

One of the biggest challenges of porogen removal from PECVD OSG is selectivity. The removal of organic porogen should occur without modification of the organo-silica skeleton. The skeleton modification may lead to unwanted densification or hydrophilization of the OSG (and consequently increase in *k*-value). For instance, the porogen removal by only thermal annealing requires temperatures higher than 350˚C that also leads to PR creation and skeleton cross -linking that results in OSG densification [20]. This is due to porogen thermo-dissociation temperature that is higher than temperature required for skeleton cross-linking [20]. Therefore, the porogen removal has to be realized in lower temperatures than 350 ˚C. One possible way to realize selective porogen removal is annealing the OSGs at 280 ˚C in H_2-based plasma afterglow treatment (H_2-AFT) as discussed in section 5.5 . This process is similar to zero damage photeresist mask removal process reported elsewhere [21,22]. The organic photo masks containing C-C, C=C and C-H bonds can be selectively removed from Si-CH_3-bond containing SiOCH low-*k* dielectrics, without any Si-CH_3 bonds scission as demonstrated in section 5.5.1. Normally, the Si-CH_3 bonds scission leads to their replacement with Si-OH bonds and subsequent hydrophilization of OSG that results in drastic increase of *k*-value (k_{H2O} is around 80 at 100 kHz) as discussed in section 1.7.1. The PR or the porogen also contain C=C and C-C bonds or C-H bonds, therefore should be also selectively removed from low-*k* film matrix. In order to demonstrate this, we studied the effects of 350 s H_2-AFT at 280 °C and UV treatments at 350°C on as-deposited matrix-porogen PECVD films of 60 nm. PECVD low-*k* films remain hydrophobic after H_2-AFT at 280 °C and UV treatments at 350°. The water contact angles with surfaces for all the films

were approximately 90 degree (see Table 6.2). The thickness loss and organic removal efficiency was evaluated by UV-SE. Less than 1% of thickness loss was measured for H_2-AFT.

6.5 Optical properties of porogen-residue-free films

Another challenge is related to quantitative evaluation of PR content in OSG matrix. Their quantitative evaluation cannot be performed by FTIR spectroscopy that has a very limited sensitivity to PR because of non-polar nature of C-C and C=C bonds [23]. Therefore, quantitative detection of PR might be possible by Raman spectroscopy [14] but this metrology sometimes is challenging because of overlap of PR related absorption and photoinduced luminescence. Another problem is that low-*k* films can degrade under laser radiation used for generation of the scattering light. For this reason we used a non-direct method, UV spectroscopic ellipsometry as discused in section 2.5.1.1. Figure 6.2 shows the optical properties of the as deposited matrix-porogen film, the H_2-AFT and the UV-cured film.

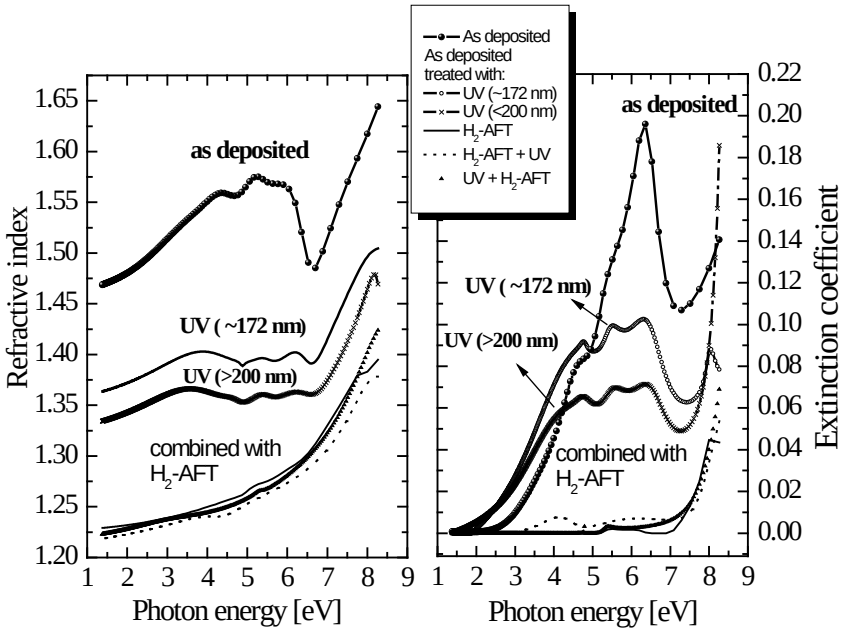

Figure 6.2. Optical properties of differently prepared OSG as measured by UV-SE: as deposited film (matrix-porogen); as deposited matrix-porogen films cured with narrowband UV-light wavelength of 172 nm (7.21 eV) and broad band UV with wavelengths higher than 200 nm (6.2 eV) , H_2-AFT and two combined H_2-AFT and 172 nm UV cures.

The extinction coefficient of the as deposited film (with porogen) is the highest due to the highest porogen content. The H_2-AFT treatment results in complete removal of the porogen and PR and the final absorption becomes similar to the UV spectra of the low-*k* matrix material as shown in Figure 6.1. On the contrary, the standard UV-curing processes using narrow band (~172 nm) or broadband (> 200 nm) UV-source results in the PR creation that is reflected in increased extinction coefficient (Figure 6.2). Furthermore, the relative changes in refractive indices of the as deposited film and treated ones reflect to the porosity increase (the pore volume has RI of air close to 1). The H_2-AFT treatments result in the highest RI reduction due to the porosity increase caused by enhanced porogen removal. In order to estimate the amount of the organic residues, we used mass balance metrology. We measured the mass loss of 300 mm wafers with 60 nm films treated with the H_2-AFT and/or 172 nm UV. The results show that the conventional 172 nm UV-curing process leaves approximately 46 % more mass in comparison to the H_2-AFT treatments. The results agree with the UV-SE data, it is that less extinction corresponding to higher mass loss.

6.6 Limited depth of porogen removal

One limiting factor for porogen removal depth is the penetration depth of the H radicals into porous low-*k*. The penetration depth of the H radicals is limited by their loss in low-*k* pores as a result of recombination on the low-*k* pore walls or chemical reaction with porogen or PR. The time dependent depth of penetration of H radicals for different low-*k* films was discussed in the chapter 5. It was demonstrated that it saturates logarithmically with time (section 5.5.2). In order to determine the depth of H radicals' penetration we treated the as deposited matrix-porogen film of 190 nm time of 350 s of H_2-AFT. Next, we measured the thickness of the porogen depleted layer by UV-SE using double-layer SE model. The depth of porogen removal was determined to be about 160 nm after 350 s of H_2-AFT. Therefore the thickness limit to achieve the uniform films using a subsequent H_2-AFT and UV-curing is about 160 nm. A thicker film fabrication should involve sequential film deposition combined with H_2-AFT curing. The UV curing should be then performed as a last step due to much higher penetration depth of UV-light (>172 nm) that is defined by Lambert-Beer law as compared to H radicals that is defined by diffusion-recombination of H-atoms on pore walls.

6.7 Effect of porogen and porogen residues on the mechanical properties of the PECVD low-k films.

In order to study the effect of porogen or PR on mechanical properties, the YM and open porosity were measured: the as deposited film, the UV-treated (standard) film, and the films after combined H_2-AFT and UV treatments. The mechanical properties of the low-*k* films were evaluated using Nano Indentation

(NI) [24]. Since the film thicknesses were relatively small, a relative YM comparison of different OSGs with similar thickness was still possible [25, 26].
Figure 6.3 shows YM versus open porosity and *k*-values. The drop in YM and increase of the open porosity after all the treatments is due to the porogen or the PR removal. As we reported previously (section 5.5) the H_2-AFT of conventionally UV-cured film (UV + H_2-AFT) results in the porosity increase, *k*-value decrease and a reduction of mechanical properties. Those changes were due to the PR removal after UV. This observation is indicated by the dashed arrows in Figure 6.3. However, when the porogen is removed by the H_2-AFT prior to the UV-curing (H_2-AFT + UV) YM of the obtained film exceeds that of the conventionally UV-cured film. The latter observation is indicated by the dotted arrows.

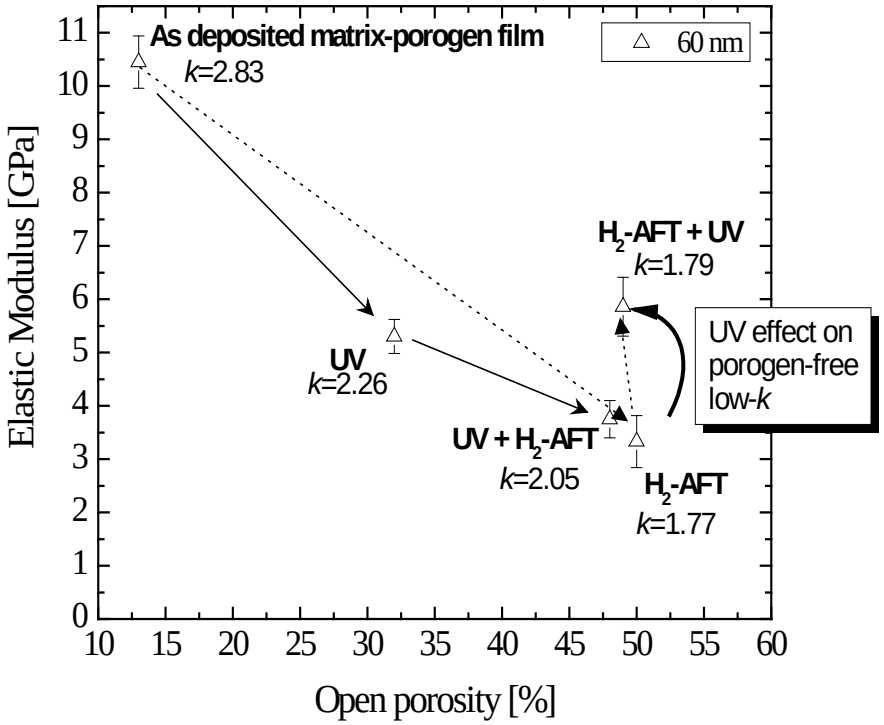

Figure 6.3 Young's modulus as measured by NI versus Open Porosity as measured by TEP. The *k*-values for all conditions were measured by Hg-probe system at 100 kHz.

We propose that the porogen removal prior to the UV-curing prevents a cross-linking of the porogen inside the SiOCH skeleton. Therefore, the subsequent creation of the PR inside the low-k film skeleton is avoided. Moreover, the cross-linkage of the mechanically strong SiOCH skeleton is not limited by the presence of organic PR as shown in Therefore, much stronger Si-O bonds are created in the SiOCH skeleton in the absence of porogen. The Si-O links significantly improve YM of the film.

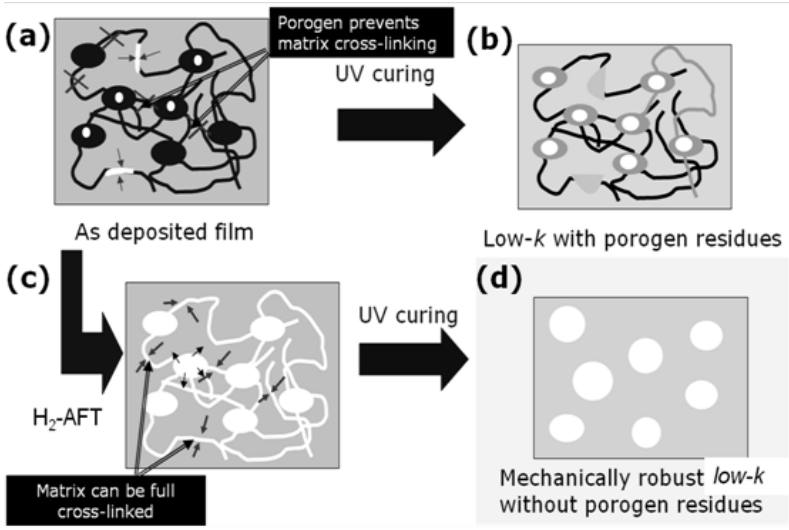

Figure 6.4 Sketch of the simplified multi-phase structure of PECVD material after: (a) deposition, (b) conventional UV-curing, (c) H_2-AFT treatment, and (d) UV-curing when porogen was removed by H_2-AFT. Areas with colors white, light grey and black denote air, organo-silica skeleton and porogen, respectivelly. Dark gray on picture (c) represents porogen residues.

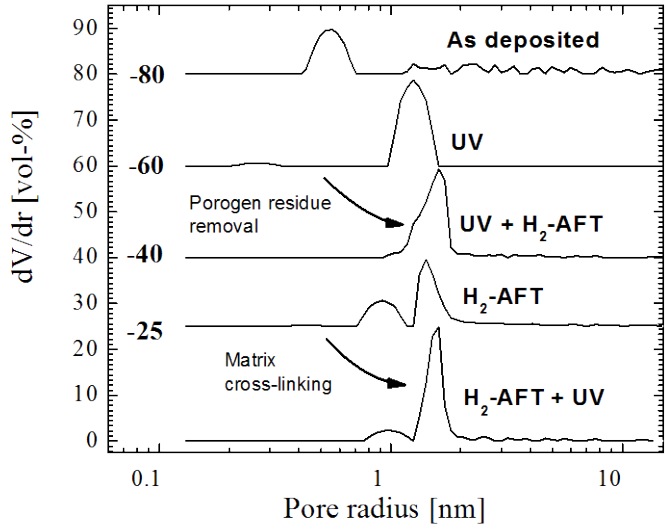

Figure 6.5 PSD of the as deposited and the treated PECVD OSGs as measured by Ellipsometric Porosimetry. The PSD were calculated from the desorption branches. Distributions have been shifted vertically for clarity.

The pore size distribution (PSD) measurements (Figure 6.5) agree with the sketch as shown in Figure 6.4.The as deposited OSG is micro porous (Figure 6.4a) and it has 13% of open porosity. After the conventional UV-curing the porosity increases and the pores become larger. However, the pore radius of the conventionally UV-cured OSG is partly defined by the presence of PR on the pore walls (Figure 6.4b). This is clearly reflected in the enlarged pores after the PR removal by H_2-AFT. The PSD-measurement of the H_2-AFT treated PECVD films reveals that, PSD of the matrix contains both: micropores and mesopores (Figure 6.4c). When PR-free matrix is exposed to UV light the micropores disappear due to the creation of additional cross-links (SiOCH matrix densification), and as a result the OSG becomes mesoporous.

6.8 Effect of UV-wavelength used for hardening of organic-free films

In the previous sections we show that we can obtain mechanically-robust and organic-free films. The films were hardened with a narrow-band 172 nm UV-light source. This section focuses on the importance of UV-wavelength used for the organics-free film hardening. The UV-irradiation effects on the organic-free films are expected to be different than that for the organic-containing films. This is due to presence/absence of organics (graphitized carbon or cyclic hydrocarbons) that changes optical properties of the films as shown by UV-SE (Figure 6.2). The removal of porogen from the film decreases its absorption (extinction) in the range of 3 eV (413 nm) to 6.8 eV (182 nm). Therefore, less photochemical reactions could be initiated during the UV-curing in this range, limiting its effects. Photochemical reactions are governed by Grotthus-Draper and Einstein-Stark Laws [27]. Grotthus-Draper law states that the light that is absorbed can be effective in producing photochemical change. The latter law indicates that shorter 172 nm UV is expected to cause more photochemical changes due to higher absorption by low-*k* than the light with longer wavelength i.e. 200 nm.

Another challenge, besides the selection of the optimal UVwavelength is related to nature of UVcuring process. The UV-irradiation is shown to generate a rearrangement in the bonding structure of the SiCOH-based low-*k* [12]. As a result, the mechanical properties are improved, but the hydrophobic properties are degraded due to -CH_3 group removal. Subsequent moisture absorption into the porous structure significantly increases the *k*-value of dielectric film because of high polarizability of water molecules. Most of results of low-*k* dielectrics UV-curing reported so far are related to wideband UV sources [12]. It is expected that narrow band UV sources are more efficient for understanding of precise mechanisms of modification and such data are important for optimisation of technological processes. Optical transmission measurements of SiCOH based layers showing transparency in the far UV range with increasing absorption in the VUV suggest the use of excimer light source. The main advantage of an excimer light source is that it can emit light with a very narrow spectral distribution.

Therefore, in the first sub-section (6.8.1) we present conclusions related to UV-curing of organic-free spin-on films by the excimer sources and in the second sub-section (6.8.2) we compare our findings for UV-curing systems with 2 different wavelengths on PECVD films. The UV-curing effect on the porogen-containing and porogen-free films is investigated.

6.8.1 Spin-on films cured by excimer UV sources: 172 nm, 222 nm, and 308 nm

The samples used in this study were silica-based low-*k* films deposited on 200 mm silicon wafers by spin-on method (non-cured film similar to N in Table 2.2). The films had 10-12 % carbon-containing-hydrophobic groups, 32 % porosity, and a pore size close to 2 nm after a standard curing (thermal annealing). The *k*-value of the films was in the range of 2.3-2.4. Such prepared samples were irradiated by plasma-based, planar VUV (vacuum ultra-violet) source, which provides single or multiple bands between 120 nm and 350 nm (Figure 6.6). For this evaluation, 172 nm, 222 nm and 308 nm were used. The plasma is induced in a chamber with excimer gas mixture. The light from the plasma is emitted into processing chamber through a special quartz window. The spectral distribution of the emitted light depends on excimer gas composition as shown in Figure 6.6. During the UV exposure, the sample chamber is flowing with N_2 (99,99% purity) and continuously pumped down. N_2 pressure is about 1 Torr with flow 0.1 liter per minute.

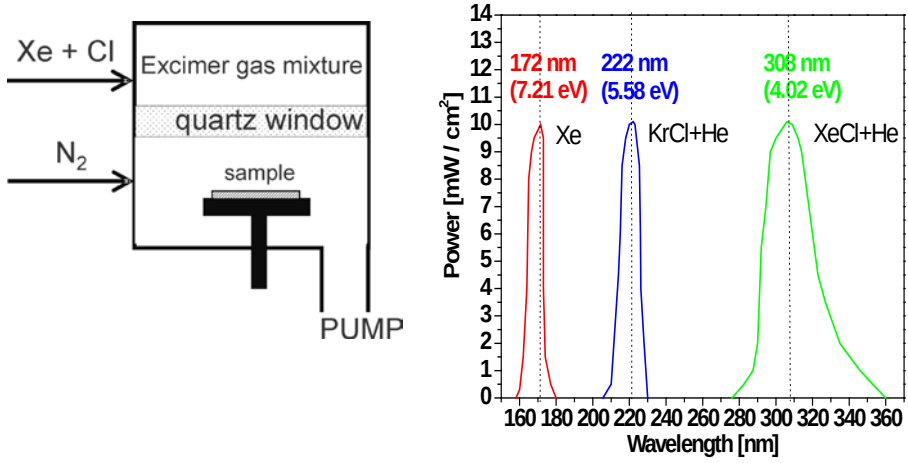

Figure 6.6 The scheme of VUV-source used for curing (left hand side) and spectral distribution of used UV-wavelengths (right hand graph).

The extinction coefficient of the spin-on low-*k* film (no UV treatment) is shown in Figure 6.2. The pristine sample has strong absorption (proportional to

extinction coefficient) below 182 nm (6.8 eV). It indicates that the UV region below 182 nm is photochemically active according to a fundamental law of photochemistry [27].

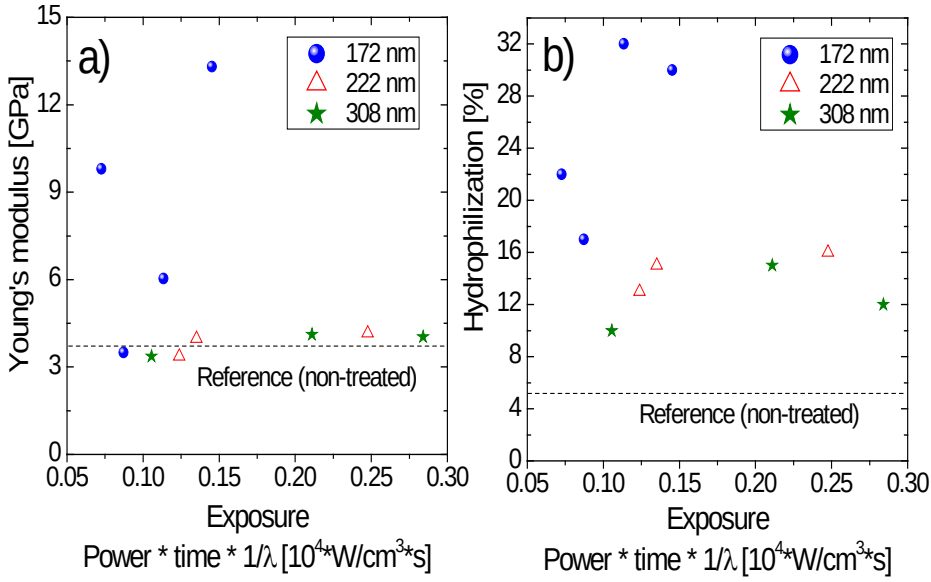

Figure 6.7 Young's modules as measured by LAwave (a) and Hydrophilicity as measured by WEP versus UV exposure (b). The dotted line represents values for non-treated sample.

Figure 6.7 reflects changes of YM and hydrophobic properties of the films after UV irradiation. The X axis presents exposure in Figure 6.7. The exposure is product of UV power, time of treatment and light frequency. The highest changes in YM are observed for 172 nm (Figure 6.7a). This improvement of mechanical properties indicates that wavelength of light below 182 nm causes the highest efficiency of photochemical reactions. The dielectric films treated with 222 and 308 nm UV reveals small improvement of YM. This correlates well with degree of hydrophilization as measured by WEP (Figure 6.7b). The hydrophilisiation of UV treated low-k dielectrics can be related to photo-dissociation of the carbon containing groups and a cross-linking mechanism of the Si-O-Si network.

Figure 6.8 shows ratio Si-O-Si (1050 cm^{-1}) cage bond to Si-CH_3 (1276 cm^{-1}) FTIR peaks versus exposure. This ratio reflects the compromise between hydrophilicity and mechanical properties. Increasing the number of Si-O-Si groups gives better mechanical properties. While the number of Si-O-Si groups increases, a reduction of the number of CH_3 (methyl) groups is observed [28]. The methyl groups are hydrophobic due to low polarizability. Depletion of CH_3 groups leads to hydrophilization of the low-*k*.

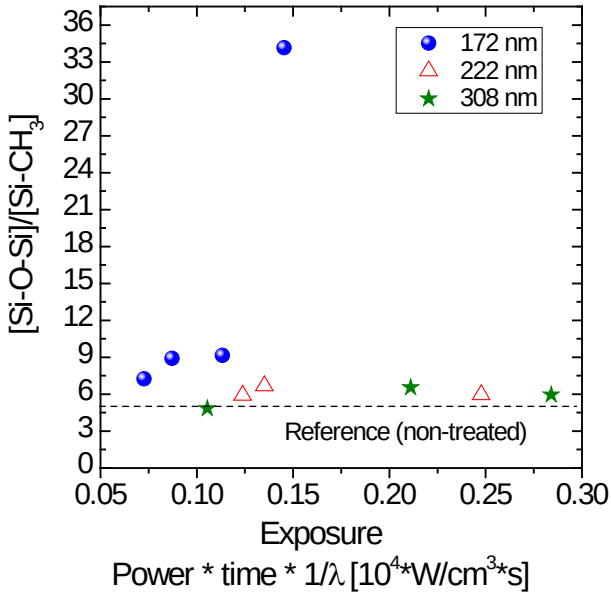

Figure 6.8 The ratio of the integrated absorbance of Si-O-Si (950 cm^{-1} to 1250 cm^{-1}) groups to Si-CH_3 groups (1265 cm^{-1} - 1280 cm^{-1}) versus exposure. The absorbance values were measured by FTIR. The dotted line represents values for non-treated sample.

Table 6.1 Basic characteristics of the as deposited and treated films. The film is similar to N film in Table 2.2. However, the reference N film used here is non-UV cured.

Nr.	Wave length [nm]	Time [min]	Power [mW/cm^2]	FTIR Si-O/Si-CH_3	TEP Pore radii [nm]	TEP Open Porosity [%]	WEP Hydrophil. [%]
1	172	10	1.5	8.90	0.80	32	17
2	172	5	2.5	7.24	0.75	26	22
3	172	10	2.5	34.14	0.60	27	30
4	172	3	6.5	9.15	0.60	32	32
5	222	10	3	6.68	0.85	33	15
6	222	5	5.5	5.90	0.90	33	13
7	222	10	5.5	5.94	0.80	32	16
8	308	5	6.5	4.83	0.90	32	10
9	308	10	6.5	6.52	0.80	34	15
10	308	5	17.5	5.94	0.90	31	12
11	Pristine	-	-	4.61	1.00	32	5

The results of our tests and settings of the UV system are summarized in Table 6.1. These data show that the highest modification of low-*k* films occurs after 172 nm irradiation due to strong absorption of our material in this region. This correlates with a reduction of porosity and a mean pore radius (as measured by TEP, see section 2.5.2.1). Moreover the ratio Si-O/Si-CH_3 (as calculated from FTIR) reflects that improvement of mechanical properties leads to reduction of the number of hydrophobic Si-CH_3 groups. This correlates with WEP data. Mechanical properties are improved but hydrophobic properties are degraded. In the region of 200 nm – 400 nm the impact of photochemical reactions is low because of low low-*k* absorption. Moreover the Si–CH_3 bond scission in a low-*k* matrix has been reported to be defined by excitation to a singlet state that requires energy around 6.3 eV (190–197 nm) [29]. The photolysis of Si-CH_3 bonds besides hydrophilization of low-*k* films produces active silyl states. The active silyl states can react with another silyl state or Si-OH. This leads to creation of Si-Si links and Si-O-Si links in the skeleton of the film. The improved cross-linking of the film results in its better mechanical properties.

In summary the largest improvement of the mechanical properties of the low-*k* studied occurs during 172 nm UV-irradiation. This is due to two reasons. The first reason is related to optical properties of the film defining its absorption edge. The absorption edge of the SOG low-*k* matrix lies below 180 nm. The second reason is due to photo-chemical threshold for photolysis of Si-CH_3 bonds that lies below 200 nm. The photolysis of Si-CH_3 bonds significantly increase the amount of possible reactions in the film structure that leads to improvement of its mechanical properties.However, improving the mechanical properties of low-*k* films by the UV light irradiation also leads to their significant hydrophilization. This phenomenon is related to removing of hydrophobic carbon-containing groups as a result of UV induced photo-dissociation of Si-CH_3 groups and Si-O-Si cross-linking mechanism (resulting in removal of Si-CH_3 groups). The degree of hydrophilization of 172 nm UV cured films was higher than in the case of 222 nm and 308 nm UV. One reason could be related to the smaller degree of photo-chemical reactions due to lower UV light absorption for 222 nm and 308 nm wavelengths.

6.8.2 PECVD films with and without porogen cured with: narrow-band 172 nm and broad band 200 nm UV sources

In the previous section we show that the effect of UV-curing significantly differs for shorter UV wavelength of 172 nm and longer UV wavelengths than 200 nm on organic free spin-on films. This section we show that the latter observation is valid for PECVD films. Moreover, we demonstrate that the UV-irradiation of the porogen containing film with wavelengths higher than 200 nm results in the significant improvement of their Young's modulus. On the contrary the films cured with UV of 200 nm without porogen show the minimal improvement of Young's modulus in contrast to 172 nm UV-cured ones. This is explained by the significantly reduced film absorption of UV-light above 200 nm (due to porogen removal) that influences degree of possible photochemical reactions as discussed in previous

section 6.8.1. Therefore in our new PECVD curing approach the UV below 200 nm should be used to achieve a considerable improvement in the mechanical properties.

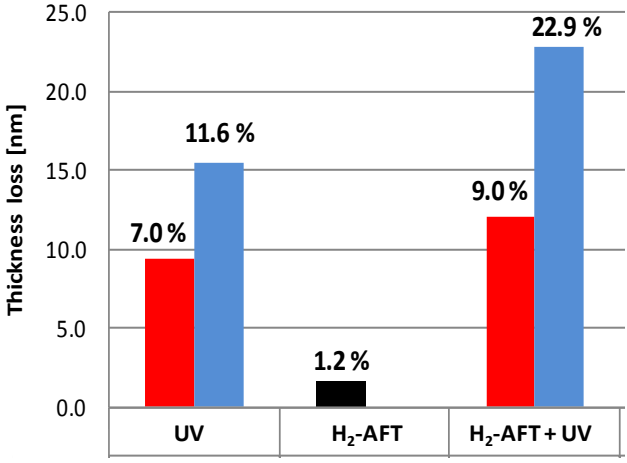

Figure 6.9 Thickness loss for the PECVD films treted with narrow band 172 nm (blue bars) and broadband 200 nm (red bars) UV sources. The thickess loss reflects film shrinkage after UV-irradiation.

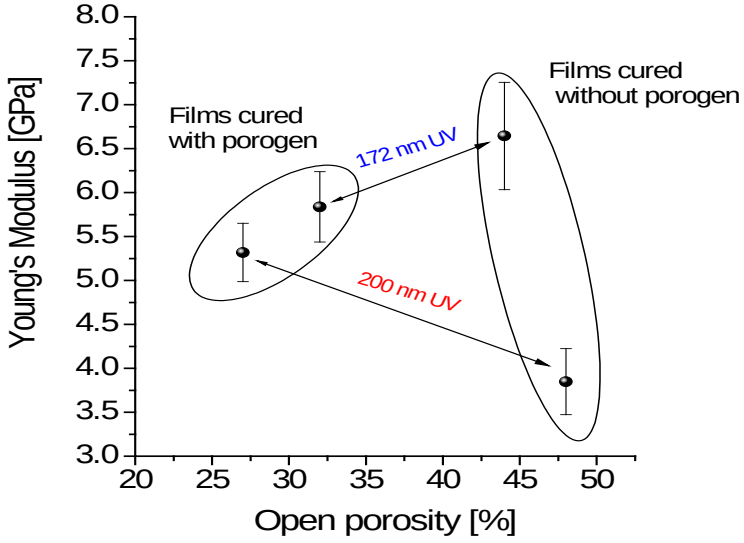

Figure 6.10 Young's modulus as measured by NI versus Open Porosity as measured by TEP. The arrows indicate effect of the narrow band 172 nm and broadband 200 nm UV sources on the porogen containing and porogen free films.

One of the film cross-linking signatures is its shrinkage after UV-hardening process. The shrinkage is reflected in thickness loss of the film (measured by UV-SE) after UV-irradiation as shown in Figure 6.9. One can see that irradiation of the porogen-containing and porogen-free films by narrow band UV source of 172 nm lead to higher thickness loss than for broadband light with wavelength higher than 200 nm. This indicates that degree of film cross-linking is higher when narrow band 172 nm UV source is used for film curing also. Moreover, there is a clear difference in the film thickness loss depending on the UV wavelength used for curing. This difference is smaller for the porogen-containing films "UV" and higher for the porogen-free films "H_2-AFT +UV". For instance, the thickness loss is significantly higher for 172 nm UV than for 200 nm UV when films are cured without porogen "H_2-AFT + UV". The "H_2-AFT" bar reflects the minimal change of thickness when porogen is removed by H_2-AFT. This proves that H_2-AFT does not result in the film cross-linking.

The degree of the film cross-linking reflected in its thickness loss (Figure 6.9) corresponds to the improvement of Young's modulus as shown in Figure 6.10. Figure 6.10 shows Young's modulus as function of film open porosity. The porosity is lower when films are UV-cured with porogen. This is due to the fact that some part of the porogen is converted by UV-light into porogen residues as discussed in Chapter 5 and section 6.7. The achieved YM are slightly better when porogen-containing film is cured with 172 nm UV source. On the contrary the improvement in YM is almost 2 times higher for 172 nm UV than for 200 nm UV if the films are cured without porogen. This shows that presence/absence of porogen during UV-curing have strong impact on this effect. This is due to change of the film absorbtion induced by organic porogen removal. Reduction of the film absorption in the range of 200 nm to 400 nm significantly limits the improvement of YM films for UV-light longer than 200 nm. Therefore, in order to achieve a mechanically robust film in the proposed scheme the 172 nm UV-light must be used.

6.9 Fabrication of the porogen-free films with variable thicknesses

In order to confirm our above findings and show the possibility of thicker film fabrication by the proposed new method we cured the porogen-free glasses with variable thicknesses and compared their properties to the conventional OSGs cured with porogen. The as deposited films (Ea in Table 2.2) with thicknesses of 65 nm, 120 nm and 190 nm, 2x120 nm and 5x120 nm were prepared using subsequent H_2-AFT and 172 nm UV-cure. The 2x120 nm and 5x120 nm OSGs were prepared by repeated PECVD of 120 nm films combined with the subsequent 350 s H_2-AFT. The basic properties of the obtained OSGs are reported in Table 6.2. first two films of 58 nm and 105 nm, uniform from top to bottom, were obtained by subsequent H_2-AFT and 172 nm UV-curing. The open porosity and the mean pore radii of uniform OSGs with thicknesses of 58 nm and 105 nm were measured by TEP. Both glasses have 46 % of porosity and mean pore radii of 1.5 nm. The YM were 5.82±0.82 GPa for the 58 nm glass and 5.46±0.51 GPa for the 105 nm glass. In the case of the 190 nm film,

the porogen was only partly removed due to the limited penetration of H-atoms to about 160 nm. The subsequent UV-light irradiation of 190 nm film results in creation of a bi-layer OSG. Presumably, the transport of decomposed porogen fragments induced by UV-light resulted in increased film shrinkage as compared to the thinner films (enhanced cross-linkage of the SiOCH matrix). We additionally investigated the multi-layered OSGs. The optical properties of those glasses as measured by UV-SE were fitted with a good accuracy using a single layer ellipsometric model. Therefore the 2x120 nm and 5x120 nm have homogeneous optical properties; this indicates bulk uniformity. The OSGs were cured with the same times as porogen containing ones with the same thickness. The results clearly show in Table 6.2 that the same UV-curing time results in much higher improvement of YM and H of porogen-free films. Moreover, the extended UV-curing time to 1800 s of porogen containing 600 nm OSG results in significantly lower YM and hardness than 835 s UV-cured porogen-free OSG. It is also important to mention that longer UV-cure times lead to hydrophilization due to photo-dissociation of Si-CH_3 groups from OSG and a subsequent moisture absorption from ambient [30,31] (see also section 6.8.1). The latter phenomenon results in slightly higher *k*-values and lower WCA of thicker porogen-free OSG since UV-curing time was longer. This effect is less pronounced for porogen containing OSG since decomposed organic porogen fragments such as CH_x groups can passivate dangling bonds created as result of Si-CH_3 bond scission.

Table 6.2 Comparison of the properties of conventionally UV-cured with H_2-AFT + UV cured OSGs. The used abbreviations denote: Thinit (initial thickness), Thfinal (final thickness), WCA (water contact angle), MPR (mean pore radii), H (hardness). The conventional spin-on film characteristics prepared by nano-clustering of silica nano-particles were added for comparison.

Th_{int} [nm]	AFT [s]	UV [s]	Th_{final} [nm]	CA [deg]	*k* at 100 kHz	YM [GPa]	H [GPa]	OP [%]	RI 632 nm	PR [nm]
65	350	81	58	93	1.79	5.82±0.82	0.63±0.07	46	1.223	1.5
120	350	166	105	91	1.87	5.46±0.51	0.60±0.08	46	1.228	1.5
190	350	249	154	88	2.24	7.08±0.62	0.77±0.06	N/A	N/A	N/A
240	2x350 +	333	191	79	2.30	8.38±0.52	0.80±0.08	43	1.250	1.4
600	5x350 +	835	481	67	2.60	9.50±0.61	1.00±0.05	41	1.266	1.4
67	-	83	59	93	2.26	5.30±0.42	0.49±0.03	32	1.371	1.0
190	-	249	180	93	2.30	4.48±0.16	0.39±0.03	32	1.373	1.9
600	-	835	498	91	2.30	4.61±0.32	0.57±0.08	32	1.375	1.0
600	-	1800	462	57	2.49	5.72±0.41	0.69±0.09	30	1.408	1.0
140	Spin-on film			91	2.30	6.54±0.77	0.80±0.08	32	1.277	1.0

Finally we demonstrate that novel concept of the low-*k* film fabrication allows to achieve remarkably higher YM normalized to *k*-value in comparison with other low-*k* materials studied at imec. This can be demonstrated by comparing properties of 105 nm film (Table 6.2) with low-*k* films evaluated at imec as shown in Figure 6.11. We select three fundamental film properties: *k*-value, pore size and mechanical properties. These properties out of many others need to be controlled in order to integrate low-*k* dielectric as discussed in section 1.6. Figure 6.11 clearly shows that improved approach of PECVD film fabrication demonstrated better characteristic compared to other films. Moreover, new material fulfils the studied ITRS roadmap requirements (marked by green area). Therefore, the presented method shows the potential for fabrication of low-*k* dielectric films for future microelectronic technology nodes.

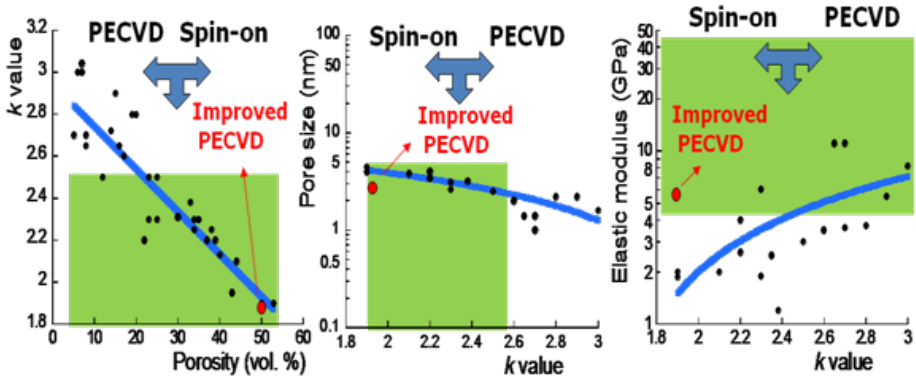

Figure 6.11 Comparison of three fundamental properties of the variable low-k materials evaluated at imec: *k*-value, pore size, and elastic modulus (Young modulus). The green area is the ITRS roadmap specification. The arrows indelicate that below *k*- value of 2.5 spin-on films were integrated and above the k-value of 2.5 PECVD films. The red points show the properties of the PECVD low-*k* film fabricated using novel concept proposed in this thesis.

6.10 Mechanism of mechanical properties improvement

Extraordinary mechanical properties of the H_2-AFT and UV treated films can be reasonably interpreted within the framework of the continuous random network theory and percolation of rigidity concepts first developed by Philips [32] and expanded upon by Thorpe [33]. The percolation of rigidity defines a compositional point in a network where the system transitions from an underconstrained non-rigid state to an overconstrained rigid state. Systems above the percolation threshold would thus be expected to have superior mechanical properties as compared to those below the threshold, owing to the increased structural constraints. The key parameter in this analysis is the average connectivity number

<r>. The connectivity number is the average number of bonds per network forming atom. Network forming atoms have two or more bonds to other network forming atoms, and atoms having only one bond, such as hydrogen, do not contribute to the network and are not counted in the analysis. Dohler et al. [34] determined that the percolation of rigidity occurs at an average connectivity number of 2.4 for solids in which all atoms are able to form two or more bonds. This connectivity number of 2.4 for SiOCH materials is when only T-groups ($O{\equiv}Si\text{-}CH_3$) are present in the structural composition of the low-*k* film [35]. This is the case for our films as evidenced by FTIR data (Figure 6.12)

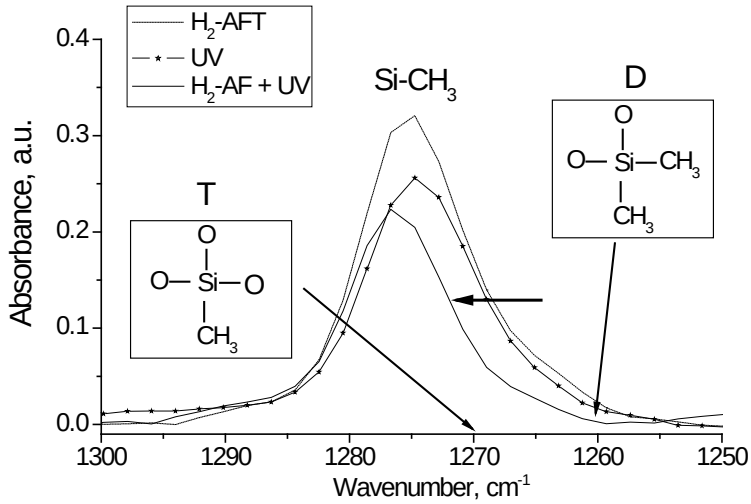

Figure 6.12 The infra-red absorption (as measured by FTIR) of terminal Si-CH_3 groups from the 60 nm OSGs treated with: 172 nm UV, H_2-AFT and subsequent H_2-AFT and 172 nm UV.

The important difference is the shift of the Si-CH_3 absorption band (1250-1300 cm^{-1}) of H_2-AFT + UV treated film. This band can vary in position based upon the degree of oxidation of Si atom, with increasing oxidation shifting the band to higher wavenumbers [36]. The three most basic possibilities for the configuration are designed as "M" (~1250 cm^{-1}), "D"(~1260 cm^{-1}), "T" (~1270 cm^{-1}), reflecting either mono-, di-, or trisubstitution of the silicon atom by oxygen[35, 36]. Therefore, for the H_2-AFT + UV treated glass, the shift of Si-CH_3 absorption band could be explained by the presence of mainly a T-rich structure, indicating the incorporation of more oxygen into the OSG and potential cross-linking.

In order to prove our statement above we compared shift in Si-CH_3 group absorbance of porogen-free films cured with 200 nm UV and 172 nm UV as shown in Figure 6.13. The 200 nm UV cured films shows significantly lower YM than 172 nm UV-cured ones as discussed in section 6.8.2 (Figure 6.10). This corresponds with almost no shift in Si-CH_3 group absorbance that shows that D groups are still

present in 200 nm UV-cured films. The presence of D groups in the film structure results in its weaker mechanical properties. In contrast 172 nm UV cured films contains only T-groups and shows almost twice as higher mechanical properties for comparable porosity level (Figure 6.10).

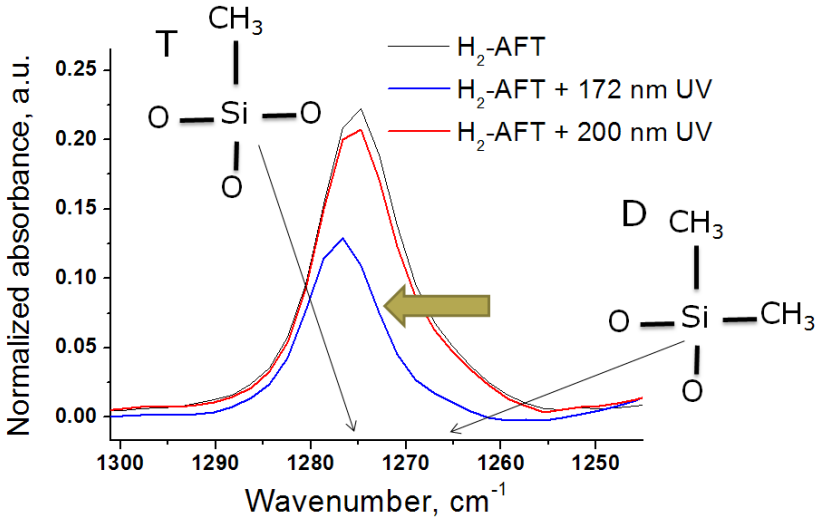

Figure 6.13 The infra-red absorption (as measured by FTIR) of terminal Si-CH_3 groups from the 120 nm OSGs treated with: H_2-AFT and subsequent H2-AFT and 172 nm or 200 nm UV.

6.11 Chapter Summary

In summary, we demonstrated that porogen present during UV-curing of PECVD deposited OSG deteriorate its SiOCH matrix cross-linking, and that results in the reduced mechanical properties of the final film. We propose an improved fabrication procedure of enhanced chemical vapor deposited (PECVD) low-*k* films. The new procedure is performed by conventional UV-curing of PECVD film skeleton when the porogen is already completely removed. The removal of the organic porogen without Si-CH_3 bonds scission is found to be possible by annealing of the low-*k* film in a H_2-based plasma afterglow. The effective depth of the porogen removal depends on the penetration depth of the active H radicals into the porous SiOCH matrix and it is found to be approximately 160 nm. The proposed method allows us to obtain porogen residue-free low-*k* films with variable thicknesses. The obtained films demonstrate extraordinary high Young's modules of 5 - 9.5 GPa for open porosity in the range of 41-46 %, *k*-value of 1.8-2.6. The extraordinary mechanical properties can be explained on the basis of percolation of rigidity theory. The presented method shows the potential for fabrication of low-*k* dielectric films for future microelectronic technology nodes.

6.12 References

[1] K. Maex, M. R. Baklanov, D. Shamiryan, F. Iacopi, S. H. Brongersma, Z. S. Yanovitskaya, J. Appl. Phys. 2003, 93, 8793.

[2] D. Shamiryan, T. Abell, F. Iacopi, K. Maex, Materials Today 2004, 34.

[3] M. R. Baklanov, K. Maex, Philos. Trans. R. Soc. London. Ser. A 2006, 364, 201.

[4] G. Dubois, R.D. Miller, W. Volksen, in Dielectric Films for Advanced Microelectronics, (Eds:M. Baklanov, M. Green, K. Maex) Jonh Wiley & Sons, Ltd, UK 2007, Ch. 2

[5] H. Y. Fan, C. Hartshorn, T. Buchheit, D. Tallant, R. Assink, R. Simpson, D. J. Kisse, D. J. Lacks, S. Torquato, C. J. Brinker, Nat. Mater 2007, 6, 418.

[6] G. Dubois, T. Magbitang, W. Volksen, E. E. Simonyi, R. D. Miller, "New Spin-On Low-k Dielectric Materials With Exceptional Mechanical Properties", presented at International Interconnects Technology Conference, 6-8 June, 2005.

[7] D. D. Burkey, K. K. Gleason, J. Appl. Phys. 2003, 93, 5143.

[8] H. Li, Y. B. Lin, T. Y. Tsui, J. J. Vlassak, J. Mat. Res. 2009, 24, 107.

[9] A. Grill, in Dielectric Films for Advanced Microelectronics, (Eds:M. Baklanov, M. Green, K. Maex) Jonh Wiley & Sons, Ltd, UK 2007, Ch. 1

[10] R. Sreenivasan, K. K. Gleason, Chem Vapor Depos 2009, 15, 77

[11] A. Grill and V. Patel, Appl. Phys. Lett. 2001, 79, 803.

[12] F. Iacopi, Y. Travaly, B. Eyckens, C. Waldfried, T. Abell, E. P. Guyer, D. M. Gage, R. H. Dauskardt, T. Sajavaara, K. Houthoofd, P. Grobet, P. Jacobs and K. Maex, J. Appl. Phys., 99, 053511 (2006).

[13] M. Ikeda, S. Nakahira, Y. Iba, H. Kitada, N. Nishikawa, M. Miyajima, S. Fukuyama, N. Shimizu, K. Ikeda, T. Ohba, I. Sagiura, K. Suzuki, Y. Nakata, S. Doi, N. Awaji, E. Yano, "A Highly Realiable Nano-Clustering Silica with Low Dielectric Constant (k<2.3) and High Electric Modulus (E=10 GPa) for Copper Damascene Process", presented at IEEE International Interconnect Technology Conference, 2003.

[14] M. Matsuura, K. Goto, N. Miura, J. M. Haag, S. Hashii, K. Asai, in Mat. Res. Soc. Symp., Vol. 914 (Eds: T. T. Tsui, Y.-C. Joo, L. Michaelson, M. Lane, A. A. Volinsky), Mater. Res. Soc. Symp. Proc., San Francisco, CA 2006, F01.

[15] G. Aksenov, D. De Roest, P. Verdonck, F. N. Dultsev, P. Marsik, D. Shamiryan, H. Arai, N. Takamure, M. Baklanov, in Mater. Res. Soc., Vol. 1156 (Eds: M. Gall, F. Iacopi, M. Koike, T. Usui), Mater. Res. Soc. Symp. Proc., San Francisco, CA 2009, D02.

[16] W. Volksen, D. M. Miller, G. Dubois, Chem. Rev. 2010, 110, 56.

[17] A. Grill in Dielectric Films for Advanced Microelectronics, (Eds:M. Baklanov, M. Green, K. Maex) Jonh Wiley & Sons, Ltd, UK 2007, Ch. 1

[18] T. Owada, N. Ohara, H. Watatani, T. Kouno, H. Kudo, H. Ochimizu, T. Sakaoda, N. Asami, Y. Ohkura, S. Fukuyama, A. Tsukune, M. Nakaishi, T. Nakamura, Y. Nara, M. Kase, "Advanced BEOL Integration Using Porous Low-*k* (k=2.25) Material With Charge Damage-less Electron Beam Cure Technique", 2009

[20] A. Zenasni, F. Ciaramella, V. Jousseaume, C. Le Cornec, G. Passemard, J. Electrochem. Soc. 2007, 154, G6.
[21] I. L. Berry, Q. Han, C. Waldfried, O. Escorcia, A. Becknell, "Use of plasma assisted sublimation to remove photoresist from porous low-k dielectrics", SEMI® Technical Symposium: Innovations in Semiconductor Manufacturing, 2004.
[22] W. Chen, Q. Y. Han, R. Most, C. Waldfried, O. Escorcia, I. Berry, Journal of the Electrochemical Society 2004, 151, F182.
[23] K. J. Miller, Journal of the American Chemical Society 1990, 112, 8533.
[24] D. J. Morris, R. F. Cook, Journal of Materials Research 2008, 23, 2443.
[25]M. Gonzalez, K. Vanstreels, A. M. Urbanowicz, "Modeling the Substrate Effects on Nanoindentation Mechanical Property Measurement", presented at 10th Int. Conf. Thermal, Mechanical and Multiphysic Simulation and Experiments in Micro-Electronic - EuroSimE, Delf, Netherlands, 27 may, 2009
[26] K. Vanstreels, A. M. Urbanowicz, J. Vac. Sci. Technol. B 2010, 28, 7.
[27] M. R. Senapati, Advanced Engineering Chemistry, p. 56, Laxmi Publications (P) Ltd., New Delhi 2006.
[28] K. Yoneda, M. Kato, K. Kobayashi, N. Matsuki, K. Matshushita, N. Ohara, A. Fukazawa and T. Kiura, in IITC, p. 220 (2005).
[29] L. Prager, P. Marsik, L. Wennrich, M. R. Baklanov, S. Naumov, L. Pistol, D. Schneider, J. W. Gerlach, P. Verdonck, M. R. Buchmeiser, Microelectron. Eng. 2008, 85, 2094.
[30] S. Eslava, F. Iacopi, A. M. Urbanowicz, C. E. A. Kirschhock, K. Maex, J. A. Martens, M. R. Baklanova, J. Electrochem. Soc.2008, 155, G231.
[31] P. Verdonck, D. De Roest, S. Kaneko, R. Caluwaerts, N. Tsuji, K. Matsushita, N. Kemeling, Y. Travaly, H. Sprey, M. Schaekers, G. Beyer, Surf. Coat. Technol. 2007, 201, 9264.
[32] J. C. Philips, J. of Non-Crystalline Sol. 1979, 34, 153.
[33] M. F. Thorpe, J. of Non-Crystalline Sol. 1983, 57, 355.
[34] G. H. Dohler, R. Dandoloff, H. Biltz, J. Non-Cryst. Sol. 1980, 42.
[35] D. D. Burkey, K. K. Gleason, J. Appl. Phys. 2003, 93, 5143.
[36] R. Anderson, L. L. Larson, C. Smith, Silicone Compounds: Register and Review, Huls America, Bristol, Pa 1987.

7 General conclusions and prospects

In this work processing challenges related to interconnect in ultra-large-scale integrated (ULSI) circuits were investigated. Interconnects are the structures used to transmit electrical signals between active areas in semiconductor chips. Copper as a wire and low dielectric constant (low-*k*) materials as insulators were introduced to relieve the increasing interconnect RC delay as continuous critical dimensions (CDs) scale down. One of the biggest challenges of Cu/low-*k* (damascene) technology is decreasing the *k*-value of low-*k* dielectrics since this requires increasing of their porosity. The porous dielectrics are more prone to processing damage due to reduced mechanical resistance and an increased permeability of process chemicals. Nowadays, porous low-*k* films based on silica and silsesquioxanes with 10-15 % of organic (carbon containing) hydrophobic groups (such as Si-CH_3) are the most favored class of materials for advanced interconnect technology nodes. The exposure of these films to a (etch) plasma ambient leads to the loss of hydrophobic groups and to the densification of their silica backbone. The extent of this damage strongly depends both on the low-*k* material properties such as the porosity and on the plasma conditions such as the chemistry and the power. The goal of this doctoral thesis was the investigation of the process induced damage of low-*k* dielectrics, methods of damage prevention and damage evaluation.

In summary the main conclusions can be stated as follows:

- New metrology concepts are required to understand and improve current damascene processing sequence of porous low-*k* materials (chapter 3)
  - The near field microwave impedance can be used for characterization of the dielectric constant of patterned structures without their metallization. This allows deconvolution of the impact of plasma processing from the metallization process impact.
  - A novel concept of low-*k* material hydrophilization monitoring using a plasma chamber and *in situ* OES measurement was proposed. This idea allows monitoring the extent of low-*k* hydrophilization immediately after its processing (in-line monitoring in plasma chamber).

- Processing plasmas produced in capacitively-coupled and inductively coupled plasma chambers always damage low-*k* film when they come into contact with it. The damage depth differs significantly, from the surface layers till 160 nm of bulk (chapters 4 and 5). It has been found that:
  - The depth of damage mainly depends on diffusion/recombination rates of active radicals in pores of low-*k* material

- Depth of damage can be reduced by surface modification i.e., using VUV radiation from He plasma, prior to the plasma process. The modification results in sealing/reducing the pore size and generates active centers that traps radicals from the processing plasma (chapter 4).

- Damage-free processing of photo mask removal can be realized using an afterglow H_2-plasma at elevated temperature (pure chemical treatment) (chapter 5) combined with porogen-residue free low-*k* (chapter 6). Although, there is a wide variety of plasma chambers, it is found that:
  - Downstream plasma chambers are most suitable for photoresist removal (chapter 5)
  - The etch clusters for optimized damascene technology should contain ICP, CCP and Downstream plasma chambers altogether (chapter 2). For zero damage ash process the usage of ICP or CCP plasma chambers should be avoided. The ICP, CCP chambers are to be used for patterning and ion-assisted cleaning/passivation processes.

- The current way of fabrication of PECVD ultra low-*k* materials ($k < 2.3$) has to be improved in order to remove C-containing porogen residues. These are found to reduce the mechanical properties and cause increased leakage of the low-*k* dielectric. In the current state of the art spin-on technology (self-assembling approach to introduce porosity) shows more potential for ultra low-*k* materials i.e. NCS (chapter 6).
  - Improvement of ultra low-*k* PECVD materials can be realized by removing the porogen prior to UV-curing for instance using annealing in an H atoms atmosphere (chapter 6)
  - Selection of UV-wavelength used for UV-hardening of low-*k* materials is critical. Optimal UV-wavelength for porogen-residue free low-*k* films is found to be around 172 nm due UV-absorption threshold of those materials (chapter 6).

To conclude, four major recommendations related to damascene technology are proposed in this thesis. The first recommendation is about the development of new metrology and analytical methods discussed in chapter 3. This is crucial for optimal monitoring of the solutions related to process optimization and material properties improvement. Next three recommendations are related to improvements of the plasma processing and improvement of low-*k* material properties. Two ways of improvement of plasma processing are discussed in the chapters 4 and 5. The first improvement is related to the copper oxide reduction using ammonium plasma. This NH_3 plasma damages investigated low-*k* materials with a depth of approximately 90 nm. This depth of damage can be significantly reduced by a protective He plasma pretreatment of the dielectric film surface.

It was demonstrated in chapter 4 that VUV radiation for He plasma, which has limited penetration to the low-*k* (10-20 nm) can densify/seal the low-*k* surface. This modification results in significantly reduced/prevented penetration of NH_x

species in the low-*k* pores preventing its bulk damage. The second recommendation is related to the plasma-assisted removal of the organic photoresist mask from low-*k* material. Due to similarity of the chemical nature of low-*k* dielectric and photoresist mask (both contain C-H bonds), the removal of the latter shows challenges related to selectivity. Most of the treatments that remove organic photoresist mask remove also Si-CH_3 bonds from low-*k* films. This results in hydrophilization of the low-*k* film (plasma damage). It is demonstrated in chapter 5 that any direct plasma processing damages low-*k*, in both ICP and CCP plasma chambers. The selective removal of the photeresist mask can however be realized in downstream plasma system using H_2 or He/H_2 downstream plasmas. In a downstream chamber the plasma area is separated from the material. This allows pure chemical treatments (ions and direct UV exposure are eliminated by a special grids). As such these downstream plasmas are the most selective in comparison with any other physicochemical treatment. It was also found that H_2 and He/H_2 downstream plasmas remove porogen residue from the low-*k* materials without scission of Si-CH_3 bonds. The porogen residue is graphitized (sp^2) C and is created during the UV-assisted curing of low-*k* material. The porogen residue removal results in degradation of mechanical properties of the PECVD ultra low-*k* films. This might be one of the limiting factors of scaling down *k*-value for these materials. Therefore, the ultra low-*k* PECVD must be optimized in order to avoid porogen residues in their structure. Such optimization based on the findings from chapter 5 is presented in chapter 6. In chapter 6 a new concept of fabrication of porogen-free ultra low-*k* PECVD materials is demonstrated. The results show that mechanical properties per achieved *k*-value significantly exceed those for the conventional PECVD ultra-low-*k* dielectrics. For instance, the Young's modulus of conventional SiOCH-based glass with 32 % open porosity hardened with porogen is 4.60 GPa, this value is shown to increase up to 5.46 GPa with even 46 % open porosity, when the glasses are UV-cured (hardened) after porogen removal. This increase of porosity is accompanied by significant reduction of the dielectric constant from 2.3 to 1.9.

Above findings fit well with the goal of this thesis defined in section 1.9. The new damage monitoring concepts, damage prevention method, damage-fee ash process and novel concept of PECVD low-*k* dielectric fabrication were proposed. All these findings and their relation to challenges of damascene technology were schematically shown in Figure 1.17. Furthermore, scientific bases of the proposed solutions were addressed. However, the plasma radical's transport in porous low-*k* films as well as optimization of the novel concept of the low-*k* fabrication is a subject for the future work. More attention should be concentrated on revealing the exact mechanism of diffusion-recombination of active plasma radicals, especially in microporous materials. Diffusion-recombination models for such type of materials, where pore size is comparable with the size of diffusing-recombining radical or molecule, are not well developed. Furthermore, the optimization of the novel low-*k* materials requires parametric study. The effect of variable UV-curing times and deposition conditions on final mechanical properties per *k*-value should be studied in order to achieve optimal film parameters.